Glassy Dynamics in Dense Active Matter

Citation for published version (APA):
Debets, V. E. (2023). *Glassy Dynamics in Dense Active Matter*. [Phd Thesis 1 (Research TU/e / Graduation TU/e), Applied Physics and Science Education]. Eindhoven University of Technology.

Document status and date:
Published: 07/07/2023

Document Version:
Publisher’s PDF, also known as Version of Record (includes final page, issue and volume numbers)

Please check the document version of this publication:

- A submitted manuscript is the version of the article upon submission and before peer-review. There can be important differences between the submitted version and the official published version of record. People interested in the research are advised to contact the author for the final version of the publication, or visit the DOI to the publisher's website.
- The final author version and the galley proof are versions of the publication after peer review.
- The final published version features the final layout of the paper including the volume, issue and page numbers.

Link to publication

General rights
Copyright and moral rights for the publications made accessible in the public portal are retained by the authors and/or other copyright owners and it is a condition of accessing publications that users recognise and abide by the legal requirements associated with these rights.

- Users may download and print one copy of any publication from the public portal for the purpose of private study or research.
- You may not further distribute the material or use it for any profit-making activity or commercial gain
- You may freely distribute the URL identifying the publication in the public portal.

If the publication is distributed under the terms of Article 25fa of the Dutch Copyright Act, indicated by the “Taverne” license above, please follow below link for the End User Agreement:

www.tue.nl/taverne

Take down policy
If you believe that this document breaches copyright please contact us at:

openaccess@tue.nl

providing details and we will investigate your claim.

Download date: 08. Apr. 2024

Glassy Dynamics in Dense Active Matter

Vincent Emanuel Debets

A catalogue record is available from the Eindhoven University of Technology Library.
ISBN: 978-90-386-5794-3

Cover design by: Vincent Debets & Heleen Tummers

Printed by: AIO Printing

Copyright © 2023 Vincent E. Debets. All Rights Reserved.

Glassy Dynamics in Dense Active Matter

PROEFSCHRIFT

ter verkrijging van de graad van doctor aan de
Technische Universiteit Eindhoven, op gezag van de
rector magnificus, prof. dr. S. K. Lenaerts, voor een
commissie aangewezen door het College voor
Promoties in het openbaar te verdedigen
op vrijdag 7 juli 2023, om 13:30 uur

door

Vincent Emanuel Debets

geboren te Roermond

Dit proefschrift is goedgekeurd door de promotoren en de samenstelling van de promotiecommissie is als volgt:

voorzitter:	prof. dr. W.M.M. Kessels
promotor:	dr. L.M.C. Janssen
2e promotor:	prof. dr. C. Storm
promotiecommissieleden:	prof. dr. A. Lyulin
	prof. dr. T. Franosch (University of Innsbruck)
	prof. dr. G. Szamel (Colorado State University)
	prof. dr. H. Löwen (Heinrich-Heine University Düsseldorf)
	dr. O. Dauchot (ESPCI Paris-PSL University)

Het onderzoek of ontwerp dat in dit proefschrift wordt beschreven is uitgevoerd in overeenstemming met de TU/e Gedragscode Wetenschapsbeoefening.

Contents

1 Introduction **1**
- 1.1 Supercooled liquids and the glass transition 2
  - 1.1.1 Hallmarks of glassy dynamics 6
- 1.2 Active motion in biology and soft matter 7
- 1.3 Dense active matter 9
  - 1.3.1 Active glasses 9
- 1.4 Outline of this thesis 12

2 Theoretical description of active glassy matter **15**
- 2.1 Active particle models 16
  - 2.1.1 Active Brownian particles (ABPs) 16
  - 2.1.2 Active Ornstein-Uhlenbeck particles (AOUPs) 20
- 2.2 Mori-Zwanzig formalism 21
- 2.3 Mode-coupling theory (MCT) 23

3 Cage length controls the nonmonotonic dynamics of active glassy matter **27**
- 3.1 Introduction 28
- 3.2 Simulation details 28
- 3.3 Athermal active particles 30
- 3.4 Thermal active particles 32
- 3.5 Conclusions 35
- 3.A Cage length estimation 36
- 3.B Additional data 37

4 The influence of particle softness on active glassy dynamics **39**
- 4.1 Introduction 40
- 4.2 Methods 40
- 4.3 Nonmonotonic behavior robust to changing softness 42
- 4.4 Approaching dynamical arrest 45
- 4.5 Conclusions 47

4.A Cage length estimation 48
4.B Static structure factor 49

5 Mode-coupling theory for mixtures of athermal self-propelled particles 51
5.1 Introduction 52
5.2 Multi-component active mode-coupling theory 52
5.3 Active-MCT numerics 58
5.4 Simulation details 58
5.5 Comparison with simulations 59
5.6 Conclusions 62

6 Active glassy dynamics is unaffected by the microscopic details of self-propulsion 65
6.1 Introduction 66
6.2 Active particle models 67
6.3 Mode-coupling theory 68
6.4 Active-MCT numerics 70
6.5 Simulation details 71
6.6 Free-particle dynamics 72
6.7 Glassy dynamics 73
6.8 Comparison with simulations 75
6.9 Conclusions 76
6.A Mode-coupling theory for active Ornstein-Uhlenbeck particles 77
6.B Rotational symmetry 83
6.C Mode-coupling theory for 3D active Brownian particles 84

7 Nonequilibrium correlation functions in thermal and athermal dense active fluids 91
7.1 Introduction 92
7.2 Integration through transients 93
7.3 Active-MCT and ITT numerics 96
7.4 Simulation details 96
7.5 Density correlations 97
7.6 Velocity correlations 98
    7.6.1 Active-active velocity correlation 99
    7.6.2 Active-passive and passive-passive velocity correlations 101
7.7 Conclusions 104
7.A Symmetry properties 105
7.B Analytical details 106
    7.B.1 Correlation of swim velocity corrections 106
    7.B.2 Nonequilibrium static structure factor 107
    7.B.3 Active-active velocity correlation 107

7.B.4 Active-passive velocity correlations 108
7.C Additional data for athermal systems 110
7.D Passive-passive velocity correlation for a Brownian system 110

8 Glassy dynamics in chiral fluids 113
8.1 Introduction 114
8.2 Simulation details 115
8.3 Nonmonotonic dynamics 116
8.4 cABP in a harmonic trap 118
8.5 Collective motion 119
8.6 Hammering dynamics 120
8.7 Conclusions 122
8.A Long-time diffusion coefficient at fixed active speed or spinning frequency 122
8.B Glassy features 123
8.C MSD of a cABP in a harmonic trap 125
8.D Additional data 128

9 Conclusions and outlook 131
9.1 Conclusions 132
9.2 Outlook 133

Bibliography 137

Summary 151

Samenvatting 153

Curriculum Vitae 155

List of publications 157

Dankwoord 159

Chapter 1

Introduction

Abstract. In this chapter, we introduce active glassy matter as an interesting new class of materials in biophysics and nonequilibrium soft condensed matter. We first discuss the distinct nonequilibrium natures of both glassy and active matter. This is followed by a detailed account of the importance of active glassy behavior in the context of biology and the theoretical challenges that arise when combining the two. We present the main goal of this thesis and the chapter is finalized by a brief outline of the remainder of the thesis.

1.1 Supercooled liquids and the glass transition

Glass constitutes arguably one of the most intriguing and perhaps paradoxical materials in existence, though to most people this might not be immediately apparent. Indeed its abundance in everyday life, e.g., glass cups, window panes, and vases, might easily suggest otherwise. Moreover, glass has already been manufactured by humans approximately six thousand years ago [1] and is thus hardly a revolutionary substance. But glass is much more than the transparent material (silicon dioxide) that it is commonly associated with. In fact, it represents an entire class of materials ranging from plastics, optical fibers, electronics, lenses, to even living matter [2, 3], and is sometimes referred to as a unique state of matter complementing conventional ones such as gas, liquid, and crystalline (see Fig. 1.1a). Comparing with these, the glass could be said to lie somewhere in between the disordered liquid and crystalline solid state, as it lacks any long-range structural order (like a liquid) but at the same time is solid (like a crystal) [4]. The term *disordered (or amorphous) solid* is therefore also used interchangeably with a glass.

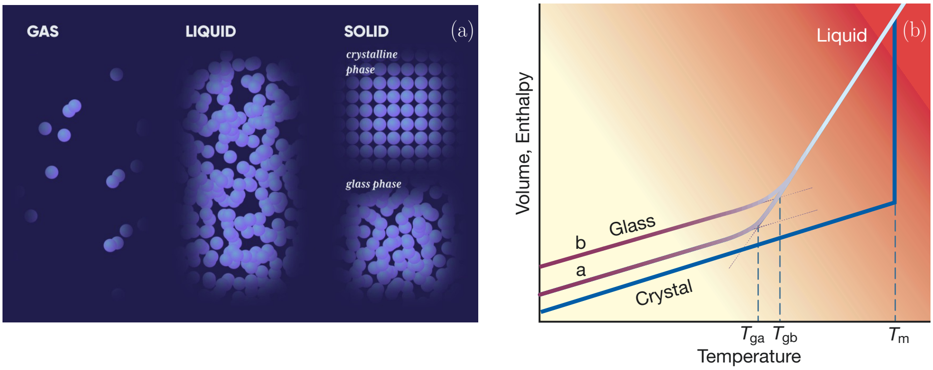

Figure 1.1: (a) Schematic visualization on the microscopic level of different phases of matter, i.e., gas, liquid, crystal, and glass. The latter is solid like the crystalline phase but looks surprisingly similar to the liquid phase. (b) Plot of the volume or enthalpy of a fluid as a function of temperature at constant pressure. As it cools below the melting temperature T_{m}, it reaches a supercooled state. Further cooling culminates in a glass transition at T_{ga} or T_{gb} for relatively slow and fast cooling rates respectively. Figures are adapted from [4, 5].

A natural question is then how any material reaches such a state. The two most common pathways are by sufficiently rapidly cooling (lower temperature) or compressing (larger density) a material beyond its crystallization point and have it enter what is known as the *supercooled liquid* regime [4, 6] (see Fig. 1.1b). In this regime, the liquid starts to flow increasingly slowly over a relatively small range of temperature or density which is usually quantified by a dramatic increase in the viscosity η. Convention then dictates that when a material's viscosity exceeds a critical threshold (for atomic and molecular glasses $\eta_\mathrm{c} = 10^{12}\mathrm{Pa}\cdot\mathrm{s}$ [7], which is orders of magnitude more viscous than for instance water, $\eta \sim 10^{-3}\mathrm{Pa}\cdot\mathrm{s}$, and honey, $\eta \sim 10^{1}\mathrm{Pa}\cdot\mathrm{s}$, at room temperature), it does not flow on any meaningful time scale and becomes a glass. In other words, it has undergone a glass transition. It is important to note that this is a purely dynamical transition and that the crystal (if one exists) still represents the true equilibrium state of the material. This explains why a sufficient cooling or compression rate is necessary, as it prevents the material from attaining the crystal state before it has undergone a glass transition. More crucially, this also highlights the general nonequilibrium nature of glasses and supercooled liquids.

Although the large scale behavior of glasses is fairly well understood on a phenomenological level (exemplified by their many applications), it is at the microscopic (or particle-based) level that things start to become puzzling and why to this date what is known as the 'glass problem' still enjoys great attention in theoretical physics [8, 9]. In particular, the dramatic increase in viscosity during supercooling is accompanied by only a marginal change in the structure [4, 9, 10]. This means that on the microscopic scale a glass is almost indistinguishable from a liquid (as opposed to the ordered crystalline state, see Fig. 1.1), making it far from evident which physical mechanisms are responsible for the glass transition.

To illustrate this in more detail, let us seek a description of a material on this level. For that we usually start from what is known as the microscopic density,

$$\rho(\mathbf{r},t) = \sum_{i=1}^{N} \delta(\mathbf{r} - \mathbf{r}_i(t)), \tag{1.1}$$

which is proportional to the probability of encountering a particle i at a position $\mathbf{r}$ and a time t, with N the total number of particles in our material and $\delta(\mathbf{x})$ denoting the Dirac delta function. Note that for simplicity we only focus on particle positions but other phase space variables such as velocities or orientations of molecules can be naturally added if deemed useful. Arguably one of the simplest probes to infer structural information is the so-called static structure factor which is readily obtained in scattering experiments [11, 12]. This function correlates two (conjugate) Fourier components of the microscopic density (or density modes), $\rho(\mathbf{k},t) = \sum_{i=1}^{N} e^{i\mathbf{k}\cdot\mathbf{r}_i(t)}$, at a wavevector $\mathbf{k}$ that measures the inverse length scale, and is given by [13],

$$S(k) = \frac{1}{N} \left\langle \rho^*(\mathbf{k},0)\ \rho(\mathbf{k},0) \right\rangle. \tag{1.2}$$

Here, the brackets denote an ensemble average and for an isotropic system $S(k)$ only depends on the wavenumber $k = |\mathbf{k}|$. Physically, it may be interpreted as the density response of our material to an external perturbation with wavelength $2\pi/k$ [13]. To understand its behavior, we show in Fig. 1.2 several examples of $S(k)$ for a system of colloidal spheres as we transition from a liquid to a glass state. Most noticeable is the main peak at $k \sim 2\pi/\sigma$ (with σ the diameter of the particles) implying that the strongest response occurs at roughly the nearest-neighbor distance. Moreover, it is apparent that only subtle changes to $S(k)$ are induced upon vitrification which is a clear reflection of their similar microscopic structures (see also Fig. 1.1).

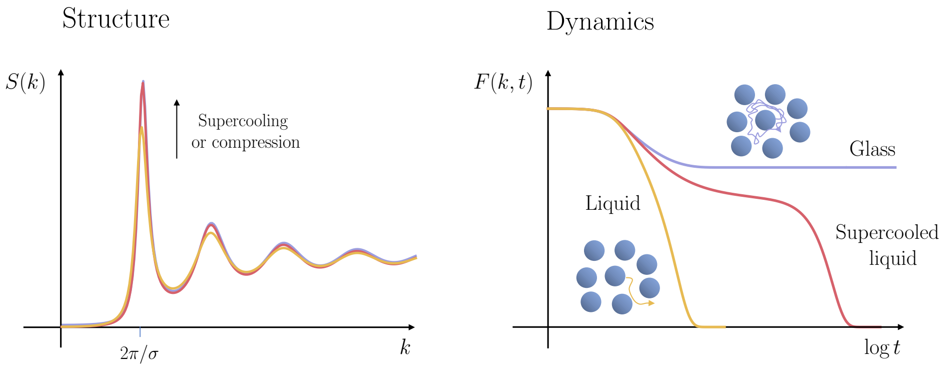

Figure 1.2: Schematic visualization of the microscopic structure and dynamics, as probed by the static structure factor $S(k)$ and the intermediate scattering function $F(k,t)$ respectively, of a system of colloidal spheres upon approaching the glass transition. Note that the values of $S(k)$ look very similar, while the corresponding values for $F(k,t)$ are highly different. In the glass state particles are caged by their surroundings, whereas in the liquid state they can easily break out and move through the material.

To study the microscopic dynamics of our material, it is customary to consider the dynamic counterpart of $S(k)$, that is, the intermediate scattering function, which has the same advantage as $S(k)$ of also being directly obtainable from scattering experiments [11, 12]. This function measures the decay of collective density fluctuations of wavelength $2\pi/k$ [13] or, more simply, it measures the resemblance between a microscopic configuration and its subsequent one a time t later, probed over a length scale $2\pi/k$. It is defined as [13]

$$F(k,t) = \frac{1}{N} \left\langle \rho^*(\mathbf{k},0)\ \rho(\mathbf{k},t) \right\rangle . \tag{1.3}$$

In Fig. 1.2 we also show typical intermediate scattering functions for a system of colloidal spheres upon supercooling. A quick glance immediately reveals the dramatic slowdown associated with the glass transition. Specifically, in the liquid regime $F(k,t)$ decays rapidly to zero which implies that the material quickly takes on new microscopic configurations and explains why it is able to flow easily. When approaching the glass state the decay is instead seen to take increasingly long (also note the logarithmic time scale). In other words, the relaxation time of $F(k,t)$, which is directly related to the viscosity, increases by orders of magnitude. We also witness the emergence of a plateau at intermediate timescales, which is a manifestation of the so-called cage effect [14, 15] (see Fig. 1.2). This effect provides a conceptual explanation for the two-step relaxation by considering particles being surrounded by neighboring particles, i.e., their cage, and rattling inside it. In this way, part of the overlap with the initial configuration is lost though certainly not all and therefore $F(k,t)$ reaches a plateau. For the system to truly relax and thus able to flow, particles have to escape their cages, which becomes progressively difficult (longer plateaus) upon approaching the glass transition. At some point, particles are not even able to do so entirely on any reasonable time scale and are in a sense stuck in their initial microscopic configuration, yielding a rigid and thus glass state. Note that this is exactly the phenomenology that has been sketched on the macroscopic scale, only now recovered from a fully microscopic perspective. This also reveals the direct connection between the relaxation time of $F(k,t)$ and the viscosity.

The glass problem is thus characterized by a seemingly large discrepancy between structure and dynamics, which is unusual for phase transitions in physics, and, from a dynamical perspective, essentially leaves us with two possibilities. First, it is not implausible that a more intricate form of structural order actually emerges in the glass during vitrification which cannot be properly captured by standard two-point correlations such as the static structure factor. This would point to studying more involved structural features. Indeed, recent results focusing on more complex and/or higher-order structural correlations show more significant changes and thus look promising [10, 16–20]. At the same time, their physical interpretation is not always straightforward (especially in the Fourier domain) and the variety in systems is fairly limited still.

Alternatively, one can search for a dynamical feedback mechanism that is capable of amplifying the subtle structural changes, e.g., in $S(k)$, into the vastly different dynamics. This seems like a daunting task and indeed no theory to date is capable of fully describing the microscopic relaxation dynamics using only structural features as input. The only first-principles-based approach that has at least been partly able to make reasonable predictions about structural glass-forming liquids is the mode-coupling theory (MCT) [15, 21, 22]. This theory can predict both the caging behavior and the dramatic increase in relaxation time of $F(k,t)$ with a reasonable degree of quantitative accuracy based solely on the corresponding $S(k)$. However, it fails to capture more intricate features of glassy dynamics that are discussed below and for which fundamental insights are mostly obtained from simulations. Finally, we mention that there exists a wealth of other and more phenomenological theories on the structural glass transition [9, 10, 23], though in this thesis emphasis is placed on a fully microscopic description.

1.1.1 Hallmarks of glassy dynamics

The most distinctive features of the glass transition are the dramatic slowdown of the dynamics and its apparent disconnect with structure. But as a material slows down in the supercooled regime, several other generic hallmarks of glassy dynamics also manifest themselves which we will now briefly discuss.

Let us start with the concept of fragility which relates to the rate at which the viscosity (or relaxation time) of a material changes with the temperature or density [4, 6, 7]. If this occurs in an Arrhenius (or exponential) fashion, that is, the material vitrifies relatively gradually, one usually speaks of a so-called *strong* glass former. If the material instead exhibits a more abrupt super-Arrhenius growth it is often classified as being *fragile*. Naturally, most glasses fall somewhere in between the range from strong to fragile and in several cases can even crossover from one to the other [24]. As a rule of thumb, it is often claimed that network-forming glasses such as silica tend to be strong, whereas simpler isotropic systems like colloidal spheres are more fragile [25]. However, a fully microscopic understanding of this behavior is still fundamentally lacking and could hold great promise for especially the processability of glasses [26].

Another key hallmark of glassy dynamics is dynamical heterogeneity [27–31]. It denotes the fact that structural relaxation in a supercooled liquid becomes increasingly heterogeneous, with certain domains of particles within the material rearranging, while other parts remain relatively immobile. As a result, the relaxation time of individual constituent particles becomes progressively disparate. It is still unclear whether such domains emerge from increasingly rare localized relaxation events that locally facilitate further ones or if it requires a growing collective effort to induce these events in the first place. Moreover, we emphasize that this remains a transient effect and over time certain initially immobilized regions can become part of a rearranging one and vice versa.

Dynamical heterogeneity is also believed to be linked to another aspect of glassy dynamics, namely the breakdown of the Stokes-Einstein relation (SER) [32–34]. This equation asserts that the viscosity η (or relaxation time τ), self-diffusion coefficient D, and temperature T should obey $\eta D/T =$ constant. In normal liquids the SER usually holds, while in most supercooled liquids it becomes progressively violated as a result of the stronger increase of the viscosity than the corresponding decrease of the diffusion coefficient (note that D can thus also be used to measure the slowdown of the dynamics upon supercooling). This has been explained by realizing that diffusion is primarily dominated by the fastest particles whereas viscosity relates to structural relaxation that is governed by the slowest ones. As such, the breakdown of the SER is anticipated to be a manifestation of dynamical heterogeneity [33, 34] and is also not fully microscopically understood.

The final aspect of glassy dynamics we will highlight, aging, is intimately linked to its nonequilibrium nature [4, 35, 36]. It is usually understood as the gradual movement towards the true underlying equilibrium state which leads to both structural and dynamical properties slowly varying over time, that is, the material ages. Aging effects have been shown to become more dramatic when a liquid is rapidly quenched into the supercooled or glass state as it gives the material in a sense no time to adept to its new conditions. Moreover, relaxation times in the glass state are by definition exceedingly long and thus aging can literally take lifetimes. Finally, to allow for a supercooled liquid to reach a (quasi-)equilibrated state (in which it does not age) without crystallizing, it is often customary in especially colloidal experiments and computer simulations to frustrate the underlying crystalline state by for instance introducing a degree of polydispersity in particle sizes [6, 37, 38]. This makes such liquids much more convenient to study.

1.2 Active motion in biology and soft matter

Since its salient features are still not fully understood, it should come as no surprise that the glass problem remains one of the archetypical fields of study in nonequilibrium physics. In the last few decades a new candidate has, however, also presented itself and gained much interest in that broad area of research. So-called active matter represents a relatively new class of materials comprised of particles that are able to harvest energy internally or directly from their environment and (continuously) convert it into either self-propelled or self-rotating motion (or a combination of both). As such, they are intrinsically out of equilibrium on the single-particle level which is fundamentally different from glasses that are in a sense brought out of equilibrium externally and collectively during a temperature or density quench.

Among the first systems to be recognized as active (that is, in a physical sense) are macroscopic swarms and flocks of animals whose qualitative features have been successfully described using the pioneering Vicsek model [39] and its subsequent field-theoretic version [40]. Interestingly, this model requires only two minimal physical ingredients, i.e., a constant self-propulsion speed and local alignment of self-propulsion velocities. Its success has therefore clearly illustrated the potential of active matter theory to serve as a novel statistical-physics-based approach to understand seemingly more complex aspects of living systems. Indeed, since then, active-matter physics has spread throughout the entirety of biology and across many different length scales. This includes (but is not limited to) for instance, human crowds [41, 42], embryos [43], tissues [44], cell layers and clusters [45–48], motile microorganisms [49, 50], and even subcellular units such as chloroplasts [51] and molecular motor proteins [52]. It is worth noting that in all these cases active motion is driven by ATP on the molecular level.

In part inspired by the intricate (and often collective) features of biological active entities, a growing effort has concomitantly been put into the production and study of *synthetic* active particles. Such artificial structures also span a variety of length scales but can in principle employ highly different mechanisms to induce active motion. Notable examples are vibrating granular disks or ellipsoids [53–55], swimming droplets [56, 57], Janus colloids driven by light or concentration gradients [58–62], electromagnetic colloids [63–65], and man-made molecular motors [66, 67].

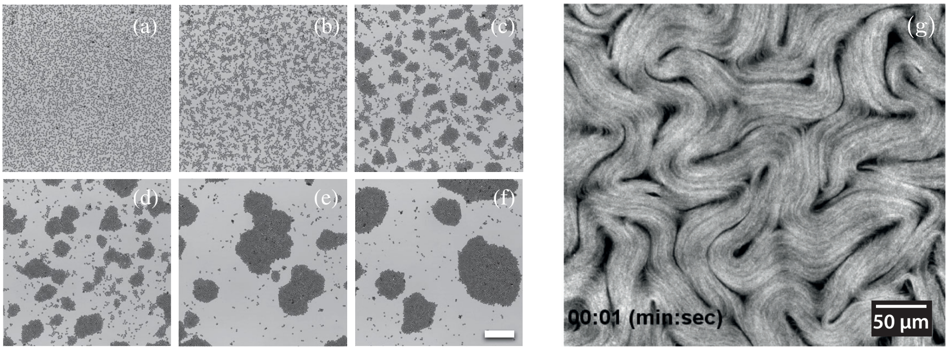

Figure 1.3: Experimental realizations of two distinctly nonequilibrium active matter features. (a-f) Time lapse of motility induced phase separation (MIPS) where self-propelling Janus colloids spontaneously aggregate without any explicit attractive interactions. (g) Despite being in the overdamped regime, turbulent-like flows (or active turbulence) emerge(s) in an active microtubule-kinesin suspension. Results are adapted from [68, 69] respectively.

Whether living or synthetic, what makes active materials so fascinating is their intrinsic nonequilibrium nature. This can give rise to novel and collective behavior that is notoriously inaccessible to conventional passive matter (see Fig. 1.3). In that regard, two particularly well-known and distinctly active features are motility induced phase separation (MIPS) [68, 70–72] and active turbulence [73, 74], though there exist many more [53, 75–77]. On a fundamental level one of the key goals of active matter research is to explore and understand how active properties on the single-particle level translate to such (and potentially new) emergent collective phenomena. From a more applied perspective, one can then test whether these may rationalize part of the hierarchical organization ubiquitous in living matter or if they can be exploited in the synthetic realm to attain 'smart' and bioinspired materials.

1.3 Dense active matter

Initially, active matter studies have been primarily focused on the single-particle level up to the moderate-density regime [78], but more recently interest has also shifted toward increasing densities [79, 80]. In this regime particle-particle interactions become increasingly more dominant and indeed a monodisperse active liquid also starts to crystallize when pushed to a sufficiently large density which culminates in what is known as an active crystal [77, 81–84]. Naturally, the point at which it exactly crystallizes heavily depends on the details of active motion, as rapidly self-propelling particles can fluidize an active crystal. It has even been shown that, in principle, extreme activity can stabilize a fluid state of self-propelling hard spheres at almost random close packing [85].

1.3.1 Active glasses

In practice active particles are, however, seldom fully monodisperse or symmetric due to, for instance, experimental challenges during the synthesis of colloids or heterogeneity in cells. This severely complicates crystallization and brings us to the main focal point of this thesis, i.e., active glassy materials. Such dense and disordered materials exhibit glass-like behavior on the collective scale despite their constituent particles seeking to convert energy into active motion on the microscopic scale. As such, they combine the two aforementioned and unique fields in nonequilibrium physics, thereby opening up the way for the potential discoveries of fundamentally new physics.

Besides representing a fascinating fundamental challenge, active glassy matter also carries notable relevance in the biological realm. In fact, it is the manifestation of glass-like (or jamming[1]) behavior in a variety of living systems (see Fig. 1.4 for some examples) and their implications in biological function that has encouraged researchers to truly appreciate this subclass of materials.

On the intracellular level, both eukaryotic and prokaryotic cells (which physically can be regarded as an active liquid) have been shown to exhibit glassy features such as an increased viscosity upon changing the properties of their respective cytoplasm [3, 87, 89, 90]. Moreover, the depletion of ATP and metabolic activity inside the cells strongly

---

[1] The fluid-solid transition in disordered active materials has in literature interchangeably been referred to as both a glass and jamming transition. Strictly, a glass transition emerges from the competition between crowding and particle agitation, whereas jamming is understood as a purely geometric effect in the absence of any intrinsic microscopic dynamics such as active motion [79, 80, 86]. We therefore prefer to characterize the dynamical slowdown in dense active matter as glassy rather than jamming.

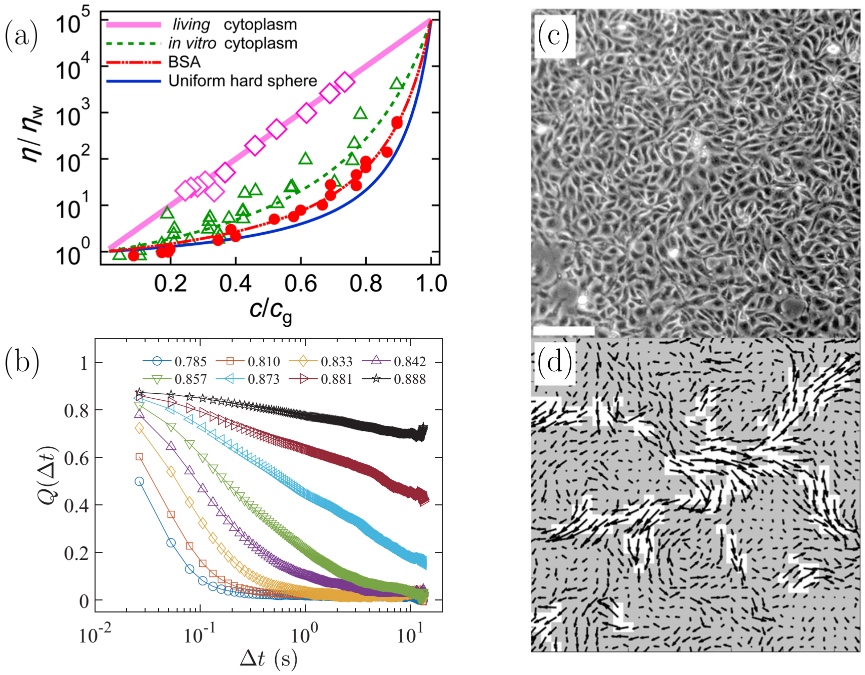

Figure 1.4: Examples of active glassy behavior in biological systems. (a) the normalized viscosity of human cells and *E. coli* bacteria increases dramatically with internal macromolecule concentration and has a stronger fragility than simple hard spheres. (b) The overlap function [similar probe as $F(k,t)$] decreases significantly more slowly upon increased density in a dense suspension of bacteria. (c) Snapshot of Madine-Darby canine kidney cells (MDCK) close to a glass transition and (d) the associated dynamically heterogeneous velocity field. Results are adapted from [2, 87, 88] respectively.

influence their glassy behavior, notably the fluidity and the fragility. In other words, nonequilibrium active processes have a distinct impact on the glassy dynamics which cannot be solely attributed to crowding effects inside the cell.

As living cells have the ability to autonomously locomote, they can also be considered as individual active particles. Taking this analogy further one can physically interpret amorphous cell collectives that can transition from a rigid to a malleable state essentially as active glassy materials. Indeed, glassy dynamics has for instance been witnessed in a cell sheet of Madine-Darby canine kidney (MDCK) cells where the relaxation dynamics has been shown to slow down with increasing cell density [2]. This has been quantified by a significant decrease of the diffusion coefficient of individual cells (which is roughly equivalent to a strong increase in the relaxation time or viscosity). Moreover, several more salient features such as fragile and dynamically heterogeneous behavior have also been observed. Strikingly, the dynamical heterogeneity appears to originate from nontrivial correlations in the instantaneous velocities of cells. Such correlations are crucially absent in passive materials [91] and thus represent a distinct active manifestation of a conventional glassy hallmark.

In recent years, more examples of intercellular active glassy behavior have also been found in the context of asthma, wound healing, embryonic development, and cancer [45, 92–96]. In all these cases the common denominator appears to be transitions of the involved cell collective from a stationary (glass-like) to a migratory (liquid-like) state (or vice versa) via active processes such as enhanced cell motility. It is therefore not unimaginable that cell activity serves as a direct and crucial means to control cellular glassiness and perhaps steer biological function. Though this remains speculative, it has recently been argued that glassy behavior is indeed essential during tissue development and in cancer [96, 97].

From a material science perspective, the ability to externally dictate the activity of individual particles comprising a glassy material (via e.g., an electromagnetic field) ideally allows for a controlled transition between the fluid and amorphous solid, or even direct control over its viscosity. Though this holds great promise for adaptive materials that may be used in engineering applications, the experimental realization of synthetic active glasses still proves to be challenging. Only recently, the first active colloidal supercooled liquids and glasses have been synthesized using Janus particles driven by diffusiophoresis [98, 99]. This has been shortly followed by a granular active glass using ellipsoidal particles [55]. The importance of these studies cannot be overstated as they allow for easier physical insights to be extracted that are usually more difficult to obtain from complex glassy living matter.

Overall, active glassy matter is rapidly surfacing as an important subclass of materials which explains why a growing body of literature has concomitantly been devoted to gaining deeper understanding of its phenomenology via both theory [100–110] and computer simulations [48, 85, 91, 111–121]. This has so far primarily been done by means of simple model systems which only incorporate persistent self-propelled motion and crowding effects to represent the active and glassy phenomenology respectively (common examples are given in Chapter 2). Despite their minimal nature, such models still show remarkably rich behavior and exemplify the nontrivial effects active motion can have on glassy dynamics. The main appeal of this approach then comes from the possibility to more easily extract fundamental insights from the observed behavior. In turn these can serve as a benchmark to interpret the dynamics of more complex active glassy materials. Fundamentally understanding the role of active motion on glassy dynamics and to what degree active systems can be mapped onto passive ones has thus emerged as a highly interesting and important new area of research that we seek to further explore in this thesis.

1.4 Outline of this thesis

Active glassy matter thus enjoys incredibly interesting implications in relation to biology, while also providing novel pathways to amorphous materials with tunable properties. At the same, it presents an intriguing fundamental challenge as it is faced with a still incomplete understanding of the conventional glassy phenomenology to which a second source of nonequilibrium dynamics is added. This highlights the dire need of a better fundamental understanding of such active glassy behavior, which constitutes the central goal of this thesis. More specifically, we want to explore the possible existence of universal governing principles in dense active matter, the role of nontrivial velocity correlations in light of the conventional structure-dynamics relation, the importance of the microscopic details of active dynamics as particle-particle interactions become increasingly more dominant, and novel extensions of standard active glassy model systems.

Accordingly, in **Chapter 2**, we first introduce the model active particles that comprise our active glassy fluid. This is followed by a brief summary of the so-called Mori-Zwanzig projection operator formalism which represents a generic nonequilibrium physics framework that will be employed to theoretically study active glassy dynamics.

Even for our choice of simple model systems, the glassy dynamics can be conspicuously different from their passive Brownian counterpart. Controversially, this difference has been shown to manifest itself via either a speedup, slowdown, or nonmonotonic change of the glassy relaxation dynamics. We rationalize these seemingly contrasting views in **Chapter 3** by identifying the ratio of the short-time active length scale to the cage length, i.e., the length scale of local particle caging, as a vital and unifying control parameter for active glassy matter. We also provide a physical explanation for this insight based on the most efficient scanning of local particle cages.

The observed universal active glassy behavior is further validated in **Chapter 4**. We demonstrate that the cage length argument remains fully intact for both more deeply supercooled particles and particles with a longer range and softer interaction potential. We also show that only when the active length scale surpasses the cage length, distinct qualitative changes with respect to an equivalent passive Brownian particle system start to manifest themselves.

In **Chapter 5**, to address the structure-dynamics relation in active glassy matter, we develop a generic active mode-coupling theory (MCT) for mixtures of athermal self-propelled particles. The theory naturally requires nontrivial spatial velocity correlations that complement the structure factor as static input. It also gives predictions that are qualitatively fully consistent with computer simulations.

Due to the dominant role of particle-particle interactions, it is well established that the details of the microscopic dynamics, e.g., Newtonian or Brownian, do not influence the long-time passive glassy behavior. In **Chapter 6**, we verify that this also holds true for our active particle models by deriving and solving active MCTs that explicitly take into account the active degrees of freedom. We find that our models give almost identical results for the intermediate scattering function over a large variety of control parameters implying that the microscopic details of their self-propulsion do not alter the active glassy behavior.

One of the key hallmarks of dense active matter are (spontaneously emerging) spatial velocity correlations. In **Chapter 7**, we present a fully microscopic method to calculate nonequilibrium correlations for a dense active fluid. We analytically calculate qualitatively consistent static structure factors and active velocity correlations. Our theoretical results are complemented with simulations which exemplify the disruptive role thermal noise has on such velocity correlations.

In **Chapter 8**, we extend our simulations to also include chiral motion (or circle swimming) which anticipates the rich variety of asymmetries that can be attained in, e.g., the shape or self-propulsion mechanism of active particles. We demonstrate that when our chiral fluid is pushed to glassy conditions, it exhibits highly nontrivial dynamics, especially compared to a standard linear active fluid that is usually considered. Despite the added complexity, we present a full rationalization for all identified dynamical regimes.

The thesis is finalized by a brief recap of our main findings and conclusions in **Chapter 9**. These are also placed in a broader context after which we discuss some avenues for further research.

Chapter 2

Theoretical description of active glassy matter

Abstract. In this chapter, we introduce several theoretical concepts that will be frequently employed throughout the rest of this thesis. In particular, we provide a detailed formulation of the two active particle models that are at the core of this thesis and discuss some of their intrinsic features. We also give a brief summary of the so-called Mori-Zwanzig projection operator formalism and mode-coupling theory which, in conjunction with the active particle models, serve as the foundation of our subsequent theoretical Chapters 5 to 7.

2.1 Active particle models

As detailed in the previous chapter, the central aim of this thesis is to provide fundamental insights into glassy active matter, which we hope can serve as a benchmark or foundation for subsequent work involving more realistic dense active materials in both the biological and synthetic realm. This implies that we take a bottom-up approach and employ minimal models to comprise our dense active fluid. In particular, we use the paradigmatic active Brownian particle (ABP) and the active Ornstein-Uhlenbeck particle (AOUP) models which we now briefly introduce. Before proceeding, we already mention that since most active matter systems (especially biological ones) are in the low-Reynolds regime, where viscous forces dominate over inertial ones, and hydrodynamic interactions are expected to be screened in dense conditions (which for passive glassy systems is strictly true), we take both overdamped and dry conditions.

2.1.1 Active Brownian particles (ABPs)

Perhaps one of the most cardinal aspects that distinguishes active from passive matter is the former's ability to perform autonomous and persistent locomotion. In the simplest approach we can assume that this locomotion takes on the form of a constant self-propulsion speed, that is, particles (cells, bacteria, Janus colloids etc.) convert energy into motion at a roughly constant rate. Moreover, whether due to for instance collisions with the surrounding solvent molecules, cell membrane fluctuations, or internal reorganization of the cytoskeleton, both the direction of the self-propulsion and the (center-of-mass) position of the particles can change over time. Usually, if one looks at sufficiently large length and time scales, these changes are assumed to occur approximately randomly and in an uncorrelated fashion. However, in some cases asymmetries in, e.g., the shape, mass distribution, or self-propulsion mechanism, are inherently present which can additionally lead to chiral or spinning motion.

Combining these ingredients, we arrive at arguably one of the most well-studied minimal model systems for active matter, i.e., the active Brownian particles or ABPs [78] (see Fig. 2.1 for a schematic depiction of these particles). In this model the equation of motion for the position $\mathbf{r}_i$ of each particle i is given by

$$\dot{\mathbf{r}}_i = \zeta^{-1} \left(\mathbf{F}_i + \mathbf{f}_i \right) + \boldsymbol{\xi}_i, \tag{2.1}$$

where ζ is the friction coefficient imposed by the surroundings, $\boldsymbol{F}_i$ is the interaction force between particles, and $\boldsymbol{\xi}_i$ represents a Gaussian thermal noise with zero mean and variance $\left\langle \boldsymbol{\xi}_i(t)\boldsymbol{\xi}_j(t') \right\rangle_{\mathrm{noise}} = 2D_{\mathrm{t}}\mathbf{I}\delta_{ij}\delta(t-t')$, with D_{t} the diffusion coefficient and $\mathbf{I}$ the unit matrix. The self-propulsion speed v_0 is constant so that the active force equals $\mathbf{f}_i = \zeta v_0 \mathbf{e}_i$. The directions of the self-propulsion in two (2D) and three

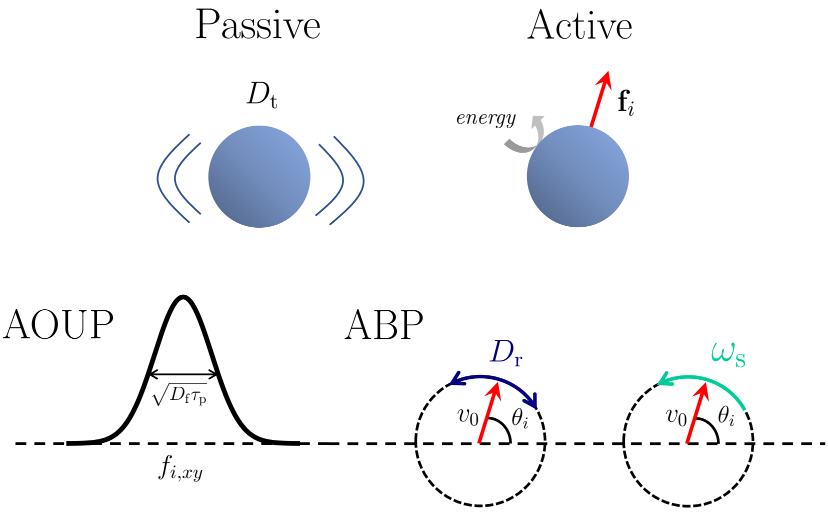

Figure 2.1: Schematic visualization of both the active Brownian particle (ABP) and the active Ornstein-Uhlenbeck particle (AOUP) model in two dimensions. Both models include thermal translational diffusive motion with a diffusion coefficient D_t and an active self-propulsion force $\mathbf{f}_i$. Their difference rests in the implementation of the active force $\mathbf{f}_i$. For ABPs it is chosen to yield a constant active speed v_0 while its orientation angle θ_i can undergo random rotational diffusion (D_r) and deterministic spinning motion (ω_s). In comparison, the AOUP model lets both Cartesian components of the active force $f_{i,xy}$ evolve in time such that their value is Gaussian-distributed with a standard deviation $\sqrt{D_\mathrm{f}\tau_\mathrm{p}}$.

(3D) dimensions are parametrized as $\mathbf{e}_i = [\cos(\theta_i), \sin(\theta_i)]$ (with $\theta_i \in [0, 2\pi]$) and $\mathbf{e}_i = [\cos(\phi_i)\sin(\theta_i), \sin(\phi_i)\sin(\theta_i), \cos(\theta_i)]$ (with $\phi_i \in [0, 2\pi]$, $\theta_i \in [0, \pi]$) respectively, and evolve in time according to [104, 122],

$$\dot{\theta}_i = \chi_i + \omega_\mathrm{s} \quad \text{(2D)} \qquad\qquad \dot{\mathbf{e}}_i = (\boldsymbol{\chi}_i + \boldsymbol{\omega}_\mathrm{s}) \times \mathbf{e}_i \quad \text{(3D)}. \tag{2.2}$$

Here, ω_s represents a constant spinning frequency, which is only nonzero for chiral ABPs, χ_i a Gaussian noise process with zero mean and variance $\langle \chi_i(t)\chi_j(t')\rangle_\mathrm{noise} = 2D_\mathrm{r}\delta_{ij}\delta(t-t')$, and D_r the rotational diffusion coefficient. Moreover, $\boldsymbol{\omega}_\mathrm{s}$ and $\boldsymbol{\chi}_i$ denote the 3D vector analogues of ω_s and χ_i respectively.

Having specified the involved equations, it is also worth pointing out that the diffusion coefficient is directly related to the thermal energy (or temperature) via the following fluctuation-dissipation relation, $D_\mathrm{t} = k_\mathrm{B}T\zeta^{-1}$, and thus D_t and T are often used interchangeably to quantify translational diffusion in the ABP model. For spherical particles immersed in a solvent, the fluctuation-dissipation theorem predicts even a direct connection between the translational and rotational diffusion coefficients, i.e., $D_\mathrm{r} = 3D_\mathrm{t}/\sigma^2$ with σ the diameter. We, however, refrain from using this relation and take D_r as an independent control parameter to account for the fact that many active particles can also reorient via other mechanisms than thermal fluctuations (e.g., internal changes in the cell or rotations of bacterial flagella). Importantly, in the context of active matter, when one mentions an athermal active system (as opposed to a thermal one) it is thus usually implied that translational diffusion is absent, $D_\mathrm{t} = 0$, while rotational diffusion is kept intact, $D_\mathrm{r} > 0$.

To better understand the model, it is instructive to consider the dilute regime where interactions are absent ($\mathbf{F}_i = 0$) and focus on so-called linear swimmers for which spinning motion is assumed to be dominated over by rotational diffusion ($\omega_\mathrm{s} = 0$). In this case the model can be analytically shown to yield a persistent random walk (PRW) with a mean square displacement (MSD) [78, 123]

$$\left\langle \delta r^2(t) \right\rangle = 2dD_\mathrm{t}t + 2dD_\mathrm{a}\left(\tau_\mathrm{p}(e^{-t/\tau_\mathrm{p}} - 1) + t\right). \tag{2.3}$$

Such a PRW in dimension d is characterized by a persistence time $\tau_\mathrm{p} = [(d-1)D_\mathrm{r}]^{-1}$, and an active ($D_\mathrm{a} = v_0^2\tau_\mathrm{p}/d$) and passive ($D_\mathrm{t}$) diffusion coefficient. The nature of these terms can be extracted via an inspection of the short- and long-time behavior of Eq. (2.3) (see also Fig. 2.2 for an example plot of the MSD). In particular, at short-to-intermediate times ($t \lesssim \tau_\mathrm{p}$) the motion is comprised of a diffusive and ballistic contribution $\left\langle \delta r^2(t) \right\rangle \approx 2dD_\mathrm{t}t + v_0^2t^2$. This shows that after an initial diffusive regime particles migrate persistently with their intrinsic active speed v_0 over a time scale roughly equal to the persistence time τ_p. In the long-time limit ($t \gg \tau_\mathrm{p}$), as a result of particles having frequently changed the direction of their active force, the motion becomes fully diffusive with an enhanced (or effective) diffusion coefficient $\left\langle \delta r^2(t) \right\rangle \approx 2d(D_\mathrm{a} + D_\mathrm{t})t \equiv 2dD_\mathrm{eff}t$. This also means that in the limit $\tau_\mathrm{p} \to 0$ (with $D_\mathrm{a} \sim$ constant), ABPs become essentially equivalent to 'warmer' passive Brownian particles with an enhanced diffusion coefficient $D_\mathrm{eff} = D_\mathrm{a} + D_\mathrm{t}$. Overall, the ABP thus allows some variety in its choice of control parameters. A natural choice and one that connects to experiments would be to focus on v_0 and τ_p. However, from a fundamental perspective it is sometimes more useful to vary D_a and τ_p to ensure constant long-time diffusive behavior that can be directly compared to a passive reference system.

Interestingly, a simple PRW has already proven capable of (at least to first order) describing the dynamics of many active particles in the dilute regime, such as bacteria [124], chloroplasts [51], and Janus colloids [58–62], human cells on a substrate [125], and in a collagen network [126]. For the colloidal particles, even more intricate spatiotemporal

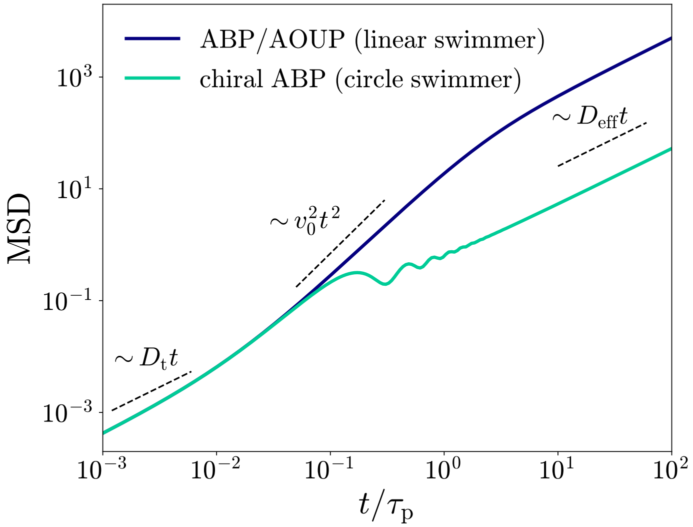

Figure 2.2: Example solutions of the MSD for ABPs and AOUPs (linear swimmers) [Eq. (2.3)] and for chiral ABPs (circle swimmers) [Eq. (2.4)] in the dilute limit. Parameters are $D_\mathrm{t} = 0.1$, $v_0 = 5$, $\tau_\mathrm{p} = 1$, and $\omega_\mathrm{s} = 20$. Relevant scalings are added to illustrate the transition between diffusive and ballistic regimes.

features like an intermediate scattering function have been accurately fitted with analytical results obtained for ABPs [58]. This indicates that, despite its simplicity, the (non-chiral) ABP model can make a connection with much more involved experimental systems. Moreover, by means of simulations it has been shown that the ABP model can also capture many aspects of interacting active particles, thus exemplifying its central role in active matter theory [127–132].

However, as already mentioned, there also exist situations for which spinning motion cannot be neglected. This severely complicates the ABP model which is likely why so-called chiral ABPs or circle swimmers (with $\omega_\mathrm{s} \neq 0$) are mostly considered only in two spatial dimensions and have so far received less attention compared to their non-chiral counterpart. In this case it can be shown that in the dilute regime the MSD obeys [123, 133]

$$\begin{aligned} \left\langle \delta r^2(t) \right\rangle = 4D_\mathrm{t} t + \frac{2v_0^2\tau_\mathrm{p}^2}{\left(1+(\omega_\mathrm{s}\tau_\mathrm{p})^2\right)^2} \Big[&(\omega_\mathrm{s}\tau_\mathrm{p})^2 - 1 + \left(1+(\omega_\mathrm{s}\tau_\mathrm{p})^2\right) t/\tau_\mathrm{p} \\ &+ e^{-t/\tau_\mathrm{p}} \left[\left(1-(\omega_\mathrm{s}\tau_\mathrm{p})^2\right)\cos(\omega_\mathrm{s} t) - 2\omega_\mathrm{s}\tau_\mathrm{p}\sin(\omega_\mathrm{s} t) \right] \Big], \end{aligned} \tag{2.4}$$

where the trigonometric functions impose oscillatory behavior, which represents a clear signature of the induced circular motion (see Fig. 2.2 for an example plot of the MSD). These oscillations (and thus the impact of chirality) become more prominent as $\omega_\mathrm{s}\tau_\mathrm{p}$ increases. Still, in the long-time limit ($t \gg \tau_\mathrm{p}$, $t \gg \omega_\mathrm{s}^{-1}$) the oscillations die out and the dynamics once again become diffusive with an effective diffusion coefficient $D_\mathrm{eff} = D_\mathrm{t} + \frac{v_0^2\tau_\mathrm{p}}{2}\frac{1}{1+(\omega_\mathrm{s}\tau_\mathrm{p})^2}$. This implies that spinning motion always reduces the long-time diffusivity of ABPs in the dilute regime.

2.1.2 Active Ornstein-Uhlenbeck particles (AOUPs)

To complement the ABPs, the active Ornstein-Uhlenbeck particle (AOUP) model has concomitantly been introduced. Its main appeal, especially in more fundamental theoretical and simulation studies, comes from it including self-propulsion but generally being more analytically tractable when compared to the ABP model [134, 135]. Employing the same equation of motion for the center-of-mass position $\mathbf{r}_i$, i.e., Eq. (2.1), the crucial difference between both models rests in the manner in which the active force (or velocity) is assumed to change over time. Instead of fixing its magnitude, the active force evolves in time according to an Ornstein-Uhlenbeck process which amounts to the following equation [91, 102–104, 112, 113]

$$\dot{\mathbf{f}}_i = \tau^{-1}\mathbf{f}_i + \boldsymbol{\eta}_i, \tag{2.5}$$

Here, τ depicts the characteristic decay time of the self-propulsion and $\boldsymbol{\eta}_i$ is an internal Gaussian noise process with zero mean and variance $\left\langle \boldsymbol{\eta}_i(t)\boldsymbol{\eta}_j(t')\right\rangle_\mathrm{noise} = 2D_f\mathbf{I}\delta_{ij}\delta(t-t')$ governed by a diffusion coefficient D_f.

It is now once more instructive to look at its behavior in the dilute limit ($\mathbf{F}_i = 0$). Remarkably, solving the model yields the same MSD as for the linear ABP model [Eq. (2.3)] with in this case $\tau_\mathrm{p} = \tau$ and $D_\mathrm{a} = D_f\tau_\mathrm{p}^2/\zeta^2$. In other words, both models yield a PRW and with the help of the MSD they can be directly mapped onto each other. This also allows us to define an average active speed for the AOUP model given by $v_0 \sim \sqrt{dD_\mathrm{f}\tau_\mathrm{p}}/\zeta$. Furthermore, this provides an interesting pathway to systematically explore the role of these two self-propulsion mechanisms when venturing into the dense regime.

Despite their apparent similarity, there are also important differences between both models. First, the inclusion of chiral motion into the AOUP model is less straightforward and is therefore usually not considered. It is thus mostly used to describe linear swimmers. Moreover, the Ornstein-Uhlenbeck process is Gaussian which always leads to monotonically decaying correlation functions. This is not necessarily true for the ABP model, which can for instance exhibit overshoots in the intermediate scattering function as a result of persistent swimming [58, 110, 136]. The extent to which these differences are crucial in dense conditions where interactions become dominant remains to be explored and holds particular relevance to biological systems for which a self-propulsion mechanism is typically not easily extracted.

Finally, we mention that another important minimal model for active particles is the so-called run-and-tumble particles [124, 137]. We also emphasize that beyond the above discussed model systems there exists many more in-depth theoretical and simulation models of active particles that have successfully described a wealth of interesting systems including but not limited to living tissues, individual cells, molecular motors, and active filaments [138]. These are outside the scope of this thesis but form natural extensions for further research.

2.2 Mori-Zwanzig formalism

The glassy behavior of our active model systems will be primarily quantified in terms of dynamic correlation functions such as the intermediate scattering function. As a starting point for a theoretical analysis of these correlation functions, one can use the Mori-Zwanzig projection operator formalism [139, 140], which we will briefly summarize in this section. The main idea is to separate the time-evolution of a dynamic correlation function into the space spanned by the variables of interest and a space orthogonal to it, which is of assumed lesser importance. Ideally, such a separation allows one to project or integrate out these orthogonal variables, thereby reducing the parameter space and making calculations more tractable, without losing crucial information. As such, it represents a coarse-graining procedure whose success naturally relies on an astute choice of the relevant variables. Typically, one wants to isolate slowly time-varying functions so that the orthogonal subspace only contains rapidly fluctuating ones. This requires a clear separation of timescales, which, fortunately, is a key feature of glassy dynamics.

To sketch the formalism, let us consider any 'slow' vector $\mathbf{A}$ whose elements $A_i = [\mathbf{A}]_i$ are functions of phase space (which in our case is mostly constituted by the positions and active forces of all particles). The auto-correlation function of $\mathbf{A}$ is then formally given by $\mathbf{C}(t) = \langle \mathbf{A}^* \mathbf{A}(t) \rangle = \left\langle \mathbf{A}^* e^{\Omega^\dagger t} \mathbf{A} \right\rangle$, or equivalently in Laplace space, $\mathbf{C}(z) = \left\langle \mathbf{A}^* (z - \Omega^\dagger)^{-1} \mathbf{A} \right\rangle$ [141, 142]. Here, averaging $\langle \ldots \rangle$ is done with respect to a steady-state probability distribution function (PDF) which for a passive system in equilibrium is proportional to the Boltzmann factor. The adjoint evolution operator $\Omega^\dagger$ can be retrieved from the relevant (Langevin) equations of motion of the particles and works on everything to its right except for the PDF.

We then introduce a projection operator onto the subspace spanned by $\mathbf{A}$, i.e., $\mathcal{P} = |A_i\rangle G^{-1}_{ij} \langle A^*_j|$, where we have introduced $\mathbf{G} = \langle \mathbf{A}^* \mathbf{A} \rangle$, and the superscript -1 depicts the inverse matrix of the respective correlation function, that is, $G^{-1}_{ij} \equiv [\mathbf{G}^{-1}]_{ij}$. We also mention that a summation over repeated indices is implied and that the normalization factor G_{ij}^{-1} guarantees the idempotency of $\mathcal{P}$. To develop an equation of motion for $\mathbf{C}(t)$ we focus on the Laplace-transform of its time-derivative,

$$z\mathbf{C}(z) - \mathbf{G} = \left\langle \mathbf{A}^*\Omega^\dagger(z - \Omega^\dagger)^{-1}\mathbf{A}\right\rangle. \tag{2.6}$$

Invoking Dyson decomposition, i.e., $(z - \Omega^\dagger)^{-1} = (z - \Omega^\dagger\mathcal{Q})^{-1} + (z - \Omega^\dagger\mathcal{Q})^{-1}\Omega^\dagger\mathcal{P}(z - \Omega^\dagger)^{-1}$, with $\mathcal{Q} = \mathcal{I} - \mathcal{P}$, one can rewrite the above equation as

$$z\mathbf{C}(z) - \mathbf{G} = \langle \mathbf{A}^*\Omega^\dagger(\mathcal{P} + \mathcal{Q})(z - \Omega^\dagger)^{-1}\mathbf{A}\rangle = -\mathbf{H}\cdot\mathbf{G}^{-1}\cdot\mathbf{C}(z) + \mathbf{K}(z)\cdot\mathbf{G}^{-1}\cdot\mathbf{C}(z), \tag{2.7}$$

where we have introduced the so-called diffusion or frequency matrix $\mathbf{H} = -\langle\mathbf{A}^*\Omega^\dagger\mathbf{A}\rangle$ and memory kernel $\mathbf{K}(z) = \langle\mathbf{A}^*\Omega^\dagger\mathcal{Q}(z - \mathcal{Q}\Omega^\dagger\mathcal{Q})^{-1}\mathcal{Q}\Omega^\dagger\mathbf{A}\rangle$. This equation can then be converted back into the time-domain which yields

$$\frac{\partial}{\partial t}\mathbf{C}(t) + \mathbf{H}\cdot\mathbf{G}^{-1}\cdot\mathbf{C}(t) - \int_0^t dt'\mathbf{K}(t - t')\cdot\mathbf{H}^{-1}\cdot\mathbf{C}(t') = 0. \tag{2.8}$$

We emphasize that this equation is fully exact, but at the same time severely limited by the presence of the memory kernel. The latter term is usually highly nontrivial and necessitates the use of approximations. In this thesis we will employ approximations based on mode-coupling theory (MCT) to make the memory kernel tractable and find a fully self-consistent equation of motion. More details are provided in the next section and the relevant Chapters 5 to 7.

Occasionally, however, the above form of the memory kernel does not yet lend itself to MCT-like approximations (for instance for passive Brownian particles) [143, 144]. In those cases it is customary to convert it into what is known as an irreducible memory kernel. For this we introduce a second projection operator, which usually takes on the form $\mathcal{P}' = |A_i\rangle H_{i;j}^{-1}\langle A_j^*|\Omega^\dagger$ (with $\mathcal{Q}' = \mathcal{I} - \mathcal{P}'$), and use Dyson decomposition to arrive at

$$\mathbf{K}(z) = \mathbf{M}(z) - \mathbf{M}(z)\cdot\mathbf{H}^{-1}\cdot\mathbf{K}(z). \tag{2.9}$$

Here, $\mathbf{M}(z) = \langle\mathbf{A}^*\Omega^\dagger\mathcal{Q}(z - \mathcal{Q}\Omega^\dagger\mathcal{Q}'\mathcal{Q})^{-1}\mathcal{Q}\Omega^\dagger\mathbf{A}\rangle$ represents the irreducible memory kernel. Using the above result in conjunction with Eq. (2.7) we may find

$$(\mathbf{I} + \mathbf{M}(z)\cdot\mathbf{H}^{-1})\cdot(z\mathbf{C}(z) - \mathbf{G}) + \mathbf{H}\cdot\mathbf{G}^{-1}\cdot\mathbf{C}(z) = 0. \tag{2.10}$$

Converting back to the time domain we find another equation of motion for our correlation function $\mathbf{C}(t)$, which is now given by

$$\frac{\partial}{\partial t}\mathbf{C}(t) + \mathbf{H}\cdot\mathbf{G}^{-1}\cdot\mathbf{C}(t) + \int_0^t dt'\mathbf{M}(t - t')\cdot\mathbf{H}^{-1}\cdot\frac{\partial}{\partial t'}\mathbf{C}(t') = 0, \tag{2.11}$$

and can, in some situations, be more suitable for MCT-like approximations.

2.3 Mode-coupling theory (MCT)

The Mori-Zwanzig (MZ) projection operator formalism forms the starting point of arguably one of the most well-known theories of the glass transition, namely mode-coupling theory (MCT) [15, 21, 22]. In this thesis we will incorporate the above introduced active particle models into MCT as to extend its predictive reach to active glassy systems. This adds to several recent attempts that have already successfully included active motion into the framework of MCT [100, 101, 103, 104, 106, 122]. In general, such an extension comes at the cost of more complexity. To allow for a gentler exposure to these so-called active mode-coupling theories in later chapters we, in this section, therefore first present a concise and conceptual derivation of conventional passive MCT.

Let us consider a fluid of N Brownian particles at a number density $\rho = N/V$. Each particle i moves in time according to Eq. (2.1), only without any self-propulsion ($\mathbf{f}_i = \mathbf{0}$). Based on the equation of motion one can extract the relevant adjoint evolution or Smoluchowski operator which is given by

$$\Omega^\dagger = \sum_{i=1}^{N} D_\mathrm{t} \left(\nabla_i + \beta \mathbf{F}_i\right) \cdot \nabla_i, \tag{2.12}$$

where $\beta = (k_\mathrm{B}T)^{-1}$ is the inverse thermal energy. Note that this operator effectively governs the time-evolution of observables [141].

Since our phase space consists solely of particle positions $\mathbf{r}_i$ (currents are absent in a Brownian system) and we seek a description of slowly-varying local density fluctuations in a glassy system, it is natural to choose as our variable of interest the (normalized) density mode $\rho_\mathbf{k} = \frac{1}{\sqrt{N}} \sum_{i=1}^{N} e^{i\mathbf{k}\cdot\mathbf{r}_i}$. Using this in the MZ-formalism, the relevant correlation function becomes the intermediate scattering function, $C(t) = \left\langle \rho_\mathbf{k}^* e^{\Omega^\dagger t} \rho_\mathbf{k} \right\rangle \equiv F(k,t)$, where we mention that it has reduced to a scalar quantity. The resulting equation of motion, that is, Eq. (2.11), in this case yields

$$\frac{\partial}{\partial t} F(k,t) + \frac{D_\mathrm{t} k^2}{S(k)} F(k,t) + D_\mathrm{t} k^2 \int_0^t dt' M(k,t-t') \frac{\partial}{\partial t'} F(k,t') = 0. \tag{2.13}$$

Here, $S(k)$ is the static structure factor and we have readily evaluated the frequency term, $H(k) = -\left\langle \rho_\mathbf{k}^* \Omega^\dagger \rho_\mathbf{k} \right\rangle = D_\mathrm{t} k^2$, that governs the short-time decay of the intermediate scattering function. The latter has been straightforwardly calculated by means of partial integration, realizing that the interaction force is derived from the interaction potential U, i.e., $\mathbf{F}_i = \nabla_i U$, and the probability distribution function admits a Boltzmann solution, $P_\mathrm{eq} \propto e^{-\beta U}$.

The only term left to calculate is the memory kernel $M(t)$, which represents a highly nontrivial correlation between so-called fluctuating forces, $\left|\mathcal{Q}\Omega^\dagger \rho(\mathbf{k})\right\rangle$ and $\left\langle \rho^*(\mathbf{k}) \Omega^\dagger \mathcal{Q}\right|$.

To make this term tractable we require approximations. In MCT the first of these involves a projection of the fluctuating forces onto density doublets. The motivation behind this choice is that, due to the operator $\mathcal{Q}$, the fluctuating forces reside in a subspace orthogonal to the density singlets and therefore the lowest order projection of another assumed 'slow' variable is on density doublets. As such, we define the projection operator as

$$\mathcal{P}_2 = \frac{1}{2}\sum_{\mathbf{q}_1\mathbf{q}_2} |\rho(\mathbf{q}_1)\rho(\mathbf{q}_2)\rangle S^{-1}(q_1)S^{-1}(q_2)\langle\rho^*(\mathbf{q}_1)\rho^*(\mathbf{q}_2)|, \tag{2.14}$$

with wavevectors $\mathbf{q}$, and use it to approximate

$$M(k,t) \approx \left\langle \rho^*(\mathbf{k})\Omega^\dagger \mathcal{Q}\mathcal{P}_2 e^{\mathcal{Q}\Omega^\dagger\mathcal{Q}'\mathcal{Q}t}\mathcal{P}_2\mathcal{Q}\Omega^\dagger\rho(\mathbf{k})\right\rangle. \tag{2.15}$$

Note that for the normalization of $\mathcal{P}_2$, we have assumed Gaussian factorization of the higher order static correlations [145], i.e.,

$$\langle\rho^*(\mathbf{q}_1)\rho^*(\mathbf{q}_2)\rho(\mathbf{q}_3)\rho(\mathbf{q}_4)\rangle \approx S(q_1)S(q_2)(\delta_{\mathbf{q}_1,\mathbf{q}_3}\delta_{\mathbf{q}_2,\mathbf{q}_4} + \delta_{\mathbf{q}_2,\mathbf{q}_3}\delta_{\mathbf{q}_1,\mathbf{q}_4}), \tag{2.16}$$

with $\delta_{\mathbf{q}_1,\mathbf{q}_3}$ the Kronecker delta. The projection onto density doublets results in the appearance of three terms: the vertices (left and right) and a dynamical four-point density correlation function with projected dynamics. Using the convolution approximation [146],

$$\langle\rho^*(\mathbf{k})\rho(\mathbf{q}_1)\rho(\mathbf{q}_2)\rangle \approx \frac{1}{\sqrt{N}}\delta_{\mathbf{k},\mathbf{q}_1+\mathbf{q}_2}S(k)S(q_1)S(q_2), \tag{2.17}$$

and employing partial integration, one can calculate the left vertex as

$$\begin{aligned}\left\langle\rho^*(\mathbf{k})\Omega^\dagger\mathcal{Q}\rho(\mathbf{q}_1)\rho(\mathbf{q}_2)\right\rangle S^{-1}(q_1)S^{-1}(q_2) &= \frac{D_t}{\sqrt{N}}\delta_{\mathbf{k},\mathbf{q}_1+\mathbf{q}_2} \\ \times\left[k^2 - (\mathbf{k}\cdot\mathbf{q}_1)S^{-1}(q_1) - (\mathbf{k}\cdot\mathbf{q}_2)S^{-1}(q_2)\right], &\end{aligned} \tag{2.18}$$

and the right one in an identical manner. To deal with the dynamical four-point density correlation function we invoke the second step of the MCT approximation, which is to factorize it as a product of two-point density correlations with full dynamics,

$$\begin{aligned}\left\langle\rho^*(\mathbf{q}_1)\rho^*(\mathbf{q}_2)e^{\mathcal{Q}\Omega^\dagger\mathcal{Q}'\mathcal{Q}t}\rho(\mathbf{q}_3)\rho(\mathbf{q}_4)\right\rangle &\approx \left\langle\rho^*(\mathbf{q}_1)e^{\Omega^\dagger t}\rho(\mathbf{q}_1)\right\rangle \\ \times\left\langle\rho^*(\mathbf{q}_2)e^{\Omega^\dagger t}\rho(\mathbf{q}_2)\right\rangle(\delta_{\mathbf{q}_1,\mathbf{q}_3}\delta_{\mathbf{q}_2,\mathbf{q}_4} + \delta_{\mathbf{q}_2,\mathbf{q}_3}\delta_{\mathbf{q}_1,\mathbf{q}_4}). &\end{aligned} \tag{2.19}$$

Combining these results, evaluating all Kronecker deltas, and taking the continuum limit $\sum_{\mathbf{q}} \to \frac{V}{(2\pi)^d}\int d\mathbf{q}$, where V the volume or area and d the dimension of the system, then finally yields

$$M(k,t) \approx \frac{\rho}{2}\int\frac{d\mathbf{q}}{(2\pi)^d}V(\mathbf{k},\mathbf{q},\mathbf{k}-\mathbf{q})F(q,t)F(|\mathbf{k}-\mathbf{q}|,t)V(\mathbf{k},\mathbf{q},\mathbf{k}-\mathbf{q}). \tag{2.20}$$

In particular, the vertices are given by

$$V(\mathbf{k},\mathbf{q},\mathbf{k}-\mathbf{q}) = D_t \left[\mathbf{k}\cdot\mathbf{q}\; c(q) + \mathbf{k}\cdot(\mathbf{k}-\mathbf{q})\; c(|\mathbf{k}-\mathbf{q}|)\right], \tag{2.21}$$

where $c(q) = \rho^{-1}[1 - S^{-1}(q)]$ denotes the direct correlation function.

In summary, by applying the MCT approximations $M(k,t)$ has become a functional of $F(k,t)$. As a result, the equation governing the time evolution of the intermediate scattering function is now self-consistent and can be solved numerically for $F(k,t)$ using only the static structure factor $S(k)$ and thermodynamic control parameters as input.

Chapter 3

Cage length controls the nonmonotonic dynamics of active glassy matter

Abstract. Active matter is inherently out-of-equilibrium and even the glassy dynamics of our simple models, i.e., active Brownian particles (ABPs) and active Ornstein-Uhlenbeck particles (AOUPs), can already be markedly different from their passive counterparts. Controversially, this difference has been shown to manifest itself via either a speedup, slowdown, or nonmonotonic change of the glassy relaxation dynamics. In this chapter, we rationalize these seemingly contrasting views on the departure from equilibrium by identifying the ratio of the short-time length scale to the cage length, i.e., the length scale of local particle caging, as a vital and unifying control parameter for active glassy matter. In particular, we explore the glassy dynamics of both thermal and athermal ABPs and AOUPs upon increasing the persistence time. We find that for all studied systems there is an optimum of the dynamics; this optimum occurs when the cage length coincides with the corresponding short-time length scale of the system, which is either the persistence length for athermal systems or a combination of the persistence length and a diffusive length scale for thermal systems. This new insight, for which we also provide a simple physical argument, allows us to reconcile and explain the manifestly disparate departures from equilibrium reported in many previous studies of dense active materials.

The contents of this chapter are based on the following publication:
V.E. Debets, X.M. de Wit, and L.M.C. Janssen, *Phys. Rev. Lett.* 127, 278002 (2021)

3.1 Introduction

As detailed in the previous chapter, two simple model systems, which are widely used in theoretical and simulation studies of dense active matter, are so-called active Brownian particles (ABPs) [101, 123, 147–150] and active Ornstein-Uhlenbeck particles (AOUPs) [134, 151, 152]. These models differ in the manner in which they model active forces, either describing them as forces with a constant magnitude undergoing rotational diffusion (ABPs), or letting them evolve in time via an Ornstein-Uhlenbeck process (AOUPs). However, even for these relatively simple model active particles, the departure from equilibrium in dense systems is confounded by surprising and seemingly contrasting results. Notably, in several studies the long-time particle dynamics has been shown to change nonmonotonically upon increasing the persistence of the constituent particles [102, 111–113], while other works find either monotonically enhanced [85, 112, 153, 154] or decreased [91, 112] dynamics. To account for the change in dynamics, it was recently proposed by Liluashvili *et al.* [153] that the so-called cage length l_{c} [21, 155], i.e. the space each particle is permitted before encountering its neighboring particles, might be a crucial length scale that provides an offset beyond which active motion influences glassy behavior in thermal hard-sphere systems.

In this chapter we show that the cage length is an even more important parameter than previously suggested, and in fact holds the key to rationalizing and reconciling the apparently disparate views on the departure from thermal equilibrium for both thermal and athermal dense active systems. Briefly, we explore the dynamics of interacting ABPs and AOUPs upon increasing the persistence time, while at the same time fixing their effective temperature. For all considered settings, we retrieve a nonmonotonic dependence of the long-time diffusion coefficient whose qualitative shape, consisting of an initial increase and later decrease, also remains the same. By replacing the persistence time by the ratio of the relevant short-time length scale (either the sole persistence length for athermal systems or a combination of the persistence length and a diffusive length scale for thermal systems) to the cage length as our control parameter, we find the optimum of the dynamics in all cases to coincide with a value equal to one. We discuss how this can explain a large number of previous findings and thus establish this ratio as the central and unifying dimensionless length scale for active glassy materials.

3.2 Simulation details

As our model system we take a three-dimensional (3D) Kob-Andersen binary mixture consisting of $N_{\mathrm{A}} = 800$ and $N_{\mathrm{B}} = 200$ quasi-hard self-propelling spheres of type A and B respectively. Each particle i is described by the following overdamped equation of motion [85, 104, 122]

$$\dot{\mathbf{r}}_i = \zeta^{-1}\left(\mathbf{F}_i + \mathbf{f}_i\right) + \boldsymbol{\xi}_i, \tag{3.1}$$

where $\mathbf{r}_i$ denotes the position of particle i, ζ the friction coefficient, $\mathbf{F}_i$ and $\mathbf{f}_i$ the interaction and self-propulsion force acting on particle i respectively, and $\boldsymbol{\xi}_i$ a Gaussian noise with zero mean and variance $\left\langle \boldsymbol{\xi}_i(t)\boldsymbol{\xi}_j(t')\right\rangle_{\text{noise}} = 2k_BT\zeta^{-1}\mathbf{I}\delta_{ij}\delta(t-t')$, with $k_BT \equiv T$ the thermal energy (temperature), t the time, and $\mathbf{I}$ the unit matrix. The interaction force $\mathbf{F}_i = -\sum_{j\neq i}\nabla_i V_{\alpha\beta}(r_{ij})$ is derived from a quasi-hard-sphere powerlaw potential $V_{\alpha\beta}(r) = 4\epsilon_{\alpha\beta}\left(\frac{\sigma_{\alpha\beta}}{r}\right)^{36}$ [156, 157] and the interaction parameters, i.e. $\epsilon_{\text{AA}} = 1$, $\epsilon_{\text{AB}} = 1.5$, $\epsilon_{\text{BB}} = 0.5$, $\sigma_{\text{AA}} = 1$, $\sigma_{\text{AB}} = 0.8$, $\sigma_{\text{BB}} = 0.88$, are, in combination with setting the friction coefficient to unity $\zeta = 1$, chosen to give good glass-forming mixtures [37, 158].

The distinction between ABP and AOUP models rests in their time evolution of the self-propulsion force $\mathbf{f}_i$. For ABPs the absolute value of the force f remains constant in time, i.e. $\mathbf{f}_i = f\mathbf{e}_i$, while the orientation $\mathbf{e}_i$ undergoes rotational diffusion [104, 122],

$$\dot{\mathbf{e}}_i = \boldsymbol{\chi}_i \times \mathbf{e}_i, \tag{3.2}$$

subject to a Gaussian noise process with zero mean and variance $\left\langle \boldsymbol{\chi}_i(t)\boldsymbol{\chi}_j(t')\right\rangle_{\text{noise}} = 2D_{\text{r}}\mathbf{I}\delta_{ij}\delta(t-t')$ whose amplitude is determined by the rotational diffusion coefficient D_{r}. In comparison, for AOUPs the self-propulsion force evolves in time according to [91, 102–104, 112, 113]

$$\dot{\mathbf{f}}_i = \tau^{-1}\mathbf{f}_i + \boldsymbol{\eta}_i, \tag{3.3}$$

Here, τ depicts the characteristic decay time of the self-propulsion and $\boldsymbol{\eta}_i$ is an internal Gaussian noise process with zero mean and variance $\left\langle \boldsymbol{\eta}_i(t)\boldsymbol{\eta}_j(t')\right\rangle_{\text{noise}} = 2D_f\mathbf{I}\delta_{ij}\delta(t-t')$ governed by a diffusion coefficient D_f.

If we neglect particle interactions, both models yield a persistent random walk (PRW) with mean square displacement (MSD) [104]

$$\left\langle \delta r^2(t)\right\rangle = 6Tt + 6T_{\text{a}}\left(\tau_{\text{p}}(e^{-t/\tau_{\text{p}}} - 1) + t\right). \tag{3.4}$$

Such a PRW is characterized by a persistence time $\tau_{\text{p}} = (2D_{\text{r}})^{-1}$ (ABP), $\tau_{\text{p}} = \tau$ (AOUP), an active temperature $T_{\text{a}} = f^2\tau_{\text{p}}/3$ (ABP), $T_{\text{a}} = D_f\tau_{\text{p}}^2$ (AOUP), and the (passive) temperature T. In particular, at short times ($t \ll \tau_{\text{p}}$) the motion is comprised of a diffusive and ballistic contribution $\left\langle \delta r^2(t)\right\rangle \approx 6Tt + 3T_{\text{a}}t^2/\tau_{\text{p}}$, and in the long-time limit ($t \gg \tau_{\text{p}}$) it becomes fully diffusive with an enhanced diffusion coefficient $\left\langle \delta r^2(t)\right\rangle \approx 6(T_{\text{a}} + T)t \equiv 6T_{\text{eff}}t$. Moreover, in the limit $\tau_{\text{p}} \to 0$ (with $T_{\text{a}} \sim$ constant), both models become equivalent to a Brownian system at a temperature equal to the effective temperature $T_{\text{eff}} = T_{\text{a}} + T$. To compare both models we will take as our control parameters T, τ_p, T_{eff}, and the number density ρ.

Simulations are carried out using LAMMPS (18 Sep 2020 version) [159]. We impose periodic boundary conditions, fix the cubic box size to set the number density, let the system run sufficiently long to ensure that no significant aging takes place, and afterwards track the particles over time. All results are presented in reduced units where σ_{AA}, ϵ_{AA}, $\epsilon_{\mathrm{AA}}/k_{\mathrm{B}}$, and $\zeta\sigma_{\mathrm{AA}}^2/\epsilon_{\mathrm{AA}}$ represent the units of length, energy, temperature, and time respectively [160]. For more details on the simulation protocol we refer to the Supplementary Information of Ref. [118].

3.3 Athermal active particles

For simplicity, we initially focus on athermal systems ($T = 0$, $T_{\mathrm{eff}} = T_{\mathrm{a}}$), choose three state points [$T_{\mathrm{eff}} = 2.448$, $\rho = 1.25$], [$T_{\mathrm{eff}} = 1.5$, $\rho = 1.2$], [$T_{\mathrm{eff}} = 0.528$, $\rho = 1.1$] where the systems exhibit mildly supercooled behavior, and vary the persistence time τ_{p} to study the departure from equilibrium. An additional advantage of the chosen state points resides in the self-similar nature of the powerlaw potential. This implies that for such a potential the behavior of a passive Brownian system is fully characterized by the parameter $\Gamma = T\rho^{-12}$ [13, 156, 158]. More concretely, since Γ (using T_{eff} instead of T) is the same for all three studied state points, they should yield equivalent dynamics when we take the limit $\tau_{\mathrm{p}} \to 0$, allowing for a convenient comparison.

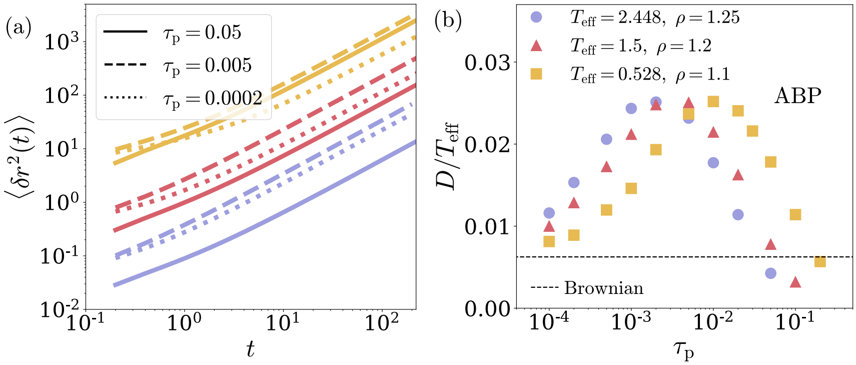

Figure 3.1: (a) MSDs of athermal ABPs for different persistence times τ_{p}. The results for [$T_{\mathrm{eff}} = 2.448$, $\rho = 1.25$] (blue), [$T_{\mathrm{eff}} = 1.5$, $\rho = 1.2$] (red), and [$T_{\mathrm{eff}} = 0.528$, $\rho = 1.2$] (orange) are multiplied by a factor 1, 10, and 200 respectively for visibility. (b) The corresponding self-diffusion coefficients normalized by the effective temperature. Upon increasing τ_{p} the dynamics initially speeds up before slowing down and dropping below the value obtained from equivalent ($T = T_{\mathrm{eff}}$) passive Brownian dynamics simulations (dashed line).

Starting with the ABP model, we study its $T = 0$ dynamics by retrieving the MSD, which is shown for a subset of values of τ_{p} in Fig. 3.1a. It can be seen that for long times the particles migrate diffusively (MSD $\propto t$), while, for all state points, they are fastest (largest MSD) when $\tau_\mathrm{p} = 0.005$, indicating that the departure from equilibrium occurs in a nonmonotonic fashion. Such nonmonotonic dependence on the persistence time is also consistent with previous results for quasi-hard-sphere athermal AOUPs [91, 112]. However, we note that for the studied state points the particles are slowest (smallest MSD) at different persistence times (either $\tau_\mathrm{p} = 0.0002$ or $\tau_\mathrm{p} = 0.05$). One might be tempted to interpret this as their equivalency being lost upon departing from equilibrium, but this is in fact not the case.

To demonstrate that there is indeed a large degree of universality hidden in the chosen state points, we explore the dependence of the dynamics on τ_p in more detail by calculating (based on the MSDs) the self-diffusion coefficient $D = \lim_{t\to\infty} \left\langle \delta r^2(t) \right\rangle / 6t$ and plotting the resulting values normalized by T_eff in Fig. 3.1b. Interestingly, the results now seem almost identical except for an offset in the persistence time (explaining the differences in the MSDs). We may additionally note that for small τ_p the self-diffusion coefficients approach, as expected, the value obtained from passive Brownian dynamics simulations (at $T = T_\mathrm{eff}$), while for large τ_p it drops below this value implying that, on average, the particles migrate more slowly than their passive counterparts. Due to the similar shapes of the plots in Fig. 3.1b, we anticipate that a different control parameter might be able to correct for the observed offset. Fortunately, the ABP model system comes naturally equipped with a length scale, namely the persistence length $l_\mathrm{p} = f\tau_\mathrm{p}$, and indeed when we plot the results as a function of $l_\mathrm{p}/l_\mathrm{c}$ they fully collapse (see Fig. 3.2a). Inspection of Fig. 3.2a then shows that the optimum value of D coincides with a value $l_\mathrm{p} \sim 0.12\sigma_\mathrm{AA}$, which is entirely consistent with the size of the *cage length* l_c (estimated via a nearest-neighbor analysis at a density $\rho = 1.2$, see Section 3.A for details; note that the Lindemann rule yields 0.13 times the particle diameter for monodisperse hard spheres [13]). Since we are at relatively high densities and therefore the cage length is approximately the same for $\rho = 1.1, 1.2, 1.25$ (see Section 3.A), this also explains why the results collapse almost perfectly. Moreover, we have verified that this collapse is robust when changing to a different Γ value deeper in the supercooled regime Fig. 3.6. We may also qualitatively rationalize the central role of the cage length by picturing particles trying to escape from their cage formed by neighboring particles. This process should proceed most effectively when particles can scan all the edges for an opening as fast as possible, which occurs when the persistence length is of the same order as the cage length. In contrast, when $l_\mathrm{p} \ll l_\mathrm{c}$ it would take much longer to reach the edges of the cage, while for $l_\mathrm{p} \gg l_\mathrm{c}$ a particle tends to stick in one edge of the cage for a relatively long time.

Next, we test whether the observed behavior persists for the athermal AOUP model. For the AOUPs one can invoke the equivalency of the MSDs [see Eq. (3.4)] to define a persistence length as $l_\mathrm{p} = (3D_f\tau_\mathrm{p})^{1/2}\tau_\mathrm{p}$, where $(3D_f\tau_\mathrm{p})^{1/2}$ may be interpreted as the

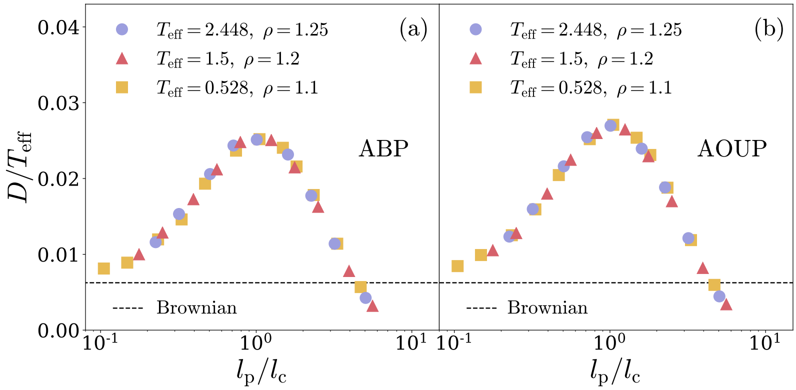

Figure 3.2: The normalized self-diffusion coefficient D/T_{eff} as a function of the ratio of the persistence to the cage length $l_\mathrm{p}/l_\mathrm{c}$ for (a) athermal ABPs and (b) athermal AOUPs. Both models yield almost identical results for both state points, with an optimum around the cage length $l_\mathrm{p}/l_\mathrm{c} \sim 1.0$ (with $l_\mathrm{c} \sim 0.12\sigma_{\mathrm{AA}}$). The result from passive Brownian dynamics simulations ($l_\mathrm{p} = 0$) is the same for all state points, and is added as a reference (dashed line).

approximate average self-propulsion force. Using $l_\mathrm{p}/l_\mathrm{c}$ as our control parameter, we have plotted the calculated values of D/T_{eff} (for the same state points as used for the ABPs) in Fig. 3.2b. Remarkably, the results once more collapse and the differences with the ABP model appear to be only marginal. This suggests that the specific microscopic details of these active self-propulsion mechanisms are of lesser importance in high-density systems. Intuitively, given that the particle motion becomes more impeded by repulsion at high densities and the system is starting to approach an arrested state, one would also expect the precise single-particle dynamics to become less relevant.

Finally, we mention that in previous work involving softer interaction potentials the initial increase in D vanishes and only the drop after passing a critical value of τ_p remains [91]. We have verified that when we change the power in our interaction potential from 36 to either 18 or 12, the initial increase in D is indeed strongly suppressed, but the subsequent drop still occurs at approximately the same persistence length. This will be addressed in more detail in Chapter 4.

3.4 Thermal active particles

To establish whether the observed behavior undergoes qualitative changes when thermal motion is added to the active-particle models, we now compare the following three state points [$T_{\rm eff} = 3.0,\ T = 0.0,\ \rho = 1.2$], [$T_{\rm eff} = 3.0,\ T = 1.5,\ \rho = 1.2$], [$T_{\rm eff} = 3.0,\ T = 2.0,\ \rho = 1.2$]. Note that all points have an equal effective temperature, but in one case only active motion adds to this value, while in the other two both active and passive motion contribute.

Again starting with the ABP model, we have calculated the MSDs for the mentioned state points; the corresponding values of $D/T_{\rm eff}$ are plotted as a function of $\tau_{\rm p}$ in Fig. 3.3. Upon first glance, the qualitative shape of the thermal ABP curves look similar to its athermal counterpart. In particular, all results approach the anticipated value of Brownian particles at $T = 3.0$ for small $\tau_{\rm p}$ and show the same nonmonotonic behavior.

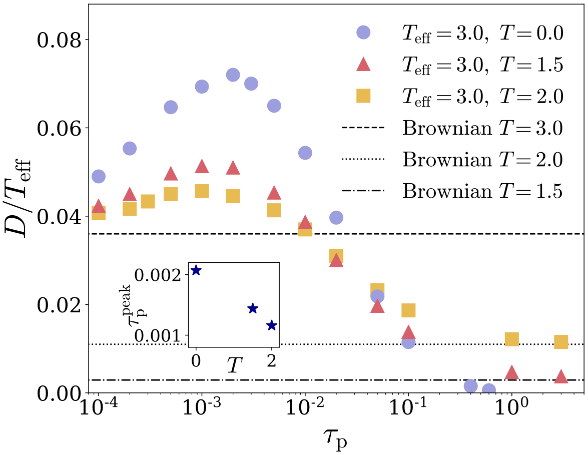

Figure 3.3: The normalized self-diffusion coefficient $D/T_{\rm eff}$ as a function of $\tau_{\rm p}$ for thermal ($T = 1.5, 2.0$) and athermal ($T = 0.0$) ABPs at fixed values of $T_{\rm eff} = 3.0$, $\rho = 1.2$. Increasing $\tau_{\rm p}$ initially yields faster, but eventually slower, dynamics than Brownian particles at $T = 3.0$ (dashed line); in the limit of large $\tau_{\rm p}$, thermal ABPs approach the $T = 1.5, 2.0$ passive Brownian limit (dashed-dotted, dotted lines) while athermal ABPs yield $D/T_{\rm eff} \to 0$. The inset shows the persistence time $\tau_{\rm p}^{\rm peak}$ corresponding to the peak value of D, which decreases as a function of T.

There are, however, also some notable differences. In the limit of large $\tau_{\rm p}$, for instance, the thermal results seem to approach the same dynamics as a Brownian particle at either $T = 1.5$ or $T = 2.0$ (which suggests that superimposing active onto passive motion always enhances the dynamics), whereas the self-diffusion coefficient of the athermal particles manifestly goes to zero. We can explain these observations by noting that for a fixed $T_{\rm a}$, taking the limit of very large $\tau_{\rm p}$ also implies that the average self-propulsion force becomes very small. As a result, the athermal particles take increasingly long to break out of their cages, resulting in progressively slow dynamics, while the motion of the thermal particles becomes completely dominated by the passive contribution.

Another difference is the smaller height of the peak value for the thermal ABPs, which is simply due to the active motion contributing not as much to T_{eff} in comparison to the athermal ABPs. More interesting is the location of the peak values. For athermal systems, we find that a smaller active (or effective) temperature T_{a} will result in an optimum self-diffusion at a larger persistence time (see Fig. 3.1b). One might therefore expect that the optimum value in our considered thermal systems, which have a smaller value of $T_{\mathrm{a}} = 1.0, 1.5$ compared to its athermal analogue (with $T_{\mathrm{a}} = 3.0$), would also be at a larger value for τ_{p}. Surprisingly, Fig. 3.3 shows the opposite. This suggests that taking $l_{\mathrm{p}}/l_{\mathrm{c}}$ as a control parameter will not result in the peak value being at the same location.

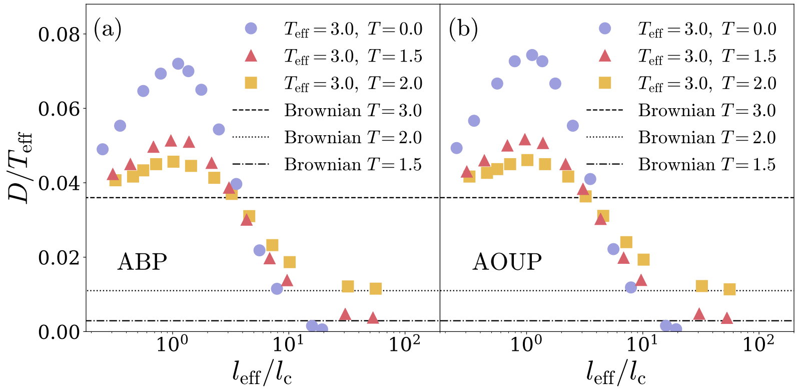

Figure 3.4: The normalized self-diffusion coefficient D/T_{eff} as a function of the normalized effective short-time length scale $l_{\mathrm{eff}}/l_{\mathrm{c}}$ for (a) the ABP and (b) the AOUP model, at fixed values $T_{\mathrm{eff}} = 3.0$, $\rho = 1.2$. Both the thermal $T = 1.5, 2.0$ and athermal $T = 0.0$ results have an optimum value around the cage length $l_{\mathrm{eff}}/l_{\mathrm{c}} \sim 1.0$. The passive Brownian reference at $T = 1.5$ (dashed-dotted line), $T = 2.0$ (dotted line), and $T = 3.0$ (dashed line) is shown for comparison.

To resolve this discrepancy, we realize that thermal active systems are in fact governed by an additional source of motion that is inherently absent in athermal systems. Explicitly, for athermal active systems only the self-propulsion contributes to the motion of the particles and thus the short-time length scale is the persistence length. In contrast, for thermal systems, the added thermal motion enhances the length scale at short times. For $t < \tau_{\mathrm{p}}$ we may expand the single-particle MSD up to second order to give $\langle \delta r^2(t) \rangle \approx 6Tt + 3T_{\mathrm{a}} t^2/\tau_{\mathrm{p}}$. We can then introduce $l_{\mathrm{eff}} = \left(\langle \delta r^2(\tau_{\mathrm{p}}) \rangle\right)^{1/2}$ (using the second-order MSD) as an enhanced effective (short-time) length scale and use it as our control parameter for thermal systems (note that for $T = 0$, we still have $l_{\mathrm{eff}} = l_{\mathrm{p}}$). Indeed, when we plot the values of D/T_{eff} as a function of $l_{\mathrm{eff}}/l_{\mathrm{c}}$ (see Fig. 3.4a), we find that not only do the optima coincide, but the point at which they do is again fully consistent with the cage length, i.e. $l_{\mathrm{eff}}/l_{\mathrm{c}} \sim 1.0$. It thus seems that the addition of thermal motion changes the relevant short-time length scale, but it does not alter the physical picture of particles exhibiting the strongest enhanced dynamics when they can explore their cage as effectively as possible.

We finalize our results by mentioning that the observed behavior is once more unaltered when we interchange the thermal ABP for the thermal AOUP model. In particular, the differences in the obtained values for D/T_{eff} and their dependence on $l_{\mathrm{eff}}/l_{\mathrm{c}}$ are only minute (see Fig. 3.4).

3.5 Conclusions

To summarize, our work demonstrates that the cage length plays a vital role in the context of high-density active glassy materials. In particular, its relation to the relevant short-time active length scale, i.e. the sole persistence length for athermal systems or a combination of the persistence length and a diffusive length scale for thermal systems, fully determines whether the relaxation dynamics is enhanced or suppressed with respect to a Brownian system at an equal effective temperature. Indeed, an inspection of several previous findings [91, 102, 112, 113], which have reported different departures from equilibrium, shows that their seemingly contrasting findings can be fully reconciled by identifying whether the studied parameter regimes corresponded to short-time length scales on either side or around the cage length. Moreover, our results are robust to the microscopic details of the self-propulsion, rendering the ratio of the short-time active length scale to the cage length the crucial control parameter in both ABPs and AOUPs. We also observe that, consistent with previous work on hard-sphere ABPs [85, 153], superimposing active onto thermal motion always speeds up the relaxation dynamics. To further establish the importance of this ratio, it will be interesting to study its role in more detail for strict hard-sphere systems, whose passive dynamics should be independent of temperature. In comparison, our simulations with softer interaction potentials show the same the physical picture as sketched in this work, although the initial enhancement of the dynamics becomes more suppressed (see Chapter 4 for more details). The question how this picture extends to more complex and attractive interaction potentials, as well as biologically relevant active glasses such as confluent cell models [2, 48, 80, 161], should be investigated in future work to ultimately fully elucidate the rich non-equilibrium glassy dynamics of active matter.

Appendix

3.A Cage length estimation

To find an estimate of the size of the cage length we have calculated the AA-component, with A the majority species of the system, of the radial distribution function $g_{\mathrm{AA}}(r)$. Specifically, we have retrieved it at a density $\rho = 1.2$ (since this density is most used throughout the main text), effective temperatures $T_{\mathrm{eff}} = 1.5,\ 3.0$, and for both a passive Brownian system ($\tau_{\mathrm{p}} = 0$) and an athermal ABP system at a persistence time corresponding to its maximum long-time diffusion coefficient ($\tau_{\mathrm{p}} = 0.002$). The results are shown in fig. Fig. 3.5. One can interpret the position of the first minimum ($r \sim 1.4\sigma_{\mathrm{AA}}$) as the size of the shell of directly-neighboring (type A) particles. Taking the weighted average (using $g_{\mathrm{AA}}(r)$ as our weight function) of all distances up until this point thus allows us to find the approximate average distance r_{nn} between a particle and its nearest neighbors. Given that our particles are quasi-hard spheres and a particle of type A thus has a diameter of roughly $1.0\sigma_{\mathrm{AA}}$, we can estimate the cage length via $l_{\mathrm{c}} = r_{\mathrm{nn}} - \sigma_{\mathrm{AA}}$. Based on this procedure we find $l_{\mathrm{c}} \sim 0.12\sigma_{\mathrm{AA}}$ for $T_{\mathrm{eff}} = 1.5$ and $l_{\mathrm{c}} \sim 0.11\sigma_{\mathrm{AA}}$ for $T_{\mathrm{eff}} = 3.0$, for both the passive Brownian and athermal ABP system. Moreover, when we change the density to $\rho = 1.1,\ 1.25$, we find $l_{\mathrm{c}} \sim 0.14\sigma_{\mathrm{AA}},\ 0.11\sigma_{\mathrm{AA}}$ respectively, while a calculation at $\rho = 1.2$ for the athermal AOUP model or the thermal ABP model gives the same results as the athermal ABP model at an equal effective temperature. Overall, this shows that the size of the cage is fairly robust, although it slightly increases with decreasing density, and in the main text we choose to set it at a value $l_{\mathrm{c}} \sim 0.12\sigma_{\mathrm{AA}}$.

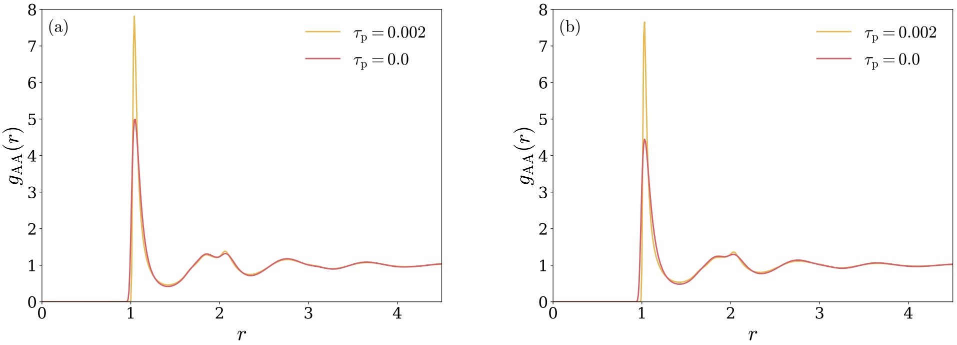

Figure 3.5: Plots of the AA-component of the radial distribution function as a function of the distance r. Presented results correspond to Brownian particle ($\tau_{\mathrm{p}} = 0$) or athermal ABPs ($\tau_{\mathrm{p}} = 0.002$) at a density $\rho = 1.2$ and an effective temperature of (a) $T_{\mathrm{eff}} = 1.5$ and (b) $T_{\mathrm{eff}} = 3.0$.

3.B Additional data

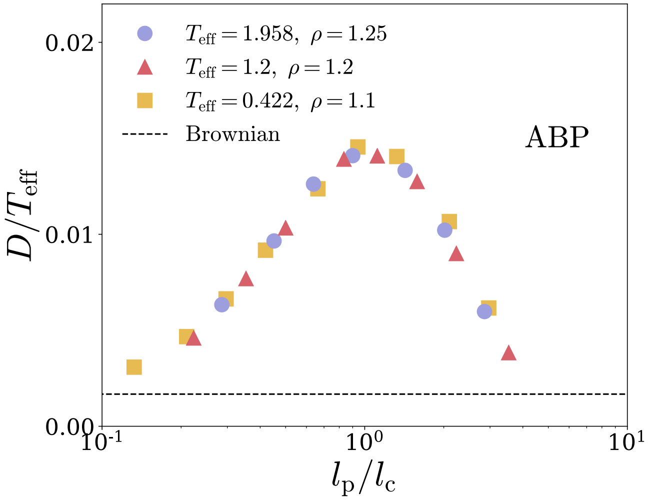

Figure 3.6: The normalized self-diffusion coefficient $D/T_{\rm eff}$ as a function of the normalized persistence length $l_{\rm p}/l_{\rm c}$ for a system of athermal ABPs. Results correspond to different combinations of $T_{\rm eff}$ and ρ with the same value for $\Gamma = T_{\rm eff}\rho^{-12}$. The dashed lines denote the value, which is the same for all settings in each panel, obtained from equivalent ($T = T_{\rm eff}$) Brownian dynamics simulations. We also mention that the cage length $l_{\rm c} = 0.12\sigma_{\rm AA}$ used for normalization is the one estimated for a power $n = 36$ at a density $\rho = 1.2$.

Chapter 4

The influence of particle softness on active glassy dynamics

Abstract. In the previous chapter we have shown that the glassy relaxation dynamics of active quasi-hard spheres is nonmonotonic and most enhanced by activity when the intrinsic active length scale (e.g., the persistence length) is equal to the cage length, i.e., the length scale of local particle caging. This optimal enhancement effect is claimed to result from the most efficient scanning of local particle cages. In this chapter we demonstrate that this effect and its physical explanation are fully retained for softer active spheres. We perform extensive simulations of athermal active Brownian particles (ABPs) and show that the nonmonotonic change of the relaxation dynamics remains qualitatively similar for varying softness. We explain quantitative differences by relating them to the longer range of the softer interaction potential, which decreases the cage length and obscures the intrinsic active motion. Moreover, we observe that only when the persistence length surpasses the cage length, distinct qualitative changes with respect to an equivalent passive Brownian particle system start to manifest themselves. Overall, our results further strengthen the importance of the cage length and its relation to the relevant active length scale in the context of active glassy materials.

The contents of this chapter are based on the following publication:
V.E. Debets and L.M.C. Janssen, *Phys. Rev. Research* 4, L042033 (2022)

4.1 Introduction

In the previous chapter, we have shown for quasi-hard active spheres that the cage length, i.e., the typical size associated with the caging of particles by their nearest neighbors, plays an important role in the context of active glassy matter [100, 118]. Specifically, it provides a reference length to which the intrinsic short-time active length scale can be related. That is, for active length scales smaller than the cage length, dense active matter exhibits enhanced relaxation dynamics with respect to an equivalent Brownian system, while upon surpassing the cage length the relaxation dynamics starts to slowdown and eventually becomes slower than that of the passive reference system. A proposed physical mechanism underlying the observed behavior is the most efficient scanning of particle cages. This should yield the fastest relaxation dynamics and occurs when the cage length and the active length scale coincide. Consequently, the non-trivial and nonmonotonic influence of activity on glassy dynamics can be understood from a conceptually relatively simple argument. How well this explanation generalizes to more complex particle-particle interactions remains, however, to be established.

In this chapter, we take a first step in the direction of more diverse interaction potentials, and demonstrate that the physical picture sketched above remains fully intact for active spheres of different softness. In short, we study the dynamics of athermal active Brownian particles (ABPs) whose interactions are governed by a repulsive powerlaw potential with a variable power controlling the softness of the particles. We vary the persistence length of the constituent particles at a fixed active temperature and retrieve a qualitatively similar nonmonotonic dependence of the relaxation dynamics for each considered softness. In all cases the optimum of the dynamics coincides with the point at which the persistence length is approximately equal to the cage length. We also explore the dependence of the relaxation dynamics on the active temperature upon approaching dynamical arrest, and find that the cage length marks the threshold value beyond which the active system starts behaving qualitatively distinct (manifested by changes in the fragility) from its passive Brownian counterpart. Note that our findings for ABPs should also apply to the equally suitable active Ornstein Uhlenbeck particle (AOUP) model, since the microscopic details of these simple model systems do not significantly influence the long-time glassy behavior [118]. Overall, our work serves to further establish the importance of the cage length and in particular its relation to the short-time active length scale in the context of active glassy matter.

4.2 Methods

The simulation model we use is a three-dimensional (3D) Kob-Andersen binary mixture consisting of $N_{\mathrm{A}} = 800$ and $N_{\mathrm{B}} = 200$ athermal self-propelling soft spheres of type A and B respectively. The position $\mathbf{r}_i$ of each particle i evolves in time t according to [85, 104, 122]

$$\dot{\mathbf{r}}_i = \zeta^{-1} \left(\mathbf{F}_i + \mathbf{f}_i \right), \tag{4.1}$$

where ζ is the friction coefficient and $\mathbf{f}_i$ the self-propulsion force acting on particle i. The interaction force $\mathbf{F}_i = -\sum_{j \neq i} \nabla_i V_{\alpha\beta}(r_{ij})$ is derived from a repulsive powerlaw potential $V_{\alpha\beta}(r) = 4\epsilon_{\alpha\beta} \left(\frac{\sigma_{\alpha\beta}}{r} \right)^n$ with a variable power n, which controls the softness of the particles (smaller n corresponds to softer particles). The interaction parameters, i.e. $\epsilon_{\mathrm{AA}} = 1$, $\epsilon_{\mathrm{AB}} = 1.5$, $\epsilon_{\mathrm{BB}} = 0.5$, $\sigma_{\mathrm{AA}} = 1$, $\sigma_{\mathrm{AB}} = 0.8$, $\sigma_{\mathrm{BB}} = 0.88$, are, in combination with setting the friction coefficient to unity $\zeta = 1$, chosen to give good glass-forming mixtures [37, 158]. Following the ABP model [101, 123, 147–150] for our self-propulsion force, we let the absolute value of the force f remain constant in time, i.e. $\mathbf{f}_i = f\mathbf{e}_i$, while the orientation $\mathbf{e}_i$ undergoes rotational diffusion [104, 122],

$$\dot{\mathbf{e}}_i = \boldsymbol{\chi}_i \times \mathbf{e}_i, \tag{4.2}$$

subject to a Gaussian noise process with zero mean and variance $\left\langle \boldsymbol{\chi}_i(t) \boldsymbol{\chi}_j(t') \right\rangle_{\mathrm{noise}} = 2D_{\mathrm{r}} \mathbf{I} \delta_{ij} \delta(t - t')$ with D_{r} the rotational diffusion coefficient and $\mathbf{I}$ the unit matrix. In the absence of particle-particle interactions, each particle performs a persistent random walk (PRW) and its mean square displacement (MSD) is given by [104]

$$\left\langle \delta r^2(t) \right\rangle = 6T_{\mathrm{a}} \left(\tau_{\mathrm{p}} (e^{-t/\tau_{\mathrm{p}}} - 1) + t \right). \tag{4.3}$$

Inspection of Eq. (4.3) shows that the single-particle motion is characterized by a persistence time $\tau_{\mathrm{p}} = (2D_{\mathrm{r}})^{-1}$ and an active temperature $T_{\mathrm{a}} = f^2 \tau_{\mathrm{p}}/3$. In particular, at short times ($t \ll \tau_{\mathrm{p}}$) the motion is ballistic $\left\langle \delta r^2(t) \right\rangle \approx 3T_{\mathrm{a}} t^2/\tau_{\mathrm{p}}$, and in the long-time limit ($t \gg \tau_{\mathrm{p}}$) it becomes fully diffusive $\left\langle \delta r^2(t) \right\rangle \approx 6T_{\mathrm{a}} t$. This implies that in the limit $\tau_{\mathrm{p}} \to 0$ (with $T_{\mathrm{a}} \sim$ constant), our active system reduces to a Brownian one at a temperature T equal to the active temperature T_{a}. To study the effect of particle softness on the active glassy dynamics we take as our control parameters T_{a}, the powerlaw exponent n, and, to quantify how far we are from the passive limit, the persistence length $l_{\mathrm{p}} = f\tau_{\mathrm{p}}$ [118].

Simulations are performed by solving the Langevin equation [Eq. (4.1)] via a forward Euler scheme using LAMMPS [159]. We set the number density to $\rho = 1.2$ via the size of the periodic simulation box, run the system sufficiently long (typically between 500 and 20000 time units) to prevent aging, and afterwards track the particles over time for at least twice the initialization time. Unless otherwise stated we use for the powerlaw potential a cutoff radius of $r_{\mathrm{c}} = 2.5\sigma_{\alpha\beta}$. All results are presented in reduced units where σ_{AA}, ϵ_{AA}, $\epsilon_{\mathrm{AA}}/k_{\mathrm{B}}$, and $\zeta\sigma_{\mathrm{AA}}^2/\epsilon_{\mathrm{AA}}$ represent the units of length, energy, temperature, and time respectively [160]. We also mention that, to correct for diffusive center-of-mass motion, all particle positions are retrieved relative to the momentary center of mass [160].

4.3 Nonmonotonic behavior robust to changing softness

In our model system the active particles become more disparate from conventional passive particles upon increasing their persistence. To understand how this relates to particle softness, we have first extracted the long-time diffusion coefficient $D = \lim_{t\to\infty} \left\langle \delta r^2(t) \right\rangle /6t$ as a function of the persistence length l_p for different powers n. The resulting values normalized by the active temperature T_a are plotted in Fig. 4.1a. For each value of n we have fixed T_a at a value such that the system exhibits mildly supercooled behavior and in the passive limit ($l_\mathrm{p} \to 0$) all different powers give the same value for the normalized diffusion coefficient. This allows for a convenient comparison. An inspection of the results shows that the qualitative shape of the curves is unaltered when increasing the particle softness. In particular, all curves demonstrate a nonmonotonic dependence on l_p with initially enhanced, but eventually slower long-time diffusion than an equivalent Brownian particle at $T = T_\mathrm{a}$. This is consistent with previous results [91, 118]. Moreover, we observe that in the limit of small l_p the diffusion coefficients tend, as expected, towards Brownian dynamics result, while for large l_p they seemingly go to zero.

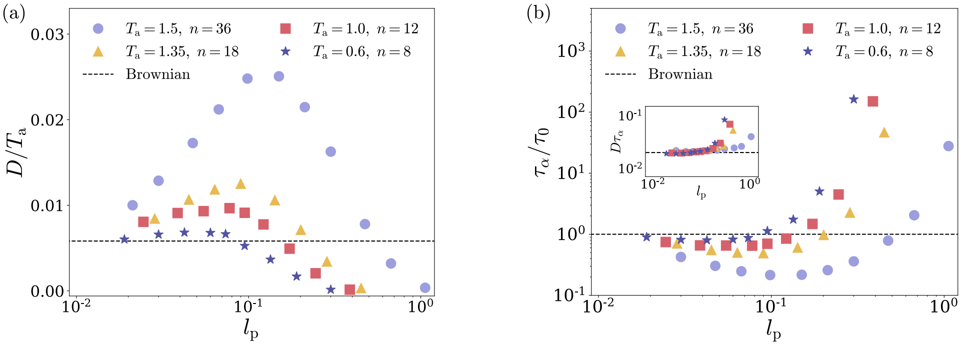

Figure 4.1: The normalized (a) long-time diffusion coefficient D/T_a and (b) relaxation time τ_α/τ_0 as a function of the persistence length l_p for athermal self-propelling spheres with different softness (governed by the power n). Increasing l_p initially yields faster, but eventually slower, relaxation dynamics than Brownian particles at a temperature $T = T_\mathrm{a}$ (dashed line). The enhancement and optimum of the dynamics are suppressed and shifted to smaller l_p values respectively for increasing softness (smaller n). The inset of panel (b) denotes the Stokes-Einstein relation $D\tau_\alpha$, which remains constant and independent of particle softness until a threshold value of l_p on the order of the cage length is surpassed.

Two notable quantitative differences are, however, also visible. It can be seen that the peak height strongly decreases when transitioning from quasi-hard ($n = 36$) to relatively soft ($n = 8$) spheres, and the location of the peak also shifts to smaller values. In previous work it has been demonstrated that the location of the peak for quasi-hard spheres corresponds to the point where the persistence length l_{p} is (approximately) equal to the cage length $l_{\mathrm{c}} \sim 0.1$ [118] (see Section 4.A for more details on the estimation of the cage length), i.e., the length scale of local particle caging [13]. Our results seem to corroborate this claim. A physical explanation for this behavior might then be attributed to the optimal scanning of particle cages which in turn yields the fastest relaxation dynamics. Following this reasoning we believe that, at least in part, both the peak height and peak location decrease to smaller values as a result of the longer range of softer powerlaw potentials (note that we have introduced a long-range potential cutoff of $r_{\mathrm{c}} = 2.5\sigma_{\alpha\beta}$). Due to the increased range, short-time particle motion becomes more perturbed by interactions so that individual soft particles cannot benefit from an efficient cage scanning as much, which explains the decreased peak height. Furthermore, the cage also becomes effectively smaller so that the optimum value coincides with a smaller persistence length.

To test this claim, we have repeated the simulations used for the results in Fig. 4.1a with a smaller potential cutoff radius of $r_{\mathrm{c}} = 1.0\sigma_{\alpha\beta}$. In this case the range of the potential becomes shorter. It should also become less dependent on the value of n, since the potential immediately starts steeply increasing when the inter-particle distance becomes smaller than r_{c} for all considered powers, whereas this happens more gradually (especially for $n = 8, 12$) with a large cutoff radius. The resulting normalized long-time diffusion coefficients are shown in Fig. 4.2 where we mention that the corresponding Brownian dynamics results (at a temperature $T = T_{\mathrm{a}}$), although not exactly the same, remained of the same order ($D/T_{\mathrm{a}} \sim 0.1$) such that the results for different powers can still be accurately compared. Interestingly, the results now overlap much more and can be even seen to almost collapse. Additionally, the peak location is shifted to a larger value of $l_{\mathrm{c}} \sim 0.2$, which is still of the same order as the cage length, and seems to confirm the notion that the range of the potential determines the location of the peak. The fact that all powers now display a clear peak of approximately the same (relative) height also suggests that the steepness of the potential is an important governing factor of the peak height.

Next, to put our initial results (using a long-range cutoff $r_{\mathrm{c}} = 2.5\sigma_{\alpha\beta}$) into a broader context we have also retrieved the self-intermediate scattering function, i.e., $F^{\mathrm{s}}(k, t) = \left\langle e^{i\mathbf{k}\cdot\mathbf{r}_j(0)} e^{i\mathbf{k}\cdot\mathbf{r}_j(t)} \right\rangle$, for the majority type A species. Based on these we have extracted the alpha-relaxation time τ_α, which is defined via $F^{\mathrm{s}}(k, \tau_\alpha) = e^{-1}$ at a wavenumber $k = 7.2$ corresponding to the first peak of the AA-component of the partial static structure factor (the location of the peak is fairly robust to changes in softness and persistence, see Fig. 4.6). The results for τ_α, normalized by the relaxation time τ_0 obtained for an equivalent ($T = T_{\mathrm{a}}$) passive system, are plotted in Fig. 4.1b. It can be seen that the

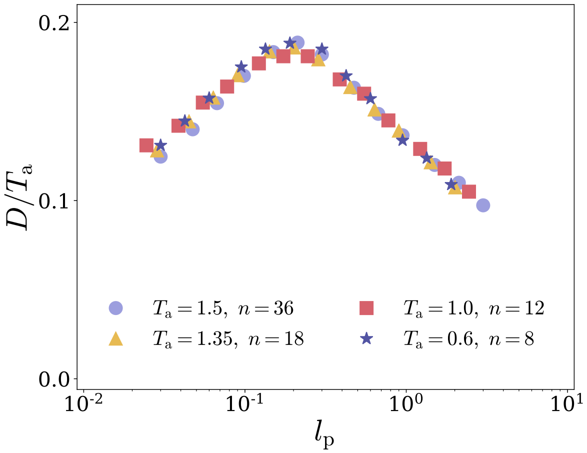

Figure 4.2: Plots of the normalized long-time diffusion coefficient D as a function of the persistence length l_p for different particle softness (governed by the power n). In comparison to the results presented in Fig. 4.1a, the cutoff radius of the powerlaw potential is taken at a smaller value of $r_c = 1.0\sigma_{\alpha\beta}$.

qualitative behavior of the relaxation time is fully consistent with the long-time diffusion coefficients. In particular, τ_α initially decreases to a minimum value (indicating the fastest relaxation dynamics), which is smaller than a corresponding Brownian particle ($\tau_\alpha/\tau_0 < 1$), while for large l_p it increases significantly beyond this value ($\tau_\alpha/\tau_0 \gg 1$). Enhanced softness again flattens the curves and shifts the optimum to a smaller value of l_p. We also note that the location of the minima of τ_α coincides with the maxima of D. Finally, we mention that the qualitative behavior of D and τ_α is already, to a large degree, visible in the height of the first peak of the static structure factor (see Figs. 4.6 and 4.7).

To gain some insight into the influence of particle softness and persistence on our glassy model system as a whole, we have also combined the relaxation time and long-time diffusion coefficient to calculate the Stokes-Einstein relation (SER), i.e., $D\tau_\alpha$, which has been plotted in the inset of Fig. 4.1b. For passive systems at large enough temperatures this relation usually remains constant, while upon vitrification significant deviations may occur [160, 162, 163]. These deviations have often been attributed to the manifestation of dynamical heterogeneity, although some controversy persists [164]. An inspection of our results shows that the SER initially takes on approximately the same value regardless of the particle softness. The values are also similar to the ones obtained for an equivalent Brownian system ($D\tau_\alpha \sim 0.02$ for each considered softness), which suggests that at least for persistence lengths below the cage length the active system exhibits no distinct qualitative changes with respect to its passive counterpart. In comparison, upon further increasing l_p we observe a sudden rise of $D\tau_\alpha$ for all powers n. Interestingly, the point at which this happens seems not to concur with the optimum of the dynamics, but instead with the point at which the active dynamics becomes slower than that of the equivalent Brownian system ($\tau_\alpha/\tau_0 > 1$). Thus, the onset of slow dynamics, which is here induced by increasing the persistence length, coincides with the breakdown of the SER. This is consistent with passive glassy phenomenology where the onset of slow dynamics is typically induced by supercooling.

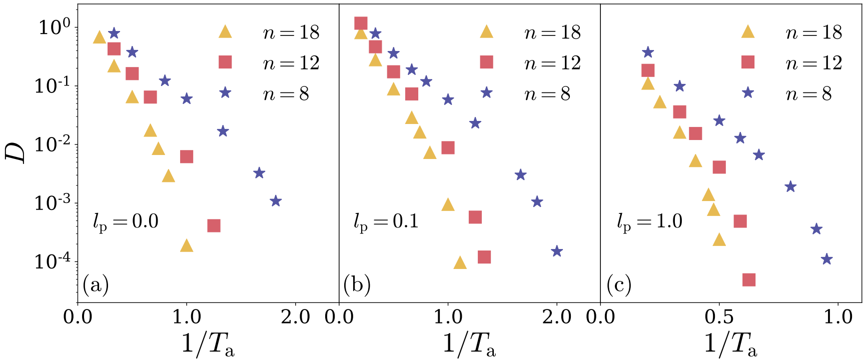

Figure 4.3: Plots of the long-time diffusion coefficient D as a function of the inverse active temperature $1/T_\mathrm{a}$ for different particle softness (governed by the power n) and persistence lengths l_p. When the persistence length becomes larger than the cage length ($l_\mathrm{p} \gtrsim 0.1$), the active temperature at which D tends to zero starts to significantly increase.

4.4 Approaching dynamical arrest

Up until this point we have kept the active temperature fixed for each particle softness and focused primarily on the dependence on the persistence length. We now proceed by taking a more in-depth look at the qualitative and quantitative behavior of the dynamics as a function of T_a. In other words, we take a closer look at how our system approaches a dynamically arrested state. Based on the nonmonotonic behavior observed at a constant active temperature, we choose to concentrate on three distinct values of $l_\mathrm{p} = 0.0, 0.1, 1.0$, which, in relation to the cage length l_c, serve to probe the regimes $l_\mathrm{p} \ll l_\mathrm{c}$, $l_\mathrm{p} \sim l_\mathrm{c}$, and $l_\mathrm{p} \gg l_\mathrm{c}$ respectively. For these values we have calculated the long-time diffusion coefficients D (see Supplemental Material of Ref. [120] for several plots of corresponding MSDs that illustrate the emergence of glassy dynamics) and plotted them as a function of $1/T_\mathrm{a}$ for different particle softness n in Fig. 4.3 (note that for $l_\mathrm{p} = 0$, T_a represents the temperature T). We observe that in all cases the particles become slower when they are stiffer. Moreover, we see that the active temperature at which D tends to zero remains approximately the same for $l_\mathrm{p} = 0.0, 0.1$, while it is significantly increased for $l_\mathrm{p} = 1.0$. This implies that the slowdown of the dynamics when the persistence length surpasses the cage length (see for instance Fig. 4.1) is robust for different active temperatures and is thus retained when approaching a more dynamically arrested state of our active system.

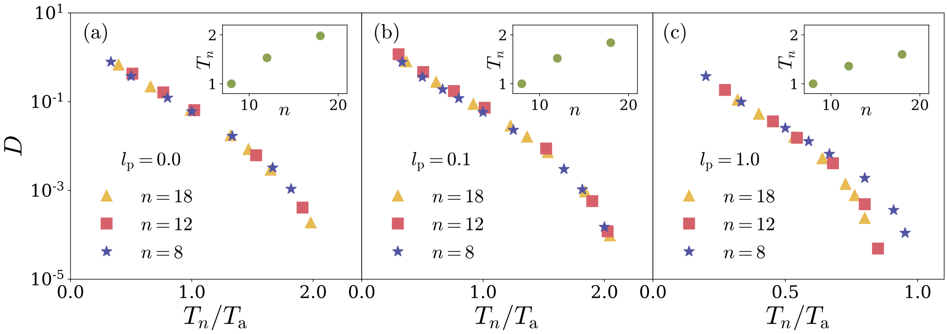

Figure 4.4: Plots of the long-time diffusion coefficient D as a function of the normalized inverse active temperature T_n/T_a for different particle softness (governed by the power n) and persistence lengths l_p. The scaling parameter T_n has been chosen to maximize the overlap between different curves and is plotted in the insets. For values approximately smaller than the cage length ($l_\mathrm{p} \lesssim 0.1$) all curves collapse onto a master curve indicating that the fragility is independent of the softness. For larger values of l_p qualitative changes occur for different particle softness.

To test whether going beyond the cage length also marks the emergence of qualitative changes between different particle softness, we have sought to rescale the inverse active temperature with a scaling parameter T_n. This procedure is inspired by the fact that in previous work on a similar passive system it has been shown that (at least up to a power $n = 18$) the long-time diffusion coefficients D can be scaled onto a master curve (implying fragility invariance) depending solely on the scaled inverse temperature T_n/T [158]. The results of this rescaling process for our model system are demonstrated in Fig. 4.4 and indeed, in the limit of passive particles ($l_\mathrm{p} = 0$) we also find that a scaling is possible, where we mention that the obtained values of D are quantitatively consistent with the ones reported in Ref. [158]. Interestingly, such a scaling is not limited to a passive system, since our active system at $l_\mathrm{p} = 0.1$ also exhibits a collapse of the data points. In fact, we have verified that the data for $l_\mathrm{p} = 0.0$ and $l_\mathrm{p} = 0.1$ can even be collapsed onto each other, which suggests that their fragility is approximately equal and independent of n. On the other hand, we see that for a relatively large persistence length $l_\mathrm{p} = 1.0$ a collapse is not possible and the fragility depends explicitly on n. It thus seems that only when the persistence length becomes larger than the cage length, qualitative differences with respect to a passive reference system and between different particle softness start to manifest themselves. In other words, this suggests that for all values $l_\mathrm{p} \lesssim l_\mathrm{c}$, our athermal active system can essentially be considered as a passive system with enhanced dynamics.

4.5 Conclusions

In this chapter, we have, by means of extensive computer simulations of athermal active Brownian particles (ABPs), explored the subtle relationship between active motion and particle softness in the glassy regime. Our results demonstrate that the qualitative behavior of the relaxation dynamics at a fixed active temperature is robust to changes in softness. In particular, the relaxation dynamics exhibits a nonmonotonic dependence on the persistence length (the intrinsic active length scale) with an optimum (largest speedup) corresponding to the point where the persistence length coincides approximately with the cage length. Small quantitative differences for varying softness have in turn been rationalized by considering the longer range of the softer interaction potential, which decreases the cage length and obscures the intrinsic active motion. As a result, the optimum of the dynamics shifts to smaller persistence lengths and becomes flattened for increasing softness.

When the persistence length is instead kept fixed at a value approximately equal to the cage length we witness the appearance of a universal curve (see Fig. 4.4b) onto which the long-time diffusion coefficients for different softness (up to a power $n = 18$) fully collapse as a function of the scaled active temperature. In fact, even the results of an equivalent Brownian system can be added to this universal curve (see Fig. 4.4a). Consequently, the relaxation dynamics of the active system at relatively small persistence lengths does not exhibit any significant qualitative changes with respect to its passive counterpart and its fragility is independent of the softness. In contrast, when the persistence length is set at a significantly larger value than the cage length we find that both the active temperature at which the long-time diffusion coefficient tends to zero starts to significantly increase and a collapse of the long-time diffusion coefficients is no longer possible. The latter indicates that the qualitative features of vitrification, e.g., the fragility, explicitly depend on particle softness.

Overall, our work shows that the cage length marks the offset beyond which active glassy matter becomes qualitatively different from conventional passive glassy materials. It therefore further strengthens the importance of the cage length and its relation to the relevant active length scale in the context of active glassy dynamics. As a followup it might be worthwhile to check the role of the cage length for model biological glass-formers such as confluent cell layers [2, 48, 80, 161] or for (colloidal) systems involving more complex and possibly attractive interaction potentials. Alternatively, a more detailed study on the qualitative changes for different softness in the limit of large persistence [119, 165] or an analysis of our results in relation to a recently introduced mean-field softness [166] are equally interesting, but for now left for future work.

Finally, we want to mention that in recent years much work has also been devoted to the escape properties of a single active particle from a potential trap or within a porous environment [167–173]. It would be interesting to check whether the analogy between a potential trap or porous environment and a dynamic cage of surrounding particles can be exploited to better understand the qualitative features, particularly the nonmonotonic behavior, of dense active matter.

Appendix

4.A Cage length estimation

To find an estimate of the size of the cage length we have calculated the AA-component, with A the majority species of the system, of the radial distribution function $g_{\mathrm{AA}}(r)$. In particular, we have retrieved it for both a passive Brownian system ($l_{\mathrm{p}} = 0$) and at the point where the long-time diffusion coefficient is approximately most enhanced ($l_{\mathrm{p}} = 0.1$). The results are shown in Fig. 4.5. One can interpret the position of the first minimum ($r \sim 1.4\sigma_{\mathrm{AA}}$) as the size of the shell of directly-neighboring (type A) particles. Taking the weighted average (using $g_{\mathrm{AA}}(r)$ as our weight function) of all distances up until this point thus allows us to find the approximate average distance r_{nn} between a particle and its nearest neighbors. An estimate of the cage length can then be obtained via $l_{\mathrm{c}} = r_{\mathrm{nn}} - \sigma_{\mathrm{AA}}$ (with σ_{AA} the diameter of the type A particle). Based on this procedure we find for both considered persistence lengths $l_{\mathrm{c}} \sim 0.12\sigma_{\mathrm{AA}}$ for $n = 36$, $T_{\mathrm{a}} = 1.5$, $l_{\mathrm{c}} \sim 0.12\sigma_{\mathrm{AA}}$ for $n = 18$, $T_{\mathrm{a}} = 1.35$, $l_{\mathrm{c}} \sim 0.11\sigma_{\mathrm{AA}}$ for $n = 12$, $T_{\mathrm{a}} = 1.0$, and $l_{\mathrm{c}} \sim 0.11\sigma_{\mathrm{AA}}$ for $n = 8$, $T_{\mathrm{a}} = 0.6$. However, it should be noted that as particles become softer (smaller n) the diameter of a particle and thus the cage length becomes less well-defined due to the longer range of the potential. This causes the small quantitative changes we observe in our results.

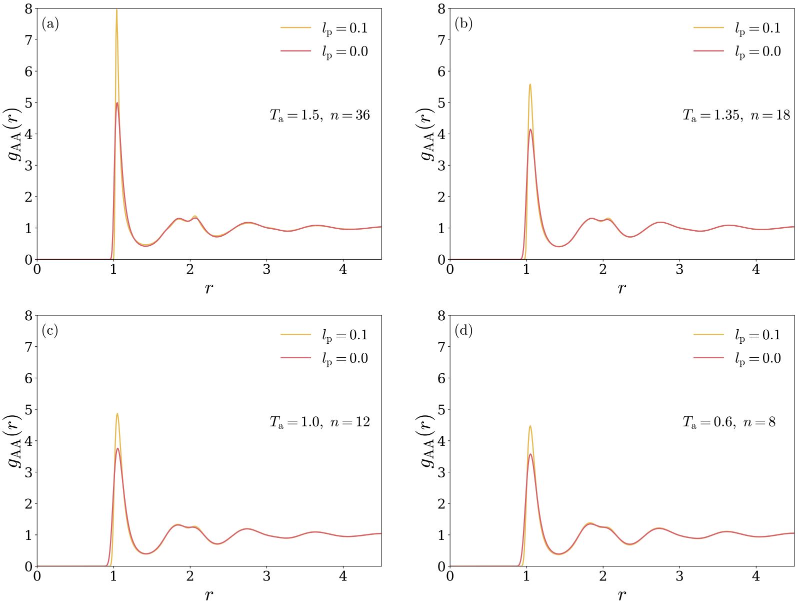

Figure 4.5: Plots of the AA-component of the radial distribution function as a function of the distance r. Results correspond to different persistence lengths l_p and values of the particle softness n. It can be seen that the qualitative behavior is not strongly influenced by the softness.

4.B Static structure factor

In previous work it has been shown that the nonmonotonic behavior of the dynamics in some cases is also reflected in the height of the first peak of the static structure factor [112]. We have therefore extracted the static structure factor of the majority A species $S_\mathrm{AA}(k) = \left\langle \sum_{j=1}^{N_\mathrm{A}} e^{-i\mathbf{k}\cdot\mathbf{r}_j} \sum_{l=1}^{N_\mathrm{A}} e^{i\mathbf{k}\cdot\mathbf{r}_l} \right\rangle$ as a function of the wavenumber k for different values of the softness and persistence length l_p. A subset of these have been plotted in Fig. 4.6. It can be seen that the location of the first peak changes only marginally for the considered softness and persistence values. Moreover, especially for the steeper potentials ($n = 18, 36$) we observe nonmonotonic behavior of the peak height. To study this in more detail we have extracted the peak value of the static structure factor and plotted it as a function of l_p in Fig. 4.7. Interestingly, the qualitative behavior is highly similar to that of D and τ_α shown in Fig. 1 in the main text.

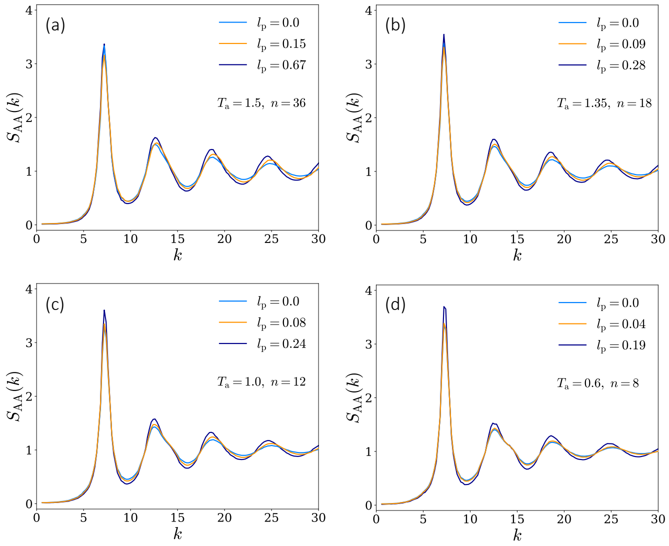

Figure 4.6: The static structure factor of the majority A species $S_{\mathrm{AA}}(k) = \left\langle \sum_{j=1}^{N_{\mathrm{A}}} e^{-i\mathbf{k}\cdot\mathbf{r}_j} \sum_{l=1}^{N_{\mathrm{A}}} e^{i\mathbf{k}\cdot\mathbf{r}_l} \right\rangle$ as a function of the wavenumber k for different l_{p} keeping the active temperature T_{a} fixed. It can be seen that the height of the first peak, which can be used as a proxy for glassiness [112], shows nonmonotonic behavior.

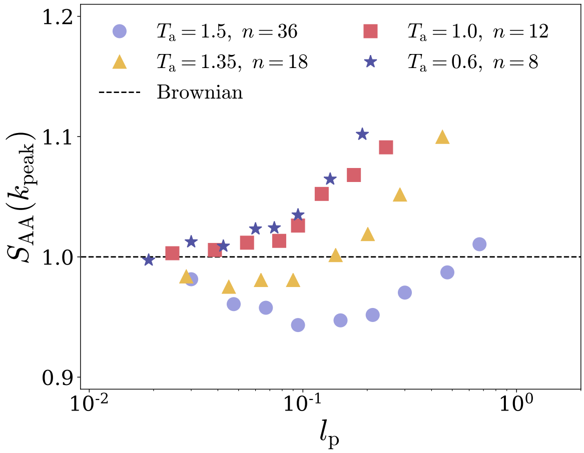

Figure 4.7: The peak value of static structure factor of the majority A species as a function of l_{p} for different values of the softness. The qualitative behavior is in accordance with that of D and τ_α shown in Fig. 1 in the main text.

Chapter 5

Mode-coupling theory for mixtures of athermal self-propelled particles

Abstract. To better grasp the subtle effect of active motion on the process of vitrification, a number of active mode-coupling theories (MCTs) have recently been developed. Allowing a more fundamental perspective than simulations, these have proven capable of qualitatively predicting important parts of the active glassy phenomenology. However, most efforts so far have only considered single-component materials, and their derivations are arguably more complex than the standard MCT case, which might hinder broader usage. In this chapter, we present a detailed derivation of a distinct active MCT for mixtures of athermal self-propelled particles that is more transparent than previously introduced versions. The key insight is that we can follow a similar strategy for our overdamped active system as is typically used for passive underdamped MCT. Interestingly, when only considering one particle species, our theory gives the *exact* same result as the one obtained in previous work which employed a highly different mode-coupling strategy. Moreover, we assess the quality of the theory and its novel extension to multi-component materials by using it to predict the dynamics of a Kob-Andersen mixture of athermal active Brownian quasi-hard spheres. We demonstrate that our theory is able to capture all qualitative features, most notably the location of the optimum of the dynamics when the persistence length and cage length coincide, for each combination of particle types.

The contents of this chapter are based on the following publication:
V.E. Debets and L.M.C. Janssen, *Mode-coupling theory for mixtures of athermal self-propelled particles*, (submitted)

5.1 Introduction

After studying the effect of active motion on glassy dynamics from a pure simulation perspective in the previous two chapters, we now seek to also complement our results with a more theoretical approach. For passive materials, one of the few first-principles-based theories that is capable of making reasonable predictions about their glassy dynamics is mode-coupling theory (MCT) [15, 21, 174–176] (and its hierarchical extension GMCT [145, 177–186]). Requiring only the static structure factor as input, it can predict the full relaxation dynamics via the intermediate scattering function with qualitative, and in few instances even semi-quantitative, agreement. In an attempt to better comprehend active glassy dynamics, and inspired by the previous successes of MCT, several works have recently set out to extend the theory by also including self-propelled particle motion [100, 101, 103, 104, 106–108, 110, 187]. This has resulted in a number of so-called active MCTs that qualitatively capture part of the active glassy phenomenology. However, most efforts have so far only considered monodisperse systems, and their mathematical derivations are rather involved, which might discourage a broader usage of the theories.

In this chapter, to add to our theoretical understanding of active glassy dynamics, we present an active MCT for mixtures of athermal self-propelled particles that is distinct from, and conceptually more transparent than, previously introduced versions. We consider an overdamped active system for which we can follow a similar strategy as typically used for the well-established passive underdamped MCT [175]. This helps make the derivation more insightful and, since we do not have to specify the time evolution of our active force, allows it to be more general. Interestingly, we show that for a monodisperse system our theory yields the *exact* same equation for the intermediate scattering function as has been previously derived in another (seemingly more involved) mode-coupling theory [101, 103]. Finally, we test our theory's predictive capabilities for multicomponent systems by comparing it to simulation results obtained for a Kob-Andersen mixture of athermal active Brownian quasi-hard spheres. We find that for all particle types our theory gives qualitatively consistent predictions and thus captures a non-trivial maximum of the dynamics when the persistence length equals the so-called cage length.

5.2 Multi-component active mode-coupling theory

As our model system we consider an athermal N-particle active fluid of volume V which consists of m different species α with component number densities $\rho_\alpha = N_\alpha/V$. In the overdamped limit, the motion in time t of each individual particle is described via the following equation [85, 104, 122]

$$\dot{\mathbf{r}}_i^\alpha = \zeta_\alpha^{-1} \left(\mathbf{F}_i^\alpha + \mathbf{f}_i^\alpha \right). \tag{5.1}$$

Here, $\mathbf{r}_i^\alpha$ denotes the position of the ith particle of type α, the over-dot derivation with respect to time, ζ_α the (species-dependent) friction constant, and $\mathbf{F}_i^\alpha$ and $\mathbf{f}_i^\alpha$ the interaction and self-propulsion force acting on particle i respectively. Normally, one proceeds by also introducing a time-evolution equation for the self-propulsion force. This will turn out not to be necessary for our derivation and we will therefore refrain from doing so to improve the generality of our derivation. Examples of popular model systems include so-called active Ornstein Uhlenbeck (AOUPs) [91, 102–104, 112, 113] and active Brownian particles (ABPs) [100, 101].

Let us now introduce the velocity of each particle, i.e., $\mathbf{p}_i^\alpha = \dot{\mathbf{r}}_i^\alpha$, and use it to complement the particle positions as our degrees of freedom (essentially replacing the active forces). Note that for thermal particles this is not feasible since $\mathbf{p}_i^\alpha$ would become discontinuous due to the thermal noise term. The joint N-particle probability distribution of positions and velocities $P_N(\Gamma; t)$ then evolves in time via

$$\dot{P}_N(\Gamma; t) = \Omega P_N(\Gamma; t), \tag{5.2}$$

where $\Gamma = (\{\mathbf{r}_i^\alpha\}, \{\mathbf{p}_i^\alpha\})$ depicts the degrees of freedom and Ω is the Smoluchowski operator which can be inferred from the equations of motion for the positions and velocities (see [135] for an example with AOUPs). Now we assume that our system can reach a steady-state characterized by a probability distribution $P_N^{\mathrm{ss}}(\Gamma)$ that obeys [101, 103]

$$\Omega P_N^{\mathrm{ss}}(\Gamma) = 0. \tag{5.3}$$

Using the steady-state distribution one can define the time-correlation function $\mathbf{C}(t)$ of any dynamical vector $\mathbf{A}(t)$ whose elements $A_i(t) = [\mathbf{A}(t)]_i$ are functions of the degrees of freedom as

$$\mathbf{C}(t) = \langle \mathbf{A}^*(0)\mathbf{A}(t) \rangle = \left\langle \mathbf{A}^* e^{\Omega^\dagger t} \mathbf{A} \right\rangle, \tag{5.4}$$

with averages $\langle \ldots \rangle$ taken with respect to $P_N^{\mathrm{ss}}(\Gamma)$, $\mathbf{A} = \mathbf{A}(0)$, the asterisk depicting complex conjugation, and the adjoint (or backward) Smoluchowski operator $\Omega^\dagger$ working on everything to its right except the probability distribution. Moreover, taking the derivative with respect to time and setting it to zero we also obtain the useful property $\langle \mathbf{A}^* \dot{\mathbf{A}} \rangle = \langle \mathbf{A}^* \Omega^\dagger \mathbf{A} \rangle$.

The strategy of mode-coupling theory is then to choose for the elements of the dynamical vector slow or quasi-conserved quantities of the system. We will focus on the conventional ones usually considered in the derivation of underdamped passive MCT, i.e., the density modes and their respective time-derivatives or current modes [15, 175, 181]. Note that we thus assume that current modes retain their slow character, which might not necessarily be true in an active matter setting. In particular, we have

$$\mathbf{A} = \left[\rho^1_{\mathbf{k}}, \ldots, \rho^m_{\mathbf{k}}, j^1_{\mathbf{k}}, \ldots, j^m_{\mathbf{k}}\right] = \left[\boldsymbol{\rho}_{\mathbf{k}}, \mathbf{j}_{\mathbf{k}}\right], \tag{5.5}$$

where $\rho^\alpha_{\mathbf{k}} = \sum_{i=1}^{N_\alpha} e^{i\mathbf{k}\cdot\mathbf{r}^\alpha_i}/\sqrt{N_\alpha}$ and $j^\alpha_{\mathbf{k}} = -i\dot{\rho}^\alpha_{\mathbf{k}}$ are the density and current modes respectively, N_α the number of particles of type α, and $\mathbf{k}$ a wave vector which probes the length scale of interest.

Having specified our vector we can then employ the Mori-Zwanzig formalism [139, 140] to develop an equation of motion for its time-correlation function. We define a projection operator onto the subspace spanned by $\mathbf{A}$ as $\mathcal{P} = \sum_{i,j} |A_i\rangle G^{-1}_{ij} \langle A^*_j|$ (and its complement $\mathcal{Q} = \mathcal{I} - \mathcal{P}$), where we have introduced $\mathbf{G} = \langle \mathbf{A}^* \mathbf{A} \rangle$. The superscript -1 denotes the inverse matrix of the respective quantity, i.e. $G^{-1}_{ij} \equiv [\mathbf{G}^{-1}]_{ij}$. Note that the normalization G^{-1}_{ij} ensures the idempotence of $\mathcal{P}$. Following standard procedure (see Section 2.2) one may find

$$\dot{\mathbf{C}}(t) + \mathbf{H} \cdot \mathbf{G}^{-1} \cdot \mathbf{C}(t) + \int_0^t dt' \; \mathbf{K}(t-t') \cdot \mathbf{G}^{-1} \cdot \mathbf{C}(t') = 0, \tag{5.6}$$

where $\mathbf{H} = -\left\langle \mathbf{A}^* \Omega^\dagger \mathbf{A} \right\rangle = -\langle \mathbf{A}^* \dot{\mathbf{A}} \rangle$ denotes the frequency matrix and

$$\mathbf{K}(t) = -\left\langle \mathbf{A}^* \Omega^\dagger \mathcal{Q} e^{\mathcal{Q}\Omega^\dagger \mathcal{Q} t} \mathcal{Q} \Omega^\dagger \mathbf{A} \right\rangle \tag{5.7}$$

the memory function.

Given the division of our dynamical vector into density and current modes, it is now convenient to segment $\mathbf{C}(t)$ into four separate (m, m) matrices via

$$\mathbf{C}(t) = \begin{bmatrix} \mathbf{C}_{\rho\rho} & \mathbf{C}_{\rho j} \\ \mathbf{C}_{j\rho} & \mathbf{C}_{jj} \end{bmatrix}. \tag{5.8}$$

Similar to previous work in active MCT we assume that current densities vanish after integrating out the velocities (or active forces) [101, 103]. In other words, we assume that

$$\int d\mathbf{p}^1_1 \ldots d\mathbf{p}^m_{N_\mathrm{m}} \; \mathbf{p}^\alpha_i P^\mathrm{ss}_N(\Gamma) = 0. \tag{5.9}$$

Consequently, we have $\langle \rho^{\alpha*}_{\mathbf{k}} \dot{\rho}^\beta_{\mathbf{k}} \rangle = 0$. If we then use that $\langle \rho^{\alpha*}_{\mathbf{k}} \rho^\beta_{\mathbf{k}} \rangle = S_{\alpha\beta}(k)$ and $\langle j^{\alpha*}_{\mathbf{k}} j^\beta_{\mathbf{k}} \rangle = k^2 \omega_{\alpha\beta}(k)$, it can be shown that

$$\mathbf{G} = \begin{bmatrix} \mathbf{S}(k) & \mathbf{0} \\ \mathbf{0} & k^2 \boldsymbol{\omega}(k) \end{bmatrix}, \quad \mathbf{G}^{-1} = \begin{bmatrix} \mathbf{S}^{-1}(k) & \mathbf{0} \\ \mathbf{0} & k^{-2} \boldsymbol{\omega}^{-1}(k) \end{bmatrix}. \tag{5.10}$$

Here, we have introduced the static structure factor $S_{\alpha\beta}(k)$ and the static velocity-structure correlation function (both of which are symmetric in their species label),

$$\omega_{\alpha\beta}(k) = \frac{\zeta_\alpha^{-1}\zeta_\beta^{-1}}{\sqrt{N_\alpha N_\beta}} \hat{\mathbf{k}} \cdot \left\langle \sum_{i=1}^{N_\alpha} \left(\mathbf{F}_i^\alpha + \mathbf{f}_i^\alpha \right) e^{-i\mathbf{k}\cdot\mathbf{r}_i^\alpha} \sum_{j=1}^{N_\beta} \left(\mathbf{F}_j^\beta + \mathbf{f}_j^\beta \right) e^{i\mathbf{k}\cdot\mathbf{r}_j^\beta} \right\rangle \cdot \hat{\mathbf{k}}. \tag{5.11}$$

Interestingly, the latter function is identical to the one introduced in a different active MCT approach [103] and has subsequently been studied in several numerical works [91, 112, 113]. It serves to quantify correlations between the velocities of individual particles and represents a distinct nonequilibrium feature (see also Chapter 7). That is, it is a constant in the passive limit and develops significant oscillations upon increasing the persistence of particles.

To find a suitable expression for the frequency matrix we will also assume that the time-correlated version of $\boldsymbol{\omega}(k)$ decays exponentially over a timescale equal to the persistence time τ_p of the active force (assumed to be the same for all species). This corresponds to the fact that the velocities decorrelate over a similar characteristic time as the active forces and implies that we have

$$\langle j_{\mathbf{k}}^{\alpha *} \dot{j}_{\mathbf{k}}^{\beta} \rangle \approx -\frac{k^2}{\tau_\mathrm{p}} \omega_{\alpha\beta}(k) \tag{5.12}$$

and thus

$$\mathbf{H} = \begin{bmatrix} \mathbf{0} & -ik^2\boldsymbol{\omega}(k) \\ -ik^2\boldsymbol{\omega}(k) & k^2\boldsymbol{\omega}(k)/\tau_\mathrm{p} \end{bmatrix}. \tag{5.13}$$

Note that this approximation likely becomes progressively worse for larger persistence as velocities are probably decorrelating on shorter time scales due to collisions with other particles.

Finally, we realize that

$$\begin{aligned} \mathcal{Q}\Omega^\dagger |\mathbf{A}\rangle &= |\dot{\mathbf{A}}\rangle + |\mathbf{A}\rangle \cdot \mathbf{G}^{-1} \cdot \mathbf{H} \\ &= \left[|\mathbf{0}\rangle, |\dot{\mathbf{j}}_{\mathbf{k}}\rangle - ik^2 |\boldsymbol{\rho}_{\mathbf{k}}\rangle \cdot \mathbf{S}^{-1}(k) \cdot \boldsymbol{\omega}(k) + \tau_\mathrm{p}^{-1} |\mathbf{j}_{\mathbf{k}}\rangle \right] \equiv \left[|\mathbf{0}\rangle, |\mathbf{R}_r\rangle \right]. \end{aligned} \tag{5.14}$$

Combining the above derived results and focusing on the lower-left term of $\mathbf{C}(t)$, whose elements are proportional to the time derivative of the intermediate scattering function $F_{\alpha\beta}(k,t) = \langle \rho_{\mathbf{k}}^{\alpha *} \rho_{\mathbf{k}}^{\beta}(t) \rangle$, allows us to write down a dynamical equation for it, which is given by

$$\begin{aligned} \ddot{F}_{\alpha\beta}(k,t) + \frac{1}{\tau_\mathrm{p}} \dot{F}_{\alpha\beta}(k,t) + \sum_{\gamma\delta} k^2 \omega_{\alpha\gamma}(k) S_{\gamma\delta}^{-1}(k) F_{\delta\beta}(k,t) \\ + \int_0^t dt' M_{\alpha\gamma}(k, t-t') \omega_{\gamma\delta}^{-1}(k) \dot{F}_{\delta\beta}(k,t') = 0. \end{aligned} \tag{5.15}$$

The most involved term in this equation is the memory kernel which is formally written as

$$M_{\alpha\beta}(k,t) = -\frac{1}{k^2}\langle R_l^\alpha e^{\mathcal{Q}\Omega^\dagger\mathcal{Q}t} R_r^\beta\rangle, \tag{5.16}$$

with $|\mathbf{R}_r\rangle$ as defined in Eq. (5.14) and $\langle\mathbf{R}_l| = \langle\mathbf{j}_\mathbf{k}^*|\Omega^\dagger - ik^2\boldsymbol{\omega}(k)\cdot\mathbf{S}^{-1}(k)\cdot\langle\boldsymbol{\rho}_\mathbf{k}^*| + \tau_\mathrm{p}^{-1}\langle\mathbf{j}_\mathbf{k}^*|$. To proceed and make analytical progress we need to approximate this term. Therefore, we apply standard techniques from conventional MCT and replace its projected with full dynamics, while also projecting on density doublets [142, 181, 186]. In other words, we have

$$\begin{aligned} M_{\alpha\beta}(k,t) &\approx -\frac{1}{k^2}\langle R_l^\alpha \mathcal{P}_2 e^{\Omega^\dagger t}\mathcal{P}_2 R_r^\beta\rangle \\ &= -\frac{1}{4k^2}\sum_{\mathbf{q}_1\ldots\mathbf{q}_4}\sum_{\mu_1\ldots\mu_4}\sum_{\nu_1\ldots\nu_4}\langle R_l^\alpha\rho_{\mathbf{q}_1}^{\mu_1}\rho_{\mathbf{q}_2}^{\mu_2}\rangle S_{\mu_1\nu_1}^{-1}(q_1)S_{\mu_2\nu_2}^{-1}(q_2) \\ &\quad\times\langle\rho_{\mathbf{q}_1}^{\nu_1 *}\rho_{\mathbf{q}_2}^{\nu_2 *}e^{\Omega^\dagger t}\rho_{\mathbf{q}_3}^{\mu_3}\rho_{\mathbf{q}_4}^{\mu_4}\rangle S_{\mu_3\nu_3}^{-1}(q_3)S_{\mu_4\nu_4}^{-1}(q_4)\langle\rho_{\mathbf{q}_3}^{\nu_3 *}\rho_{\mathbf{q}_4}^{\nu_4 *}R_r^\beta\rangle \end{aligned} \tag{5.17}$$

where we have used the projection operator,

$$\mathcal{P}_2 = \frac{1}{2}\sum_{\mathbf{q}_1\mathbf{q}_2}\sum_{\mu_1\mu_2}\sum_{\nu_1\nu_2}|\rho_{\mathbf{q}_1}^{\mu_1}\rho_{\mathbf{q}_2}^{\mu_2}\rangle S_{\mu_1\nu_1}^{-1}(q_1)S_{\mu_2\nu_2}^{-1}(q_2)\langle\rho_{\mathbf{q}_1}^{\nu_1 *}\rho_{\mathbf{q}_2}^{\nu_2 *}|. \tag{5.18}$$

Our aim is now to calculate explicit expressions for the so-called vertices, i.e., $\langle R_l^\alpha\rho_{\mathbf{q}_1}^{\mu_1}\rho_{\mathbf{q}_2}^{\mu_2}\rangle$ and $\langle\rho_{\mathbf{q}_3}^{\nu_3 *}\rho_{\mathbf{q}_4}^{\nu_4 *}R_r^\beta\rangle$. For this we first note that due to our assumption of vanishing currents [see Eq. (5.9)], terms of the form $\langle j_\mathbf{k}^{\alpha *}\rho_{\mathbf{q}_1}^{\beta}\rho_{\mathbf{q}_2}^{\gamma}\rangle$ are equal to zero. Furthermore, we will employ the convolution approximation [142]

$$\langle\rho_\mathbf{k}^{\alpha *}\rho_{\mathbf{q}_1}^{\beta}\rho_{\mathbf{q}_2}^{\gamma}\rangle \approx \delta_{\mathbf{k},\mathbf{q}_1+\mathbf{q}_2}\sum_\lambda\frac{1}{\sqrt{N_\lambda}}S_{\lambda\alpha}(k)S_{\lambda\beta}(q_1)S_{\lambda\gamma}(q_2), \tag{5.19}$$

with δ_{ij} a Kronecker delta, and make use of the fact that due to time-translational invariance we may rewrite $\langle\dot{j}_\mathbf{k}^{\alpha *}\rho_{\mathbf{q}_1}^{\beta}\rho_{\mathbf{q}_2}^{\gamma}\rangle = -\langle j_\mathbf{k}^{\alpha *}\dot{\rho}_{\mathbf{q}_1}^{\beta}\rho_{\mathbf{q}_2}^{\gamma}\rangle - \langle j_\mathbf{k}^{\alpha *}\rho_{\mathbf{q}_1}^{\beta}\dot{\rho}_{\mathbf{q}_2}^{\gamma}\rangle$. The last expression we require is for terms of the form $\langle\dot{\rho}_\mathbf{k}^{\alpha *}\dot{\rho}_{\mathbf{q}_1}^{\beta}\rho_{\mathbf{q}_2}^{\gamma}\rangle$. In particular, we propose a multi-component extension of a previously introduced convolution approximation for correlation functions involving active particle velocities (see Ref. [103]). This yields

$$\begin{aligned} \langle\dot{\rho}_\mathbf{k}^{\alpha *}\dot{\rho}_{\mathbf{q}_1}^{\beta}\rho_{\mathbf{q}_2}^{\gamma}\rangle &= \frac{\zeta_\alpha^{-1}\zeta_\beta^{-1}}{\sqrt{N_\alpha N_\beta}}\mathbf{k}\cdot\left\langle\sum_{i=1}^{N_\alpha}\left(\mathbf{F}_i^\alpha+\mathbf{f}_i^\alpha\right)e^{-i\mathbf{k}\cdot\mathbf{r}_i^\alpha}\sum_{j=1}^{N_\beta}\left(\mathbf{F}_j^\beta+\mathbf{f}_j^\beta\right)e^{i\mathbf{q}_1\cdot\mathbf{r}_j^\beta}\sum_{l=1}^{N_\gamma}e^{i\mathbf{q}_2\cdot\mathbf{r}_l^\gamma}\right\rangle\cdot\mathbf{q}_1 \\ &\approx \delta_{\mathbf{k},\mathbf{q}_1+\mathbf{q}_2}\sum_\lambda\frac{1}{\sqrt{N_\lambda}}\mathbf{k}\cdot\mathbf{q}_1\omega_{\alpha\lambda}(k)\omega_{\lambda\lambda}^{-1}(\infty)\omega_{\lambda\beta}(q_1)S_{\lambda\gamma}(q_2), \end{aligned} \tag{5.20}$$

where we have introduced

$$\omega_{\alpha\beta}(\infty) = \delta_{\alpha\beta}\frac{1}{3\zeta_\alpha^2 N_\alpha}\langle\sum_{j=1}^{N_\alpha}(\mathbf{F}_j^\alpha + \mathbf{f}_j^\alpha)^2\rangle. \tag{5.21}$$

We emphasize that for a single component system ($m = 1$) Eq. (5.20) reduces to the one presented in Ref. [103].

Using these results one can then show that the memory kernel simplifies to

$$M_{\alpha\beta}(k,t) \approx \frac{1}{4Vk^2}\sum_{\mathbf{q}\mathbf{q}'}\sum_{\mu\nu}\sum_{\mu'\nu'} V^\alpha_{\mu\nu}(\mathbf{k},\mathbf{q})\langle\rho_{\mathbf{q}}^{\mu*}\rho_{\mathbf{k}-\mathbf{q}}^{\nu*}e^{\Omega^\dagger t}\rho_{\mathbf{q}'}^{\mu'}\rho_{\mathbf{k}-\mathbf{q}'}^{\nu'}\rangle V^\beta_{\mu'\nu'}(\mathbf{k},\mathbf{q}'), \tag{5.22}$$

with the vertices given by

$$V^\alpha_{\mu\nu}(\mathbf{k},\mathbf{q}) = \sum_\gamma \frac{1}{\sqrt{\rho_\gamma}}\omega_{\alpha\gamma}(k)\big[\mathbf{k}\cdot\mathbf{q}\ \delta_{\gamma\nu}C_{\gamma\mu}(q) + \mathbf{k}\cdot(\mathbf{k}-\mathbf{q})\ \delta_{\gamma\mu}C_{\gamma\nu}(|\mathbf{k}-\mathbf{q}|)\big], \tag{5.23}$$

which in turn are described by a modified direct correlation function,

$$C_{\alpha\beta}(q) = \sum_{\gamma\epsilon}\left[\delta_{\alpha\beta} - \omega^{-1}_{\alpha\gamma}(\infty)\omega_{\gamma\epsilon}(q)S^{-1}_{\epsilon\beta}(q)\right]. \tag{5.24}$$

To make our equation self-consistent (and thus solvable) we factorize the four-point density correlation function, i.e.,

$$\begin{aligned}\langle\rho_{\mathbf{q}}^{\mu*}\rho_{\mathbf{k}-\mathbf{q}}^{\nu*}e^{\Omega^\dagger t}\rho_{\mathbf{q}'}^{\mu'}\rho_{\mathbf{k}-\mathbf{q}'}^{\nu'}\rangle \approx{}& F_{\mu\mu'}(q,t)F_{\nu\nu'}(|\mathbf{k}-\mathbf{q}|,t)\ \delta_{\mathbf{q},\mathbf{q}'}\\ &+ F_{\mu\nu'}(q,t)F_{\nu\mu'}(|\mathbf{k}-\mathbf{q}|,t)\ \delta_{\mathbf{k}-\mathbf{q},\mathbf{q}'}.\end{aligned} \tag{5.25}$$

so that we have

$$M_{\alpha\beta}(k,t) \approx \frac{1}{2k^2}\sum_{\mathbf{q}}\sum_{\mu\nu}\sum_{\mu'\nu'} V^\alpha_{\mu\nu}(\mathbf{k},\mathbf{q})F_{\mu\mu'}(q,t)F_{\nu\nu'}(|\mathbf{k}-\mathbf{q}|,t)V^\beta_{\mu'\nu'}(\mathbf{k},\mathbf{q}), \tag{5.26}$$

and, taking the thermodynamic limit, we finally obtain

$$M_{\alpha\beta}(k,t) \approx \frac{1}{16\pi^3k^2}\int d\mathbf{q}\sum_{\mu\nu}\sum_{\mu'\nu'} V^\alpha_{\mu\nu}(\mathbf{k},\mathbf{q})F_{\mu\mu'}(q,t)F_{\nu\nu'}(|\mathbf{k}-\mathbf{q}|,t)V^\beta_{\mu'\nu'}(\mathbf{k},\mathbf{q}). \tag{5.27}$$

Interestingly, when only considering one particle type ($m = 1$) the equation of motion for the intermediate scattering function and specifically the derived memory kernel are identical to the ones for AOUPs and ABPs (neglecting thermal noise) obtained in previous work which employed a highly different (and seemingly more involved) mode-coupling strategy [101, 103]. Moreover, in the passive limit where $\tau_{\mathrm{p}}\omega_{\alpha\beta}(k) = D_{\mathrm{t}}\delta_{\alpha\beta}$ (with D_{t} the translational diffusion coefficient) our equation reduces to the MCT-equation derived for mixtures of Brownian particles [142, 186].

5.3 Active-MCT numerics

To self-consistently solve the derived active MCT equations, one needs to complement the theory with a numerical scheme. For this we invoke the rotational symmetry of our system to rewrite the three-dimensional integral over $\mathbf{q}$ in Eq. (6.14) in terms of the bipolar coordinates $q = |\mathbf{q}|$ and $p = |\mathbf{k} - \mathbf{q}|$. The single wavenumber integrals are in turn approximated by a Riemann sum on an equidistant grid $k\sigma = [0.2, 0.6, \ldots, 39.8]$ where σ is the unit of length [188]. The integration over time in Eq. (5.15) is evaluated by means of Fuchs' algorithm [189]. In particular, we evaluate the first $N_t/2 = 16$ points in time via a Taylor expansion with a step size $\Delta t = 10^{-6}$, numerically integrate Eq. (6.14) for the next $N_t/2$ points in time, duplicate the timestep, and repeat this integration process until the long-time limit is reached.

5.4 Simulation details

Given the extension of our theory to multi-component materials, we test its predictions for a model binary active glassformer as a proof of principle. In particular, we choose to study the dynamics of a Kob-Andersen (KA) mixture [37] consisting of $N_{\mathrm{A}} = 800$ and $N_{\mathrm{B}} = 200$ quasi-hard active spheres. The evolution of each particle i is described by Eq. (6.1), with the interaction force $\mathbf{F}_i$ derived from a steep repulsive power-law potential $V_{\alpha\beta}(r) = 4\epsilon_{\alpha\beta}\left(\frac{\sigma_{\alpha\beta}}{r}\right)^{36}$ [156, 157]. The corresponding interaction parameters are given by $\epsilon_{\mathrm{AA}} = 1$, $\epsilon_{\mathrm{AB}} = 1.5$, $\epsilon_{\mathrm{BB}} = 0.5$, $\sigma_{\mathrm{AA}} = 1$, $\sigma_{\mathrm{AB}} = 0.8$, $\sigma_{\mathrm{BB}} = 0.88$, which, combined with setting $\zeta_{\alpha\beta} = 1$, allow for glassy behavior by suppressing crystallization [37, 158]. For the self-propulsion force $\mathbf{f}_i^\alpha$ we use the active Brownian particle (ABP) model [100, 101]. That is, the absolute value of the force f remains constant over time, $\mathbf{f}_i^\alpha = f\mathbf{e}_i^\alpha$, while the orientation $\mathbf{e}_i^\alpha$ undergoes random diffusion on the unit sphere, i.e.,

$$\dot{\mathbf{e}}_i^\alpha = \boldsymbol{\chi}_i^\alpha \times \mathbf{e}_i^\alpha. \tag{5.28}$$

Here, $\boldsymbol{\chi}_i^\alpha$ represents a Gaussian noise with zero mean and variance $\left\langle \boldsymbol{\chi}_i^\alpha(t)\boldsymbol{\chi}_j^\beta(t') \right\rangle_{\mathrm{noise}} = 2D_{\mathrm{r}}\mathbf{I}\delta_{ij}\delta_{\alpha\beta}\delta(t-t')$, with $\mathbf{I}$ the unit matrix and D_{r} the rotational diffusion coefficient (taken to be the same for each particle type).

In the dilute limit when particle-particle interactions are assumed to be absent, each of our particles performs a persistent random walk (PRW). As a result, their mean square displacement (MSD) is given by [104]

$$\left\langle \delta r^2(t) \right\rangle = 6T_{\mathrm{eff}}\left(\tau_{\mathrm{p}}(e^{-t/\tau_{\mathrm{p}}} - 1) + t\right), \tag{5.29}$$

where we have introduced the persistence time $\tau_{\mathrm{p}} = (2D_{\mathrm{r}})^{-1}$ and an effective temperature $T_{\mathrm{eff}} = f^2\tau_{\mathrm{p}}/3$. A closer look at Eq. (5.29) reveals that for $t \ll \tau_{\mathrm{p}}$, the motion is ballistic $\left\langle \delta r^2(t) \right\rangle \approx 3T_{\text{eff}}t^2/\tau_{\text{p}}$, while diffusive motion, $\left\langle \delta r^2(t) \right\rangle \approx 6T_{\text{eff}}t$, is obtained for long times ($t \gg \tau_{\text{p}}$). We can therefore conclude that in the limit $\tau_{\text{p}} \to 0$ (with $T_{\text{eff}} \sim$ constant), our active system reduces to a Brownian one at a temperature $T = T_{\text{eff}}$. It is thus convenient to introduce T_{eff} as our control parameter, which we complement with the persistence length $l_{\text{p}} = f\tau_{\text{p}}$ as a measure for how far we are from the Brownian limit [118].

Each individual simulation consists of solving the overdamped equation [Eq. (6.1)] in time with a forward Euler scheme using LAMMPS [159]. We set the cutoff radius of the repulsive potential at $r_{\text{c}} = 2.5\sigma_{\alpha\beta}$ and fix the size of the cubic periodic simulation box to $L = 9.41$, such that the number density is $\rho = 1.2$. We run the system sufficiently long (typically between 200 and 1000 time units) to prevent aging, and afterwards track the particles over time for at least twice the initialization time. All results are presented in reduced units where σ_{AA}, ϵ_{AA}, $\epsilon_{\text{AA}}/k_{\text{B}}$, and $\zeta\sigma_{\text{AA}}^2/\epsilon_{\text{AA}}$ represent the units of length, energy, temperature, and time respectively [160]. To correct for the influence of diffusive center-of-mass motion, all particle positions are retrieved relative to the momentary center of mass [160].

5.5 Comparison with simulations

In previous work involving the same model glassformer, it has been shown that for a fixed effective temperature T_{eff}, the dynamics exhibits a nonmonotonic dependence on the persistence length l_{p} [118]. As an initial assessment of the quality of our theory, it is interesting to see whether it is capable of predicting this nontrivial behavior. Before we test our theoretical prediction, however, we first want to verify the nonmonotonic dynamics. For this we have extracted the long-time diffusion coefficient $D = \lim_{t\to\infty} \left\langle \delta r^2(t) \right\rangle /6t$ as a function of the persistence length l_{p} at a fixed value of $T_{\text{eff}} = 4.0$. The resulting values are shown in Fig. 5.1 and clearly illustrate nonmonotonic dynamics for both particle species (A and B). Moreover, we find that, consistent with literature [118], the maximum of the dynamics corresponds to the point where the persistence length is approximately equal to the cage length, i.e., $l_{\text{p}} \sim 0.1$.

Having benchmarked our simulation results we now proceed to the active MCT predictions. Based on the retrieved particle trajectories we have calculated the static structure factors $S_{\alpha\beta}(k)$ and velocity-structure correlation functions $\omega_{\alpha\beta}(k)$, which in turn have been rewritten in terms on an equidistant grid via cubic spline. Using these as input for our active MCT, we have calculated the predicted intermediate scattering function $F_{\alpha\beta}(k,t)$. The AA contribution (normalized by the static structure factor) is plotted as a function of time for a subset of persistence lengths in Fig. 5.2. Interestingly, this scattering function decays to zero fastest at an intermediate persistence length, and hence the theory seems able to capture the nonmonotonic dependence of the relaxation

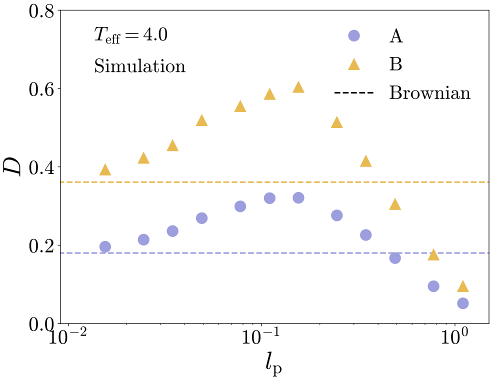

Figure 5.1: The long-time diffusion coefficient D of both the A- and B-type particles as a function of the persistence length l_{p} at a constant effective temperature $T_{\mathrm{eff}} = 4.0$. The results are directly obtained from the simulation data and the value retrieved from passive Brownian dynamics simulations ($l_{\mathrm{p}} = 0$) is added as a reference (dashed lines).

dynamics.

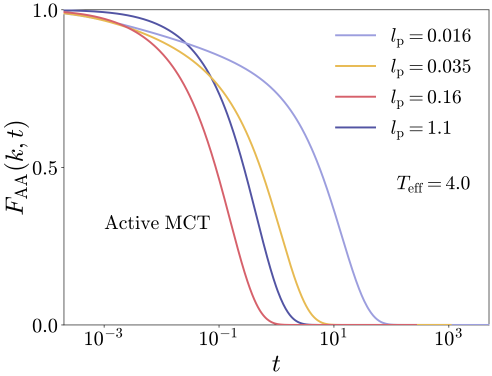

Figure 5.2: The intermediate scattering function of the majority A species $F_{AA}(k,t)$ [normalized by the static structure factor $S_{AA}(k)$] as a function of time t for different persistence lengths l_{p} at a constant effective temperature $T_{\mathrm{eff}} = 4.0$. The results are obtained using active MCT for a wavenumber k corresponding to the main peak of the static structure factor.

To quantify the observed behavior in more detail, we have also retrieved the MCT-predicted alpha-relaxation time via $F_{\alpha\beta}(k,\tau_\alpha)/S_{\alpha\beta}(k) = e^{-1}$ where the wavenumber k

corresponds to the main peak of $S_{\alpha\beta}(k)$. The results are presented in Fig. 5.3 and show clear nonmonotonic and almost identical behavior for all combinations of particle types (either AA, BB, or AB). Note that the fastest relaxation dynamics corresponds to the smallest value of τ_α (in contrast to the largest value of D). Moreover, the optimum of the dynamics again coincides with the point where the persistence length is approximately equal to the cage length, i.e., $l_\mathrm{p} \sim 0.1$. Our theory is thus capable of accurately depicting the qualitative behavior of the relaxation dynamics upon increasing the persistence of the constituent particles.

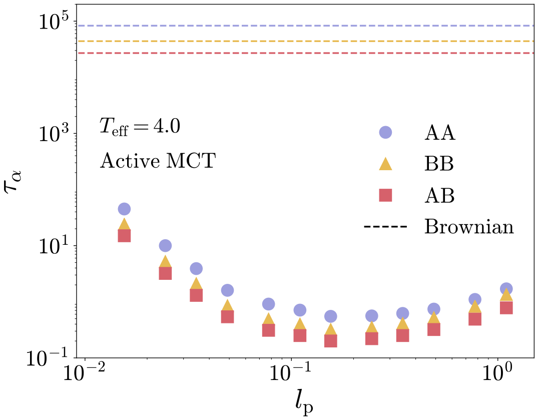

Figure 5.3: The alpha relaxation time τ_α as a function of the persistence length l_p obtained from the active MCT intermediate scattering function $F_{\alpha\beta}(k,t)$. Results correspond to an effective temperature $T_\mathrm{eff} = 4.0$ and are obtained for all particle type combinations. For completeness, the standard MCT prediction based on the structure factor of a passive Brownian system ($l_\mathrm{p} = 0.0$) is added as a reference (dashed lines).

We finalize our discussion by highlighting two noticeable quantitative features. First we find that in all cases our theory predicts faster relaxation dynamics for the smaller type B particles, which is consistent with our simulation results (see Fig. 5.1) and is intuitively to be expected [160]. More strikingly, we also observe that our active MCT predicts a dramatic speedup of the dynamics (orders of magnitude decrease of the relaxation time) compared to that obtained from standard MCT for an analogous passive Brownian system at the same effective temperature ($l_\mathrm{p} = 0.0$, $T = T_\mathrm{eff}$). At first glance this might seem surprising, and while it is probably influenced by the assumptions made in the theory, we argue that this behavior is at least partly to be anticipated. To illustrate this we have calculated, based on simulation data, the self-intermediate scattering function, i.e., $F^\mathrm{s}_\alpha(k,t) = \left\langle e^{-i\mathbf{k}\cdot\mathbf{r}^\alpha_j(0)} e^{i\mathbf{k}\cdot\mathbf{r}^\alpha_j(t)} \right\rangle$, for the majority type A particles and the corresponding alpha relaxation time τ_α^{s} defined via $F_\alpha^{\mathrm{s}}(k,\tau_\alpha^{\mathrm{s}}) = e^{-1}$. The results for different effective temperatures at a fixed persistence length ($l_{\mathrm{p}} = 0.1$, i.e., on the order of the cage length corresponding to the optimum of the dynamics) are shown in Fig. 5.4. For comparison, we have also added the values obtained for a passive Brownian system ($l_{\mathrm{p}} = 0.0$, $T = T_{\mathrm{eff}}$). We can see that as we lower the (effective) temperature, the relaxation time in both cases increases, but the relative difference between the passive and optimum active dynamics is simultaneously being amplified and can reach differences of several orders of magnitude. Thus, as we approach dynamical arrest by lowering T_{eff}, an optimal active system becomes relatively much more dynamic (i.e., more liquid-like) than its Brownian counterpart. Given that our passive MCT predicts an extremely large relaxation time, it is thus to some degree expected that the optimal active dynamics yields a relaxation time that is orders of magnitude smaller.

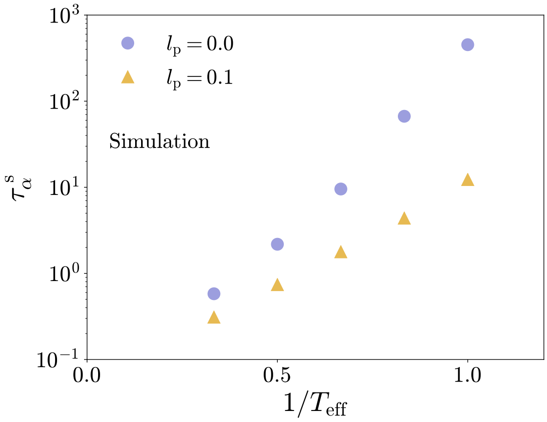

Figure 5.4: The alpha relaxation time τ_α^{s} as a function of the inverse effective temperature for a passive Brownian system ($l_{\mathrm{p}} = 0.0$, $T = T_{\mathrm{eff}}$) and an active system with a persistence length on the order of the cage length ($l_{\mathrm{p}} = 0.1$). The results are extracted from the self-intermediate scattering of the majority A species $F_{\mathrm{A}}^{\mathrm{s}}(k,t)$ which has been directly calculated from the simulation data.

5.6 Conclusions

To conclude, we have presented a fully time-dependent microscopic mode-coupling theory for mixtures of athermal self-propelled particles. The crucial insight for our derivation is that, since we neglect thermal diffusion, the total velocity of each particle is well-behaved; Therefore we can introduce these velocities (instead of the active forces) as our degrees of freedom complementing the particle positions. This then allows us to follow a similar strategy for our overdamped active system as is typically used for passive underdamped MCT [175]. Moreover, it also enables us to leave the time-evolution of the active force unspecified, thereby adding to the generality of the theory. The main result consists of an equation of motion for the (partial) intermediate scattering function, which can be self-consistently solved using the static structure factor and a distinctly non-equilibrium static velocity-structure correlation function as input. Remarkably, for a monodisperse system this equation turns out to be *exacty* equal to one that has been derived in a previous (and possibly more convoluted) active mode-coupling theory [101, 103].

As an initial assessment of the quality of the theory and especially to test its novel extension to multi-component materials, we have used it to predict the dynamics of a Kob-Andersen mixture of athermal active Brownian particles. Such particles exhibit nonmonotonic behavior for increasing particle persistence and thus form a stringent test for the theory. Our theory is indeed able to capture all qualitative features, most notably the location of the optimum of the dynamics when the persistence length and cage length coincide, for each combination of particle types. On a quantitative level active MCT predicts (upon approaching dynamical arrest) a dramatic enhancement of the dynamics (multiple orders of magnitude) compared to that obtained from standard MCT for an analogous passive Brownian system. Though surprising, we show that this effect can in fact be anticipated from simulations. Given the success of our theoretical framework to give qualitatively consistent results, it would be interesting to see whether the analogy between overdamped athermal active systems and underdamped passive ones can be further exploited to better understand the intriguing phenomenology of active glassy matter.

Chapter 6

Active glassy dynamics is unaffected by the microscopic details of self-propulsion

Abstract. For passive glassy materials, it is well established (at least in three dimensions) that the details of the microscopic dynamics, e.g., Newtonian or Brownian, do not influence the long-time glassy behavior. In this chapter, we investigate whether this still holds true in the non-equilibrium active case by considering our two main active particle models, i.e., active Ornstein-Uhlenbeck particles (AOUPs) and active Brownian particles (ABPs). In particular, we seek to gain more insight into the role of the self-propulsion mechanism on the glassy dynamics by deriving a mode-coupling theory (MCT) for thermal AOUPs, which can be directly compared to a recently developed MCT for ABPs. Both theories explicitly take into account the active degrees of freedom. We solve the AOUP- and ABP-MCT equations in two dimensions and demonstrate that both models give almost identical results for the intermediate scattering function over a large variety of control parameters (packing fractions, active speeds, and persistence times). We also confirm this theoretical equivalence between the different self-propulsion mechanisms numerically via simulations of a polydisperse mixture of active quasi-hard spheres, thereby establishing that, at least for these model systems, the microscopic details of self-propulsion do not alter the active glassy behavior.

The contents of this chapter are based on the following publication:
V.E. Debets and L.M.C. Janssen, *J. Chem. Phys.* 157, 224902 (2022)

6.1 Introduction

Intuitively, it might be expected that dense active matter will eventually be dominated by interactions. However, activity can certainly influence glassy materials in non-trivial ways [85, 91, 102, 105, 111, 113, 118, 119]. The question of what this influence precisely encompasses, and to what degree it depends on the specific details of the active self-propulsion mechanism, has therefore unfolded itself as an increasingly interesting new area of research and constitutes one of key objectives of this thesis. As mentioned previously, the main difference between our active matter models, i.e., active Brownian particles (ABPs) and active Ornstein Uhlenbeck particles (AOUPs), rests in the implementation of the self-propulsion force, which either has a constant magnitude and undergoes rotational diffusion (ABPs), or evolves in time according to an Ornstein-Uhlenbeck process (AOUPs). This difference, however, is washed out on a coarse-grained level where the active degrees of freedom are integrated out, in which case both models become identical [104]. Since most theoretical attempts to study dense assemblies of these model active particles have required coarse-graining [101–104, 122, 190], it has not yet been possible to pinpoint the effect of the specific self-propulsion mechanism on the glassy dynamics.

An exception to the coarse-grained strategy is recent work where a mode-coupling theory (MCT) for two-dimensional (2D) ABPs has been developed in which the active degrees of freedom, i.e., the orientations of the active force, are explicitly taken into account [100, 106–108]. This has revealed several non-trivial short-time features which cannot be captured when employing coarse-grained approaches. A key question, however, remains whether these microscopic details play a significant role in the long-time glassy dynamics of dense active matter. For passive systems it is well-confirmed that (at least in three-dimensional systems) both Brownian and Newtonian dynamics yield identical long-time behavior, and hence the microscopic details of motion are irrelevant for the glassy dynamics. This has been demonstrated both in theory and simulations [22, 160, 181, 191, 192]. It would be interesting to see if such an equivalence is maintained for active systems. Since particle motion becomes more impeded by repulsion at high densities, one would expect the precise single-particle dynamics, whether active or passive, to become increasingly less relevant.

In this chapter, we shed more light on the influence of the self-propulsion mechanism on active glassy dynamics from a theoretical perspective. We provide, for the first time, a detailed derivation of a mode-coupling theory for 2D thermal AOUPs which explicitly takes into account the active degrees of freedom (and can be straightforwardly extended to three dimensions). Our theory, which is based on similar principles as the recently developed MCT for ABPs [100, 106–108], thus allows for a convenient comparison between both models in the high-density regime. We numerically solve the relevant equations and show that for a wide variety of different settings (packing fractions, active speeds, and persistence times) ABPs and AOUPs give almost identical results after mapping their single-particle dynamics onto each other. To further verify the equivalence between both active self-propulsion models, we also directly compare our theoretical results to ones obtained from simulations of a polydisperse mixture of self-propelled quasi-hard disks.

6.2 Active particle models

Both the ABP and AOUP model describe a two-dimensional (2D) N-particle active fluid of area V (and number density $\rho = N/V$) as a collection of self-propelling and interacting particles. In particular, each particle i within the fluid evolves in time t according to [78, 85, 104, 122]

$$\frac{d\mathbf{r}_i}{dt} = \zeta^{-1}\left(\mathbf{F}_i + \mathbf{f}_i\right) + \boldsymbol{\xi}_i. \tag{6.1}$$

Here, $\mathbf{r}_i$ denotes the position of particle i, ζ the friction constant, $\mathbf{F}_i$ and $\mathbf{f}_i$ the interaction and self-propulsion force acting on particle i respectively, and $\boldsymbol{\xi}_i$ a Gaussian thermal noise with zero mean and variance $\left\langle \boldsymbol{\xi}_i(t)\boldsymbol{\xi}_j(t')\right\rangle_{\text{noise}} = 2D\mathbf{I}\delta_{ij}\delta(t-t')$, with D the thermal diffusion coefficient and $\mathbf{I}$ the unit matrix. The distinction between both models resides in the dynamics of the self-propulsion force $\mathbf{f}_i$. For AOUPs, the time evolution of the self-propulsion force is governed by an Ornstein-Uhlenbeck process [91, 102–104, 112, 113]

$$\frac{d\mathbf{f}_i}{dt} = -\tau^{-1}\mathbf{f}_i + \boldsymbol{\eta}_i, \tag{6.2}$$

where τ depicts the typical decay time of the self-propulsion and $\boldsymbol{\eta}_i$ an internal Gaussian noise process with zero mean and a variance $\left\langle \boldsymbol{\eta}_i(t)\boldsymbol{\eta}_j(t')\right\rangle_{\text{noise}} = 2D_f\mathbf{I}\delta_{ij}\delta(t-t')$ whose amplitude is controlled by the noise strength D_f. In contrast, the ABP model assumes a constant absolute value of the self-propulsion speed v_0, so that $\zeta^{-1}\mathbf{f}_i = v_0\mathbf{e}_i = v_0[\cos(\theta_i), \sin(\theta_i)]$, and lets the orientation angles θ_i undergo rotational diffusion with a diffusion coefficient D_r. This yields [78, 100, 101]

$$\dot{\theta}_i = \chi_i, \tag{6.3}$$

with χ_i a Gaussian noise process with zero mean and variance $\langle \chi_i(t)\chi_j(t')\rangle_{\text{noise}} = 2D_{\text{r}}\delta_{ij}\delta(t-t')$.

Without particle-particle interactions, both models predict a persistent random walk (PRW), which implies that the mean square displacement (MSD) of each particle is given by [104]

$$\left\langle \delta r^2(t)\right\rangle = 4Dt + 2v_{\text{a}}^2\tau_{\text{p}}\left(\tau_{\text{p}}(e^{-t/\tau_{\text{p}}} - 1) + t\right). \tag{6.4}$$

The parameters describing such a PRW are the persistence time, $\tau_\mathrm{p} = \tau$ (AOUP), $\tau_\mathrm{p} = (D_\mathrm{r})^{-1}$ (ABP), an (average) active speed $v_\mathrm{a} = v_0$ (ABP), $v_\mathrm{a} = \sqrt{2D_f\tau_\mathrm{p}}\zeta^{-1}$ (AOUP), and the thermal diffusion coefficient D. On the single-particle level both models can thus strictly be mapped onto each other via the equivalency of their MSDs.

6.3 Mode-coupling theory

To infer information on the collective level, we require the joint N-particle probability distribution of positions and self-propulsion forces/orientation angles $P_N(\Gamma;t)$. This distribution is governed by the equation

$$\frac{\partial}{\partial t}P_N(\Gamma;t) = \Omega P_N(\Gamma;t), \tag{6.5}$$

with $\Gamma = (\Gamma_\mathrm{T}, \Gamma_\mathrm{R}) = (\mathbf{r}_1, \ldots, \mathbf{r}_N, \mathbf{f}_1, \ldots, \mathbf{f}_N)$ (AOUP), $\Gamma = (\Gamma_\mathrm{T}, \Gamma_\mathrm{R}) = (\mathbf{r}_1, \ldots, \mathbf{r}_N, \theta_1, \ldots, \theta_N)$ (ABP) denoting the configuration space, and Ω the evolution operator (see Refs. [100, 103] for detailed definitions of the latter). Now we assume that our systems can reach a steady-state characterized by a probability distribution $P_N^\mathrm{ss}(\Gamma)$ that obeys [101, 103]

$$\Omega P_N^\mathrm{ss}(\Gamma) = 0. \tag{6.6}$$

In principle, we can then study our systems by calculating steady-state averages via

$$\langle \ldots \rangle = \int d\Gamma \ldots P_N^\mathrm{ss}(\Gamma). \tag{6.7}$$

However, the steady-state distribution is typically not known exactly. To proceed and make calculations tractable, we will therefore approximate our steady-state averages according to

$$\langle \ldots \rangle \approx \int d\Gamma \ldots P_\mathrm{eq}(\Gamma_\mathrm{T})P(\Gamma_\mathrm{R}), \tag{6.8}$$

where, for the AOUP model,

$$\begin{aligned} P(\Gamma_\mathrm{R}) &= \frac{1}{(2\pi D_f\tau_p)^{dN/2}}\exp\left(-\frac{\sum_i \mathbf{f}_i^2}{2D_f\tau_p}\right) \\ &= \prod_{i=1}^{N}\frac{1}{(2\pi D_f\tau_p)^{d/2}}\exp\left(-\frac{\mathbf{f}_i^2}{2D_f\tau_p}\right) \equiv \prod_{i=1}^{N} p(\mathbf{f}_i) \end{aligned} \tag{6.9}$$

represents the distribution of self-propulsion forces, which is factorized in independent Gaussian single-particle distributions $p(\mathbf{f}_i)$, while for the ABP model it is simply $P(\Gamma_\mathrm{R}) = (2\pi)^{-N}$. Note that $d = 2$ depicts the dimensionality of the system. The distribution of particle positions is the same for both models and given by the Boltzmann solution, $P_{\mathrm{eq}}(\Gamma_{\mathrm{T}}) \propto \exp(-\beta U(\Gamma_{\mathrm{T}}))$. This distribution depends solely on the total interaction potential $U(\Gamma_{\mathrm{T}})$, which induces the interaction forces $\mathbf{F}_i = -\nabla_i U(\Gamma_{\mathrm{T}})$. Moreover, we assume throughout that the Stokes-Einstein equation connects the inverse thermal energy β to the friction constant via $\beta D = \zeta$. As a first approximation, we thus calculate averages based on the distribution the system would assume if the influence of the active forces becomes negligibly small; it therefore neglects any correlations between particle velocities and positions [93, 113, 193] (though we have checked in simulations that these remain relatively small due to the presence of thermal noise) and becomes exact in the limit $v_{\mathrm{a}} \to 0$. Note that in principle this approximation is similar to the lowest order one in the integration-through-transients formalism, which has been employed in previous work on mode-coupling theory for ABPs and colloidal suspensions under shear flow [100, 106–108, 194] and will be discussed in more detail in Chapter 7. In this formalism one typically uses transient correlation functions defined with the equilibrium average to find exact expressions for transport coefficients. It has for instance been used to calculate macroscopic stresses in colloidal suspensions.

In standard mode-coupling theory, the starting point to study the glassy dynamics of a system is the set of density modes [15, 21, 195]. Since we want to explicitly include active degrees of freedom, these become more complex in active-MCT and are given by[1]

$$\rho_l(\mathbf{k}) = \begin{cases} \frac{i^{m+n}}{\sqrt{N}} \sum_{j=1}^{N} e^{i\mathbf{k}\cdot\mathbf{r}_j} H_m(\bar{f}_{j,x}) H_n(\bar{f}_{j,y}), & \text{(AOUP)} \\ \frac{1}{\sqrt{N}} \sum_{j=1}^{N} e^{i\mathbf{k}\cdot\mathbf{r}_j} e^{il\theta_j}, & \text{(ABP)} \end{cases}. \tag{6.10}$$

Here, $H_m(x)$ denotes a normalized Hermite polynomial [see Eq. (6.17)] and $\bar{\mathbf{f}} \equiv \mathbf{f}/\sqrt{2D_f\tau_p}$ a dimensionless self-propulsion force. For compactness of notation, we have introduced the index l as a general label for both AOUPs and ABPs; for AOUPs it corresponds to the degree of the Hermite polynomials $l = \{m, n\}$ with $m, n \in [0, \infty]$, whereas for ABPs it corresponds to the angular mode $l \in [-\infty, \infty]$. The equilibrium-averaged (also called transient) time-correlation between such density modes can then be defined via

$$S_{l;l'}(\mathbf{k}, t) = \left\langle \rho_l^*(\mathbf{k}) e^{\Omega^\dagger t} \rho_{l'}(\mathbf{k}) \right\rangle, \tag{6.11}$$

with $\Omega^\dagger$ the adjoint evolution operator (see Eq. (6.20) and Ref. [100]), which works on everything to its right except for the probability distribution. Note that the lowest order term $S_{0;0}(\mathbf{k}, t) \equiv F(k, t)$ is the same for both models and corresponds to the (transient) intermediate scattering function. It will therefore serve as the main probe to study glassy dynamics of our active systems. Moreover, at time zero, assuming our systems to be isotropic, the density correlation functions are easily calculated and yield

$$S_{l;l'}(k) = \langle \rho_l^*(\mathbf{k}) \rho_{l'}(\mathbf{k}) \rangle = \delta_{ll'} \Big[1 + \delta_{l0}(S(k) - 1) \Big], \tag{6.12}$$

---

[1] For a motivation of the specific form of the density modes we refer to the derivation in Section 6.A and Ref. [100]

where $S(k)$ denotes the equilibrium static structure factor, which, for instance, can be obtained from liquid state theory or simulations.

We now follow the mode-coupling strategy pioneered for ABPs in Ref. [100] and apply it to AOUPs. The full AOUP MCT derivation is detailed in Section 6.A. We finally arrive at the following general equation of motion for the dynamic density correlation functions of both models:

$$\begin{aligned}\frac{\partial}{\partial t}S_{l;l'}(\mathbf{k},t)+\sum_{l_1}\omega_{l;l_1}(\mathbf{k})S^{-1}_{l_1;l_1}(k)S_{l_1;l'}(\mathbf{k},t)+\int_0^t dt'\sum_{l_1l_2}M_{l;l_1}(\mathbf{k},t-t')\\ \times[\omega^{\mathrm{T}}_{l_1;l_2}(\mathbf{k})]^{-1}\left[\frac{\partial}{\partial t'}S_{l_2;l'}(\mathbf{k},t')+\omega^{\mathrm{R}}_{l_2;l_2}S_{l_2;l'}(\mathbf{k},t')\right]=0,\end{aligned} \tag{6.13}$$

where $\omega_{l;l'}(\mathbf{k})$ represents the collective diffusion tensor, which governs the short-time dynamics and is split in a translational (T) and rotational (R) term. The memory kernel encodes all non-trivial dynamics and is given by

$$\begin{aligned}M_{l;l'}(\mathbf{k},t)\approx\frac{\rho}{2}\int\frac{d\mathbf{q}}{(2\pi)^2}\sum_{l_1l_2}\sum_{l_3l_4}V_{ll_1l_2}(\mathbf{k},\mathbf{q},\mathbf{k}-\mathbf{q})\\ \times S_{l_1;l_3}(\mathbf{q},t)S_{l_2;l_4}(\mathbf{k}-\mathbf{q},t)V^{\mathrm{eq}}_{l'l_3l_4}(\mathbf{k},\mathbf{q},\mathbf{k}-\mathbf{q}),\end{aligned} \tag{6.14}$$

For specific details of the involved parameters, in particular the vertices $V_{ll_1l_2}(\mathbf{k},\mathbf{q},\mathbf{k}-\mathbf{q})$ and $V^{\mathrm{eq}}_{ll_1l_2}(\mathbf{k},\mathbf{q},\mathbf{k}-\mathbf{q})$, and a precise derivation we refer to Ref. [100] and Section 6.A. We mention that in comparison to the more familiar passive MCT equation [142], the equation of motion now includes a so-called hopping term $\omega^{\mathrm{R}}_{l_2;l_2}S_{l_2;l'}(\mathbf{k},t')$ inside the time integral. This term ensures the long-time decay of the active degrees of freedom [100]. Importantly, it must be emphasized that, although the structure of the MCT equation of motion is similar for both models, the individual terms in the equation are not necessarily the same. Most notably the collective diffusion tensor $\omega_{l;l'}(\mathbf{k})$ and the left vertex $V_{ll_1l_2}(\mathbf{k},\mathbf{q},\mathbf{k}-\mathbf{q})$ harbor the key differences between the AOUP and ABP model.

To summarize, using only the equilibrium static structure factor $S(k)$, the persistence time τ_{p}, active speed v_{a}, and area fraction ϕ (or number density ρ) as input parameters, we can self-consistently find a solution for $S_{l;l'}(\mathbf{k},t)$ and in particular for the intermediate scattering function $F(k,t)$. The latter can then be used to compare the glassy behavior of both models in the high-density regime.

6.4 Active-MCT numerics

To establish proof of principle, we numerically solve the active-MCT equations for a monodisperse colloidal mixture of hard disks of diameter σ. For such a mixture one can employ an analytical expression for $S(k)$ (as a function of the area fraction $\phi = \rho\pi\sigma^2$) based on density functional theory [196]. The two-dimensional integral over $\mathbf{q}$ in the memory kernel [Eq. (6.14)] is rewritten in terms of the coordinates $q = |\mathbf{q}|$ and $p = |\mathbf{k} - \mathbf{q}|$, whose individual integrals are performed on an equidistant wavenumber grid $k\sigma = [0.6, 1.0, \dots, 39.8]$. Note that we drop the smallest wavenumber $k\sigma = 0.2$ in favor of numerical stability. For computational convenience, we only take into account the lowest order non-trivial active modes, i.e., $l \in [\{0,0\}, \{1,0\}, \{0,1\}]$ (AOUP) and $l \in [-1, 0, 1]$ (ABP). It is important to realize that taking the inverse of $\omega^{\mathrm{T}}_{ll'}(\mathbf{k})$ in principle does not commute with the cutoff of active modes. We have checked that taking the inverse at a larger cutoff (up to twenty non-trivial active modes) and afterwards reducing to the lowest order active modes induces slight quantitative changes, but does not qualitatively change our results. Overall, the used cutoff yields stable solutions for the presented range of active speeds and persistence times, although we mention that above the idealized glass transition instabilities on very long time scales still persist. To handle the fact that higher order correlation functions ($S_{l;l'}(\mathbf{k}, t)$ with $l, l' \neq \{0,0\}, 0$) depend explicitly on the orientation of the wavevector $\mathbf{k}$, we can invoke transformation rules that enable us to rewrite correlators with wavevector $\mathbf{k}$ in terms of ones with a rotated wavevector $\mathbf{k}'$ (see Ref. [100] and Section 6.B for precise details). We can therefore restrict our discussion to wavevectors aligned along a specific direction, which we have chosen to be the x-axis, i.e. $\mathbf{k} = k\mathbf{e}_x$. Finally, we fix the passive diffusion coefficient at $D = 1$ so that our unit of time equals σ^2/D and perform the integration over time in Eq. (6.13) according to the algorithm presented in Ref. [100]. For this, we calculate the first $N_t/2 = 16$ points in time using a Taylor expansion with a step size $\Delta t = 10^{-6}$, numerically integrate the equations of motion for the next $N_t/2$ points in time, duplicate the timestep, and repeat the process.

6.5 Simulation details

To complement our theoretical results we also simulate both the AOUP and ABP dynamics of a slightly polydisperse mixture of $N = 1000$ quasi-hard disks. Each particle i is described by Eq. (6.1) and the interaction force $\mathbf{F}_i = -\sum_{j\neq i} \nabla_i V_{\alpha\beta}(r_{ij})$ is derived from a quasi-hard-sphere powerlaw potential $V_{\alpha\beta}(r) = \epsilon \left(\frac{\sigma_{\alpha\beta}}{r}\right)^{36}$ [156, 157]. The interaction energy ϵ, friction constant ζ, and diffusion coefficient D are all set to a value of one. To ensure polydispersity, our mixture consists of equal fractions of particles with diameters (in units of σ) $\sigma_{\alpha\alpha} = \{0.8495, 0.9511, 1.0, 1.0489, 1.1505\}$[2], which are additive so that $\sigma_{\alpha\beta} = (\sigma_{\alpha\alpha} + \sigma_{\beta\beta})/2$. Simulations are performed by solving the Langevin equation [Eq. (6.1)] via a forward Euler scheme and are carried out using LAMMPS [159]. We fix the square box size to set the area fraction at $\phi = 0.75$ (higher values tend to result in crystallization) and impose periodic boundary conditions. We then set the persistence time τ_{p} and active speed v_{a}, run the system sufficiently long to ensure no aging takes place, and afterwards track the particles over time. All simulation results are presented in units where σ, ϵ, and $\zeta\sigma^2/\epsilon$ denote the units of length, energy, and time respectively [160].

---

[2] Particle diameters are chosen such that the first four moments correspond to the results of a Gaussian distribution with a mean of 1 and a standard deviation of 0.1.

6.6 Free-particle dynamics

Before proceeding to the glassy dynamics, we first briefly discuss the free-particle dynamics in more detail to elucidate potential intrinsic differences between both models. For this we exploit the fact that at zero density the memory kernel can be set to zero and that $S(k) = 1$ [100]. This allows us to exactly solve Eq. (6.13) which

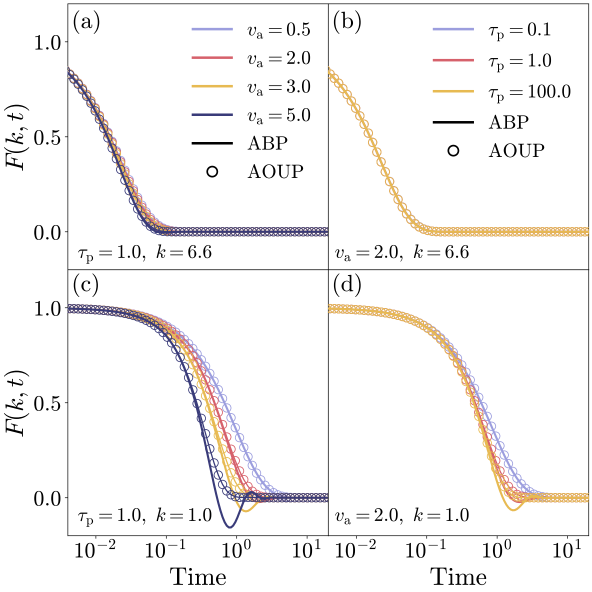

Figure 6.1: The intermediate scattering function $F(k,t)$ for free particles ($\rho = 0$) as a function of time obtained for both ABP-MCT (solid lines) and AOUP-MCT (circles) at (a-b) a wavevector $k = 6.6$ close to the first peak of the static structure factor and (c-d) a relatively small wavevector $k = 1.0$. Results correspond to (a,c) different active speeds, and (b,d) different persistence times.

yields $\mathbf{S}(\mathbf{k}, t) = \exp(-\boldsymbol{\omega}(\mathbf{k})t)$. Based on this result we have calculated the intermediate scattering function $F(k, t)$ for different active speeds and persistence times and have plotted the results in Fig. 6.1. Note that the free-particle solution allows for the inclusion of many active modes, and we have verified that these results remain unaltered upon adding more active modes. An inspection of Fig. 6.1 shows that $F(k, t)$ decays more rapidly upon increasing the active speed or persistence time. Moreover, at a large wavenumber $k = 6.6$ both models give the same results which is consistent with our initial mapping of the single-particle MSDs [see Eq. (3.4)]. Interestingly, it can be seen that at a relatively small wavenumber, $k = 1.0$, differences between both models start to manifest themselves, especially at larger values of the active speed and persistence time. In particular, the ABP model yields oscillatory behavior which has been attributed to the persistent swimming of the ABPs [58, 136]. These oscillations are absent for the AOUPs since the Ornstein-Uhlenbeck process is Gaussian and correlation functions therefore should decay monotonically. A mapping based on the MSD, which is essentially a zero-wavenumber limit of the density correlation function, thus misses these differences at finite k. In other words, the free-particle intermediate scattering function $F(k, t)$ ($\rho = 0$) can distinguish between the ABP and AOUP model.

6.7 Glassy dynamics

Let us now look at the theoretical predictions of the ABP- and AOUP-MCT frameworks at high densities to understand their glassy behavior and see whether the single-particle differences between both models persist in the glassy regime. To compare both models we have primarily focused on the intermediate scattering function $F(k, t)$, which has been plotted for a variety of different settings and both models in Fig. 6.2. We note that, despite the presence of an active self-propulsion mechanism, both ABP-MCT and AOUP-MCT still predict an idealized glass transition upon increasing the packing fraction (or density). This is characterized by the emergence of a nonzero long-time value for $F(k, t)$. Moreover, we see that increasing the active speed v_a and the persistence time τ_p always yields faster relaxation dynamics, represented by a more rapid decay to zero of $F(k, t)$. These predictions are all consistent with the previous in-depth study of ABP-MCT and simulations of a polydisperse mixture of self-propelling hard spheres [85, 100], though we mention that an increase of the persistence time at a fixed effective temperature (instead of the active speed) can also yield non-monotonic behavior [102]. This reentrant dynamics has already been qualitatively predicted by a recently developed MCT for athermal AOUPs [102, 103] and rationalized in terms of efficient cage exploration [118]. More strikingly, however, we observe that for all shown cases and all considered time scales, both models predict almost identical results. This implies that, at least in the numerically accessible region, the mapping between ABPs

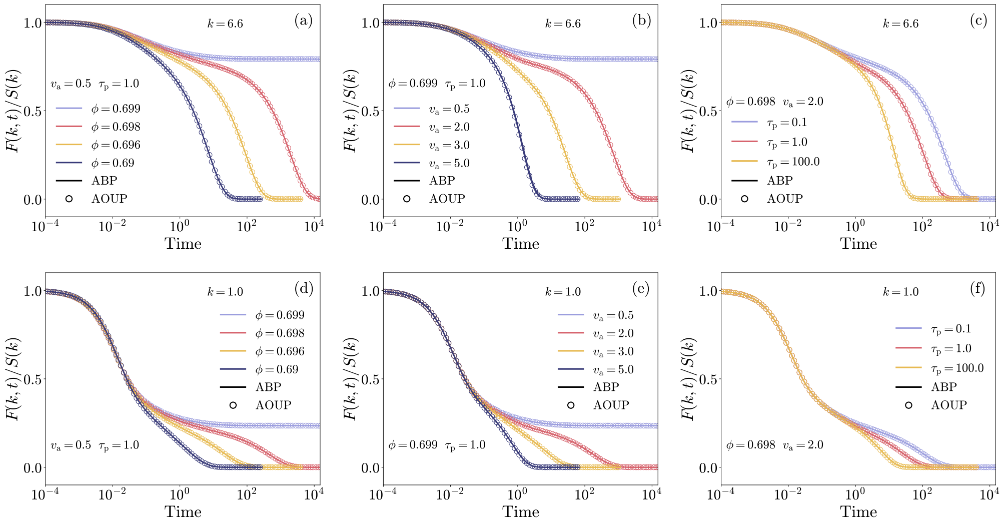

Figure 6.2: The normalized intermediate scattering function $F(k,t)/S(k)$ as a function of time obtained for both ABP-MCT (solid lines) and AOUP-MCT (circles) at (a-c) a wavevector $k = 6.6$ close to the first peak of the static structure factor and (d-f) a relatively small wavevector $k = 1.0$. Results correspond to (a,d) different packing fractions, (b,e) different active speeds, and (c,f) different persistence times.

and AOUPs based on the single-particle MSDs [Eq. (3.4)] transfers directly to the collective structural relaxation in the high-density regime. Interestingly, for a relatively small wavenumber $k = 1.0$ the differences on the single-particle level [see Fig. 6.1c-d] have even been washed out in the glassy regime with $F(k,t)$ in all cases decaying monotonically. Since an oscillatory decay of $F(k,t)$ has been attributed to persistent swimming of the ABPs, we expect that this is suppressed by particle-particle interactions at high densities. This in turn forces the models to become more equivalent and give almost identical results. We have also verified that this equivalence occurs over an even larger parameter range than presented in Fig. 6.2. This suggests that, at least for the chosen model systems, the long-time dynamics does not depend on the microscopic details of the active self-propulsion, which is consistent with recent simulations of (a)thermal ABPs and AOUPs where a different parameter regime (larger active speeds and smaller persistence times) has been probed [118]. An important consequence of this equivalence might reside in the modelling of more complex dense active systems, such as confluent cell layers [45, 48]. For such systems it is often hard to infer precise details of the microscopic self-propulsion mechanism. Our results suggest that these details might be of lesser importance when studying high-density active matter.

6.8 Comparison with simulations

To place our theoretical findings in a broader context we now proceed to the predictions from our simulations. Based on the retrieved particle trajectories we have calculated the self-intermediate scattering function, i.e., $F^{\mathrm{s}}(k,t) = \left\langle e^{-i\mathbf{k}\cdot\mathbf{r}_j(0)} e^{i\mathbf{k}\cdot\mathbf{r}_j(t)} \right\rangle$, where we mention that in simulations the statistical averaging is done with respect to the active steady-state. However, at high densities, the differences between steady-state and transient self-intermediate scattering functions have been found to be small (see Ref. [106] for a more detailed discussion). The results for both models are plotted for a variety of settings in Fig. 6.3. It can be seen that the relaxation of the self-intermediate scattering function occurs on shorter timescales upon increasing the active speed v_{a} (Fig. 6.3a) or the persistence time τ_{p} (Fig. 6.3b). These results are qualitatively consistent with our theoretical predictions for the intermediate scattering function and imply that enhanced particle speed and persistence render the material more liquid-like.

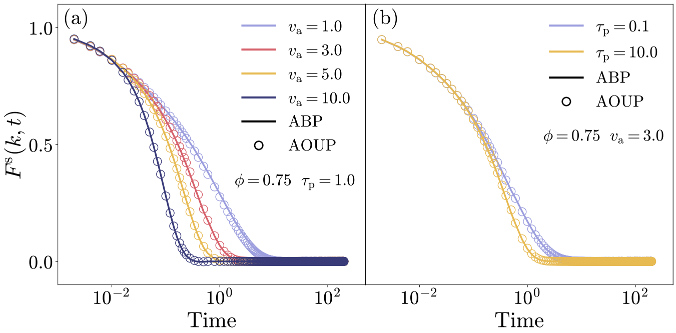

Figure 6.3: The self-intermediate scattering function $F^{\mathrm{s}}(k,t)$ as a function of time obtained from both ABP and AOUP simulations at a wavevector $k = 6.6$ close to the first peak of the static structure factor. Results correspond to different (a) active speeds, and (b) persistence times.

Interestingly, we find that, also for our simulation results, the differences between both model systems are manifestly only marginal. This further substantiates our theoretical predictions and indicates that for simple model active systems the active glassy dynamics is unaffected by the microscopic details of active self-propulsion. This behavior is analogous to more conventional passive glass-forming materials, where it is well established that, at least in three dimensions, different single-particle dynamics, e.g., Newtonian or Brownian, yield similar long-time dynamics [160, 181, 191, 192].

We finalize our discussion by mentioning that a critical assumption in the presented active-MCT theories is the replacement of the steady-state probability distribution by

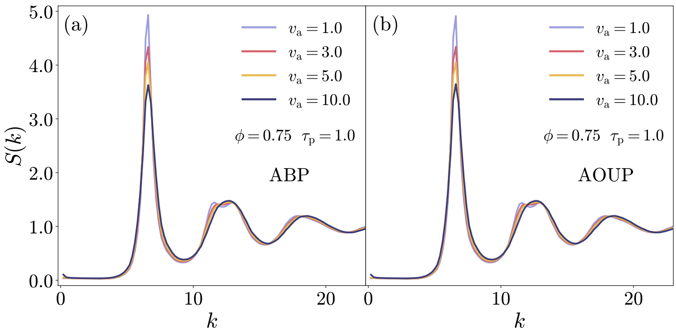

Figure 6.4: The static structure factor $S(k)$ as a function of the wavevector k obtained from both (a) ABP and (b) AOUP simulations. Results correspond to different active speeds.

its equilibrium counterpart. In other words, we assume the same (passive) structure for both models. Although unlikely, structural differences between both models might therefore still exist. To verify that our mapping of the dynamics also yields similar structures, we have retrieved the static structure factor, i.e., $S(k) = \left\langle \sum_{j=1}^{N} e^{-i\mathbf{k}\cdot\mathbf{r}_j} \sum_{l=1}^{N} e^{i\mathbf{k}\cdot\mathbf{r}_l} \right\rangle$, for the same parameters as for the self-intermediate scattering function. The results for different active speeds are plotted in Fig. 6.4. Consistent with the dynamical quantities we see that the static structure factor also remains almost unaltered when we interchange the ABP and AOUP model. Moreover, we see the height of the first peak decreasing upon increasing the active speed of the particles, which is consistent with the faster relaxation dynamics observed for the self-intermediate scattering function.

6.9 Conclusions

In this chapter, we have presented the first derivation of an MCT for thermal AOUPs that explicitly takes into account the active degrees of freedom (self-propulsion forces) via the density modes. Our derivation is based on previous work on ABP-MCT and uses the same assumption of replacing steady-state averages by their equilibrium-averaged or transient counterparts. The central result comprises an equation of motion for the (transient) intermediate scattering function, which can be self-consistently solved using only the equilibrium static structure factor and relevant control parameters (packing fraction, active speed, and persistence time) as input.

Interestingly, after mapping both models on the single-particle (or non-interacting) level via their MSDs, our newly developed AOUP-MCT gives almost identical results as ABP-MCT over a wide range of values for the different control parameters. In other words, the equivalence of both models in the non-interacting regime transfers directly to the collective relaxation in the high-density (glassy) regime. Although this is consistent with our results presented in Chapter 3, we have further confirmed the witnessed equivalence between the different self-propulsion mechanisms by performing simulations of a polydisperse mixture of active quasi-hard disks. In all cases, the differences between the AOUP and ABP simulations are minute. We thus conclude that, at least for the considered model systems, the microscopic details of the self-propulsion do not affect the active glassy behavior. For completeness, we have also derived a mode-coupling theory for three-dimensional (3D) ABPs which explicitly includes the active degrees of freedom. This is detailed in Section 6.C. Preliminary results show that the equivalence is fully retained when comparing both mode-coupling theories in 3D instead of 2D. Our claim therefore seems robust to changes in physical dimension.

As a followup it would be intriguing to see whether the witnessed equivalence between both models in the glassy regime can also be formally established given that the structure of the derived MCT equations is already identical. This could provide crucial theoretical insight into the emergent universality of dense active matter. A possible starting point for it might be to try to convert the Hermite-polynomial basis for the AOUPs into the trigonometric one adopted for the ABPs. Alternatively, one can look into the scaling laws close to the idealized glass transition, which have already been extensively studied for passive MCT [15].

It could also be interesting to test the validity of the observed equivalence for more complex active self-propulsion models or when transitioning from overdamped to underdamped active dynamics (from microswimmers to so-called microflyers [123]). Finally, we mention that the derivation of AOUP-MCT can be easily extended to three dimensions. We therefore hope that the framework of AOUP-MCT will continue to be used for comparison with simulation or experimental results in order to better understand the rich phenomenology of active glassy matter.

Appendix

6.A Mode-coupling theory for active Ornstein-Uhlenbeck particles

As our starting point for the AOUP-MCT derivation, we take the following fluctuating local density to describe the collective motion of 2D AOUPs:

$$\rho(\mathbf{r},\mathbf{f}) = \frac{1}{p(\mathbf{f})}\sum_{i=1}^{N}\delta(\mathbf{r}-\mathbf{r}_i)\delta(\mathbf{f}-\mathbf{f}_i) = \pi^{3/2}\exp\left(\bar{\mathbf{f}}^2\right)\sum_{i=1}^{N}\delta(\mathbf{r}-\mathbf{r}_i)\delta(\bar{\mathbf{f}}-\bar{\mathbf{f}}_i). \tag{6.15}$$

Here, we have introduced a dimensionless self-propulsion force $\bar{\mathbf{f}} \equiv \mathbf{f}/\sqrt{2D_f\tau_p}$ and added a prefactor for normalization. Next, we Fourier-Hermite expand the microscopic density, i.e.

$$\rho(\mathbf{r},\mathbf{f}) = \frac{1}{V}\sum_{\mathbf{k}}\sum_{mn}(-i)^{m+n}\rho_{mn}(\mathbf{k})e^{-i\mathbf{k}\cdot\mathbf{r}}H_m(\bar{f}_x)H_n(\bar{f}_y), \tag{6.16}$$

with the factor $(-i)^{m+n}$ added for technical convenience and the normalized Hermite polynomials being defined as

$$H_n(x) = \frac{1}{\sqrt{2^n n!}}(-1)^n e^{x^2}\frac{d^n}{dx^n}e^{-x^2}. \tag{6.17}$$

Invoking the orthogonality of the Hermite polynomials with respect to the measure $\exp(-\bar{\mathbf{f}}^2)$ we obtain for the density modes

$$\rho_{mn}(\mathbf{k}) = \frac{1}{\sqrt{N}}i^{m+n}\sum_{j=1}^{N}e^{i\mathbf{k}\cdot\mathbf{r}_j}H_m(\bar{f}_{j,x})H_n(\bar{f}_{j,y}). \tag{6.18}$$

The transient (or equilibrium-averaged) time-correlation between such density modes can then be defined via

$$S_{mn;m'n'}(\mathbf{k},t) = \left\langle \rho^*_{mn}(\mathbf{k})e^{\Omega^\dagger t}\rho_{m'n'}(\mathbf{k})\right\rangle, \tag{6.19}$$

where the adjoint (or backward) evolution operator is given by

$$\begin{aligned}\Omega^\dagger &= \Omega^\dagger_{\mathrm{T}} + \Omega^\dagger_{\mathrm{R}}\\ &= \sum_{i=1}^{N}\left(D\nabla_i + \zeta^{-1}(\mathbf{F}_i+\mathbf{f}_i)\right)\cdot\nabla_i + \sum_{i=1}^{N}\left(\left(D_f\frac{\partial}{\partial\mathbf{f}_i} - \tau_p^{-1}\mathbf{f}_i\right)\cdot\frac{\partial}{\partial\mathbf{f}_i}\right).\end{aligned} \tag{6.20}$$

We adopt the convention that the adjoint evolution operator works on everything to its right except for the probability distribution. Note that the lowest order term $S_{00;00}(\mathbf{k},t) \equiv F(k,t)$ corresponds to the intermediate scattering function, which will serve as the main probe to study glassy dynamics of our active system. At time zero, assuming our system to be isotropic, the density correlation functions are easily calculated and yield

$$S_{mn;m'n'}(k) = \langle\rho^*_{mn}(\mathbf{k})\rho_{m'n'}(\mathbf{k})\rangle = \delta_{mm'}\delta_{nn'}\Big[1+\delta_{m0}\delta_{n0}(S(k)-1)\Big], \tag{6.21}$$

where $S(k)$ denotes the equilibrium static structure factor.

To arrive at an equation of motion for the intermediate scattering function we will employ a similar strategy as already introduced for ABPs in Ref. [100]. Starting from the Mori-Zwanzig projector formalism [139, 140], we introduce a projector on density modes (using the shorthand notation $l \equiv \{m, n\}$ which will be done throughout)

$$\mathcal{P} = \sum_{l_1} \sum_{l_2} \big|\rho_{l_1}(\mathbf{k})\big\rangle S^{-1}_{l_1;l_2}(k) \big\langle \rho^*_{l_2}(\mathbf{k})\big| = \sum_{l_1} \big|\rho_{l_1}(\mathbf{k})\big\rangle S^{-1}_{l_1;l_1}(k) \big\langle \rho^*_{l_1}(\mathbf{k})\big|, \tag{6.22}$$

and its orthogonal counterpart $\mathcal{Q} = 1 - \mathcal{P}$. Note that the superscript -1 represents the inverse matrix of the respective quantity, i.e. $X^{-1}_{l;l'} \equiv [\mathbf{X}^{-1}]_{l;l'}$. Following standard procedure in MCT (see Section 2.2) one can then derive that

$$\begin{aligned} &\frac{\partial}{\partial t} S_{l;l'}(\mathbf{k}, t) + \sum_{l_1} \omega_{l;l_1}(\mathbf{k}) S^{-1}_{l_1;l_1}(k) S_{l_1;l'}(\mathbf{k}, t) \\ &- \int_0^t dt' \sum_{l_1} K_{l;l_1}(\mathbf{k}, t - t') S^{-1}_{l_1;l_1}(k) S_{l_1;l'}(\mathbf{k}, t') = 0. \end{aligned} \tag{6.23}$$

In this equation the collective diffusion tensor, which governs the short-time dynamics, is given by

$$\begin{aligned} \omega_{l;l'}(\mathbf{k}) = -\big\langle \rho^*_l(\mathbf{k}) \Omega^\dagger \rho_{l'}(\mathbf{k}) \big\rangle &= \Big[k^2 D \delta_{ll'} + \zeta^{-1} \sqrt{D_f \tau_p} S_{l;l}(k) \; \mathbf{k} \cdot (\boldsymbol{\delta}_{ll'^-} - \boldsymbol{\delta}_{ll'^+}) \Big] \\ &+ \Big[(m + n) \tau_p^{-1} \delta_{ll'} \Big] \equiv \omega^{\mathrm{T}}_{l;l'}(\mathbf{k}) + \omega^{\mathrm{R}}_{l;l'}, \end{aligned} \tag{6.24}$$

where we have introduced the two-vector $([\cdot, \cdot])$ shorthand notation

$$\boldsymbol{\delta}_{ll'^\pm} = \left[\sqrt{m' + \frac{1}{2} \pm \frac{1}{2}} \; \delta_{m,m'\pm 1} \delta_{nn'}, \sqrt{n' + \frac{1}{2} \pm \frac{1}{2}} \delta_{n,n'\pm 1} \delta_{mm'} \right]. \tag{6.25}$$

The memory kernel, which represents all nontrivial dynamics, can be formally written as

$$K_{l;l'}(\mathbf{k}, t) = \Big\langle \rho^*_l(\mathbf{k}) \Omega^\dagger \mathcal{Q} e^{\mathcal{Q}\Omega^\dagger \mathcal{Q} t} \mathcal{Q} \Omega^\dagger \rho_{l'}(\mathbf{k}) \Big\rangle = \Big\langle \rho^*_l(\mathbf{k}) \Omega^\dagger_{\mathrm{T}} \mathcal{Q} e^{\mathcal{Q}\Omega^\dagger \mathcal{Q} t} \mathcal{Q} \Omega^\dagger_{\mathrm{T}} \rho_{l'}(\mathbf{k}) \Big\rangle. \tag{6.26}$$

Here we have used that, since the active degrees of freedom (self-propulsion forces) never slow down, the $\Omega^\dagger_{\mathrm{R}}$-terms do not contribute to the vertices, i.e. $\mathcal{Q}\Omega^\dagger_{\mathrm{R}} \rho_l(\mathbf{k})\big\rangle = \big\langle \rho_l(\mathbf{k}) \Omega^\dagger_{\mathrm{R}} \mathcal{Q} = 0$. Consequently, only the translational degrees of freedom yield slow dynamics and we therefore seek to convert the memory kernel to an irreducible (friction) memory kernel by means of the operators

$$\mathcal{P}' = -\sum_{l_1 l_2} \big|\rho_{l_1}(\mathbf{k})\big\rangle [\omega^{\mathrm{T}}_{l_1;l_2}(k)]^{-1} \big\langle \rho^*_{l_2}(\mathbf{k})\big| \Omega^\dagger_{\mathrm{T}}, \tag{6.27}$$

and $\mathcal{Q}' = 1 - \mathcal{P}'$. Invoking Dyson decomposition, we may write

$$K_{l;l'}(\mathbf{k}, t) = M_{l;l'}(\mathbf{k}, t) - \int_0^t dt' \sum_{l_1 l_2} M_{l;l_1}(\mathbf{k}, t - t') [\omega^{\mathrm{T}}_{l_1;l_2}(\mathbf{k})]^{-1} K_{l_2;l'}(\mathbf{k}, t'), \tag{6.28}$$

with the irreducible memory kernel defined as

$$M_{l;l'}(\mathbf{k},t) = \left\langle \rho_l^*(\mathbf{k})\Omega_{\mathrm{T}}^\dagger \mathcal{Q} e^{\mathcal{Q}\Omega^\dagger \mathcal{Q}' \mathcal{Q} t} \mathcal{Q}\Omega_{\mathrm{T}}^\dagger \rho_{l'}(\mathbf{k}) \right\rangle . \tag{6.29}$$

Now we can combine Eqs. (6.23) and (6.28) to arrive at an equation of motion for the intermediate scattering function, which lends itself to mode-coupling-like approximations:

$$\begin{aligned} &\frac{\partial}{\partial t} S_{l;l'}(\mathbf{k},t) + \sum_{l_1} \omega_{l;l_1}(\mathbf{k}) S^{-1}_{l_1;l_1}(k) S_{l_1;l'}(\mathbf{k},t) + \int_0^t dt' \sum_{l_1 l_2} M_{l;l_1}(\mathbf{k},t-t') \\ &\qquad \times [\omega^{\mathrm{T}}_{l_1;l_2}(\mathbf{k})]^{-1} \left[\frac{\partial}{\partial t'} S_{l_2;l'}(\mathbf{k},t') + \omega^{\mathrm{R}}_{l_2;l_2} S_{l_2;l'}(\mathbf{k},t') \right] = 0, \end{aligned} \tag{6.30}$$

We mention that this equation is identical in structure to the one obtained for ABPs in Ref. [100] and reiterate that, in comparison to the more familiar passive MCT equation, there is an additional hopping term $\omega^{\mathrm{R}}_{l_2;l_2} S_{l_2;l'}(\mathbf{k},t')$ inside the time integral. This term ensures the long-time decay of the active degrees of freedom. At the same time, we also emphasize that the individual terms in the equation are not necessarily the same as the ones presented in Ref. [100] for ABPs, and these terms will therefore harbor the differences between the AOUP and ABP model.

To proceed and find a solution for the active-MCT equation, we project the fluctuating forces $\mathcal{Q}\Omega_{\mathrm{T}}^\dagger \rho_{l'}(\mathbf{k})$ onto density doublets. Specifically, we introduce, assuming Gaussian factorization for higher order static correlations [145] and making use of the fact that $S^{-1}_{l_1;l_2}(q)$ is diagonal, the projection operator

$$\mathcal{P}_2 = \frac{1}{2} \sum_{\mathbf{q}_1 \mathbf{q}_2} \sum_{l_1 l_2} \big| \rho_{l_1}(\mathbf{q}_1) \rho_{l_2}(\mathbf{q}_2) \big\rangle S^{-1}_{l_1;l_1}(q_1) S^{-1}_{l_2;l_2}(q_2) \big\langle \rho^*_{l_1}(\mathbf{q}_1) \rho^*_{l_2}(\mathbf{q}_2) \big|, \tag{6.31}$$

and use it to approximate

$$\begin{aligned} M_{l;l'}(\mathbf{k},t) &\approx \left\langle \rho_l^*(\mathbf{k})\Omega_{\mathrm{T}}^\dagger \mathcal{Q} \mathcal{P}_2 e^{\mathcal{Q}\Omega^\dagger \mathcal{Q}' \mathcal{Q} t} \mathcal{P}_2 \mathcal{Q}\Omega_{\mathrm{T}}^\dagger \rho_{l'}(\mathbf{k}) \right\rangle \\ &= \frac{1}{4} \sum_{\mathbf{q}_1 \dots \mathbf{q}_4} \sum_{l_1 \dots l_4} \left\langle \rho_l^*(\mathbf{k})\Omega_{\mathrm{T}}^\dagger \mathcal{Q} \rho_{l_1}(\mathbf{q}_1) \rho_{l_2}(\mathbf{q}_2) \right\rangle S^{-1}_{l_1;l_1}(q_1) S^{-1}_{l_2;l_2}(q_2) \\ &\quad \times \left\langle \rho^*_{l_1}(\mathbf{q}_1) \rho^*_{l_2}(\mathbf{q}_2) e^{\mathcal{Q}\Omega^\dagger \mathcal{Q}' \mathcal{Q} t} \rho_{l_3}(\mathbf{q}_3) \rho_{l_4}(\mathbf{q}_4) \right\rangle S^{-1}_{l_3;l_3}(q_3) S^{-1}_{l_4;l_4}(q_4) \\ &\quad \times \left\langle \rho^*_{l_3}(\mathbf{q}_3) \rho^*_{l_4}(\mathbf{q}_4) \mathcal{Q}\Omega_{\mathrm{T}}^\dagger \rho_{l'}(\mathbf{k}) \right\rangle . \end{aligned} \tag{6.32}$$

To make this expression tractable we explicitly calculate both vertices. For convenience, we split the translational evolution operator into a passive and active contribution, i.e. $\Omega_{\mathrm{T}}^{\dagger} = \Omega_{\mathrm{eq}}^{\dagger} + \delta\Omega_{\mathrm{T}}^{\dagger}$, with $\delta\Omega_{\mathrm{T}}^{\dagger} = \sum_i^N \zeta^{-1}\mathbf{f}_i \cdot \nabla_i$. Moreover, invoking the following orthogonality relation for Hermite polynomials,

$$\begin{aligned}\pi^{-1/2}\int_{\infty}^{\infty} dx\ H_m(x)H_n(x)H_s(x)e^{-x^2} &= \sqrt{m!\ n!\ s!}\ \times \\ \left[\left(\frac{m+n-s}{2}\right)!\ \left(\frac{s+n-m}{2}\right)!\ \left(\frac{s+m-n}{2}\right)!\right]^{-1}&,\end{aligned} \tag{6.33}$$

when $m+n+s$ is even, $m+n \geq s$, $s+n \geq m$, and $s+m \geq n$, or zero otherwise, and the conventional convolution approximation [146], allows us to define a generalized convolution approximation given by

$$\langle \rho_l^*(\mathbf{k})\rho_{l_1}(\mathbf{q}_1)\rho_{l_2}(\mathbf{q}_2)\rangle \approx \frac{1}{\sqrt{N}}\delta_{\mathbf{k},\mathbf{q}_1+\mathbf{q}_2} b_{m,m_1,m_2} b_{n,n_1,n_2} S_{ll}(q)S_{l_1l_1}(q_1)S_{l_2l_2}(q_2). \tag{6.34}$$

Here, we have introduced the geometric factor

$$\begin{aligned}b_{n,n_1,n_2} &= (-1)^{-(n-n_1-n_2)/2}\sqrt{n_1!\ n_2!\ n!} \\ \left[\left(\frac{n_1+n_2-n}{2}\right)!\ \left(\frac{n+n_2-n_1}{2}\right)!\ \left(\frac{n+n_1-n_2}{2}\right)!\right]^{-1}&,\end{aligned} \tag{6.35}$$

when $n+n_1+n_2$ is even, $n+n_1 \geq n_2$, $n_1+n_2 \geq n$, and $n+n_2 \geq n_1$, or zero otherwise. Using the generalized convolution approximation we have for the passive contribution of the left vertex

$$\begin{aligned}\left\langle \rho_l^*(\mathbf{k})\Omega_{\mathrm{eq}}^{\dagger}\mathcal{Q}\rho_{l_1}(\mathbf{q}_1)\rho_{l_2}(\mathbf{q}_2)\right\rangle S_{l_1;l_1}^{-1}(q_1)S_{l_2;l_2}^{-1}(q_2) &= \frac{\rho D}{\sqrt{N}} \\ \times\ \delta_{\mathbf{k},\mathbf{q}_1+\mathbf{q}_2}\Big(\mathbf{k}\cdot\mathbf{q}_1\ \delta_{l_10}\delta_{ll_2}c(q_1) + \mathbf{k}\cdot\mathbf{q}_2\ \delta_{l_20}\delta_{ll_1}c(q_2)\Big)&,\end{aligned} \tag{6.36}$$

where $c(q) = \rho^{-1}[1 - S^{-1}(k)]$ depicts the direct correlation function. Note that the passive contribution is thus a straightforward generalization of the standard MCT vertex. Furthermore, the passive contribution to the right vertex can be shown to take on an identical form.

For the active contribution to the left vertex, i.e.,

$$\Big\langle \rho_l^*(\mathbf{k})\delta\Omega_{\mathrm{T}}^{\dagger}\mathcal{Q}\rho_{l_1}(\mathbf{q}_1)\rho_{l_2}(\mathbf{q}_2)\Big\rangle S_{l_1;l_1}^{-1}(q_1)S_{l_2;l_2}^{-1}(q_2), \tag{6.37}$$

we recall that $\mathcal{Q} = \mathcal{I} - \mathcal{P}$ and first consider the term

$$-\Big\langle \rho_l^*(\mathbf{k})\delta\Omega_{\mathrm{T}}^{\dagger}\mathcal{P}\rho_{l_1}(\mathbf{q}_1)\rho_{l_2}(\mathbf{q}_2)\Big\rangle S_{l_1;l_1}^{-1}(q_1)S_{l_2;l_2}^{-1}(q_2). \tag{6.38}$$

Using the generalized convolution approximation and Eq. (6.24), this term can be written as

$$-\frac{\zeta^{-1}}{\sqrt{N}}\sqrt{D_f\tau_p}\;\delta_{\mathbf{k},\mathbf{q}_1+\mathbf{q}_2}S_{l;l}(k)\;\mathbf{k}\cdot\left(\mathbf{b}_{l^-l_1l_2}-\mathbf{b}_{l^+l_1l_2}\right), \tag{6.39}$$

where we have introduced

$$\boldsymbol{b}_{ll_1^{\pm}l_2}=\left[\sqrt{m_1+\frac{1}{2}\pm\frac{1}{2}}\;b_{m,m_1\pm1,m_2}b_{n,n_1,n_2},\;\sqrt{n_1+\frac{1}{2}\pm\frac{1}{2}}\;b_{m,m_1,m_2}b_{n,n_1\pm1,n_2}\right]. \tag{6.40}$$

Next, we also require an expression for

$$\left\langle\rho_l^*(\mathbf{k})\delta\Omega_{\mathrm{T}}^{\dagger}\rho_{l_1}(\mathbf{q}_1)\rho_{l_2}(\mathbf{q}_2)\right\rangle S^{-1}_{l_1;l_1}(q_1)S^{-1}_{l_2;l_2}(q_2). \tag{6.41}$$

Exploiting the relation $2xH_n(x)=\sqrt{2(n+1)}H_{n+1}(x)+\sqrt{2n}H_{n-1}(x)$ and using the generalized convolution approximation, the above term can be calculated to give

$$\begin{aligned}-\frac{\zeta^{-1}}{\sqrt{N}}\sqrt{D_f\tau_p}S_{l;l}(k)\delta_{\mathbf{k},\mathbf{q}_1+\mathbf{q}_2}\Big[\mathbf{q}_1\cdot\Big(\mathbf{S}_{ll_1^-l_2}(q_1)-\mathbf{b}_{ll_1^+l_2}\Big)&\\ S^{-1}_{l_1;l_1}(q_1)+\mathbf{q}_2\cdot\Big(\mathbf{S}_{ll_2^-l_1}(q_2)-\mathbf{b}_{ll_2^+l_1}\Big)\,S^{-1}_{l_2;l_2}(q_2)\Big]&,\end{aligned} \tag{6.42}$$

and is written in terms of

$$\begin{aligned}\boldsymbol{S}_{ll_1^{\pm}l_2}(q)=&\left[\sqrt{m_1+\frac{1}{2}\pm\frac{1}{2}}\;b_{m,m_1\pm1,m_2}b_{n,n_1,n_2}S_{m_1\pm1n_1;m_1\pm1n_1}(q),\right.\\&\left.\sqrt{n_1+\frac{1}{2}\pm\frac{1}{2}}b_{n,n_1\pm1,n_2}b_{m,m_1,m_2}S_{m_1n_1\pm1;m_1n_1\pm1}(q)\right].\end{aligned} \tag{6.43}$$

The only term left to calculate is the active contribution to the right vertex. However, this term can be shown to yield a value of zero and thus does not contribute to the vertices. Combining all results we then have for the memory kernel

$$\begin{aligned}M_{l;l'}(\mathbf{k},t)\approx\;&\frac{\rho^2}{4N}\sum_{\mathbf{q}\mathbf{q}'}\sum_{l_1\ldots l_4}V_{ll_1l_2}(\mathbf{k},\mathbf{q},\mathbf{k}-\mathbf{q})\\&\times\left\langle\rho^*_{l_1}(\mathbf{q})\rho^*_{l_2}(\mathbf{k}-\mathbf{q})e^{\mathcal{Q}\Omega^{\dagger}\mathcal{Q}'\mathcal{Q}t}\rho_{l_3}(\mathbf{q}')\rho_{l_4}(\mathbf{k}-\mathbf{q}')\right\rangle V^{\mathrm{eq}}_{l'l_3l_4}(\mathbf{k},\mathbf{q}',\mathbf{k}-\mathbf{q}').\end{aligned} \tag{6.44}$$

with the vertices given by

$$V^{\mathrm{eq}}_{ll_1l_2}(\mathbf{k},\mathbf{q},\mathbf{k}-\mathbf{q})=\;D\left[\mathbf{k}\cdot\mathbf{q}\;\delta_{l_10}\delta_{ll_2}\;c(q)\;+\mathbf{k}\cdot(\mathbf{k}-\mathbf{q})\;\delta_{l_20}\delta_{ll_1}\;c(|\mathbf{k}-\mathbf{q}|)\right], \tag{6.45}$$

and

$$\begin{aligned} V_{ll_1l_2}(\mathbf{k},\mathbf{q},\mathbf{k}-\mathbf{q}) &= V^{\mathrm{eq}}_{ll_1l_2}(\mathbf{k},\mathbf{q},\mathbf{k}-\mathbf{q}) - \frac{\zeta^{-1}\sqrt{D_f\tau_p}}{\rho} S_{l;l}(k) \\ &\Big[\mathbf{k}\cdot\left(\mathbf{b}_{l^-l_1l_2} - \mathbf{b}_{l^+l_1l_2}\right) + \mathbf{q}\cdot\left(\mathbf{S}_{ll_1^-l_2}(q) - \mathbf{b}_{ll_1^+l_2}\right) S^{-1}_{l_1;l_1}(q) \\ &+ (\mathbf{k}-\mathbf{q})\cdot\left(\mathbf{S}_{ll_2^-l_1}(|\mathbf{k}-\mathbf{q}|) - \mathbf{b}_{ll_2^+l_1}\right) S^{-1}_{l_2;l_2}(|\mathbf{k}-\mathbf{q}|)\Big]. \end{aligned} \tag{6.46}$$

To further simplify the expression of the memory kernel, we employ the MCT-approximation and replace the four-point correlation function with projected dynamics by a product of two-point density correlation functions with full dynamics. This yields

$$\begin{aligned} \left\langle \rho^*_{l_1}(\mathbf{q})\rho^*_{l_2}(\mathbf{k}-\mathbf{q}) e^{\mathcal{Q}\Omega^\dagger\mathcal{Q}'\mathcal{Q}t}\rho_{l_3}(\mathbf{q}')\rho_{l_4}(\mathbf{k}-\mathbf{q}')\right\rangle &\approx S_{l_1;l_3}(\mathbf{q},t) \\ S_{l_2;l_4}(\mathbf{k}-\mathbf{q},t)\ \delta_{\mathbf{q},\mathbf{q}'} + S_{l_1;l_4}(\mathbf{q},t)S_{l_2;l_3}(\mathbf{k}-\mathbf{q},t)\ \delta_{\mathbf{k}-\mathbf{q},\mathbf{q}'} & \end{aligned} \tag{6.47}$$

After taking the thermodynamic limit, one finally arrives at

$$\begin{aligned} M_{l;l'}(\mathbf{k},t) \approx \frac{\rho}{2}\int \frac{d\mathbf{q}}{(2\pi)^2} \sum_{l_1l_2}\sum_{l_3l_4} V_{ll_1l_2}(\mathbf{k},\mathbf{q},\mathbf{k}-\mathbf{q}) \\ \times S_{l_1;l_3}(\mathbf{q},t)S_{l_2;l_4}(\mathbf{k}-\mathbf{q},t)V^{\mathrm{eq}}_{l'l_3l_4}(\mathbf{k},\mathbf{q},\mathbf{k}-\mathbf{q}), \end{aligned} \tag{6.48}$$

which, using only the equilibrium static structure factor $S(k)$ as initial boundary condition, allows us to self-consistently find a solution for $S_{l;l'}(\mathbf{k},t)$ and in particular for the intermediate scattering function $S_{00;00}(\mathbf{k},t) \equiv F(k,t)$. We conclude by mentioning that the above derivation can also be straightforwardly extended to three dimensions. This only requires the introduction of an additional Hermite polynomial (for the z-component of the active force) in the density mode after which the same steps can be carried out.

6.B Rotational symmetry

Due to the inclusion of the active degrees of freedom, dynamic correlation functions depend explicitly on the direction of the wavevector $\mathbf{k}$. However, we can bypass this problem by invoking the rotational symmetry of our system to align every wavevector entering correlation functions along a chosen direction. Suppose we rotate our coordinate axes clockwise over an angle θ (or all particles counter clockwise) such that

$$\mathbf{r}_j \to \mathbf{r}'_j = \mathbf{D}(\theta)\cdot\mathbf{r}_j, \quad \mathbf{f}_j \to \mathbf{f}'_j = \mathbf{D}(\theta)\cdot\mathbf{f}_j,$$

with the rotation matrix given by

$$\mathbf{D}(\theta) = \begin{pmatrix} \cos(\theta) & -\sin(\theta) \\ \sin(\theta) & \cos(\theta) \end{pmatrix}.$$

As a result the AOUP density mode transforms like

$$\rho_{mn}(\mathbf{k}) \to \frac{1}{\sqrt{N}} i^{m+n} \sum_{j=1}^{N} e^{i\mathbf{k}'\cdot\mathbf{r}_j} H_m(\bar{f}'_{j,x}) H_n(\bar{f}'_{j,y}),$$

where $\mathbf{k}' = \mathbf{D}^{\mathrm{T}}(\theta)\cdot\mathbf{k}$ depicts the rotated wavevector. Realising that $\Omega^\dagger$, $P_{\mathrm{eq}}(\Gamma_{\mathrm{T}})$, and $P(\Gamma_{\mathrm{R}})$ are invariant under such a rotation, and rewriting $H_l(\bar{f}'_{j,x})H_m(\bar{f}'_{j,y})$ back in terms of $\bar{\mathbf{f}}_j$ allows us to transform correlation functions with wavevector $\mathbf{k}$ to ones with wavevector $\mathbf{k}'$. Note that $\mathbf{k}$ is thus rotated clockwise. This allows us to restrict our discussion to wavevectors aligned along a specific direction, which we have chosen to be the x-axis.

6.C Mode-coupling theory for 3D active Brownian particles

Our derivation[3] for the ABP-MCT starts by defining an appropriate fluctuating local density to describe the collective motion of 3D ABPs. In this case we have

$$\rho(\mathbf{r},\theta,\phi) = \frac{1}{4\pi p(\theta,\phi)} \sum_{j=1}^{N} \delta(\mathbf{r}-\mathbf{r}_j)\delta(\theta-\theta_j)\delta(\phi-\phi_j), \tag{6.49}$$

where the angles $\theta \in [0,\pi]$ and $\phi \in [0,2\pi]$ quantify the orientation of the active velocity and $p(\theta,\phi) = \sin(\theta)/4\pi$ is the distribution of active velocity orientations (corresponding to random motion on the unit sphere). Expanding the density then yields,

$$\rho(\mathbf{r},\theta,\phi) = \frac{1}{V}\frac{1}{\sqrt{4\pi}} \sum_{\mathbf{k}} \sum_{l=0}^{\infty} \sum_{m=-l}^{l} (-i)^l \rho_{lm}(\mathbf{k}) e^{-i\mathbf{k}\cdot\mathbf{r}} Y_l^m(\theta,\phi)^*, \tag{6.50}$$

with $Y_l^m(\theta,\phi)$ spherical harmonics and the factor $(-i)^l$ added for technical convenience. Exploiting the orthogonality of spherical harmonics with respect to $\sin(\theta)$, we find for the density modes

$$\rho_{lm}(\mathbf{k}) = \frac{1}{\sqrt{N}} \sqrt{4\pi} i^l \sum_{j=1}^{N} e^{i\mathbf{k}\cdot\mathbf{r}_j} Y_l^m(\theta_j,\phi_j). \tag{6.51}$$

The transient (or equilibrium-averaged) time-correlation between such density modes can then be defined via

$$S_{lm;l'm'}(\mathbf{k},t) = \left\langle \rho^*_{lm}(\mathbf{k}) e^{\Omega^\dagger t} \rho_{l'm'}(\mathbf{k}) \right\rangle. \tag{6.52}$$

---

[3] This derivation has been performed in close collaboration with X.M. de Wit.

Here, we reiterate that averaging is done according to Eq. (6.8) with the orientational distribution function in this case given by $P(\Gamma_{\mathrm{R}}) = \prod_{j=1}^{N} p(\theta_j, \phi_j)$. The adjoint (or backward) evolution operator is given by [197]

$$\begin{aligned}\Omega^\dagger = \Omega_{\mathrm{T}}^\dagger + \Omega_{\mathrm{R}}^\dagger = &\sum_{j=1}^{N} \left(D\nabla_j + \zeta^{-1}\mathbf{F}_j\right) \cdot \nabla_j + v_0 \mathbf{e}_j \cdot \nabla_j \\ &+ \sum_{j=1}^{N} D_{\mathrm{r}} \left(\frac{1}{\tan\theta_j} \frac{\partial}{\partial\theta_j} + \frac{\partial^2}{\partial\theta_j^2} + \frac{1}{\sin^2\theta_j} \frac{\partial^2}{\partial\phi_j^2} \right),\end{aligned} \tag{6.53}$$

and works on everything to its right except for the probability distribution. They are again defined such that lowest order term $S_{00;00}(\mathbf{k}, t) \equiv F(k, t)$ corresponds to the intermediate scattering function, which will serve as the main probe to study glassy dynamics of our active system. At time zero, assuming our system to be isotropic, the density correlation functions are easily calculated and yield

$$S_{lm;l'm'}(k) = \langle \rho_{lm}^*(\mathbf{k}) \rho_{l'm'}(\mathbf{k}) \rangle = \delta_{ll'}\delta_{mm'} \Big[1 + \delta_{l0}\delta_{m0}(S(k) - 1) \Big], \tag{6.54}$$

where $S(k)$ denotes the equilibrium static structure factor.

We can then employ the Mori-Zwanzig formalism (see Section 2.2) with the projection operator (adopting the shorthand notation $n \equiv \{l, m\}$),

$$\mathcal{P} = \sum_{n_1} \sum_{n_2} \big|\rho_{n_1}(\mathbf{k})\big\rangle S_{n_1;n_2}^{-1}(k) \big\langle \rho_{n_2}^*(\mathbf{k})\big| = \sum_{n_1} \big|\rho_{n_1}(\mathbf{k})\big\rangle S_{n_1;n_1}^{-1}(k) \big\langle \rho_{n_1}^*(\mathbf{k})\big|, \tag{6.55}$$

to arrive at

$$\begin{aligned}&\frac{\partial}{\partial t} S_{n;n'}(\mathbf{k}, t) + \sum_{n_1} \omega_{n;n_1}(\mathbf{k}) S_{n_1;n_1}^{-1}(k) S_{n_1;n'}(\mathbf{k}, t) \\ &- \int_0^t dt' \sum_{n_1} K_{n;n_1}(\mathbf{k}, t - t') S_{n_1;n_1}^{-1}(k) S_{n_1;n'}(\mathbf{k}, t') = 0.\end{aligned} \tag{6.56}$$

In this equation the collective diffusion tensor, which governs the short-time dynamics, is now given by

$$\begin{aligned}\omega_{n;n'}(\mathbf{k}) = -\left\langle \rho_n^*(\mathbf{k}) \Omega^\dagger \rho_{n'}(\mathbf{k}) \right\rangle = &\Big[k^2 D \delta_{nn'} - v_0 S_{n;n}(k) i^{(l'-l)+1} \delta_{|l-l'|,1} \sqrt{\frac{2l'+1}{2l+1}} C_{10l'0}^{l0} \\ &\times \left(C_{11l'm'}^{lm} \frac{-q_x + iq_y}{\sqrt{2}} \delta_{m,m'+1} + C_{1-1l'm'}^{lm} \frac{q_x + iq_y}{\sqrt{2}} \delta_{m,m'-1} + q_z C_{10l'm'}^{lm} \delta_{mm'} \right) \Big] \\ &+ \Big[l(l+1) D_{\mathrm{r}} \delta_{nn'} \Big] \equiv \omega_{n;n'}^{\mathrm{T}}(\mathbf{k}) + \omega_{n;n'}^{\mathrm{R}},\end{aligned} \tag{6.57}$$

where we have used that

$$\sin\theta\cos\phi Y_l^m = \sqrt{\frac{2\pi}{3}}(Y_1^1 - Y_1^{-1})Y_l^m, \tag{6.58}$$

$$\sin\theta\sin\phi Y_l^m = i\sqrt{\frac{2\pi}{3}}(Y_1^1 + Y_1^{-1})Y_l^m, \tag{6.59}$$

$$\cos\theta Y_l^m = \sqrt{\frac{4\pi}{3}}Y_1^0 Y_l^m, \tag{6.60}$$

and introduced the Clebsch-Gordan (CG) coefficients $C^{LM}_{l_1m_1l_2m_2}$ which arise when multiplying two spherical harmonics, i.e.,

$$Y_{l_1}^{m_1}Y_{l_2}^{m_2} = \sum_{LM}\sqrt{\frac{(2l_1+1)(2l_2+1)}{4\pi(2L+1)}}C^{L0}_{l_10l_20}C^{LM}_{l_1m_1l_2m_2}Y_L^M, \tag{6.61}$$

where in our case we only have $l_1 = 1$ and $m_1 = -1, 0, 1$ which constrains the summation according to $|l_1 - l_2| \leq L \leq l_1 + l_1$, $m_1 + m_2 = M$, and $|M| \leq L$. Moreover, the memory kernel is formally written as

$$K_{n;n'}(\mathbf{k},t) = \left\langle \rho_n^*(\mathbf{k})\Omega^\dagger\mathcal{Q}e^{\mathcal{Q}\Omega^\dagger\mathcal{Q}t}\mathcal{Q}\Omega^\dagger\rho_{n'}(\mathbf{k})\right\rangle = \left\langle \rho_n^*(\mathbf{k})\Omega_{\mathrm{T}}^\dagger\mathcal{Q}e^{\mathcal{Q}\Omega^\dagger\mathcal{Q}t}\mathcal{Q}\Omega_{\mathrm{T}}^\dagger\rho_{n'}(\mathbf{k})\right\rangle. \tag{6.62}$$

where we have once more exploited the fact that the rotational degrees of freedom never slow down. Using an irreducible projection operator of the form Eq. (6.27) we can arrive in analogous fashion as for the AOUPs (see Section 6.A) at the following, customary, equation of motion for the intermediate scattering function

$$\begin{aligned}\frac{\partial}{\partial t}S_{n;n'}(\mathbf{k},t) + \sum_{n_1}\omega_{n;n_1}(\mathbf{k})S^{-1}_{n_1;n_1}(k)S_{n_1;n'}(\mathbf{k},t) + \int_0^t dt' \sum_{n_1n_2} M_{n;n_1}(\mathbf{k},t-t') \\ \times [\omega^{\mathrm{T}}_{n_1;n_2}(\mathbf{k})]^{-1}\left[\frac{\partial}{\partial t'}S_{n_2;n'}(\mathbf{k},t') + \omega^{\mathrm{R}}_{n_2;n_2}S_{n_2;n'}(\mathbf{k},t')\right] = 0.\end{aligned} \tag{6.63}$$

We then start the mode-coupling approximations by projecting the irreducible memory kernel on density doublets [see Eqs. (6.31) and (6.32)] which yields,

$$\begin{aligned}M_{n;n'}(\mathbf{k},t) \approx \frac{1}{4}\sum_{\mathbf{q}_1\ldots\mathbf{q}_4}\sum_{n_1\ldots n_4}\left\langle\rho_n^*(\mathbf{k})\Omega_{\mathrm{T}}^\dagger\mathcal{Q}\rho_{n_1}(\mathbf{q}_1)\rho_{n_2}(\mathbf{q}_2)\right\rangle S^{-1}_{n_1;n_1}(q_1)S^{-1}_{n_2;n_2}(q_2) \\ \times\left\langle\rho_{n_1}^*(\mathbf{q}_1)\rho_{n_2}^*(\mathbf{q}_2)e^{\mathcal{Q}\Omega^\dagger\mathcal{Q}'\mathcal{Q}t}\rho_{n_3}(\mathbf{q}_3)\rho_{n_4}(\mathbf{q}_4)\right\rangle S^{-1}_{n_3;n_3}(q_3)S^{-1}_{n_4;n_4}(q_4) \\ \times\left\langle\rho_{n_3}^*(\mathbf{q}_3)\rho_{n_4}^*(\mathbf{q}_4)\mathcal{Q}\Omega_{\mathrm{T}}^\dagger\rho_{n'}(\mathbf{k})\right\rangle.\end{aligned} \tag{6.64}$$

To further simply this expression we require explicit expressions for the vertices where we will treat the passive and the active contributions separately, that is, we split $\Omega_{\mathrm{T}}^{\dagger} = \Omega_{\mathrm{eq}}^{\dagger} + \delta\Omega_{\mathrm{T}}^{\dagger}$, with $\delta\Omega_{\mathrm{T}}^{\dagger} = \sum_i^N v_0 \mathbf{e}_i \cdot \nabla_i$. Let us now first focus on the passive contributions. For this we introduce a generalized convolution approximation given by [198]

$$\langle \rho_n^*(\mathbf{k}) \rho_{n_1}(\mathbf{q}_1) \rho_{n_2}(\mathbf{q}_2) \rangle \approx \frac{1}{\sqrt{N}} \delta_{\mathbf{k},\mathbf{q}_1+\mathbf{q}_2} \delta_{m,m_1+m_2} \tilde{C}_{l_1 m_1 l_2 m_2}^{lm} S_{n;n}(k) S_{n_1;n_1}(q_1) S_{n_2;n_2}(q_2). \tag{6.65}$$

Here, we have defined

$$\tilde{C}_{l_1 m_1 l_2 m_2}^{lm} \equiv i^{l_1+l_2-l} \sqrt{\frac{(2l_1+1)(2l_2+1)}{2l+1}} C_{l_1 0 l_2 0}^{l0} C_{l_1 m_1 l_2 m_2}^{lm}, \tag{6.66}$$

which is invariant under the exchange $(l_1, m_1 \leftrightarrow l_2, m_2)$ due to symmetry properties of the CG-coefficients. Using the generalized convolution approximation, the identity $Y_l^{m*} = (-1)^m Y_l^{-m}$, the symmetry rule $C_{l_1 m_1 l_2 m_2}^{lm} = (-1)^{l_2+m_2} \sqrt{\frac{2l+1}{2l_1+1}} C_{l_1 -m_1 l_2 m_2}^{l-m}$, and the expansion Eq. (6.61) one can show that the equilibrium part of the left vertex becomes

$$\begin{aligned} \left\langle \rho_n^*(\mathbf{k}) \Omega_{\mathrm{eq}}^{\dagger} \mathcal{Q} \rho_{n_1}(\mathbf{q}_1) \rho_{n_2}(\mathbf{q}_2) \right\rangle S_{n_1;n_1}^{-1}(q_1) S_{n_2;n_2}^{-1}(q_2) &= \frac{\rho D}{\sqrt{N}} \\ \times \delta_{\mathbf{k},\mathbf{q}_1+\mathbf{q}_2} \Bigg(\mathbf{k} \cdot \mathbf{q}_1 \ \delta_{n_1 0} \delta_{n n_2} c(q_1) + \mathbf{k} \cdot \mathbf{q}_2 \ \delta_{n_2 0} \delta_{n n_1} c(q_2) \Bigg)&, \end{aligned} \tag{6.67}$$

where $c(q) = \rho^{-1}[1 - S^{-1}(k)]$ depicts the direct correlation function. We also mention that the equilibrium part of the right vertex can be shown to take on an identical form.

Continuing with the active contribution of the left vertex we first consider the term,

$$- \left\langle \rho_n^*(\mathbf{k}) \delta\Omega_{\mathrm{T}}^{\dagger} \mathcal{P} \rho_{n_1}(\mathbf{q}_1) \rho_{n_2}(\mathbf{q}_2) \right\rangle S_{n_1;n_1}^{-1}(q_1) S_{n_2;n_2}^{-1}(q_2). \tag{6.68}$$

Using the generalized convolution approximation and Eq. (6.57), this term can be written as

$$-\frac{v_0}{\sqrt{N}} S_{n;n}(k) \delta_{\mathbf{k},\mathbf{q}_1+\mathbf{q}_2} \mathbf{k} \cdot \mathbf{T}'_{lm} \cdot \tilde{\mathbf{C}}_{l_1 m_1 l_2 m_2}^{lm}, \tag{6.69}$$

where we have defined

$$\begin{aligned} \mathbf{T}'_{lm} = &\begin{pmatrix} -\sqrt{\frac{1}{2}} C_{11l+1m-1}^{lm} & \sqrt{\frac{1}{2}} C_{1-1l+1m+1}^{lm} & 0 & -\sqrt{\frac{1}{2}} C_{11l-1m-1}^{lm} & \sqrt{\frac{1}{2}} C_{1-1l-1m+1}^{lm} & 0 \\ -i\sqrt{\frac{1}{2}} C_{11l+1m-1}^{lm} & i\sqrt{\frac{1}{2}} C_{1-1l+1m+1}^{lm} & 0 & -i\sqrt{\frac{1}{2}} C_{11l-1m-1}^{lm} & i\sqrt{\frac{1}{2}} C_{1-1l-1m+1}^{lm} & 0 \\ 0 & 0 & C_{10l+1m}^{lm} & 0 & 0 & C_{10l-1m}^{lm} \end{pmatrix} \\ &\cdot \begin{pmatrix} -\mathbf{I}\sqrt{\frac{2l+3}{2l+1}} C_{1,0,l+1,0}^{l,0} & \mathbf{0} \\ \mathbf{0} & \mathbf{I}\sqrt{\frac{2l-1}{2l+1}} C_{1,0,l-1,0}^{l,0} \end{pmatrix} \end{aligned} \tag{6.70}$$

and

$$\tilde{\mathbf{C}}^{lm}_{l_1m_1l_2m_2} = \left[\tilde{C}^{l+1m-1}_{l_1m_1l_2m_2},\ \tilde{C}^{l+1m+1}_{l_1m_1l_2m_2},\ \tilde{C}^{l+1m}_{l_1m_1l_2m_2},\ \tilde{C}^{l-1m-1}_{l_1m_1l_2m_2},\ \tilde{C}^{l-1m+1}_{l_1m_1l_2m_2},\ \tilde{C}^{l-1m}_{l_1m_1l_2m_2}\right]^T, \tag{6.71}$$

with $\mathbf{I}$ a 3×3 identity matrix and the superscript T denoting a transpose.

Next, we have the term,

$$\left\langle \rho^*_n(\mathbf{k})\delta\Omega^\dagger_{\mathrm{T}}\rho_{n_1}(\mathbf{q}_1)\rho_{n_2}(\mathbf{q}_2)\right\rangle S^{-1}_{n_1;n_1}(q_1)S^{-1}_{n_2;n_2}(q_2). \tag{6.72}$$

Employing relations Eqs. (6.58) to (6.61) in conjunction with the generalized convolution approximation allows us to rewrite the above expression after some tedious but straightforward algebra as,

$$\frac{v_0}{\sqrt{N}} S_{n;n}(k)\delta_{\mathbf{k},\mathbf{q}_1+\mathbf{q}_2}\left[\mathbf{q}_1 \cdot \mathbf{T}_{l_1m_1} \cdot \mathbf{S}^{lm}_{l_1m_1l_2m_2}(q_1) + \mathbf{q}_2 \cdot \mathbf{T}_{l_2m_2} \cdot \mathbf{S}^{lm}_{l_2m_2l_1m_1}(q_2)\right]. \tag{6.73}$$

Here, we have introduced

$$\begin{aligned}\mathbf{T}_{lm} = &\begin{pmatrix} -\sqrt{\frac{1}{2}}C^{l-1m+1}_{11lm} & \sqrt{\frac{1}{2}}C^{l-1m-1}_{1-1lm} & 0 & -\sqrt{\frac{1}{2}}C^{l+1m+1}_{11lm} & \sqrt{\frac{1}{2}}C^{l+1m-1}_{1-1lm} & 0 \\ i\sqrt{\frac{1}{2}}C^{l-1m+1}_{11lm} & i\sqrt{\frac{1}{2}}C^{l-1m-1}_{1-1lm} & 0 & i\sqrt{\frac{1}{2}}C^{l+1m+1}_{11lm} & i\sqrt{\frac{1}{2}}C^{l+1m-1}_{1-1lm} & 0 \\ 0 & 0 & C^{l-1m}_{10lm} & 0 & 0 & C^{l+1m}_{10lm} \end{pmatrix} \\ &\cdot \begin{pmatrix} -\mathbf{I}\sqrt{\frac{2l+1}{2l-1}}C^{l-1,0}_{1,0,l,0} & \mathbf{0} \\ \mathbf{0} & \mathbf{I}\sqrt{\frac{2l+1}{2l+3}}C^{l+1,0}_{1,0,l,0} \end{pmatrix}\end{aligned} \tag{6.74}$$

and

$$\begin{aligned}\mathbf{S}^{lm}_{l_1m_1l_2m_2}(q_1) = \Bigg(&\left[S^{-1}_{l_1m_1;l_1m_1}(q_1)\right] \cdot \Big[\tilde{C}^{lm}_{l_1-1m_1+1l_2m_2}S_{l_1-1m_1+1;l_1-1m_1+1}(q_1), \\ &\tilde{C}^{lm}_{l_1-1m_1-1l_2m_2}S_{l_1-1m_1-1;l_1-1m_1-1}(q_1),\ \tilde{C}^{lm}_{l_1-1m_1l_2m_2}S_{l_1-1m_1;l_1-1m_1}(q_1), \\ &\tilde{C}^{lm}_{l_1+1m_1+1l_2m_2}S_{l_1+1m_1+1;l_1+1m_1+1}(q_1),\ \tilde{C}^{lm}_{l_1+1m_1-1l_2m_2}S_{l_1+1m_1-1;l_1+1m_1-1}(q_1), \\ &\tilde{C}^{lm}_{l_1+1m_1l_2m_2}S_{l_1+1m_1;l_1+1m_1}(q_1)\Big]\Bigg)^T,\end{aligned} \tag{6.75}$$

The final term left to calculate is the active contribution to the right vertex, though it turns out that this equals zero (which can be immediately seen from the fact that $\delta\Omega^\dagger_T\rho_{n'}(\mathbf{k})$ lies in the subspace spanned by single density modes [100] and thus $\mathcal{Q}\delta\Omega^\dagger_T\rho_{n'}(\mathbf{k})\rangle = 0$). Overall, we then have for the memory kernel

$$\begin{aligned}M_{n;n'}(\mathbf{k},t) \approx\ & \frac{\rho^2}{4N}\sum_{\mathbf{q}\mathbf{q}'}\sum_{n_1\ldots n_4} V_{nn_1n_2}(\mathbf{k},\mathbf{q},\mathbf{k}-\mathbf{q}) \\ & \times \left\langle \rho^*_{n_1}(\mathbf{q})\rho^*_{n_2}(\mathbf{k}-\mathbf{q})e^{\mathcal{Q}\Omega^\dagger\mathcal{Q}'\mathcal{Q}t}\rho_{n_3}(\mathbf{q}')\rho_{n_4}(\mathbf{k}-\mathbf{q}')\right\rangle V^{\mathrm{eq}}_{n'n_3n_4}(\mathbf{k},\mathbf{q}',\mathbf{k}-\mathbf{q}').\end{aligned} \tag{6.76}$$

with the vertices given by

$$V^{\mathrm{eq}}_{nn_1n_2}(\mathbf{k},\mathbf{q},\mathbf{k}-\mathbf{q}) = \; D\left[\mathbf{k}\cdot\mathbf{q}\;\delta_{n_10}\delta_{nn_2}\;c(q)\;+\mathbf{k}\cdot(\mathbf{k}-\mathbf{q})\;\delta_{n_20}\delta_{nn_1}\;c(|\mathbf{k}-\mathbf{q}|)\right], \tag{6.77}$$

and

$$\begin{aligned} V_{nn_1n_2}(\mathbf{k},\mathbf{q},\mathbf{k}-\mathbf{q}) = V^{\mathrm{eq}}_{nn_1n_2}(\mathbf{k},\mathbf{q},\mathbf{k}-\mathbf{q}) - \frac{v_0}{\rho}S_{l;l}(k)\Big[\mathbf{k}\cdot\mathbf{T}'_{lm}\cdot\tilde{\mathbf{C}}^{lm}_{l_1m_1l_2m_2} \\ -\mathbf{q}\cdot\mathbf{T}_{l_1m_1}\cdot\mathbf{S}^{lm}_{l_1m_1l_2m_2}(q) - (\mathbf{k}-\mathbf{q})\cdot\mathbf{T}_{l_2m_2}\cdot\mathbf{S}^{lm}_{l_2m_2l_1m_1}(|\mathbf{k}-\mathbf{q}|). \end{aligned} \tag{6.78}$$

Finally, we invoke the standard mode-coupling approximation and replace the four-point correlation with projected dynamics by the product of two-point correlations with full dynamics so that after taking the thermodynamic limit we have

$$\begin{aligned} M_{n;n'}(\mathbf{k},t) \approx \frac{\rho}{2}\int\frac{d\mathbf{q}}{(2\pi)^3}\sum_{n_1n_2}\sum_{n_3n_4}V_{nn_1n_2}(\mathbf{k},\mathbf{q},\mathbf{k}-\mathbf{q}) \\ \times S_{n_1;n_3}(\mathbf{q},t)S_{n_2;n_4}(\mathbf{k}-\mathbf{q},t)V^{\mathrm{eq}}_{n'n_3n_4}(\mathbf{k},\mathbf{q},\mathbf{k}-\mathbf{q}). \end{aligned} \tag{6.79}$$

Using the equilibrium static structure factor $S(k)$ as initial boundary condition and the approximated memory kernel, we can now self-consistently find a solution for $S_{n;n'}(\mathbf{k},t)$ and in particular for the intermediate scattering function $S_{00;00}(\mathbf{k},t) \equiv F(k,t)$.

Chapter 7

Nonequilibrium correlation functions in thermal and athermal dense active fluids

Abstract. One of the key hallmarks of dense active matter in the liquid, supercooled, and solid phases is so-called equal-time velocity correlations. Crucially, these correlations can emerge spontaneously, i.e., they require no explicit alignment interactions, and therefore represent a generic feature of dense active matter. This means that for a meaningful comparison or possible mapping between active and passive liquids one not only needs to understand their structural properties, but also the impact of these velocity correlations. This has already prompted several simulation and theoretical studies, though they are mostly focused on athermal systems and thus overlook the effect of translational diffusion. In this chapter, we present a fully microscopic method to calculate nonequilibrium correlations in systems of thermal active Brownian particles (ABPs). We use the integration through transients (ITT) formalism together with active mode-coupling theory (MCT) and analytically calculate qualitatively consistent static structure factors and active velocity correlations. We complement our theoretical results with simulations of both thermal and athermal ABPs which exemplify the disruptive role that thermal noise has on velocity correlations.

The contents of this chapter are based on the following publication:
V.E. Debets*, L. Sarfati*, T. Voigtmann, and L.M.C. Janssen, *Nonequilibrium correlation functions in thermal and athermal dense active fluids* (in preparation)

7.1 Introduction

One of the most fundamental nonequilibrium characteristics of dense active matter is so-called equal-time velocity correlations [193]. These correlations quantify local cooperative (or aligned) particle motion and were first extracted in confluent cell monolayers [2, 93, 199]. Since then they have also been extensively studied in simulations of self-propelled particles where they appear in, e.g., MIPS [132], dense active (glassy) fluids [91, 112, 113, 119, 200, 201], model cell layers [202], and chiral active matter [121], while they also naturally surface in mode-coupling theories (MCTs) of dense active fluids [101, 103] (see also Chapter 5). Importantly, these correlations have mostly been shown to emerge spontaneously, that is, they in principle do not necessitate any explicit alignment interactions, and thus represent a robust feature of any dense active matter system.

This implies that for a meaningful comparison and perhaps a mapping between a dense active and passive fluid, one not only needs to understand the influence of activity on structural and dynamic correlations, but more crucially also understand the role of (equal-time) velocity correlations as they are strictly absent in equilibrium. To this end, several theoretical approaches have already been brought forward, though they primarily look at large length scales (or equivalently small wavenumbers) [132, 193, 202]. Moreover, to our knowledge most studies on velocity correlations (with Ref. [201] a notable exception) have mainly focused on athermal systems, that is, systems without translational noise, and thus do not consider the disruptive effect the latter can have on velocity correlations.

In this chapter, to add to our fundamental understanding of dense active matter, we present an entirely microscopic approach to analytically calculate nonequilibrium (equal-time) correlations for interacting thermal active Brownian particles (ABPs). Our method uses the integration through transients (ITT) formalism [194] in conjunction with active MCT [100] and is applied on the static structure factor and the so-called longitudinal velocity correlation (as they hold particular relevance for active MCTs [101, 103]). More specifically, we look at the individual correlations that comprise the total longitudinal velocity correlation, which allows us to better pinpoint its exact origins. To complement the theoretical results and rationalize the role of thermal noise, we also perform simulations of both thermal and athermal ABPs. We demonstrate that our theory can qualitatively describe the nonequilibrium structure factor and active-active velocity correlations, while our simulations clearly illustrate the dominant effect thermal noise has on velocity correlations (especially ones involving interaction forces).

7.2 Integration through transients

Given its suitability for the ITT formalism and prevalence in active matter, we take as our model dense active liquid a collection of N interacting two-dimensional (2D) ABPs (disks) at a number density $\rho = N/V$ and temperature T. The position $\mathbf{r}_i$ of each particle i evolves in time according to [78, 100, 203]

$$\frac{d\mathbf{r}_i}{dt} = \zeta^{-1}(\mathbf{F}_i + \mathbf{f}_i) + \boldsymbol{\xi}_i. \tag{7.1}$$

where ζ is the friction coefficient, $\boldsymbol{F}_i$ is the interaction force, and $\boldsymbol{\xi}_i$ represents a Gaussian thermal noise with zero mean and variance $\left\langle \boldsymbol{\xi}_i(t)\boldsymbol{\xi}_j(t') \right\rangle_{\text{noise}} = 2D_{\text{t}}\mathbf{I}\delta_{ij}\delta(t-t')$, with $D_{\text{t}} = k_B T\zeta^{-1}$ the diffusion coefficient and $\mathbf{I}$ the unit matrix. The self-propulsion speed v_0 is assumed constant so that the active force equals $\mathbf{f}_i = \zeta v_0 \mathbf{e}_i$. The orientation of the self-propulsion velocity is in turn given by $\boldsymbol{e}_i = [\cos(\theta_i), \sin(\theta_i)]$ and its angle randomly reorients with a rotational diffusion coefficient D_{r}, i.e.,

$$\dot{\theta}_i = \chi_i, \tag{7.2}$$

where χ_i denotes a Gaussian noise process with zero mean and variance $\langle \chi_i(t)\chi_j(t') \rangle_{\text{noise}} = 2D_{\text{r}}\delta_{ij}\delta(t-t')$. Based on the equations of motion one can derive the following Smoluchowski operator,

$$\Omega = \sum_{j=1}^{N} D_t \nabla_j \cdot (\nabla_j - \beta \boldsymbol{F}_j) + D_r \partial^2_{\theta_j} - v_0 \nabla_j \cdot \boldsymbol{e}(\theta_j) \tag{7.3}$$

which governs the time-evolution of the probability distribution function (PDF) of particle positions and orientations $P(t)$ via,

$$\frac{\partial P}{\partial t} = \Omega P(t). \tag{7.4}$$

In equilibrium, that is, for $v_0 = 0$, this equation admits a Boltzmann solution $P_{\text{eq}} \propto e^{-\beta U}$ with U the total potential energy from which the interaction force $\mathbf{F}_j = -\nabla_j U$ is derived and $\beta = (k_B T)^{-1}$ the inverse thermal energy.

The starting point of the ITT approach is then to employ the identity $e^{\Omega t} = 1 + \int_0^t dt' e^{\Omega t'} \Omega$ and insert it in the formal solution of the PDF, $P(t) = e^{\Omega t} P(0)$ [100, 194, 204]. Letting our ABP system switch from an equilibrated passive state ($v_0 = 0$) to an active state ($v_0 > 0$) at time $t = 0$ and assuming it has reached an active steady-state at $t \to \infty$, one can retrieve an exact expression for the active steady-state average of any observable A [100],

$$\langle A \rangle_{\text{ss}} = \langle A \rangle_{\text{eq}} - \beta v_0 \int_0^\infty dt \left\langle \sum_{j=1}^{N} \boldsymbol{e}_j \cdot \boldsymbol{F}_j e^{\Omega^\dagger t} A \right\rangle_{\text{eq}}. \tag{7.5}$$

Here, $\Omega^\dagger$ represents the adjoint Smoluchowski operator, which acts on everything to its right except the PDF and is given by

$$\Omega^\dagger = \sum_j D_\mathrm{t}(\nabla_j + \beta \boldsymbol{F}_j) \cdot \nabla_j + D_\mathrm{r}\partial_{\theta_j}^2 + v_0 \boldsymbol{e}_j \cdot \nabla_j. \tag{7.6}$$

The appeal of this approach comes from the fact that a usually intractable steady-state average $\langle \ldots \rangle_\mathrm{ss}$ is now rewritten in terms of transient quantities $\langle \ldots \rangle_\mathrm{eq}$ which are averaged with respect to the known equilibrium distribution P_eq. At the same time, the integral term in Eq. (7.5) remains highly nontrivial and provides a serious obstacle for any analytical progress.

As an initial approximation it has therefore been proposed to only consider the first term of Eq. (7.5) [100, 106–108, 110]. This has already led to the development of an active mode-coupling theory (MCT) for the transient time-dependent density correlation function [100] (see also Chapter 6),

$$S_{ll'}(\boldsymbol{k}, t) = \left\langle \rho_l^*(\boldsymbol{k}) e^{\Omega^\dagger t} \rho_{l'}(\boldsymbol{k}) \right\rangle_\mathrm{eq}, \tag{7.7}$$

where $\rho_l(\boldsymbol{k}) = \frac{1}{\sqrt{N}} i^l \sum\limits_{j=1}^{N} e^{i\boldsymbol{k}\cdot\boldsymbol{r}_j} e^{il\theta_j}$ depicts the density mode (the factor i^l is added for technical convenience, see Section 7.A for precise details). Using only the passive static structure factor $S(k)$ (from for instance liquid state theory or simulations), which enters in the initial condition via,

$$S_{ll'}(k) = \langle \rho_l^*(\boldsymbol{k}) \rho_{l'}(\boldsymbol{k}) \rangle_\mathrm{eq} = \delta_{ll'}[1 + \delta_{l0}(S(k) - 1)], \tag{7.8}$$

one can invoke this theory to find self-consistent solutions for $S_{ll'}(\boldsymbol{k}, t)$. Besides aiding to our fundamental understanding of glassy active matter [100, 106–108, 110], these solutions in conjunction with additional MCT-approximations also provide an interesting pathway to explicit analytical expressions for complete steady-state correlation functions, i.e., ones that include the integral term in Eq. (7.5). This has already been successfully explored in the context of the average swim velocity [108], but our aim is to generalize the idea and also apply it to arguably more complex static structure and velocity correlations.

In particular, let us first define the integral term in Eq. (7.5) for any static observable A as,

$$C^A(t) \equiv \left\langle \sum_{j=1}^{N} \boldsymbol{e}_j \cdot \boldsymbol{F}_j e^{\Omega^\dagger t} A \right\rangle, \tag{7.9}$$

where, for notational convenience, we have omitted the subscript 'eq' which will be done from this point onward. However, in this form $C^A(t)$ does not yet lend itself to MCT-approximations as it may lead to seemingly diverging and thus nonphysical contributions from the integral term (this has also been explicitly checked for the observables in this chapter). To avoid this problem and bound the integral term it has been suggested in Ref. [108] to further reduce $C^A(t)$ by means of an irreducible time-evolution operator, $\Omega^\dagger_{\text{irr}} = \Omega^\dagger - \mathcal{P}_v$, with

$$\mathcal{P}_v = -\sum_{ij} |\boldsymbol{F}_i \cdot \boldsymbol{e}_i\rangle \frac{\beta^2 D_t}{N} \langle \boldsymbol{F}_j \cdot \boldsymbol{e}_j| \,. \tag{7.10}$$

This definition is in part motivated by the fact that MCT-approximations are usually better suited for slow variables and thus we want to project out the active part of the evolution operator which is assumed to take on a fast character. Using Dyson decomposition one then finds

$$\int_0^\infty dt C^A(t) = \frac{\int_0^\infty dt C^A_{\text{irr}}(t)}{1 + \frac{\beta^2 D_t}{N} \int_0^\infty dt C^v_{\text{irr}}(t)} \tag{7.11}$$

where we have introduced the irreducible correlation of swim velocity corrections

$$C^v_{\text{irr}}(t) = \left\langle \sum_{j=1}^N \boldsymbol{e}_j \cdot \boldsymbol{F}_j e^{\Omega^\dagger_{\text{irr}} t} \sum_{i=1}^N \boldsymbol{e}_i \cdot \boldsymbol{F}_i \right\rangle, \tag{7.12}$$

and C^A_{irr}, which is the same correlation function as Eq. (7.9) only evolving in time with irreducible dynamics $e^{\Omega^\dagger_{\text{irr}} t}$ instead of full dynamics $e^{\Omega^\dagger t}$.

Employing customary MCT-approximations [15, 22, 142, 205], that is, two projections on density doublets, a factorization of dynamic four-point correlations into products of two-point correlations, and replacing irreducible by full dynamics, it has been shown that [108] (see also Section 7.B for more details),

$$\begin{aligned} \frac{D_t \beta^2}{N} C^v_{\text{irr}}(t) = \frac{\rho D_t}{8\pi} \int_0^\infty dq\, q^3 c(q)^2 \sum_{\lambda,\lambda'=\pm 1} \lambda\lambda' \\ \times \left(\tilde{S}_{\lambda\lambda'}(q,t) \tilde{S}_{00}(q,t) + \tilde{S}_{0\lambda}(q,t) \tilde{S}_{\lambda' 0}(q,t) \right) . \end{aligned} \tag{7.13}$$

Here, we have introduced the real quantity $\tilde{S}_{ll'}(q,t) = e^{i(l-l')\theta_q} S_{ll'}(\mathbf{q},t)$, which, due to rotational symmetry, is independent of the orientation of the wavevector θ_q and only depends on its magnitude q [108, 206]. Note that $C^v_{\text{irr}}(t)$ is now fully written in terms of transient dynamic density correlation functions $S_{ll'}(\boldsymbol{k},t)$. Moreover, it is responsible for bounding the integral term as its magnitude grows when one approaches denser conditions.

The final step then consists of applying the same MCT-approximations to $C^A_{\text{irr}}(t)$ to end up with an explicit expression for the steady-state average $\langle A \rangle_{\text{ss}}$ that only depends on $S_{ll'}(\boldsymbol{k},t)$, its passive counterpart $\langle A \rangle$, and the relevant control parameters. As such, ITT in conjunction with active MCT provides a generic framework for analytically evaluating (static) non-equilibrium averages, though we will show that it gives the most qualitatively consistent results when our observable A can already be written in terms of density doublets.

7.3 Active-MCT and ITT numerics

To utilize the proposed ITT method and calculate steady-state averages, we require explicit expressions for $S_{ll'}(\mathbf{k},t)$. We therefore numerically solve the active-MCT equations (as detailed in e.g., Refs. [100, 106, 110]) for a monodisperse colloidal system of hard disks of diameter σ. We use an equidistant wavenumber grid $k\sigma = [0.3, 0.5, \dots, 39.9]$ (note that we drop the smallest wavenumber $k\sigma = 0.1$ in favor of numerical stability) and perform the integration over time according to the algorithm presented in Ref. [100]. For the latter, we calculate the first $N_t/2 = 16$ points in time using a Taylor expansion with a step size $\Delta t = 10^{-6}$, numerically integrate the equations of motion for the next $N_t/2$ points in time, duplicate the timestep, and repeat the process. As input we employ an analytical expression for $S(k)$ attained (as a function of the area fraction $\phi = \rho\pi\sigma^2/4$) from density functional theory [196]. For computational convenience we only consider the first two non-trivial active modes $l \in [-1, 0, 1]$, which is sufficient to calculate the correlation functions discussed in this chapter, and fix the wavevector along the x-axis, i.e. $\mathbf{k} = k\mathbf{e}_x$, so that $S_{ll'}(\mathbf{k},t) = \tilde{S}_{ll'}(k,t)$ is always real. We also set the area fraction at $\phi = 0.6$ (though we have checked that $\phi = 0.5$ gives similar results) which is a trade-off between allowing sufficiently dense conditions and numerical stability for small values of k and large active speeds v_0. All results are presented in units of σ and σ^2/D for distance and time respectively. Finally, the time-integration of the ITT equations is carried out using the trapezoidal rule.

7.4 Simulation details

To complement our theoretical results and characterize the role of translational (thermal) noise on steady-state correlations in dense active matter, we perform simulations of a slightly polydisperse mixture of $N = 1000$ quasi-hard ABPs (disks). The dynamics of each particle i is governed by Eqs. (7.1) and (7.2) where the interaction force $\mathbf{F}_i = -\sum_{j\neq i}\nabla_i V_{\alpha\beta}(r_{ij})$ is derived from a quasi-hard-sphere powerlaw potential $V_{\alpha\beta}(r) = \epsilon\left(\frac{\sigma_{\alpha\beta}}{r}\right)^{36}$ [156, 157]. The interaction energy ϵ and friction constant ζ are equal to one. For the thermal simulations we fix the temperature and thus the diffusion coefficient at $T = D_\mathrm{t} = 1.0$, whereas they are strictly zero for the athermal simulations. To ensure polydispersity, our mixture consists of equal fractions of particles with diameters (in units of σ) $\sigma_{\alpha\alpha} = \{0.8495, 0.9511, 1.0, 1.0489, 1.1505\}^1$, which are additive so that $\sigma_{\alpha\beta} = (\sigma_{\alpha\alpha} + \sigma_{\beta\beta})/2$ [110]. Simulations consist of solving the Langevin equation [Eq. (7.1)] via a forward Euler scheme and are carried out using LAMMPS [159]. We fix the square box size to set the area fraction at $\phi = 0.75$ which is slightly denser than the theoretical values. This is done to mitigate the effects of motility induced phase separation (MIPS) [119] and allow for a better comparison with the ITT results which are obtained for an assumed homogeneous system. Setting the persistence time and active speed, we then run the system for approximately 200 time units to ensure we are in a steady state, and afterwards track the particle positions in time. All simulation results are presented in units where σ, ϵ, and $\zeta\sigma^2/\epsilon$ denote the units of length, energy, and time respectively [160].

7.5 Density correlations

We begin by considering the steady-state (or nonequilibrium) static structure factor, i.e., we let $A = \rho_0^*(\boldsymbol{k})\rho_0(\boldsymbol{k})$, and define it as $S_{\text{neq}}(k) = \langle \rho_0^*(\boldsymbol{k})\rho_0(\boldsymbol{k})\rangle_{\text{ss}}$. Carrying out the MCT-approximations [where we mention that, because A has the form of a density doublet, this requires one less projection on density doublets compared to $C_{\text{irr}}^v(t)$], one can find the following ITT expression (see Section 7.B for more details),

$$S_{\text{neq}}(k) = S(k) - 2\rho v_0 k\, c(k) \frac{\int_0^\infty dt\, \tilde{S}_{10}(k,t)\tilde{S}_{00}(k,t)}{1 + \frac{D_t \beta^2}{N} \int_0^\infty dt\, C_{\text{irr}}^v(t)}. \tag{7.14}$$

Note that it only depends on the magnitude k which is consistent with the fact that the active steady-state remains isotropic.

Based on the above equation we have calculated $S_{\text{neq}}(k)$ for different active speeds v_0 and persistence times $\tau_{\text{p}} = D_{\text{r}}^{-1}$. Concomitantly, we have extracted $S_{\text{neq}}(k)$ from simulation data for the same active control parameters. The results are shown in Fig. 7.1 and upon first glance look qualitatively consistent. In particular, the location of the first peak remains almost constant at $k \sim 2\pi/\sigma$, while its height decreases significantly for increasing values of v_0 and only marginally for increasing τ_{p} (note that in simulations the peak is higher due to the larger packing fraction ϕ). These features are well captured by the theoretical predictions and are likely a result of the (quasi-)hard nature of the particle interactions (constant first peak location) and the system exhibiting faster dynamics upon increased activity (decreasing first peak height). Beyond the first minimum, which is lifted slightly upwards, the influence of activity on $S_{\text{neq}}(k)$ becomes fairly small. The only exception is the splitting of the second peak at $v_0 = 0$ (a marker for local crystalline

---

[1] Particle diameters are chosen such that the first four moments correspond to the results of a Gaussian distribution with a mean of 1 and a standard deviation of 0.1.

order [207] and thus not captured by the theory), which disappears when the system becomes more active and thus more fluid.

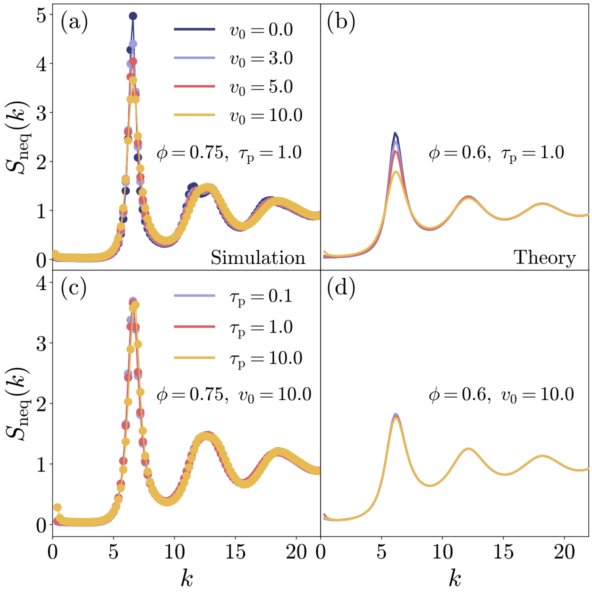

Figure 7.1: The steady-state structure factor $S_\mathrm{neq}(k)$ as a function of wavenumber k directly measured from simulation data of thermal ABPs (a,c) or obtained fully analytically via the ITT formalism (b,d). Results correspond to different active speeds (a-b) and persistence times (c-d).

At large enough persistence and active speed we also observe a small increase of $S_\mathrm{neq}(k)$ when k approaches zero which is associated with increased compressibility and usually interpreted as a precursor for MIPS [208] In that regard, it is remarkable that the ITT result is able to pick up on this as in principle it has no notion of phase separation. Finally, we have also extracted $S_\mathrm{neq}(k)$ for athermal systems (see Fig. 7.5), but their qualitative features are mostly similar to those of their thermal counterparts (assuming the system is not undergoing MIPS which dramatically changes the structure factor).

7.6 Velocity correlations

Having started from a purely structural correlation, a natural next step is now to also try to explicitly connect the structure to the (active) velocity of individual particles. For that, we take a closer look at the so-called (longitudinal) velocity correlation which is defined as,

$$\omega(k) = \frac{1}{N\zeta^2}\hat{\boldsymbol{k}} \cdot \left\langle \sum_{i=1}^{N} (\boldsymbol{F}_i + \boldsymbol{f}_i)\, e^{-i\boldsymbol{k}\cdot\boldsymbol{r}_i} \sum_{j=1}^{N} (\boldsymbol{F}_j + \boldsymbol{f}_j)\, e^{i\boldsymbol{k}\cdot\boldsymbol{r}_j} \right\rangle_{\mathrm{ss}} \cdot \hat{\boldsymbol{k}}, \tag{7.15}$$

and has already been frequently studied in the context of athermal dense active matter where it is shown to only depend on the magnitude k, develop oscillations upon increasing v_0 and τ_{p}, and become constant in the passive limit [91, 112, 113, 193]. Its behavior for a thermal system, which includes translational diffusion, in contrast remains largely unexplored and our aim is therefore to characterize this velocity correlation in thermal systems and make a comparison with the better-known athermal phenomenology.

Since it turns out that our theoretical approach is better equipped to deal with specific terms in Eq. (7.15) and to more exactly pinpoint the role of thermal noise on this correlation function, we have decided to separate the velocity correlations in three distinct contributions and consider these individually. As such, we write

$$\omega(k) = \omega_{\mathrm{a}}(k) + 2\omega_{\mathrm{c}}(k) + \omega_{\mathrm{int}}(k), \tag{7.16}$$

where $\omega_{\mathrm{a}}(k)$ represents the coupling between the active forces (or equivalently velocities), $\omega_{\mathrm{c}}(k)$ the cross correlation between active and interaction force, and $\omega_{\mathrm{int}}(k)$ the correlation between interaction forces. From this point onward, we will refer to these terms as the active-active, active-passive, and passive-passive velocity correlations respectively.

7.6.1 Active-active velocity correlation

Employing MCT-approximations one can derive an explicit ITT expression for the active-active velocity correlation which is given by (see Section 7.B.3 for a precise derivation),

$$\omega_{\mathrm{a}}(k) = \frac{v_0^2}{2} - v_0^3 \rho k c(k) \frac{\int_0^\infty dt \tilde{S}_{01}(k,t)\left[\tilde{S}_{11}(k,t) - \tilde{S}_{-11}(k,t)\right]}{1 + \frac{D_t\beta^2}{N}\int_0^\infty dt\, C^v_{\mathrm{irr}}(t)}. \tag{7.17}$$

It is worth pointing out that the observable associated with this contribution can again be rewritten in terms of density doublets [see Eq. (7.30)] and thus, similar to $S_{\mathrm{neq}}(k)$, one less projection on density doublets is required. Moreover, within the ITT approximation $\omega_{\mathrm{a}}(k)$ only depends on the magnitude of the wavevector k and not its orientation. This is in agreement with the behavior found for $\omega(k)$ in simulations and is to be expected if the active steady-state is isotropic [91, 112, 113, 193].

Using Eq. (7.17), we have calculated $\omega_{\mathrm{a}}(k)$ for different active speeds v_0 and persistence times τ_{p}. Results for the same active control parameters have also been retrieved

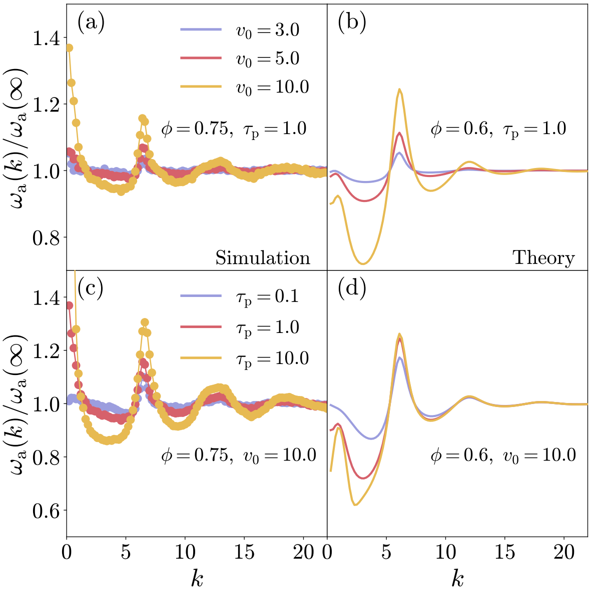

Figure 7.2: The active-active contribution to the velocity correlation function $\omega_a(k)$ (normalized by $\omega_a(\infty) = v_0^2/2$) as a function of wavenumber k directly measured from simulation data (a,c) or obtained fully analytically via the ITT formalism (b,d). Results correspond to different active speeds (a-b) and persistence times (c-d).

from the simulation data of thermal ABPs and both have been plotted in Fig. 7.2. In accordance with the athermal simulation results for $\omega(k)$ [91, 112, 113, 193], we witness the emergence of oscillations around $\omega_a(\infty) = v_0^2/2$ whose relative size increases as either v_0 or τ_p is increased. The locations of the corresponding peaks (approximately) coincide with the ones from the static structure factor and reveal a clear structural signature in this velocity correlation. Interestingly, all these qualitative features are thus also predicted by our ITT method with even a reasonable degree of quantitative accuracy. This is quite remarkable as we reiterate that the whole ITT procedure has only required an analytical passive structure factor as input and we only consider the first non-trivial active modes. At the same time, the ITT results fail to capture the correct behavior at small wavenumbers k, especially for large persistence and active speed where the value of ω_a is seen to increase dramatically. It is known, however, that MCT-approximations can sometimes yield less accurate results in the small-k limit which already occurs for passive systems [15].

To place our thermal results in a broader context, we have also extracted active-active velocity correlations from the simulation data of athermal ABPs (see Fig. 7.5). These exhibit the same qualitative behavior as the corresponding thermal results, though the magnitude of the oscillations is larger indicating that thermal noise disrupts the emergence of these correlations. Overall, the obtained results for $\omega_\mathrm{a}(k)$ clearly demonstrate the existence of spatial active velocity correlations in thermal and athermal dense active matter (which have been checked for finite size effects). This carries an important implication, as it has been argued for athermal systems that such correlations only arise when one considers the total velocity consisting of both the active and interaction force [132, 202]. Our results instead suggest that this is not strictly necessary.

7.6.2 Active-passive and passive-passive velocity correlations

In contrast to the active-active correlation, we find that the ITT approach has proven less fruitful in its efforts to describe the other two contributions [$\omega_\mathrm{c}(k)$ and $\omega_\mathrm{int}(k)$] to the total velocity correlation. For the latter term, the presence of two interaction forces hinders a direct analytical evaluation when using the standard MCT-approximations. As such, an additional projection operator seems to be necessary to separate both interaction forces but this has not yielded satisfying results. Interestingly, by means of a properly orthogonalized projection operator on density doublets one can find qualitatively consistent results for $\omega_\mathrm{int}(k)$ of a passive Brownian system (see Section 7.D for more details), which corresponds to taking only the first term in eq. Eq. (7.5). In comparison, due to the presence of only one interaction force, the active-passive correlation $\omega_\mathrm{c}(k)$ can be directly evaluated. Though its sign and order of magnitude are accurately captured, the qualitative behavior we find is inconsistent with results from simulations (see Section 7.B.4 for more details). It thus seems that a conventional projection on density doublets is insufficient to fully capture the behavior of the cross term.

As such, we primarily focus on the results obtained from both thermal and athermal simulations and try to scrutinize the role of thermal noise. Let us first focus on the active-passive velocity correlation for which the results are shown in Fig. 7.3. Note that since the active-passive velocity correlation is always negative (implying an anticipated anti-correlation between active and passive forces) and to allow for a good comparison with the other velocity correlations, we have plotted $-\omega_\mathrm{c}(k)$ and normalized the results with $\omega_\mathrm{a}(\infty) = v_0^2/2$. The first thing we observe is that both the thermal and athermal results are mostly of the same order of magnitude as the active-active velocity correlations and the relative magnitude of their asymptotic value $\omega_\mathrm{c}(\infty)$ increases with persistence and decreases for enhanced active speed.

In analogy to the active-active velocity correlation we also see, provided the active speed and persistence are large enough, a significant increase of $-\omega_\mathrm{c}(k)$ when k approaches zero that appears to be more pronounced for the athermal systems. Since the

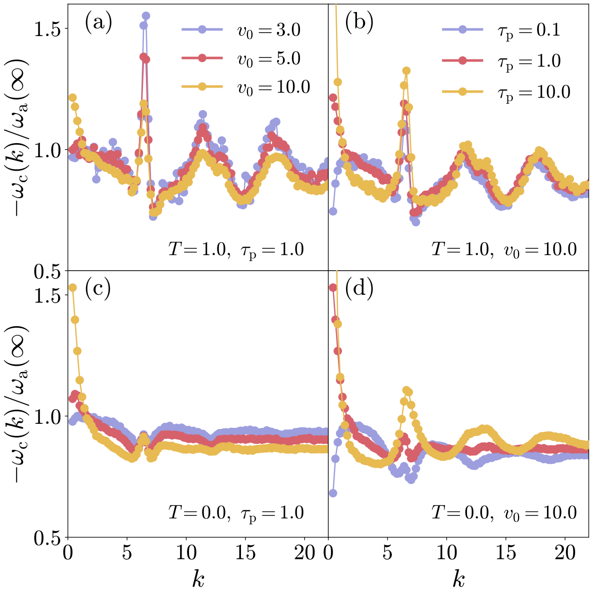

Figure 7.3: The active-passive contribution to the velocity correlation function $\omega_\mathrm{c}(k)$ (normalized by $\omega_\mathrm{a}(\infty) = v_0^2/2$ and with a prefactor of minus one to improve visibility) as a function of wavenumber k. The results are directly measured from simulation data for (a,b) a thermal system at temperature $T = 1.0$ and (c,d) an athermal system, and correspond to different active speeds (a,c) and persistence times (b,d).

small-k regime indicates long-ranged correlations it is sensible that these are stronger for an athermal system. At the same time, it is worth noting that at a small persistence of $\tau_\mathrm{p} = 0.1$ (and $v_0 = 10$) the value for $-\omega_\mathrm{c}(k)$ has already tipped over and decreases as one approaches $k \to 0$ (in both the thermal and athermal case). It would be interesting to see if this also occurs for the other curves if one probes at smaller values of k. Intuitively, there might even exist a relationship between the so-called persistence length $l_\mathrm{p} = v_0\tau_\mathrm{p}$ [118] and the wavenumber where such a tipping takes place. This could explain why we only see it at a relatively small persistence.

In comparison, for larger wavenumbers the similarity between the thermal and athermal active-passive velocity correlations is less obvious with both demonstrating oscillatory behavior (though not always with the same phase) and a sudden peak at roughly the same location as the peak of $S(k)$. Moreover, these effects for larger values of k and thus shorter length scales (on the order of a particle diameter or smaller) are much more evident for the thermal results. They are therefore probably enhanced by the thermal noise inducing larger and more erratic instantaneous repulsive forces.

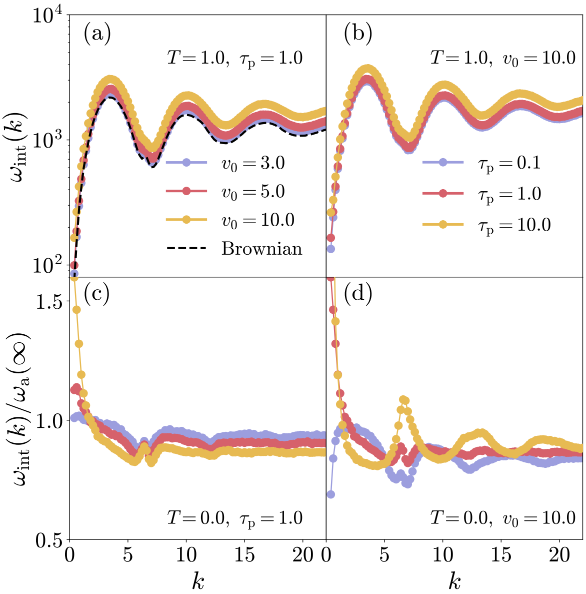

Figure 7.4: The passive-passive contribution to the velocity correlation function $\omega_{\rm int}(k)$ as a function of wavenumber k, directly measured from simulation data for (a,b) a thermal system at a temperature $T = 1.0$ and (c,d) an athermal system (for which it is normalized by $\omega_{\rm a}(\infty) = v_0^2/2$). The results correspond to different active speeds (a,c) and persistence times (b,d). The dotted line is obtained from simulations of a passive Brownian system at $T = 1.0$.

We finalize our results by examining the passive-passive velocity correlations $\omega_{\rm int}(k)$ which are shown in Fig. 7.4. Upon inspection we may immediately note that the thermal and athermal results are significantly different, both quantitatively and qualitatively. In particular, in the thermal case this term is relatively big and completely dominates over all other contributions to the velocity correlation. We expect this to be caused by translational noise occasionally inducing large instantaneous repulsive forces which greatly exceed the active force. That thermal passive motion is mostly responsible for this correlation is also reflected in the fact that the qualitative behavior and order of magnitude of $\omega_{\rm int}(k)$ are almost the same as the one obtained from an equivalent Brownian system without self-propulsion (see dotted line in Fig. 7.4). Moreover, the oscillations of $\omega_{\rm int}(k)$ are out of phase with the ones from $S_{\rm neq}(k)$ and thus the passive-passive velocity correlation seems anticorrelated with the structure.

The corresponding athermal values are instead much smaller, i.e., of the same order as the active-active and active-passive velocity correlation functions. This can be explained by realizing that in a dense athermal system interaction forces, on average, constantly counteract the self-propulsion forces and are thus expected to be of the same order of magnitude. More strikingly, the results (and thus the qualitative behavior) for $\omega_{\mathrm{int}}(k)$ seem almost indistinguishable from the active-passive velocity correlation $\omega_{\mathrm{c}}(k)$. This hints at a possible formal equivalence (or at least strong connection) between these parameters in athermal systems, which would be interesting to explore in more detail.

Overall, when comparing thermal and athermal velocity correlations in dense active fluids it thus seems sensible to focus more on active-active and active-passive correlations. Alternatively, coarse-graining the total velocity over a cleverly chosen time window might also mitigate the effects of thermal noise on the velocity correlation. This can be straightforwardly done in simulations, but is likely more tedious in a microscopic description such as ITT.

7.7 Conclusions

In this chapter, we have sought to characterize nonequilibrium (or steady-state) structure and velocity correlations in dense active systems, with a prime focus on the often overlooked influence of thermal (or translational) noise. We have done so by means of both particle-based computer simulations and a microscopic theory based on the integration through transients (ITT) formalism in conjunction with active mode-coupling theory. Consistent with literature, we find that for both thermal and athermal systems enhanced active speed and persistence diminish the structure and make the system more compressible (the latter being manifested by an increase of the nonequilibrium static structure factor in the limit of zero wavenumber). More importantly, we also demonstrate that all these features can be qualitatively predicted by our microscopic theory which only takes a passive (analytical) static structure factor as its input.

Besides structure, we have also examined all distinct contributions to the equal-time velocity correlations, i.e., spatial correlations between active velocities, interaction forces, and cross terms of one with the other. We show that our theory is equally capable of making accurate qualitative predictions for the active-active velocity correlation. These correlations are similar in both thermal and athermal active systems (though weaker for the former) and become more significant (larger oscillations and a stronger increase at small wavenumber) upon increasing the active speed or persistence. The existence of such correlations is especially interesting considering that for athermal systems it has been previously argued that spatial velocity correlations only arise when one takes into account the total velocity consisting of both the active and interaction force.

Moreover, we demonstrate that the cross correlation exhibits distinct qualitative changes due to thermal noise but only when one probes length scales on the order of a particle diameter or smaller. The correlation between interaction forces instead is completely dominated by thermal noise which leads to much larger values and different qualitative behavior on all length scales.

Overall, our results further establish ITT as a promising route to evaluate nonequilibrium averages in active matter and suggest that correlations between active velocities might carry more information than previously anticipated. They also show that thermal noise strongly influences velocity correlations that involve the instantaneous interaction force. A possible remedy for this could be to coarse-grain the total velocity over an astutely chosen time window. This can be straightforwardly done in simulations, but is likely more tedious in a microscopic description such as ITT.

As a followup, it would be highly interesting to study the small-wavenumber behavior of these individual contributions to the velocity correlation in greater detail and possibly extract scaling relations that can be compared for athermal and thermal systems [193]. This, however, requires (especially for thermal ABPs) extensive simulation efforts and is therefore left for future work.

Appendix

7.A Symmetry properties

In this appendix we formally show, basing ourselves on the derivation of the symmetry properties of the ISF in Ref. [206], how the inclusion of a factor i^l in our density mode $\rho_l(\mathbf{k})$ in combination with choosing the wavevector $\mathbf{k}$ along the x-axis ensures that the transient density correlations are always real. It has been shown that if we rotate $\boldsymbol{k}$ by an angle $\delta\theta$, the transient density correlation is modified in the following way [206]

$$S_{ll'}(\boldsymbol{k}_{+\delta\theta}, t) = e^{-i(l-l')\delta\theta} S_{ll'}(\boldsymbol{k}, t) \tag{7.18}$$

In particular, taking $\delta\theta = \pi$, one finds

$$S^{*}_{ll'}(\boldsymbol{k}, t) = (-1)^{l-l'} S_{-l,-l'}(\boldsymbol{k}, t), \tag{7.19}$$

while if we let $\delta\theta = -\theta_{\boldsymbol{k}}$, we have

$$\tilde{S}_{ll'}(k, t) \equiv S_{ll'}(k\boldsymbol{e_x}, t) = e^{i(l-l')\theta_{\boldsymbol{k}}} S_{ll'}(\boldsymbol{k}, t). \tag{7.20}$$

Next, let us define the linear transformation $\mathcal{T}$

$$\begin{pmatrix} r_x \\ r_y \\ \theta \end{pmatrix} \rightarrow \begin{pmatrix} r_x \\ -r_y \\ -\theta \end{pmatrix}, \tag{7.21}$$

which represents a symmetric transformation with respect to the x-axis, and thus leaves absolute distances invariant. Therefore, the interaction potential U is unchanged, meaning P_{eq} is invariant under $\mathcal{T}$. It is straightforward to prove that $\Omega^\dagger$ is also invariant. This implies that $S_{ll'}(k\boldsymbol{e}_x, t) = (-1)^{l-l'} S_{-l,-l'}(k\boldsymbol{e}_x, t)$, which combined with Eq. (7.19) yields

$$\tilde{S}_{ll'}(k,t) = (-1)^{l-l'} \tilde{S}_{-l,-l'}(k,t) = \tilde{S}^*_{ll'}(k,t), \tag{7.22}$$

and proves that $\tilde{S}_{ll'}(k,t)$ is always real.

7.B Analytical details

In this appendix we will present more detailed derivations of several analytical expressions shown throughout the main text of the chapter.

7.B.1 Correlation of swim velocity corrections

The irreducible correlation of swim velocity corrections, i.e., $C^v_{\mathrm{irr}}(t)$, serves to bound the ITT quantities we compute [see Eq. (7.11)]. To find an analytical expression for this term we employ standard MCT-approximations. In particular, we insert two projections onto density doublets,

$$\mathcal{P}_2 = \frac{1}{2} \sum_{\mathbf{q}_1 \mathbf{q}_2} \sum_{l_1 l_2} |\rho_{l_1}(\mathbf{q}_1)\rho_{l_2}(\mathbf{q}_2)\rangle S^{-1}_{l_1 l_1}(q_1) S^{-1}_{l_2 l_2}(q_2) \langle \rho^*_{l_1}(\mathbf{q}_1)\rho^*_{l_2}(\mathbf{q}_2)|, \tag{7.23}$$

such that

$$C^v_{\mathrm{irr}}(t) \approx \left\langle \sum_{j=1}^{N} \boldsymbol{e}_j \cdot \boldsymbol{F}_j \ \mathcal{P}_2 e^{\Omega^\dagger_{\mathrm{irr}} t} \mathcal{P}_2 \ \sum_{i=1}^{N} \boldsymbol{e}_i \cdot \boldsymbol{F}_i \right\rangle. \tag{7.24}$$

Note that, in contrast to conventional MCT, one could have also used a projection on density singlets but it can be shown that these yield vanishing contributions. For the so-called left vertex we then have (as has been previously calculated in Ref. [206])

$$\begin{aligned} V_L &\equiv \frac{1}{2} \sum_j \langle \boldsymbol{e}_j \cdot \boldsymbol{F}_j \rho_{l_1}(\boldsymbol{q}_1)\rho_{l_2}(\boldsymbol{q}_2)\rangle \, S^{-1}_{11}(q_1) S^{-1}_{22}(q_2) \\ &= -\frac{\rho(l_1+l_2)}{4\beta} \delta_{\boldsymbol{q}_1,-\boldsymbol{q}_2} \delta_{|l_1+l_2|,1} q_1 c(q_1) \left(e^{i l_2 \theta_{q_1}} \delta_{l_1,0} - e^{i l_1 \theta_{q_1}} \delta_{l_2,0} \right), \end{aligned} \tag{7.25}$$

where we have used partial integration to rewrite the interaction force. We emphasize that the left vertex also naturally arises when applying MCT-approximations to $C^A_{\mathrm{irr}}(t)$ (for any observable A). Moreover, due to the symmetry of $C^v_{\mathrm{irr}}(t)$, one can show that the right vertex takes on an identical form as the left one. The other MCT-approximation consists of factorizing the four-point density correlation and replacing irreducible with full dynamics, i.e.,

$$\begin{aligned}\left\langle \rho^*_{l_1}(\mathbf{q}_1)\rho^*_{l_2}(\mathbf{q}_2)e^{\Omega^\dagger_{\mathrm{irr}}t}\rho_{l_3}(\mathbf{q}_3)\rho_{l_4}(\mathbf{q}_4)\right\rangle &\approx S_{l_1l_3}(\mathbf{q}_1,t)\\ S_{l_2l_4}(\mathbf{q}_2,t)\;\delta_{\mathbf{q}_1,\mathbf{q}_3}\delta_{\mathbf{q}_2,\mathbf{q}_4} &+ S_{l_1l_4}(\mathbf{q}_1,t)S_{l_2l_3}(\mathbf{q}_2,t)\;\delta_{\mathbf{q}_1,\mathbf{q}_4}\delta_{\mathbf{q}_2,\mathbf{q}_3}.\end{aligned} \tag{7.26}$$

Combining these results and taking the thermodynamic limit one finally arrives at

$$\begin{aligned}\frac{D_t\beta^2}{N}C^v_{\mathrm{irr}}(t) = \frac{\rho D_t}{8\pi}\int_0^\infty dq\,q^3c(q)^2 \sum_{\lambda,\lambda'=\pm1}\lambda\lambda'\\ \times\left(\tilde{S}_{\lambda\lambda'}(q,t)\tilde{S}_{00}(q,t)+\tilde{S}_{0\lambda}(q,t)\tilde{S}_{\lambda'0}(q,t)\right),\end{aligned} \tag{7.27}$$

which is consistent with the expression shown in Refs. [108, 206].

7.B.2 Nonequilibrium static structure factor

For the static structure factor we take $A = \rho^*_0(\mathbf{k})\rho_0(\mathbf{k})$. The reference contribution to the steady-state average is thus simply $\langle A\rangle = S(k)$. For the integral term we again use a projection on density doublets, but since A is already of the form of a density doublet we only require one projection, i.e.,

$$C^A_{irr}(t) \approx \left\langle \sum_{j=1}^N \boldsymbol{e}_j\cdot\boldsymbol{F}_j\;\mathcal{P}_2e^{\Omega^\dagger_{\mathrm{irr}}t}\rho^*_0(\mathbf{k})\rho_0(\mathbf{k})\right\rangle \tag{7.28}$$

Invoking the expression for the left vertex [Eq. (7.25)], the factorization approximation [Eq. (7.26)], and the symmetry properties of $\tilde{S}_{ll'}(k,t)$ one can then find that

$$C^A_{irr}(t) \approx 2\rho\beta^{-1}kc(k)\tilde{S}_{10}(k,t)\tilde{S}_{00}(k,t) \tag{7.29}$$

which leads to Eq. (7.14) in the main text.

7.B.3 Active-active velocity correlation

To derive an expression for the active-active velocity correlation we start by noticing that the product of an active force and the zeroth density mode can be rewritten as a combination of higher-order density modes, i.e.,

$$\frac{1}{\sqrt{N}\zeta}\sum_{j=1}^N \hat{\boldsymbol{k}}\cdot\boldsymbol{f}_je^{i\boldsymbol{K}\cdot\boldsymbol{r}_j} = \frac{v_0}{2}\sum_{\epsilon=\pm1} i^\epsilon e^{i\epsilon\theta_{\boldsymbol{k}}}\rho_{-\epsilon}(\boldsymbol{K}) \tag{7.30}$$

Thus, we have for the reference contribution to the active-active velocity correlation

$$\begin{aligned}\langle A\rangle &= \frac{1}{N\zeta^2}\left\langle \sum_{i=1}^{N} \hat{\boldsymbol{k}}\cdot\boldsymbol{f}_i e^{-i\boldsymbol{k}\cdot\boldsymbol{r}_i} \sum_{j=1}^{N} \boldsymbol{f}_j\cdot\hat{\boldsymbol{k}} e^{i\boldsymbol{k}\cdot\boldsymbol{r}_j}\right\rangle \\ &= \frac{v_0^2}{4}(S_{11}(k)+S_{-1-1}(k)) = \frac{v_0^2}{2},\end{aligned} \tag{7.31}$$

while for the contribution inside the integral we again only require one projection on density doublets,

$$C^A_{\mathrm{irr}}(t) \approx \frac{1}{N\zeta^2}\left\langle \sum_{m=1}^{N} \boldsymbol{e}_m\cdot\boldsymbol{F}_m\ \mathcal{P}_2 e^{\Omega^\dagger_{\mathrm{irr}}t} \sum_{i,j} \hat{\boldsymbol{k}}\cdot\boldsymbol{f}_i e^{-i\boldsymbol{k}\cdot\boldsymbol{r}_i} \boldsymbol{f}_j\cdot\hat{\boldsymbol{k}} e^{i\boldsymbol{k}\cdot\boldsymbol{r}_j}\right\rangle \tag{7.32}$$

Invoking the expression for the left vertex [Eq. (7.25)], the factorization approximation [Eq. (7.26)], and the symmetry properties of $\tilde{S}_{ll'}(k,t)$ one may find

$$C^A_{\mathrm{irr}}(\boldsymbol{k},t) = v_0^2\beta^{-1}\rho k c(k)\tilde{S}_{01}(k,t)[\tilde{S}_{11}(k,t)-\tilde{S}_{-11}(k,t)]. \tag{7.33}$$

Using these results in combination with Eqs. (7.5) and (7.11) then yields Eq. (7.17) in the main text.

7.B.4 Active-passive velocity correlations

Despite not giving fully satisfying results, one can find (with standard MCT-approximations) an explicit expression for the active-passive velocity correlation. Let us first recall the definition of this correlation,

$$\omega_{\mathrm{c}}(k) = \frac{1}{2N\zeta^2}\sum_{\boldsymbol{K}=\pm\boldsymbol{k}}\left\langle \sum_{i,j=1}^{N} \hat{\boldsymbol{k}}\cdot\boldsymbol{F}_j\,\hat{\boldsymbol{k}}\cdot\boldsymbol{f}_i e^{i\boldsymbol{K}\cdot(\boldsymbol{r}_j-\boldsymbol{r}_i)}\right\rangle_{\mathrm{ss}} \tag{7.34}$$

where we mention that one can also compute the two cross-correlations separately, but this gives the same result as presented below. We choose to evaluate the sum directly as it allows for simplifications much earlier in the computation.

Because of rotational invariance the reference contribution to the active-passive velocity correlation is simply zero, i.e., $\langle A\rangle = 0$. For the contribution inside the integral we now require two projections on density doublets. This introduces a right vertex of the form

$$\frac{1}{2N\zeta^2}\left\langle \rho^*_{l_3}(\boldsymbol{q}_3)\rho^*_{l_4}(\boldsymbol{q}_4) \sum_{i,j=1}^{N} \hat{\boldsymbol{k}}\cdot\boldsymbol{F}_j\,\hat{\boldsymbol{k}}\cdot\boldsymbol{f}_i e^{i\boldsymbol{K}\cdot(\boldsymbol{r}_j-\boldsymbol{r}_i)}\right\rangle. \tag{7.35}$$

Performing integration by parts to remove the interaction force and summing over $\boldsymbol{K} = \pm\boldsymbol{k}$, we end up with two types of terms, which contain either averages of three (S_a) or four (S_b) density modes. For the latter, we can use a Gaussian approximation, which immediately fixes $(\boldsymbol{q}_3, l_3)$ and $(\boldsymbol{q}_4, l_4)$ to the pair $(-\boldsymbol{K}, -\epsilon), (\boldsymbol{K}, 0)$ (or vice versa), and for the former, we can use the convolution approximation [100], which will only fix $(\boldsymbol{q}_3 + \boldsymbol{q}_4, l_3 + l_4)$ to $(\boldsymbol{0}, -\epsilon)$, and leave one degree of freedom in momentum and in angular mode.

One can then show that the two respective contributions yield for the product of the four-point dynamic density correlation with the right vertex the following expressions,

$$\begin{aligned} S_a = {} & \frac{D_t v_0}{4N} \sum_{\epsilon=\pm 1} \epsilon e^{i\epsilon\theta_{\boldsymbol{k}}} \sum_{\mathbf{q}_3, l_3} (-\hat{\boldsymbol{k}} \cdot \boldsymbol{q}_3) \\ & \times \left\langle \rho_1^* \rho_2^* e^{\Omega_{\text{irr}}^\dagger t} \rho_{l_3}(\boldsymbol{q}_3) \rho_{-l_3-\epsilon}(-\boldsymbol{q}_3) \right\rangle \\ & \times S_{l_3,l_3}^{-1}(q_3) \left[S_{l_3,l_3}(|\boldsymbol{k} - \boldsymbol{q}_3|) + S_{l_3,l_3}(|\boldsymbol{k} + \boldsymbol{q}_3|) \right] \\ S_b = {} & \frac{D_t v_0}{4} k \sum_{\epsilon=\pm 1} \epsilon e^{i\epsilon\theta_{\boldsymbol{k}}} \left[\left\langle \rho_1^* \rho_2^* e^{\Omega_{\text{irr}}^\dagger t} \rho_{-\epsilon}(-\boldsymbol{k}) \rho_0(\boldsymbol{k}) \right\rangle \right. \\ & \left. - \left\langle \rho_1^* \rho_2^* e^{\Omega_{\text{irr}}^\dagger t} \rho_{-\epsilon}(\boldsymbol{k}) \rho_0(-\boldsymbol{k}) \right\rangle \right] \end{aligned} \tag{7.36}$$

Finally, introducing the left vertex [Eq. (7.25)], the factorization approximation [Eq. (7.26)], and the symmetry properties of $\tilde{S}_{ll'}(k,t)$ [Eq. (7.22)] we find for the total contribution of each term (after a change of variables),

$$\begin{aligned} C_{\text{irr}}^{A,a}(\boldsymbol{k}, t) = {} & \frac{D_t v_0}{8\pi^2 \beta} \int d\boldsymbol{q} q^2 \, c(q) \cos(\theta_{\boldsymbol{k}} - \theta_{\boldsymbol{q}})^2 \\ & \times \left(1 - S(|\boldsymbol{k} - \boldsymbol{q}|) S^{-1}(q)\right) \Big(\tilde{S}_{0,0}(q,t) \tilde{S}_{1,1}(q,t) \\ & - \tilde{S}_{0,0}(q,t) \tilde{S}_{1,-1}(q,t) + 2\tilde{S}_{01}(q,t)\tilde{S}_{10}(q,t) \Big) \\ C_{\text{irr}}^{A,b}(\boldsymbol{k}, t) = {} & \frac{D_t v_0}{2\beta} \rho c(k) k^2 \\ \times & \left(\tilde{S}_{0,0}(k,t) (\tilde{S}_{1,1}(k,t) - \tilde{S}_{1,-1}(k,t)) + 2\tilde{S}_{0,1}(k,t) \tilde{S}_{1,0}(k,t) \right), \end{aligned} \tag{7.37}$$

where $C_{\text{irr}}^A = C_{\text{irr}}^{A,a} + C_{\text{irr}}^{A,b}$. With the help of the above result one can calculate the active-passive velocity correlation but this turns out to give qualitatively inconsistent results, though the negative sign and order of magnitude are correctly captured. It is therefore likely that the second projection on density doublets introduces a new error and requires refinement to allow for a better prediction.

7.C Additional data for athermal systems

In Fig. 7.5 we have plotted results for $S_{\rm neq}(k)$ and $\omega_{\rm a}(k)$ obtained from simulations of athermal ABPs. Overall, these show similar behavior as their thermal counterparts with one notable exception, i.e., $v_0 = 10.0$, $\tau_{\rm p} = 10.0$, where the peak of $S_{\rm neq}(k)$ is seen to increase again. This, as well as the very steep rise at vanishing wavenumber, can be explained by realizing that for such large values of the active control parameters the system has undergone MIPS. We mention that the nonmonotonic behavior of the first peak height has also been reported in previous work [208].

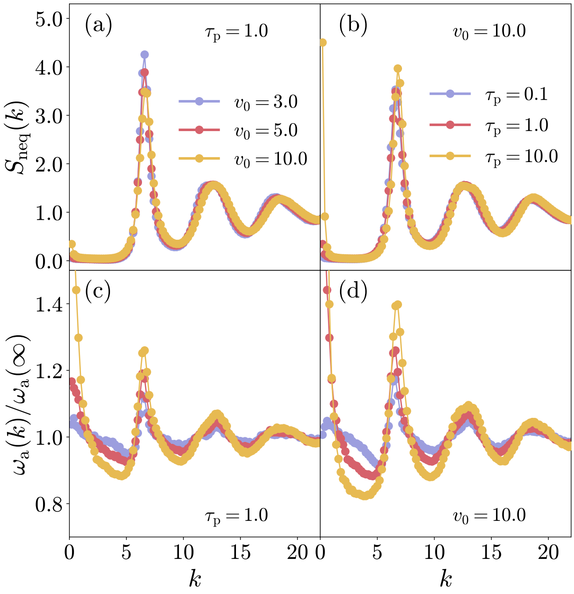

Figure 7.5: (a,b) The static structure factor and (c,d) active-active contribution to the velocity correlation function $\omega_{\rm a}(k)$ (normalized by $\omega_{\rm a}(\infty) = v_0^2/2$) as a function of wavenumber k, directly measured from simulation data for athermal system. The results correspond to different active speeds (a,c) and persistence times (b,d).

7.D Passive-passive velocity correlation for a Brownian system

As mentioned in the main text, the passive-passive velocity correlation $\omega_{\rm int}(k)$ cannot be directly evaluated when employing the standard set of MCT-approximations. This is primarily due to the two interaction forces which necessitates the use of at least one additional projection operator. Adding such a projection makes the evaluation of $C^{A}_{\mathrm{irr}}(t)$ rather intractable (or requires even more approximations). If we instead only focus on a passive system (for which the integral term in Eq. (7.5) is simply zero), analytical progress can in fact be made.

We thus seek to calculate the passive-passive velocity correlation for a Brownian system which is defined as,

$$\omega^{\mathrm{eq}}_{\mathrm{int}}(k) = \frac{1}{N\zeta^2}\left\langle \sum_{i=1}^{N} \hat{\boldsymbol{k}}\cdot\boldsymbol{F}_i e^{-i\boldsymbol{k}\cdot\boldsymbol{r}_i} \sum_{j=1}^{N} \boldsymbol{F}_j\cdot\hat{\boldsymbol{k}} e^{i\boldsymbol{k}\cdot\boldsymbol{r}_j}\right\rangle. \tag{7.38}$$

Assuming that forces are primarily mediated via direct interactions between two particles, we introduce the following orthogonalized projection on density doublets for a non-trivial sum of their wavevectors (i.e., $\mathbf{q}_1+\mathbf{q}_2=\mathbf{k}$)

$$\begin{aligned}\mathcal{P}_2^{\perp} = \sum_{\boldsymbol{q}_1,\boldsymbol{q}_2} &\left(\left|\rho_1\rho_2\right\rangle - \frac{1}{\sqrt{N}}S_1S_2\left|\rho_{1+2}\right\rangle\right)\\ &\times\frac{S_1^{-1}S_2^{-1}}{2}\left(\left\langle\rho_1^*\rho_2^*\right| - \frac{1}{\sqrt{N}}S_1S_2\left\langle\rho_{1+2}^*\right|\right)\end{aligned} \tag{7.39}$$

where we have defined $\rho_1\equiv\rho(\boldsymbol{q}_1)$ and $S_1\equiv S(q_1)$ for convenience (note that the angular indices are dropped entirely since our system is passive). Before proceeding we emphasize that orthogonalizing the projection operator is crucial to obtain meaningful results. Using this projection we can then approximate

$$\omega^{\mathrm{eq}}_{\mathrm{int}}(k) \approx \frac{1}{N\zeta^2}\left\langle \sum_{i=1}^{N} \hat{\boldsymbol{k}}\cdot\boldsymbol{F}_i e^{-i\boldsymbol{k}\cdot\boldsymbol{r}_i}\ \mathcal{P}_2^{\perp} \sum_{j=1}^{N} \boldsymbol{F}_j\cdot\hat{\boldsymbol{k}} e^{i\boldsymbol{k}\cdot\boldsymbol{r}_j}\right\rangle, \tag{7.40}$$

which in turn can be evaluated to give (after taking the thermodynamic limit)

$$\begin{aligned}\omega^{\mathrm{eq}}_{\mathrm{int}}(k) = \frac{D_t^2\rho}{8\pi^2}\int & d\boldsymbol{q}S(q)S(|\boldsymbol{k}-\boldsymbol{q}|)\\ &\times\left[\hat{\boldsymbol{k}}\cdot\boldsymbol{q}\,c(q) + \hat{\boldsymbol{k}}\cdot(\boldsymbol{k}-\boldsymbol{q})\,c(|\boldsymbol{k}-\boldsymbol{q}|)\right]^2,\end{aligned} \tag{7.41}$$

and only depends on the structure factor $S(k)$ (and the relevant control parameters).

Eq. (7.41) can be numerically solved employing a standard scheme in MCT where the wavevector integral is rewritten in terms of q and $p=|\mathbf{k}-\mathbf{q}|$ [209]. We have extracted the solutions to this equation using structure factors obtained from density functional theory [196] ($\phi=0.6$) and from our simulations with $v_0=0$. The results are plotted for different wavenumber cutoffs k_{c} in Fig. 7.6. Interestingly, it can be seen

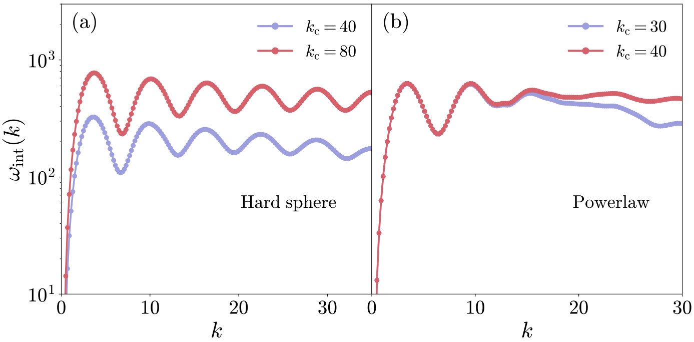

Figure 7.6: The passive-passive contribution to the velocity correlation function $\omega_{\rm int}(k)$ as a function of wavenumber k. The results are obtained by employing an orthogonalized projection on density doublets using (a) an analytical structure factor for monodisperse passive hard spheres at packing fraction $\phi = 0.6$ and (b) a structure factor measured from simulation data of a passive system at temperature $T = 1.0$ and packing fraction $\phi = 0.75$. The projection introduces an integral over k for which different cutoffs k_c have been chosen.

that the qualitative behavior is fully consistent with the results obtained directly from simulations (see dotted line in Fig. 7.4). We may also note that the results start to fall off for large wavenumbers if one chooses a cutoff that is too small. Finally, increasing the cutoff radius shifts the curves based on the analytical $S(k)$ whereas it is seen to have converged at small k for the simulation $S(k)$. This is likely a result of the hard sphere nature which should lead to diverging forces if one probes small enough length scales, that is, large enough k.

Chapter 8

Glassy dynamics in chiral fluids

Abstract. Chiral active matter is enjoying a rapid increase of interest, spurred by the rich variety of asymmetries that can be attained in e.g. the shape or self-propulsion mechanism of active particles. Though this has already led to the observance of so-called chiral crystals, active chiral glasses remain largely unexplored. A possible reason for this could be the naive expectation that interactions dominate the glassy dynamics and the details of the active motion become increasingly less relevant. In this chapter, we extend our previous modelling efforts and show that quite the opposite is true by studying the glassy dynamics of interacting chiral active Brownian particles (cABPs). We demonstrate that when our chiral fluid is pushed to glassy conditions, it exhibits highly nontrivial dynamics, especially compared to a standard linear active fluid such as common ABPs. Despite the added complexity, we are still able to present a full rationalization for all identified dynamical regimes. Most notably, we introduce a new 'hammering' mechanism, unique to rapidly spinning particles in high-density conditions, that can fluidize a chiral active solid.

The contents of this chapter are based on the following publication:
V.E. Debets, H. Löwen, and L.M.C. Janssen, *Phys. Rev. Lett.* 130, 058201 (2023)

8.1 Introduction

Active or self-propelled particle systems are intrinsically far from equilibrium, giving rise to a myriad of surprising features that are inaccessible to conventional passive matter. Well-known examples include motility induced phase separation (MIPS) [68, 70–72], accumulation around repulsive obstacles [75], spontaneous velocity alignment [53], and active turbulence [73, 74]. Interestingly, so-called linear swimmer models such as active Brownian particles (ABPs) [127–132], active Ornstein Uhlenbeck particles (AOUPs) [210], and run-and-tumble particles (RTPs) [124, 137] have already been remarkably successful in theoretically describing a significant number of these non-equilibrium features. Members of this class of particles are typically endowed with a constant (average) self-propulsion whose direction changes randomly via some form of rotational diffusion (often thermal fluctuations). However, due to for instance an asymmetric shape [211–213], mass distribution [214], or self-propulsion mechanism [215, 216], active particles also frequently self-rotate which is not included in the aformentioned models. This leads to chiral-symmetry breaking of the corresponding active motion and, at small enough densities, circular (2D) or helical trajectories (3D). A collection of these spinning particles is usually referred to as an active chiral fluid and has been shown to exhibit many interesting collective phenomena in both simulations and experiments [43, 64, 77, 213, 217–225]. Understanding the influence of chirality on active matter is therefore enjoying growing attention [226, 227], but at the same time requires more involved modelling efforts to fully comprehend.

Initial chiral active matter studies have focused primarily on the low to moderate density regime [133, 211, 216, 228, 229], but interest is now increasingly shifting towards high densities. This has already yielded several seminal works in the context of so-called chiral crystals [77, 81, 217, 230–233]. At the same time, their disordered counterpart, i.e., an active chiral glass, has received little attention. This might be attributed to the standard assumption of interactions impeding any form of active motion in the high density or glassy regime. As a result, the specific details of the active motion, whether chiral or nonchiral, should become of lesser importance upon approaching dynamical arrest. In this chapter, we demonstrate that this naive picture is too simplistic and that chiral active motion can certainly influence glassy dynamics in highly surprising ways. We, for the first time, delve into the unique physics that emerges when a chiral fluid ventures into the glassy regime. Most notably, we introduce a new 'hammering' mechanism (see Fig. 8.1), unique to rapidly spinning particles in high-density conditions, that can fluidize a chiral active solid.

In short, we explore the dynamics of interacting chiral active Brownian particles (cABPs) [133, 218] and show that when pushed to glassy conditions our chiral fluid exhibits highly nontrivial dynamics, particularly compared to standard linear active glassy matter (that is, conventional ABPs), which has already been extensively studied in theory [100–109] and simulation [48, 85, 91, 111–120]. Despite the added complexity, we are still able to present a full rationalization for all identified dynamical regimes, including the emergence of a complex reentrant behavior which we explain by invoking the aforementioned 'hammering' mechanism.

8.2 Simulation details

As our model chiral fluid we consider a two-dimensional (2D) Kob-Andersen mixture which consists of $N_\mathrm{A} = 650$ and $N_\mathrm{B} = 350$ self-propelling quasihard disks of type A and B, respectively. We assume that the self-propulsion dominates over thermal fluctuations so that we can neglect passive diffusion and the equation of motion for the position $\mathbf{r}_i$ of each particle i is given by [103]

$$\dot{\mathbf{r}}_i = \zeta^{-1}\mathbf{F}_i + \mathbf{v}_i. \tag{8.1}$$

Here, ζ represents the friction constant and $\mathbf{v}_i$ the self-propulsion velocity acting on particle i. The interaction force $\mathbf{F}_i = -\sum_{j\neq i} \nabla_i V_{\alpha\beta}(r_{ij})$ is obtained from a quasihard sphere power law potential $V_{\alpha\beta}(r) = 4\epsilon_{\alpha\beta}\left(\frac{\sigma_{\alpha\beta}}{r}\right)^{36}$ [156, 157] and the interaction parameters, i.e., $\epsilon_\mathrm{AA} = 1$, $\epsilon_\mathrm{AB} = 1.5$, $\epsilon_\mathrm{BB} = 0.5$, $\sigma_\mathrm{AA} = 1$, $\sigma_\mathrm{AB} = 0.8$, $\sigma_\mathrm{BB} = 0.88$, are, in combination with setting $\zeta = 1$, chosen to frustrate crystallization and allow for glassy behavior [37, 158]. The choice of parameters also implies that we use reduced units where σ_AA, ϵ_AA, $\epsilon_\mathrm{AA}/k_\mathrm{B}$, and $\zeta\sigma_\mathrm{AA}^2/\epsilon_\mathrm{AA}$ represent the units of length, energy, temperature, and time respectively [160]. For the self-propulsion of each particle we employ the cABP scheme [133, 218]. That is, the magnitude of the self-propulsion or active speed v_0 is assumed to remain constant in time t so that $\mathbf{v}_i = v_0\mathbf{e}_i = v_0[\cos(\theta_i), \sin(\theta_i)]$, while the orientation angle of the active velocity θ_i evolves in time according to

$$\dot{\theta}_i = \chi_i + \omega_\mathrm{s}, \tag{8.2}$$

with ω_s a constant spinning frequency, χ_i a Gaussian noise process with zero mean and variance $\langle\chi_i(t)\chi_j(t')\rangle_\mathrm{noise} = 2D_\mathrm{r}\delta_{ij}\delta(t-t')$, and D_r the rotational diffusion coefficient. As our control parameters we take ω_s, the persistence time $\tau_\mathrm{p} = D_\mathrm{r}^{-1}$, and a so-called spinning temperature $T_{\omega_\mathrm{s}} = v_0^2/2\omega_s$ which represents (up to a prefactor $4\pi\zeta$) a measure for the amount of energy that is dissipated by a single cABP during one circle motion.

Simulations are performed by solving the overdamped equation of motion [Eq. (8.1)] via a forward Euler scheme using LAMMPS [159]. We set the cutoff radius at $r_\mathrm{c} = 2.5\sigma_{\alpha\beta}$, fix the size of the periodic square simulation box to ensure that the number density equals $\rho = 1.2$, run the system sufficiently long (typically between 500 and 10000 time units) to prevent aging, and afterwards track the particles over time for at least twice the initialization time. To correct for diffusive center-of-mass motion all particle positions are retrieved relative to the momentary center of mass [160].

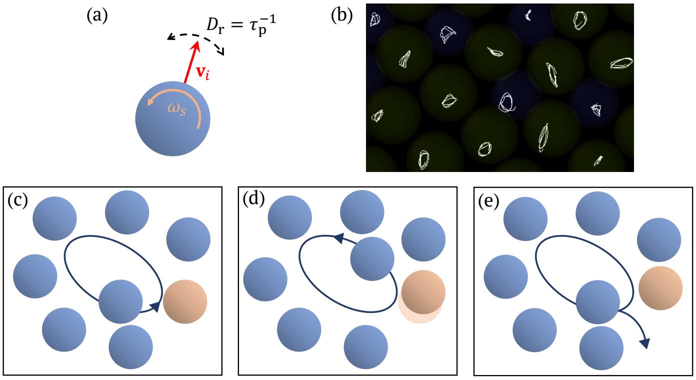

Figure 8.1: (a) Visualization of a chiral active Brownian particle (cABP). (b) Example short-time trajectories (total time is equal to three spinning periods) of cABPs at large spinning frequency and persistence exhibiting the 'hammering' effect by undergoing circular motion inside their cage of surrounding particles. (c-e) Schematic depiction of the 'hammering' effect. (c-d) For large enough persistence and spinning frequency, particles undergo back-and-forth motion inside their cage and systematically collide with the same particle whose motion is slightly altered by the collision. (e) After repeated collisions the cage of a particle is sufficiently remodelled such that the particle can break out and migrate through the material.

8.3 Nonmonotonic dynamics

We are primarily interested in characterizing how the interplay between rotational diffusion and spinning motion influences the active glassy dynamics. Therefore, we have calculated the long-time diffusion coefficient $D = \lim_{t\to\infty} \left\langle \Delta\mathbf{r}_i^2(t) \right\rangle / 4t$ of our chiral fluid for several set spinning frequencies $\omega_\mathrm{s} = 10, 100, 200$ (keeping a fixed value $T_{\omega_\mathrm{s}} = 4$ to ensure moderately supercooled behavior), while varying the persistence time. The results are plotted as a function of $\omega_\mathrm{s}\tau_\mathrm{p}$ in Fig. 8.2 and show remarkably rich dynamics. In particular, we find initial nonmonotonic behavior with a maximum at $\omega_\mathrm{s}\tau_\mathrm{p} \sim 1$. This is followed by a form of reentrant behavior which becomes much more pronounced for higher spinning frequencies. For example, at $\omega_\mathrm{s} = 200$ the diffusivity reaches a minimum with $D \sim 10^{-4}$, which is practically a frozen system like a glass, that is seen to increase with orders of magnitude. Finally, in the limit of large persistence different asymptotic values ranging from significantly enhanced to zero dynamics are reached. To contrast these complex dynamics, we emphasize that a glassy liquid of standard ABPs at constant active speed v_0 would only show a monotonic enhancement of the dynamics for increasing persistence time [85, 100]. Thus, at large densities chirality has a highly nontrivial impact on active particle motion.

Moreover, we have verified that the same qualitative behavior is observed for both a different model glassformer and a different set of parameters where we have fixed either the active speed v_0 or the spinning frequency ω_s instead of the spinning temperature T_{ω_s} (see Fig. 8.5). We also mention that the nontrivial change of the dynamics and in particular the reentrant behavior are equally visible in the static structure factor, the self- and collective intermediate scattering function, the non-Gaussian parameter, and the dynamical susceptibility (see Figs. 8.6 to 8.9). The latter two are measures for dynamical heterogeneity. The strong nonmonotonic behavior is thus a robust feature of the entire glassy phenomenology, but for convenience we continue to focus on the diffusivity.

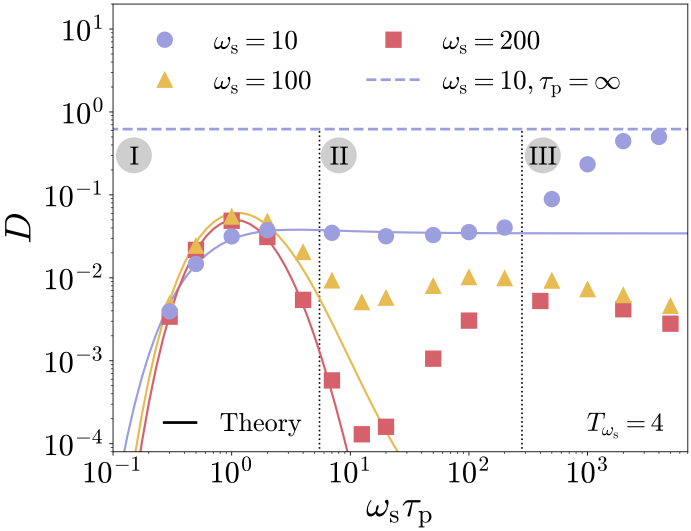

Figure 8.2: The long-time diffusion coefficient D as a function of the normalized persistence time $\omega_\mathrm{s}\tau_\mathrm{p}$ for several set values of ω_s keeping $T_{\omega_\mathrm{s}} = 4$ fixed. The resulting dynamics show highly non-trivial behavior that can be characterized by a nonmonotonic (I), reentrant (II), and large persistence (III) regime. The dashed line indicates the infinite persistence limit (from simulations) which is only nonzero for $\omega_\mathrm{s} = 10$.

8.4 cABP in a harmonic trap

Our aim now is to better understand the complex dynamics, which, for convenience, we will separate in three distinct regimes (see roman numerals in Fig. 8.2). We first turn our attention towards regime I. Here, the persistence of particles is still relatively weak and we therefore expect that especially in this regime the local environment of particles (or their cage) acts primarily as an effective confining potential. This then motivates a comparison of our simulation results to those of a single cABP in a harmonic trap of the form $U(r) = \kappa r^2/2$, with r the radial distance inside the trap and κ its strength. In particular, we have analytically derived an expression for the long-time limit of the MSD of such a trapped particle (see Section 8.C for details). This yields

$$\delta \equiv \lim_{t\to\infty} \left\langle \Delta\mathbf{r}^2(t) \right\rangle = \frac{v_0^2(1+\frac{\omega_\mathrm{k}}{\omega_\mathrm{s}\tau_\mathrm{p}})}{k^2[\omega_k^2+(1+\frac{\omega_k}{\omega_\mathrm{s}\tau_\mathrm{p}})^2]}, \tag{8.3}$$

where $k = \kappa/\zeta$, and we have introduced the dimensionless spinning frequencies $\omega_k = \omega_\mathrm{s}/k$ and $\omega_\mathrm{s}\tau_\mathrm{p}$. Due to the high-density (or glassy) conditions, we can then postulate that a particle escapes its trap when it reaches a distance equal to its diameter, that is, when $r = \sigma_\mathrm{AA}$. Assuming a Kramers-like process [234, 235], the corresponding average escape time is given by

$$t_\mathrm{esc} = t_0 e^{\frac{U(\sigma_\mathrm{AA})}{\langle U \rangle}} = t_0 e^{\frac{\sigma_\mathrm{AA}^2}{\delta}}, \tag{8.4}$$

with t_0 a constant prefactor and we have used that the average potential energy of the particle (which serves as our effective temperature) is equal to $\langle U \rangle = \kappa\delta/2$ [235]. Moreover, we assume that after each escape the particle falls into a new trap with the same properties. In other words, the particle diffuses through space by hopping from trap to trap (or equivalently cage to cage). This allows us to quantitatively estimate the long-time diffusion coefficient as $D \approx \sigma_\mathrm{AA}^2/4t_\mathrm{esc}$, which can be compared to our simulation results. Note that the qualitative behavior of our theoretically predicted D is thus fully determined by a single fit parameter k, while the absolute scale is set by the other fit parameter t_0.

The resulting theoretical predictions (fitted on the first five data points) are shown as straight lines in Fig. 8.2. Remarkably, we find almost quantitative agreement in regime I and approximately the same fit value of $k \sim 10$ for all our settings (the latter is consistent with the fact that we do not change the density or interaction potential which supposedly determine this factor). This demonstrates that the interplay between rotational diffusion and spinning motion in the small persistence regime are well captured by our simple single particle model.

8.5 Collective motion

Inspired by previous work in literature [219] we now proceed to regime III. Here, we observe a sudden increase of the diffusivity towards the infinite persistence limit for relatively small spinning frequencies ($\omega_\mathrm{s} = 10$). For larger spinning frequencies, we instead see D decreasing and probably moving towards the infinite persistence limit of $D = 0$ (see Fig. 8.10). Thus, for $\tau_\mathrm{p} \to \infty$ there exists a transition from a so-called active ($D > 0$) to an absorbing ($D = 0$) state upon increasing ω_s. This behavior is fully consistent with previous work conducted at lower densities [219]. Our work shows that this phenomenology is retained in the high density or glassy regime.

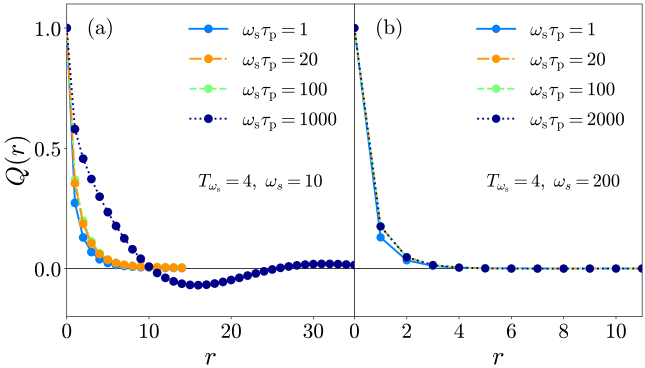

Figure 8.3: The spatial velocity correlation function $Q(r)$ as a function of the distance r. (a) At small enough spinning frequencies ($\omega_\mathrm{s} = 10$) we observe a sudden increase of spatial velocity correlations in the limit of large persistence ($\omega_\mathrm{s}\tau_\mathrm{p} = 1000$). This increase is accompanied by a similar increase of the diffusivity (see Fig. 8.2) and a negative peak indicating vortex-like behavior. (b) In comparison, when particles spin too rapidly ($\omega_\mathrm{s} = 200$) velocity correlations remain short-ranged and almost independent of persistence.

To explain why at small enough ω_s, that is, $\omega_\mathrm{s} = 10$, the diffusivity increases significantly in regime III, we employ a spatial velocity correlation function $Q(r)$ (see [132] for a precise definition). This function measures how correlated the velocities $\dot{\mathbf{r}}_i$ of different particles i are over a distance r. It thus serves as a proxy for local velocity alignment and cooperative motion ($Q(r) = 1, 0, -1$ for perfect, no, and anti velocity alignment respectively). We have plotted $Q(r)$ for $\omega_\mathrm{s} = 10$ and several values of $\omega_\mathrm{s}\tau_\mathrm{p}$ in Fig. 8.3a. In almost all cases we see a similar rapid decay to zero implying that there exists little velocity alignment and cooperative motion is absent. However, at exactly the same point where the diffusivity has increased in regime III, i.e., $\omega_\mathrm{s}\tau_\mathrm{p} = 1000$, we find that the decay of $Q(r)$ suddenly becomes much more long-ranged and even develops a negative peak (both features have been checked for finite-size effects). We interpret this as the particle motion becoming more collective and vortex-like (see Fig. 8.11 for representative velocity fields) which explains why its overall diffusion is enhanced. Moreover, note that this collective motion is only able to emerge when the amount of rotational diffusion is small enough, that is, when we are at a large enough τ_p.

In comparison, for $\omega_\mathrm{s} = 200$ we find almost no spatial velocity correlations for any value of $\omega_\mathrm{s}\tau_\mathrm{p}$ (see Fig. 8.3b), which implies that no cooperative motion takes places. We expect that this is caused by particles spinning too rapidly which prevents them from inducing any collective motion, even in the absence of rotational diffusion ($\tau_\mathrm{p} \to \infty$). Ultimately, this should lead to particles becoming trapped in circular/elliptical trajectories inside their cage, thus explaining why D goes to zero.

8.6 Hammering dynamics

We finalize our discussion by considering the intermediate persistence regime II. Interestingly, in this regime the agreement between theory and simulation only remains intact for a relatively small spinning frequency ($\omega_\mathrm{s} = 10$, see Fig. 8.2). In comparison, for larger spinning frequencies a competing mechanism emerges which is able to increase the long-time diffusivity from an almost glassy or dynamically arrested state ($D \sim 10^{-4}$) with multiple orders of magnitude. We have checked that this reentrant behavior becomes even more extreme for larger values of ω_s. The key question therefore is, what causes the dynamics to be dramatically faster if it is not cooperative diffusion (since there are almost no spatial velocity correlations, see Fig. 8.3b). To answer this we propose a new 'hammering' mechanism that is distinct for rapidly spinning chiral particles at large densities (see Fig. 8.1c-e for a schematic depiction). In short, for large enough persistence and spinning frequency, particles are expected to undergo long periods of uninterrupted back-and-forth motion inside their cage. During this they systematically collide with the same particle whose motion is slightly altered by each collision. After repeated collisions the cage of a particle is sufficiently remodelled such that the particle can break out and migrate through the material which should lead to faster dynamics.

In order to verify and explain the mechanism in more detail, we will now exclusively focus on the data obtained for $\omega_\mathrm{s} = 200$, $T_{\omega_\mathrm{s}} = 4$ (the red squares in Fig. 8.2), where the 'hammering' effect is strongest. We start by introducing the spinning radius $R = v_0/\omega_\mathrm{s}$ which in this case is smaller than a particle radius, i.e., $R = 0.2$. If the persistence time is then also larger than the spinning period $\tau_\omega = 2\pi/\omega_\mathrm{s}$ ($\tau_\mathrm{p} > \tau_\omega$ or $\omega_\mathrm{s}\tau_\mathrm{p} > 2\pi$), particles should be able to undergo full circular/elliptical motion inside their cage. This can be clearly seen when inspecting multiple short-time particle trajectories (see Fig. 8.1b and Fig. 8.12). To also quantify the periodic motion, we have extracted the normalized velocity autocorrelation function $C_{vv}(t) = \langle \dot{\mathbf{r}}_i(0) \cdot \dot{\mathbf{r}}_i(t) \rangle / \langle \dot{\mathbf{r}}_i^2 \rangle$ for a subset of $\omega_\mathrm{s}\tau_\mathrm{p}$ values and plotted them in Fig. 8.4a. In accordance with the more circular trajectories, we observe the emergence of oscillations, which roughly start when $\omega_\mathrm{s}\tau_\mathrm{p} \gtrsim 2\pi$ and become longer lived for increasing persistence.

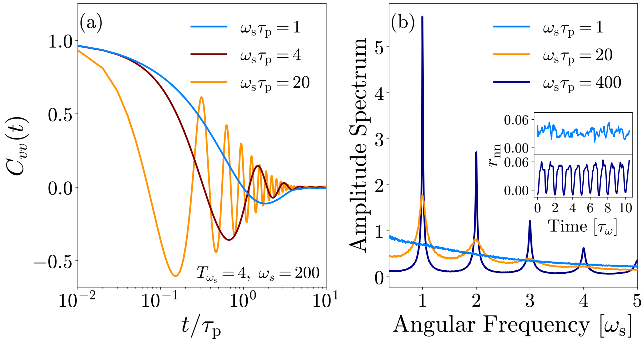

Figure 8.4: (a) The velocity autocorrelation function $C_{vv}(t)$ as a function of time t at $\omega_\mathrm{s} = 200$. As $\omega_\mathrm{s}\tau_\mathrm{p} > 1$ we see the emergence of oscillations which correspond to more circular particle motion inside the cage. (b) Amplitude spectrum of the nearest-neighbor distance $r_\mathrm{nn}(t)$ for several values of $\omega_\mathrm{s}\tau_\mathrm{p}$. Starting from $\omega_\mathrm{s}\tau_\mathrm{p} \sim 20$, i.e., the minimum in Fig. 8.2, the spectrum begins to peak at ω_s (and its multiples). This corresponds to particles periodically colliding with the same particle inside their cage. The appearance of this 'hammering' effect is especially visible in the inset where $r_\mathrm{nn}(t)$ for two example particles at $\omega_\mathrm{s}\tau_\mathrm{p} = 1$ and 400 are plotted.

Having established that particles increasingly go in circles inside their cage, we also want to show that this is indeed accompanied by systematic collisions with one (or multiple) of its surrounding particles. For this reason we have, based on short-time trajectories, extracted the nearest neighbor distance for a given particle i, $r_\mathrm{nn}(t) = \min\{|\mathbf{r}_i(t) - \mathbf{r}_j(t)|\}_{j\neq i}$, as a function of time. Two of these have been plotted as an inset in Fig. 8.4b and confirm the notion of repeated collisions. Specifically, for $\omega_\mathrm{s}\tau_\mathrm{p} = 1$, i.e., $\tau_\mathrm{p} < \tau_\omega$, the nearest neighbor distance appears to be completely random, that is, the particle undergoes random collisions with all neighboring particles. For $\omega_\mathrm{s}\tau_\mathrm{p} = 400$, i.e., $\tau_\mathrm{p} \gg \tau_\omega$, the nearest neighbor distance is instead very periodic indicating that the particle collides, moves away, collides again, and so on. We have verified that these collisions are with the same neighboring particle. To check that this behavior occurs throughout our material we have also calculated the spectrum of $r_\mathrm{nn}(t)$ for all particles (see Fig. 8.4b). We see that, starting from $\omega_\mathrm{s}\tau_\mathrm{p} \sim 20$ (the minimum in Fig. 8.2) the spectrum begins to peak at ω_s (and its multiples), thus further corroborating the idea of particles periodically colliding.

Overall, these results show that a 'hammering' mechanism is indeed present in our active chiral fluid and is likely to be responsible for the observed enhanced dynamics in regime II. Moreover, it also explains why the minimum of the dynamics is roughly at $\tau_\mathrm{p} \sim 2\tau_\omega$ since only from this point onward are particles able to, on average, make multiple systematic collisions with the same neighboring particle and start capitalizing on the 'hammering' effect.

8.7 Conclusions

To conclude, our work demonstrates that chiral glassy fluids exhibit a remarkably rich dynamical phenomenology (especially when contrasted with their nonchiral counterpart [85, 100]) that can be characterized by a nonmonotonic (I), reentrant (II), and large persistence (III) regime. We have shown how the initial behavior (I) is fully explained by treating the surroundings of a particle as a harmonic trap and considering cage hopping of a single cABP between such traps. In the limit of extremely weak rotational diffusion (III), we have observed either speeding up or slowing down of the dynamics which is related to the (in)ability of particles to align their respective velocities and induce collective swirling-like motion. Finally, to rationalize the surprising (but for large spinning frequencies highly significant) reentrant behavior (II), we have introduced and demonstrated the existence of a new 'hammering' mechanism that is distinct for rapidly spinning particles at high densities. Overall, our results pay testimony to the fact that chirality (already in its simplest form) gives rise to a plethora of nontrivial behavior, even in the glassy limit where interactions usually dominate dynamics. It would be interesting to see whether these regimes and specifically the 'hammering' mechanism can also be observed for so-called spinners where active motion is induced via rotational couplings [43] or if it can possibly be exploited in an experimental setting involving for instance active granular rotors or colloids. For the latter one might also have to consider the role of translational diffusion, which could hinder collective motion or disrupt circular motion inside the cage. Alternatively, one can think of chiral active probe particles possibly utilizing the 'hammering' effect to help extract material properties or navigate through a soft dense environment such as gels [167, 236–239].

Appendix

8.A Long-time diffusion coefficient at fixed active speed or spinning frequency

Throughout this chapter we have kept the spinning temperature $T_{\omega_\mathrm{s}} = v_0^2/2\omega_\mathrm{s}$ constant and compared several spinning frequencies. For completeness, we have also included two plots which illustrate that the nonmonotonic dynamics of D is also observed when instead fixing the active speed v_0 or the spinning frequency ω_s [see Fig. 8.5]. Moreover, at larger self-propulsion and thus when the spinning radius $R = v_0/\omega_\mathrm{s}$ exceeds a particle diameter we observe that, though the diffusivity becomes much larger, the qualitative behavior remains unaltered when compared to data at $R = 0.9$ ($v_0 = 9.0$, $\omega_\mathrm{s} = 10.0$) [see Fig. 8.5(b)].

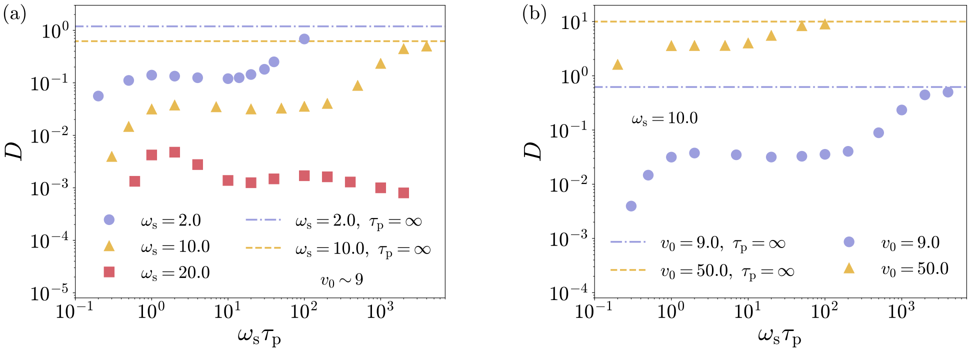

Figure 8.5: The long-time diffusion coefficient D as a function of the normalized persistence time $\omega_\mathrm{s}\tau_\mathrm{p}$ for several set values of (a) ω_s keeping the active speed $v_0 \sim 9.0$ fixed and (b) v_0 with a constant spinning frequency $\omega_\mathrm{s} = 10.0$. The resulting dynamics show nonmonotonic behavior. In both figures the dashed and dashed-dotted lines indicate the nonzero infinite persistence limits which are also obtained from simulations.

8.B Glassy features

To better understand the glassy dynamics of our model chiral fluid we, in this chapter, focus primarily on the long-time diffusion coefficient D which has been extracted from the corresponding mean square displacements (MSDs). In the context of glassy matter, this is in some cases insufficient as the glassy phenomenology can also manifest itself in, e.g., the structure, structural relaxation, and heterogeneous dynamics. These features are not fully captured by D, which is mostly used to characterize the slowdown of the dynamics that accompanies the glass transition. To address the above mentioned features, we have also calculated and plotted the static structure factor, the self- and collective intermediate scattering functions, the non-Gaussian parameter, and the dynamical susceptibility (see Figs. 8.6 to 8.9 respectively). Interestingly, all these parameters show the exact same nonmonotonic behavior as the long-time diffusion coefficient shown in Fig. 8.2. We have therefore chosen to focus solely on D throughout the chapter, but emphasize that the proposed explanation is also responsible for these other glassy features.

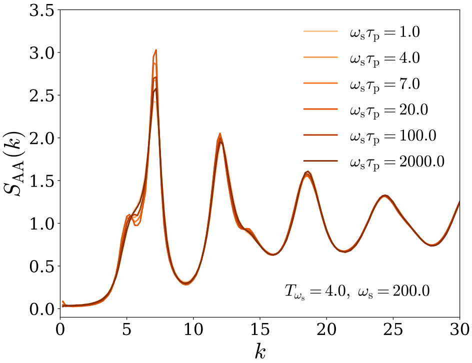

Figure 8.6: The static structure factor of the majority A species $S_\mathrm{AA}(k) = \left\langle \sum_{j=1}^{N_\mathrm{A}} e^{-i\mathbf{k}\cdot\mathbf{r}_j} \sum_{l=1}^{N_\mathrm{A}} e^{i\mathbf{k}\cdot\mathbf{r}_l} \right\rangle$ as a function of the wavenumber k for different $\omega_\mathrm{s}\tau_\mathrm{p}$ keeping the spinning frequency $\omega_\mathrm{s} = 200.0$ and the spinning temperature $T_{\omega_\mathrm{s}} = 4.0$ fixed. It can be seen that the height of the first peak, which can be used as a proxy for glassiness [112], shows nonmonotonic behavior. This is in accordance with the dynamics shown in Fig. 8.2. In addition, the nonmonotonic behavior is also visible in the shoulder of the first peak which is most apparent when the dynamics is slowest, i.e., $\omega_\mathrm{s}\tau_\mathrm{p} = 20.0$.

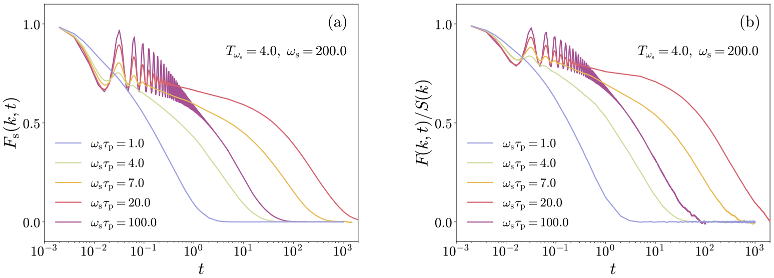

Figure 8.7: The self-intermediate scattering function of the majority A species $F_\mathrm{s}(k,t) = \left\langle e^{-i\mathbf{k}\cdot\mathbf{r}_j(0)} e^{i\mathbf{k}\cdot\mathbf{r}_j(t)} \right\rangle$ as a function of time t for different $\omega_\mathrm{s}\tau_\mathrm{p}$ keeping the spinning frequency $\omega_\mathrm{s} = 200.0$ and the spinning temperature $T_{\omega_\mathrm{s}} = 4.0$ fixed. The wavenumber k corresponds to the main peak of the structure factor shown in Fig. 8.6. We observe that the relaxation time of $F_\mathrm{s}(k,t)$ exhibits nonmonotonic behavior and is longest when $\omega_\mathrm{s}\tau_\mathrm{p} = 20.0$ which is consistent with the results for the long-time diffusion coefficient D shown in Fig. 8.2.

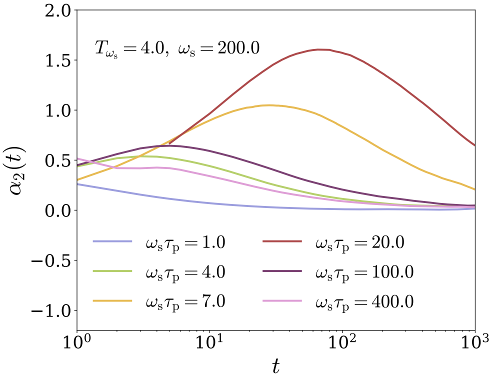

Figure 8.8: The non-Gaussian parameter $\alpha_2(t) = \left\langle \Delta\mathbf{r}_i^4 \right\rangle / 2 \left\langle \Delta\mathbf{r}_i^2 \right\rangle^2 - 1$ as a function of time t for different $\omega_s\tau_p$ keeping the spinning frequency $\omega_s = 200.0$ and the spinning temperature $T_{\omega_s} = 4.0$ fixed. The height of the peak in $\alpha_2(t)$ is an indicator for dynamical heterogeneity, while a value of zero corresponds to diffusive motion. The qualitative behavior of the dynamics (see Fig. 8.2) is mirrored in the peak height of $\alpha_2(t)$ with the slowest dynamics yielding the most heterogeneous motion.

8.C MSD of a cABP in a harmonic trap

Our aim is to derive an expression for the mean square displacement (MSD) of a 2D athermal chiral active Brownian particle (cABP) which resides in a harmonic potential of the form $U(r) = \kappa\mathbf{r}^2/2$. The time-evolution of such a particle's position $\mathbf{r}$ is described by

$$\dot{\mathbf{r}} = -k\mathbf{r} + v_0\mathbf{e}, \tag{8.5}$$

where v_0 is the active speed and $k = \zeta^{-1}\kappa$ is an inverse time scale associated with the strength of the harmonic trap κ and the friction coefficient ζ. The direction of the active velocity is governed by the unit vector $\mathbf{e} = [\cos(\theta), \sin(\theta)]$ whose orientation angle θ evolves in time according to

$$\dot{\theta} = \chi + \omega_s, \tag{8.6}$$

with ω_s a constant spinning frequency, χ_i a Gaussian noise process with zero mean and variance $\langle \chi(t)\chi(t') \rangle_{\text{noise}} = 2D_r\delta(t - t')$, and D_r the rotational diffusion coefficient.

We proceed by following the same strategy as has been previously employed to extract moments of a nonchiral ($\omega_s = 0$) ABP in a harmonic trap [240]. Alternatively, we mention that a more general form of the posed problem has already been solved previously, though using a seemingly different method [241]. Based on the equations of motion

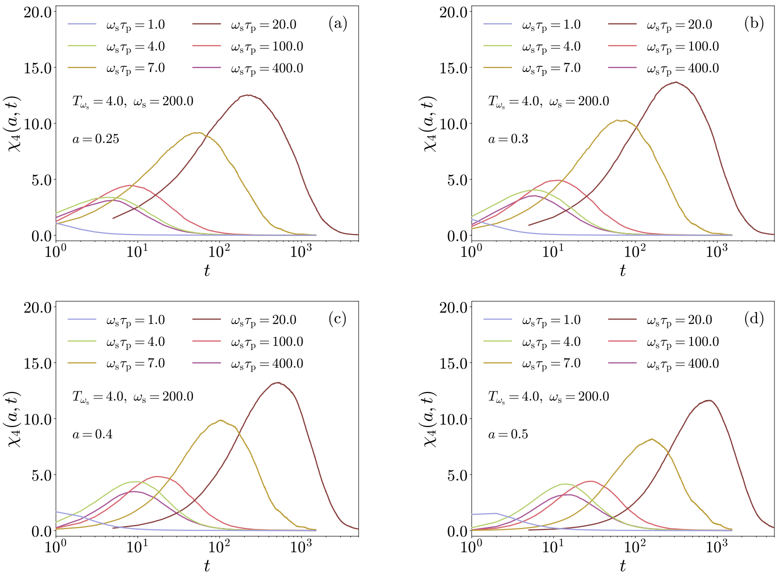

Figure 8.9: The dynamical susceptibility $\chi_4(a,t) = N_\mathrm{A}\left[\left\langle Q^2(t)\right\rangle - \left\langle Q(t)\right\rangle^2\right]$ as a function of time t for different $\omega_\mathrm{s}\tau_\mathrm{p}$ keeping the spinning frequency $\omega_\mathrm{s} = 200.0$ and the spinning temperature $T_{\omega_\mathrm{s}} = 4.0$ fixed. Results (a-d) correspond to different length scales a close to the typical cage size which have been used for the overlap function $Q(t) = N_\mathrm{A}^{-1}\sum_j \Theta(a - |\mathbf{r}_j(t) - \mathbf{r}_j(0)|)$ (with $\Theta(x)$ the Heaviside step function). The height of the peak in $\chi_4(a,t)$ is an indicator for dynamical heterogeneity and cooperative relaxation. The qualitative behavior of the dynamics (see Fig. 8.2) is mirrored in the peak height of $\chi_4(a,t)$ with the slowest dynamics yielding the most heterogeneous motion.

one can derive a Fokker-Planck equation for the probability distribution $P(\mathbf{r},\theta,t)$:

$$\frac{\partial P}{\partial t} = [k\mathbf{r} - v_0\mathbf{e}]\cdot\nabla P + 2kP + D_\mathrm{r}\frac{\partial^2}{\partial\theta^2}P - \omega_\mathrm{s}\frac{\partial}{\partial\theta}P, \tag{8.7}$$

which we in turn can convert to the Laplace domain to yield

$$-P_0 + (s-2k)\tilde{P} = [k\mathbf{r} - v_0\mathbf{e}]\cdot\nabla\tilde{P} + 2k\tilde{P} + D_\mathrm{r}\frac{\partial^2}{\partial\theta^2}\tilde{P} - \omega_\mathrm{s}\frac{\partial}{\partial\theta}\tilde{P}, \tag{8.8}$$

where $\tilde{P}(\mathbf{r},\theta,s) = \int dte^{-st}P(\mathbf{r},\theta,t)$ and $P_0 = P(\mathbf{r},\theta,0)$. If we then multiply the above equation with an arbitrary observable $\psi(\mathbf{r},\theta)$ and integrate over the configuration space $(\mathbf{r},\theta)$, we arrive at an equation of motion for $\langle\psi\rangle_s$, i.e., the mean of the observable in

Laplace space, given by

$$-\left\langle\psi\right\rangle_0+(s-2k)\left\langle\psi\right\rangle_s=v_0\left\langle\mathbf{e}\cdot\nabla\psi\right\rangle_s-k\left\langle\nabla\cdot(\mathbf{r}\psi)\right\rangle_s+D_\mathrm{r}\left\langle\frac{\partial^2}{\partial\theta^2}\psi\right\rangle_s+\omega_\mathrm{s}\left\langle\frac{\partial}{\partial\theta}\psi\right\rangle_s.\quad(8.9)$$

Here, we have introduced the mean in Laplace space as $\left\langle\ldots\right\rangle_s=\int d\mathbf{r}d\theta\ldots\tilde{P}(\mathbf{r},\theta,s)$ and an average over the initial conditions via $\left\langle\ldots\right\rangle_0=\int d\mathbf{r}d\theta\ldots P(\mathbf{r},\theta,0)$.

Letting our particle start in the center of the trap with a random orientation, i.e., $P(\mathbf{r},\theta,0)=(2\pi)^{-1}\delta(\mathbf{r})$, we seek to extract the MSD by choosing $\psi=\mathbf{r}^2$. Filling this into Eq. (8.9) we obtain

$$\left\langle\mathbf{r}^2\right\rangle_s=\frac{2v_0}{s+2k}\left\langle\mathbf{e}\cdot\mathbf{r}\right\rangle_s.\quad(8.10)$$

We continue by considering $\psi=\mathbf{e}\cdot\mathbf{r}$. Using Eq. (8.9) we find

$$\left\langle\mathbf{e}\cdot\mathbf{r}\right\rangle_s(s+k+D_\mathrm{r})=\frac{v_0}{s}+\omega_\mathrm{s}\left\langle\mathbf{e}_\perp\cdot\mathbf{r}\right\rangle_s\quad(8.11)$$

where $\mathbf{e}_\perp=[-\sin(\theta),\cos(\theta)]$. Alternatively, we may choose $\psi=\mathbf{e}_\perp\cdot\mathbf{r}$ which yields

$$\left\langle\mathbf{e}_\perp\cdot\mathbf{r}\right\rangle_s(s+k+D_\mathrm{r})=-\omega_\mathrm{s}\left\langle\mathbf{e}\cdot\mathbf{r}\right\rangle_s.\quad(8.12)$$

Combining Eqs. (8.10) to (8.12) we arrive at

$$\left\langle\mathbf{r}^2\right\rangle_s=\frac{2v_0^2(s+k+D_\mathrm{r})}{s(s+2k)[(s+k+D_\mathrm{r})^2+\omega_\mathrm{s}^2]}.\quad(8.13)$$

Converting back to the time domain then gives our final result for the MSD

$$\begin{aligned}\left\langle\mathbf{r}^2(t)\right\rangle=&\frac{v_0^2}{k\left[(k-D_\mathrm{r})^2+\omega_\mathrm{s}^2\right]\left[(k+D_\mathrm{r})^2+\omega_\mathrm{s}^2\right]}\times\Big[(k+D_\mathrm{r})[(k-D_\mathrm{r})^2+\omega_\mathrm{s}^2]+e^{-2kt}(k-D_\mathrm{r})\\&\times[(k+D_\mathrm{r})^2+\omega_\mathrm{s}^2]-2e^{-(k+D_\mathrm{r})t}k[(k^2-D_\mathrm{r}^2+\omega_\mathrm{s}^2)\cos(\omega_\mathrm{s}t)+2D_\mathrm{r}\omega_\mathrm{s}\sin(\omega_\mathrm{s}t)]\Big].\end{aligned}\quad(8.14)$$

This result can in part be verified by taking the limit of either zero spinning frequency ($\omega_\mathrm{s}\to0$) or no confining potential ($k\to0$). In both cases we find that our expression correctly reduces to previously obtained results for ABPs in a harmonic potential and non-interacting chiral ABPs respectively [123, 133, 240].

Finally, the long-time limit of Eq. (8.14) gives

$$\lim_{t\to\infty}\left\langle\mathbf{r}^2(t)\right\rangle=\frac{v_0^2(k+D_\mathrm{r})}{k[(k+D_\mathrm{r})^2+\omega_\mathrm{s}^2]}=\frac{v_0^2(1+\frac{\omega_k}{\omega_\mathrm{r}})}{k^2[\omega_k^2+(1+\frac{\omega_k}{\omega_\mathrm{r}})^2]},\quad(8.15)$$

and corresponds to Eq. (8.3). Note that, for convenience, we have rewritten it in terms of the dimensionless ratios $\omega_k=\omega_\mathrm{s}/k$ and $\omega_\mathrm{r}=\omega_\mathrm{s}/D_\mathrm{r}=\omega_\mathrm{s}\tau_\mathrm{p}$ (with $\tau_\mathrm{p}=D_\mathrm{r}^{-1}$).

We conclude by mentioning that the above derivation can rather straightforwardly be extended to also include thermal diffusive motion. This, however, only adds a constant term to Eq. (8.15) and thus does not change its qualitative behavior or the implications discussed in the main text.

8.D Additional data

In this section we present multiple figures that serve to complement several of the claims made throughout this chapter. In particular, Fig. 8.10 demonstrates that at infinite persistence a dynamic transition exists upon increasing the spinning frequency, Fig. 8.11 illustrates the emergence of collective motion in the velocity field as the particle persistence is increased, and Fig. 8.12 shows example short-time trajectories which become more circular for larger values of $\omega_\mathrm{s}\tau_\mathrm{p}$.

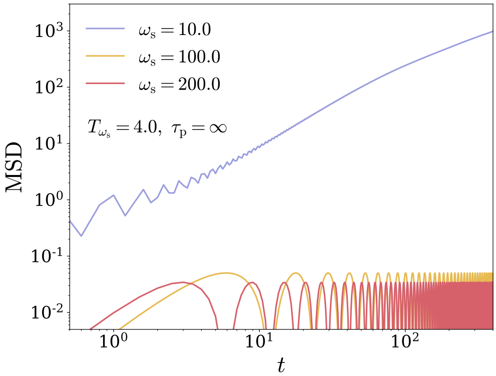

Figure 8.10: Mean square displacement (MSD) as a function of time t for different values of the spinning frequency ω_s in the limit of infinite persistence $\tau_\mathrm{p} \to \infty$ (or zero rotational diffusion). When the spinning frequency is small enough ($\omega_\mathrm{s} = 10.0$), the long-time dynamics becomes diffusive, whereas for larger spinning frequencies ($\omega_\mathrm{s} = 100.0, 200.0$), the MSD oscillates around a plateau indicating caged circular motion.

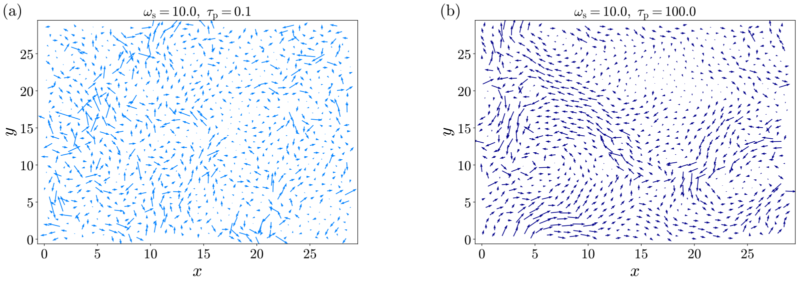

Figure 8.11: Example velocity fields of our chiral fluid at (a) $\tau_p = 0.1$ and (b) $\tau_p = 100.0$ keeping the spinning frequency $\omega_s = 10.0$ and the spinning temperature $T_{\omega_s} = 4.0$ fixed. For larger persistence the motion can be seen to become more collective and vortex-like.

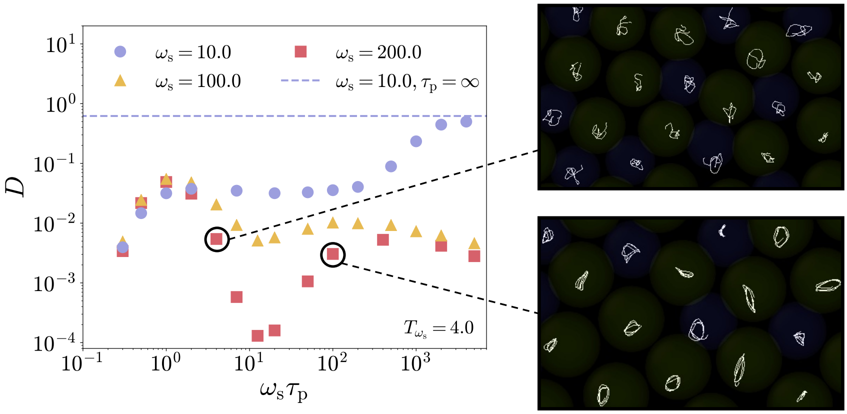

Figure 8.12: Plot of the long-time diffusion coefficient D as a function of the normalized persistence time $\omega_s\tau_p$, which is also shown in Fig. 8.2. We highlight a number of short-time trajectories (total time is equal to three spinning periods $3\tau_\omega$) for the two circled data points. It can be seen that for $\omega_s\tau_p = 4.0$ (or $\tau_p \sim \tau_\omega$) the trajectories show small signs of circular motion. In comparison, for $\omega_s\tau_p = 100.0$ (or $\tau_p \gg \tau_\omega$) the circular motion inside the cage becomes very pronounced.

Chapter 9

Conclusions and outlook

Abstract. The main objective of this thesis has been to provide fundamental insights into glassy active matter, which we hope can serve as a basis for more realistic and complex dense active materials in both the biological and synthetic realm. In this chapter, we briefly reiterate our main findings regarding this objective, after which we try to place them in a broader context and discuss potential avenues for future directions of research.

9.1 Conclusions

At the end of Chapter 1 we have laid out the overarching goal of this thesis, i.e., to uncover fundamental insight into the nature of active glassy matter. Let us therefore briefly recapitulate our main findings and discuss how they relate to this stated objective.

The first question we have addressed is the possible existence of universal governing principles in dense active matter. Indeed, it is not a priori obvious that certain universal behavior should exist at all when transitioning from dense passive to active matter. This seemed further exemplified by initial studies reporting different conflicting results – ranging from a monotonic speedup or slowdown of the dynamics to even nonmonotonic changes upon increased activity. In Chapter 3, we have fully rationalized these seemingly contradictory findings by identifying the ratio of the short-time active length scale to the cage length as a crucial control parameter for dense thermal and athermal active matter. This insight is further substantiated in Chapter 4 where we have shown it to also be robust upon supercooling and to changes in the range and softness of the particle-particle interaction potential. Moreover, we have demonstrated that the cage length marks the critical threshold beyond which active glassy matter becomes qualitatively distinct from its equivalent Brownian counterpart. This has been marked by changes in the Stokes-Einstein relation and the fragility. Despite being intrinsically out of equilibrium, we have thus identified the existence of universal behavior in active glassy matter.

In Chapter 5, we have developed a generic, that is, without specifying the details of self-propulsion, active mode-coupling theory (MCT) for mixtures of athermal self-propelled particles. The theory has been numerically solved for 3D ABPs and gives qualitatively consistent predictions of the dynamics based solely static input parameters. Importantly, the input requires not only the static structure factor but also naturally includes nontrivial velocity correlations that therefore clearly impact active glassy dynamics, which further establishes their importance in dense active matter.

In Chapter 6, we have also derived an active MCT for dense systems of thermal AOUPs and 3D ABPs that instead explicitly considers the active degrees of freedom. Solving for both model systems, we have demonstrated that the intermediate scattering function is almost identical for a wide variety of control parameters. The microscopic details of these model systems thus do not alter the active glassy behavior which reveals additional universal behavior and is fully consistent with passive glassy fluids. This may also carry notable importance in the biological realm where details of the underlying self-propulsion mechanism are typically difficult to extract.

To delve deeper into the nature of spatial velocity correlations, we have presented a fully microscopic method to calculate nonequilibrium correlations for a dense active fluid in Chapter 7. Based on this approach, we have analytically calculated qualitatively consistent static structure factors and active velocity correlations for dense active fluids.

Interestingly, this has required only a passive reference structure factor as input and thus uncovers an interesting connection between structure and such velocity correlations. We have also characterized the disruptive role thermal motion has on velocity correlations by means of simulations and shown the existence of long-ranged active velocity correlations that were previously thought to be absent.

To anticipate the rich diversity of asymmetries in, e.g., the shape or self-propulsion mechanism of active particles, we have explored chiral motion (or circle swimming) as a novel extension of standard active glassy model systems. We have demonstrated in Chapter 8 that model chiral glassy fluids exhibit a remarkably rich dynamical phenomenology, especially when contrasted with their usually considered nonchiral counterparts. We have fully rationalized all identified dynamical regimes, most notably, a strong reentrant one where the chiral fluid rapidly transitions from a glass-like to a liquid state. Chirality thus has an interesting influence on active glassy dynamics and provides a potential different pathway of controlling the viscosity of an active fluid.

9.2 Outlook

The entire field of dense active matter and its relation to conventional glassy (or amorphous) materials is only just emerging. With clear connections to biology in both health and disease, and increasing synthetic realizations that hold great promise for tunable materials, it is likely to retain an important role in biophysical and soft matter research for the foreseeable future. Many potential avenues for further research await and we finalize by discussing several suggestions.

In a biological context, tissue fluidity has been directly linked to pathology, especially in relation to cancer and asthma [92–96]. Extracting dynamical information in such a situation is, however, challenging and ideally one wants to already infer the dynamics based on a single snapshot of the cell collective, i.e., a scan. For such a single image to be truly predictive one has to understand how important velocity correlations are for the large scale glassy behavior, since these cannot be obtained directly from a snapshot. Alternatively, do there perhaps exist more intricate structural features that can reveal the existence of these correlations already from a static image? Machine learning approaches might also proof to be a useful tool to explore these questions [19, 20].

It has recently been recognized that the cell nucleus plays an important role in tissue fluidity of a carcinoma [96]. At the same time, conventional modelling efforts of cell collectives such as Voronoi, vertex, and cellular Potts models [48, 242–244] typically do not differentiate between the nucleus and the cytoplasm despite these having highly different properties. The nucleus is for instance much stiffer which in principle can have a dominant effect on glassy dynamics. It would therefore be interesting to extend existing model systems to incorporate this effect. In particular, for a confluent cell layer a cage length as highlighted in this thesis would in principle be zero, but for a cell nucleus it could instead have a finite value.

In this thesis we have mostly considered particles that are homogeneous regarding their active properties. Tumors are, however, known to be mostly heterogeneous consisting of both motile and dormant cells [96]. This raises the question whether the tumor's transition from a rigid to a fluid state is induced by a relatively small fraction of very motile cells or whether it occurs throughout the entire cell collective. Moreover, do these two scenarios lead to different glassy dynamics? Understanding the influence of heterogeneity in particle activity on glassy dynamics is thus a natural direction for followup work.

In comparison to the predominantly overdamped conditions in biology, synthetic active glasses made using granular particles experience underdamped conditions and constitute so-called microflyers [55, 123]. In principle, these thus require different model systems than the overdamped ones that have been used in this thesis. For passive materials interchanging Brownian with Newtonian dynamics has no influence on the long-time glassy behavior due to the strong impact of particle-particle interactions. Whether or when this is also true for active particles remains to be fully established.

A possible reason for the difficulty of making colloidal active glasses can lie in ensuring a stable self-propulsion mechanism at high densities. For example, mechanisms for Janus colloids based on local gradients in temperature or concentration can become compromised if particles become increasingly more surrounded by other particles and these gradients start to overlap. Such problems can perhaps be avoided when employing self-rotating particles instead of self-propelling, that is, spinners instead of swimmers [227]. Indeed using magnetic colloids the self-rotating motion can be induced externally via a magnetic field which could prove to be more practical from an experimental point of view. These have already been used to make chiral liquids which exhibit highly non-trivial behavior [64], but the glassy dynamics of a collection of spinners remains to be explored.

From a more fundamental and theoretical perspective an important question relates to the possible existence of a mapping of an active onto a passive glass. In particular, can the impact of spatial velocity correlations on glassy dynamics essentially be related to changes in the structure of a passive glass? More concretely, can we change the interaction potential between Brownian particles to instigate the same effect as activity would to long-time relaxation?

We have developed active mode-coupling theories (MCT) to better understand active glassy matter and the involved structure-dynamics relation. In principle, the framework of MCT also allows for the inclusion of spinning motion or the possibility to describe active ellipsoidal particles. These might connect better to experimental realizations of dense active matter and thus constitute concrete directions for further theoretical research.

Finally, we mention that activity provides a unique route to quench between a glass and a liquid state. How does this route compare to more conventional ones such as a temperature quench? This is a crucial question, as by now it seems more than plausible that activity constitutes an important evolved means by which nature controls cellular glassiness and thus biological function [97].

Bibliography

[1] P. R. S. Moorey, *Ancient Mesopotamian Materials and Industries: The Archaeological Evidence* (Eisenbrauns, 1999).

[2] T. E. Angelini, E. Hannezo, X. Trepat, M. Marquez, J. J. Fredberg, and D. A. Weitz, Proc. Natl. Acad. Sci. U.S.A. **108**, 4714 (2011).

[3] E. Zhou, X. Trepat, C. Park, G. Lenormand, M. Oliver, S. Mijailovich, C. Hardin, D. Weitz, J. Butler, and J. Fredberg, Proc. Natl. Acad. Sci. U.S.A. **106**, 10632 (2009).

[4] P. G. Debenedetti and F. H. Stillinger, Nature **410**, 259 (2001).

[5] "The glass phase: A physics mystery," `https://www.tue.nl/en/news/features/the-glass-phase-a-physics-mystery`, accessed: 22-03-2023.

[6] G. L. Hunter and E. R. Weeks, Rep. Prog. Phys. **75**, 066501 (2012).

[7] C. Angell, J. Non-Cryst. Solids **102**, 205 (1988).

[8] P. W. Anderson, Science **267**, 1615 (1995).

[9] L. Berthier and G. Biroli, Rev. Mod. Phys. **83**, 587 (2011).

[10] C. P. Royall and S. R. Williams, Phys. Rep. **560**, 1 (2015).

[11] W. van Megen and S. M. Underwood, Phys. Rev. E **49**, 4206 (1994).

[12] F. Fernandez-Alonso and D. Price, *Neutron Scattering* (Academic Press, 2013).

[13] J. P. Hansen and I. R. McDonald, *Theory of Simple Liquids* (Academic Press, 2013).

[14] E. R. Weeks and D. A. Weitz, Phys. Rev. Lett. **89**, 095704 (2002).

[15] W. Götze, *Complex dynamics of glass-forming liquids: A mode-coupling theory* (OUP Oxford, 2008).

[16] D. Coslovich, J. Chem. Phys. **138**, 12A539 (2013).

[17] C. P. Royall, F. Turci, and T. Speck, J. Chem. Phys. **153**, 090901 (2020).

[18] N. Lačević, F. W. Starr, T. B. Schrøder, and S. C. Glotzer, J. Chem. Phys. **119**, 7372 (2003).

[19] S. S. Schoenholz, E. D. Cubuk, D. M. Sussman, E. Kaxiras, and A. J. Liu, Nat. Phys. **12**, 469 (2016).

[20] S. S. Schoenholz, E. D. Cubuk, E. Kaxiras, and A. J. Liu, Proc. Natl. Acad. Sci. U.S.A. **114**, 263 (2017).

[21] L. M. C. Janssen, Front. Phys. **6**, 97 (2018).

[22] V. E. Debets, C. Luo, S. Ciarella, and L. M. C. Janssen, Phys. Rev. E **104**, 065302 (2021).

[23] J. S. Langer, Rep. Prog. Phys. **77**, 042501 (2014).

[24] Y. S. Elmatad, Proc. Natl. Acad. Sci. U.S.A. **108**, E230 (2011).

[25] M. Ozawa, K. Kim, and K. Miyazaki, J. Stat. Mech. Theory Exp. **2016**, 074002 (2016).

[26] K. F. Kelton, J. Phys. Condens. **29**, 023002 (2016).

[27] L. Berthier, G. Biroli, J.-P. Bouchaud, L. Cipelletti, and W. van Saarloos, *Dynamical Heterogeneities in Glasses, Colloids, and Granular Media* (Oxford University Press, 2013).

[28] M. M. Hurley and P. Harrowell, Phys. Rev. E **52**, 1694 (1995).

[29] W. Kob, C. Donati, S. J. Plimpton, P. H. Poole, and S. C. Glotzer, Phys. Rev. Lett. **79**, 2827 (1997).

[30] W. K. Kegel and A. van Blaaderen, Science **287**, 290 (2000).

[31] C. Scalliet, B. Guiselin, and L. Berthier, Phys. Rev. X **12**, 041028 (2022).

[32] J. A. Hodgdon and F. H. Stillinger, Phys. Rev. E **48**, 207 (1993).

[33] R. Zangi and L. J. Kaufman, Phys. Rev. E **75**, 051501 (2007).

[34] S. Sengupta, S. Karmakar, C. Dasgupta, and S. Sastry, J. Chem. Phys. **138**, 12A548 (2013).

[35] M. Micoulaut, Rep. Prog. Phys. **79**, 066504 (2016).

[36] W. Kob and J.-L. Barrat, Phys. Rev. Lett. **78**, 4581 (1997).

[37] W. Kob and H. C. Andersen, Phys. Rev. Lett. **73**, 1376 (1994).

[38] A. Ninarello, L. Berthier, and D. Coslovich, Phys. Rev. X **7**, 021039 (2017).

[39] T. Vicsek, A. Czirók, E. Ben-Jacob, I. Cohen, and O. Shochet, Phys. Rev. Lett. **75**, 1226 (1995).

[40] J. Toner and Y. Tu, Phys. Rev. Lett. **75**, 4326 (1995).

[41] D. Helbing, I. Farkas, and T. Vicsek, Nature **407**, 487 (2000).

[42] N. Bain and D. Bartolo, Science **363**, 46 (2019).

[43] M. Han, M. Fruchart, C. Scheibner, S. Vaikuntanathan, J. J. de Pablo, and V. Vitelli, Nat. Phys. **17**, 1260 (2021).

[44] Y. Maroudas-Sacks, L. Garion, L. Shani-Zerbib, A. Livshits, E. Braun, and K. Keren, Nat. Phys. **17**, 251 (2021).

[45] E. Lång, A. Połeć, A. Lång, M. Valk, P. Blicher, A. D. Rowe, K. A. Tønseth, C. J. Jackson, T. P. Utheim, L. M. C. Janssen, J. Eriksson, and S. O. Bøe, Nat. Commun. **9**, 3665 (2018).

[46] C. Blanch-Mercader, V. Yashunsky, S. Garcia, G. Duclos, L. Giomi, and P. Silberzan, Phys. Rev. Lett. **120**, 208101 (2018).

[47] V. E. Debets, L. M. Janssen, and C. Storm, Biophys. J. **120**, 1483 (2021).

[48] D. Bi, X. Yang, M. C. Marchetti, and M. L. Manning, Phys. Rev. X **6**, 021011 (2016).

[49] E. Lauga and T. R. Powers, Rep. Prog. Phys. **72**, 096601 (2009).

[50] M. E. Cates, Rep. Prog. Phys. **75**, 042601 (2012).

[51] N. Schramma, C. P. Israëls, and M. Jalaal, Proc. Natl. Acad. Sci. U.S.A. **120**, e2216497120 (2023).

[52] T. Sanchez, D. T. N. Chen, S. J. DeCamp, M. Heymann, and Z. Dogic, Nature **491**, 431 (2012).

[53] J. Deseigne, O. Dauchot, and H. Chaté, Phys. Rev. Lett. **105**, 098001 (2010).

[54] C. A. Weber, T. Hanke, J. Deseigne, S. Léonard, O. Dauchot, E. Frey, and H. Chaté, Phys. Rev. Lett. **110**, 208001 (2013).

[55] P. Arora, A. K. Sood, and R. Ganapathy, Phys. Rev. Lett. **128**, 178002 (2022).

[56] C. C. Maass, C. Krüger, S. Herminghaus, and C. Bahr, Annu. Rev. Condens. Matter Phys. **7**, 171 (2016).

[57] A. Izzet, P. G. Moerman, P. Gross, J. Groenewold, A. D. Hollingsworth, J. Bibette, and J. Brujic, Phys. Rev. X **10**, 021035 (2020).

[58] C. Kurzthaler, C. Devailly, J. Arlt, T. Franosch, W. C. K. Poon, V. A. Martinez, and A. T. Brown, Phys. Rev. Lett. **121**, 078001 (2018).

[59] X. Zheng, B. ten Hagen, A. Kaiser, M. Wu, H. Cui, Z. Silber-Li, and H. Löwen, Phys. Rev. E **88**, 032304 (2013).

[60] H.-R. Jiang, N. Yoshinaga, and M. Sano, Phys. Rev. Lett. **105**, 268302 (2010).

[61] G. Volpe, I. Buttinoni, D. Vogt, H.-J. Kümmerer, and C. Bechinger, Soft Matter **7**, 8810 (2011).

[62] J. R. Howse, R. A. L. Jones, A. J. Ryan, T. Gough, R. Vafabakhsh, and R. Golestanian, Phys. Rev. Lett. **99**, 048102 (2007).

[63] A. Kaiser, A. Snezhko, and I. S. Aranson, Sci. Adv. **3**, e1601469 (2017).

[64] V. Soni, E. S. Bililign, S. Magkiriadou, S. Sacanna, D. Bartolo, M. J. Shelley, and W. T. M. Irvine, Nat. Phys. **15**, 1188 (2019).

[65] A. Chardac, L. A. Hoffmann, Y. Poupart, L. Giomi, and D. Bartolo, Phys. Rev. X **11**, 031069 (2021).

[66] T. R. Kelly, H. De Silva, and R. A. Silva, Nature **401**, 150 (1999).

[67] N. Koumura, R. W. J. Zijlstra, R. A. van Delden, N. Harada, and B. L. Feringa, Nature **401**, 152 (1999).

[68] M. N. van der Linden, L. C. Alexander, D. G. A. L. Aarts, and O. Dauchot, Phys. Rev. Lett. **123**, 098001 (2019).

[69] P. Guillamat, J. Ignés-Mullol, and F. Sagués, Nat. Commun. **8**, 564 (2017).

[70] I. Buttinoni, J. Bialké, F. Kümmel, H. Löwen, C. Bechinger, and T. Speck, Phys. Rev. Lett. **110**, 238301 (2013).

[71] F. Ginot, I. Theurkauff, F. Detcheverry, C. Ybert, and C. Cottin-Bizonne, Nat. Commun. **9**, 696 (2018).

[72] J. Palacci, S. Sacanna, A. P. Steinberg, D. J. Pine, and P. M. Chaikin, Science **339**, 936 (2013).

[73] L. Giomi, Phys. Rev. X **5**, 031003 (2015).

[74] R. Alert, J. Casademunt, and J.-F. Joanny, Annu. Rev. Condens. Matter Phys. **13**, 143 (2022).

[75] A. P. Berke, L. Turner, H. C. Berg, and E. Lauga, Phys. Rev. Lett. **101**, 038102 (2008).

[76] M. Spellings, M. Engel, D. Klotsa, S. Sabrina, A. M. Drews, N. H. P. Nguyen, K. J. M. Bishop, and S. C. Glotzer, Proc. Natl. Acad. Sci. U.S.A. **112**, E4642 (2015).

[77] T. H. Tan, A. Mietke, J. Li, Y. Chen, H. Higinbotham, P. J. Foster, S. Gokhale, J. Dunkel, and N. Fakhri, Nature **607**, 287 (2022).

[78] C. Bechinger, R. Di Leonardo, H. Löwen, C. Reichhardt, G. Volpe, and G. Volpe, Rev. Mod. Phys. **88**, 045006 (2016).

[79] L. Berthier, E. Flenner, and G. Szamel, J. Chem. Phys. **150**, 200901 (2019).

[80] L. M. C. Janssen, J. Phys. Condens. **31**, 503002 (2019).

[81] A. P. Petroff, X.-L. Wu, and A. Libchaber, Phys. Rev. Lett. **114**, 158102 (2015).

[82] G. Briand and O. Dauchot, Phys. Rev. Lett. **117**, 098004 (2016).

[83] G. Briand, M. Schindler, and O. Dauchot, Phys. Rev. Lett. **120**, 208001 (2018).

[84] D. Geyer, D. Martin, J. Tailleur, and D. Bartolo, Phys. Rev. X **9**, 031043 (2019).

[85] R. Ni, M. A. C. Stuart, and M. Dijkstra, Nat. Commun. **4**, 2704 (2013).

[86] G. Parisi and F. Zamponi, Rev. Mod. Phys. **82**, 789 (2010).

[87] K. Nishizawa, K. Fujiwara, M. Ikenaga, N. Nakajo, M. Yanagisawa, and D. Mizuno, Sci. Rep. **7**, 15143 (2017).

[88] H. Lama, M. J. Yamamoto, Y. Furuta, T. Shimaya, and K. A. Takeuchi, "Emergence of bacterial glass: two-step glass transition in 2d bacterial suspension," (2022), arXiv:2205.10436 [cond-mat.stat-mech] .

[89] B. R. Parry, I. V. Surovtsev, M. T. Cabeen, C. S. O'Hern, E. R. Dufresne, and C. Jacobs-Wagner, Cell **156**, 183 (2014).

[90] B. Corci, O. Hooiveld, A. M. Dolga, and C. Åberg, Soft Matter , 2529 (2023).

[91] E. Flenner and G. Szamel, Phys. Rev. E **102**, 022607 (2020).

[92] T. J. A. Schötz Eva-Maria, Lanio Marcos and M. M. Lisa, J. R. Soc. Interface **10**, 20130726 (2013).

[93] S. Garcia, E. Hannezo, J. Elgeti, J.-F. Joanny, P. Silberzan, and N. S. Gov, Proc. Natl. Acad. Sci. U.S.A. **112**, 15314 (2015).

[94] J.-A. Park, J. H. Kim, D. Bi, J. A. Mitchel, N. T. Qazvini, K. Tantisira, C. Y. Park, M. McGill, S.-H. Kim, B. Gweon, J. Notbohm, R. Steward Jr, S. Burger, S. H. Randell, A. T. Kho, D. T. Tambe, C. Hardin, S. A. Shore, E. Israel, D. A. Weitz, D. J. Tschumperlin, E. P. Henske, S. T. Weiss, M. L. Manning, J. P. Butler, J. M. Drazen, and J. J. Fredberg, Nat. Mater. **14**, 1040 (2015).

[95] J.-A. Park, L. Atia, J. A. Mitchel, J. J. Fredberg, and J. P. Butler, J. Cell Sci. **129**, 3375 (2016).

[96] S. Grosser, J. Lippoldt, L. Oswald, M. Merkel, D. M. Sussman, F. Renner, P. Gottheil, E. W. Morawetz, T. Fuhs, X. Xie, S. Pawlizak, A. W. Fritsch, B. Wolf, L.-C. Horn, S. Briest, B. Aktas, M. L. Manning, and J. A. Käs, Phys. Rev. X **11**, 011033 (2021).

[97] L. Atia, J. J. Fredberg, N. S. Gov, and A. F. Pegoraro, Cells Dev. **168**, 203727 (2021).

[98] N. Klongvessa, F. Ginot, C. Ybert, C. Cottin-Bizonne, and M. Leocmach, Phys. Rev. Lett. **123**, 248004 (2019).

[99] N. Klongvessa, F. Ginot, C. Ybert, C. Cottin-Bizonne, and M. Leocmach, Phys. Rev. E **100**, 062603 (2019).

[100] A. Liluashvili, J. Ónody, and T. Voigtmann, Phys. Rev. E **96**, 062608 (2017).

[101] G. Szamel, J. Chem. Phys. **150**, 124901 (2019).

[102] G. Szamel, E. Flenner, and L. Berthier, Phys. Rev. E **91**, 062304 (2015).

[103] G. Szamel, Phys. Rev. E **93**, 012603 (2016).

[104] M. Feng and Z. Hou, Soft Matter **13**, 4464 (2017).

[105] L. Berthier and J. Kurchan, Nat. Phys. **9**, 310 (2013).

[106] J. Reichert, S. Mandal, and T. Voigtmann, Phys. Rev. E **104**, 044608 (2021).

[107] J. Reichert and T. Voigtmann, Soft Matter **17**, 10492 (2021).

[108] J. Reichert, L. F. Granz, and T. Voigtmann, Eur. Phys. J. E **44**, 27 (2021).

[109] S. K. Nandi, R. Mandal, P. J. Bhuyan, C. Dasgupta, M. Rao, and N. S. Gov, Proc. Natl. Acad. Sci. U.S.A. **115**, 7688 (2018).

[110] V. E. Debets and L. M. C. Janssen, J. Chem. Phys. **157**, 224902 (2022).

[111] L. Berthier, Phys. Rev. Lett. **112**, 220602 (2014).

[112] L. Berthier, E. Flenner, and G. Szamel, New J. Phys. **19**, 125006 (2017).

[113] E. Flenner, G. Szamel, and L. Berthier, Soft Matter **12**, 7136 (2016).

[114] S. Henkes, Y. Fily, and M. C. Marchetti, Phys. Rev. E **84**, 040301 (2011).

[115] R. Mandal and P. Sollich, Phys. Rev. Lett. **125**, 218001 (2020).

[116] G. Janzen and L. M. C. Janssen, Phys. Rev. Res. **4**, L012038 (2022).

[117] M. Paoluzzi, D. Levis, and I. Pagonabarraga, Commun. Phys. **5**, 111 (2022).

[118] V. E. Debets, X. M. de Wit, and L. M. C. Janssen, Phys. Rev. Lett. **127**, 278002 (2021).

[119] Y.-E. Keta, R. L. Jack, and L. Berthier, Phys. Rev. Lett. **129**, 048002 (2022).

[120] V. E. Debets and L. M. C. Janssen, Phys. Rev. Res. **4**, L042033 (2022).

[121] V. E. Debets, H. Löwen, and L. M. C. Janssen, Phys. Rev. Lett. **130**, 058201 (2023).

[122] T. F. F. Farage, P. Krinninger, and J. M. Brader, Phys. Rev. E **91**, 042310 (2015).

[123] H. Löwen, J. Chem. Phys. **152**, 040901 (2020).

[124] J. Tailleur and M. E. Cates, Phys. Rev. Lett. **100**, 218103 (2008).

[125] L. Li, S. F. Nørrelykke, and E. C. Cox, PLoS One **3**, e2093 (2008).

[126] P.-H. Wu, A. Giri, S. X. Sun, and D. Wirtz, Proc. Natl. Acad. Sci. U.S.A. **111**, 3949 (2014).

[127] Y. Fily and M. C. Marchetti, Phys. Rev. Lett. **108**, 235702 (2012).

[128] J. Bialké, T. Speck, and H. Löwen, Phys. Rev. Lett. **108**, 168301 (2012).

[129] G. S. Redner, M. F. Hagan, and A. Baskaran, Phys. Rev. Lett. **110**, 055701 (2013).

[130] C. B. Caporusso, P. Digregorio, D. Levis, L. F. Cugliandolo, and G. Gonnella, Phys. Rev. Lett. **125**, 178004 (2020).

[131] R. Ni, M. A. Cohen Stuart, and P. G. Bolhuis, Phys. Rev. Lett. **114**, 018302 (2015).

[132] L. Caprini, U. Marini Bettolo Marconi, and A. Puglisi, Phys. Rev. Lett. **124**, 078001 (2020).

[133] S. van Teeffelen and H. Löwen, Phys. Rev. E **78**, 020101 (2008).

[134] E. Fodor, C. Nardini, M. E. Cates, J. Tailleur, P. Visco, and F. van Wijland, Phys. Rev. Lett. **117**, 038103 (2016).

[135] D. Martin, J. O'Byrne, M. E. Cates, E. Fodor, C. Nardini, J. Tailleur, and F. van Wijland, Phys. Rev. E **103**, 032607 (2021).

[136] C. Kurzthaler, S. Leitmann, and T. Franosch, Sci. Rep. **6**, 36702 (2016).

[137] M. E. Cates and J. Tailleur, EPL **101**, 20010 (2013).

[138] M. R. Shaebani, A. Wysocki, R. G. Winkler, G. Gompper, and H. Rieger, Nat. Rev. Phys. **2**, 181 (2020).

[139] H. Mori, Prog. Theor. Phys. **33**, 423 (1965).

[140] R. Zwanzig, J. Chem. Phys. **33**, 1338 (1960).

[141] G. Nägele, Phys. Rep. **272**, 215 (1996).

[142] G. Nägele, J. Bergenholtz, and J. Dhont, J. Chem. Phys. **110**, 7037 (1999).

[143] B. Cichocki and W. Hess, Phys. A: Stat. Mech. **141**, 475 (1987).

[144] K. Kawasaki, Phys. A: Stat. Mech. **208**, 35 (1994).

[145] L. M. C. Janssen and D. R. Reichman, Phys. Rev. Lett. **115**, 205701 (2015).

[146] H. W. Jackson and E. Feenberg, Rev. Mod. Phys. **34**, 686 (1962).

[147] P. Romanczuk, M. Bär, W. Ebeling, B. Lindner, and L. Schimansky-Geier, Eur. Phys. J. Spec. Top. **202**, 1 (2012).

[148] S. Ramaswamy, J. Stat. Mech. Theory Exp. **2017**, 054002 (2017).

[149] Y. Fily and M. C. Marchetti, Phys. Rev. Lett. **108**, 235702 (2012).

[150] B. ten Hagen, S. van Teeffelen, and H. Löwen, J. Phys. Condens. **23**, 194119 (2011).

[151] G. Szamel, Phys. Rev. E **90**, 012111 (2014).

[152] C. Maggi, U. M. B. Marconi, N. Gnan, and R. Di Leonardo, Sci. Rep. **5**, 10742 (2015).

[153] A. Liluashvili, J. Ónody, and T. Voigtmann, Phys. Rev. E **96**, 062608 (2017).

[154] R. Mandal, P. J. Bhuyan, M. Rao, and C. Dasgupta, Soft Matter **12**, 6268 (2016).

[155] W. Kob, "Supercooled liquids, the glass transition, and computer simulations," (2002), arXiv:cond-mat/0212344 [cond-mat.stat-mech] .

[156] F. Weysser, A. M. Puertas, M. Fuchs, and T. Voigtmann, Phys. Rev. E **82**, 011504 (2010).

[157] E. Lange, J. B. Caballero, A. M. Puertas, and M. Fuchs, J. Chem. Phys. **130**, 174903 (2009).

[158] C. D. Michele, F. Sciortino, and A. Coniglio, J. Phys. Condens. **16**, L489 (2004).

[159] S. Plimpton, J. Comput. Phys. **117**, 1 (1995).

[160] E. Flenner and G. Szamel, Phys. Rev. E **72**, 031508 (2005).

[161] C. Ruscher, S. Ciarella, C. Luo, L. M. C. Janssen, J. Farago, and J. Baschnagel, J. Phys. Condens. **33**, 064001 (2021).

[162] T. Voigtmann, A. M. Puertas, and M. Fuchs, Phys. Rev. E **70**, 061506 (2004).

[163] G. Tarjus, S. A. Kivelson, Z. Nussinov, and P. Viot, J. Phys. Condens. Matter **17**, R1143 (2005).

[164] B. Charbonneau, P. Charbonneau, Y. Jin, G. Parisi, and F. Zamponi, J. Chem. Phys. **139**, 164502 (2013).

[165] R. Mandal and P. Sollich, J. Phys. Condens. Matter **33**, 184001 (2021).

[166] M. K. Nandi and S. M. Bhattacharyya, Phys. Rev. Lett. **126**, 208001 (2021).

[167] C. Kurzthaler, S. Mandal, T. Bhattacharjee, H. Löwen, S. S. Datta, and H. A. Stone, Nat. Commun. **12**, 7088 (2021).

[168] D. Wexler, N. Gov, K. O. Rasmussen, and G. Bel, Phys. Rev. Res. **2**, 013003 (2020).

[169] A. Militaru, M. Innerbichler, M. Frimmer, F. Tebbenjohanns, L. Novotny, and C. Dellago, Nat. Commun. **12**, 2446 (2021).

[170] E. Woillez, Y. Zhao, Y. Kafri, V. Lecomte, and J. Tailleur, Phys. Rev. Lett. **122**, 258001 (2019).

[171] L. Caprini, F. Cecconi, and U. Marini Bettolo Marconi, J. Chem. Phys. **155**, 234902 (2021).

[172] D. Chaudhuri and A. Dhar, J. Stat. Mech. **2021**, 013207 (2021).

[173] K. Malakar, A. Das, A. Kundu, K. V. Kumar, and A. Dhar, Phys. Rev. E **101**, 022610 (2020).

[174] W. Götze and L. Sjogren, Rep. Prog. Phys. **55**, 241 (1992).

[175] D. R. Reichman and P. Charbonneau, J. Stat. Mech. **2005**, P05013 (2005).

[176] W. Götze, J. Phys. Condens. Matter **11**, A1 (1999).

[177] L. M. C. Janssen, P. Mayer, and D. R. Reichman, Phys. Rev. E **90**, 52306 (2014).

[178] L. M. C. Janssen, P. Mayer, and D. R. Reichman, J. Stat. Mech. **2016**, 054049 (2016).

[179] C. Luo and L. M. C. Janssen, J. Chem. Phys. **153**, 214507 (2020).

[180] C. Luo and L. M. C. Janssen, J. Chem. Phys. **153**, 214506 (2020).

[181] S. Ciarella, C. Luo, V. E. Debets, and L. M. C. Janssen, Eur. Phys. J. E **44**, 91 (2021).

[182] P. Mayer, K. Miyazaki, and D. R. Reichman, Phys. Rev. Lett. **97**, 095702 (2006).

[183] G. Szamel, Phys. Rev. Lett. **90**, 228301 (2003).

[184] J. Wu and J. Cao, Phys. Rev. Lett. **95**, 078301 (2005).

[185] C. Luo, V. E. Debets, and L. M. C. Janssen, J. Chem. Phys. **155**, 034502 (2021).

[186] V. E. Debets, C. Luo, S. Ciarella, and L. M. C. Janssen, Phys. Rev. E **104**, 065302 (2021).

[187] T. F. F. Farage and J. M. Brader, "Dynamics and rheology of active glasses," (2014), arXiv:1403.0928 [cond-mat.soft] .

[188] T. Franosch, M. Fuchs, W. Götze, M. R. Mayr, and A. P. Singh, Phys. Rev. E **55**, 7153 (1997).

[189] M. Fuchs, W. Götze, I. Hofacker, and A. Latz, J. Phys. Condens. Matter **3**, 5047 (1991).

[190] S. K. Nandi and N. S. Gov, Soft Matter **13**, 7609 (2017).

[191] M. Nauroth and W. Kob, Phys. Rev. E **55**, 657 (1997).

[192] F. Sciortino and W. Kob, Phys. Rev. Lett. **86**, 648 (2001).

[193] G. Szamel and E. Flenner, EPL **133**, 60002 (2021).

[194] M. Fuchs and M. E. Cates, J. Rheol. **53**, 957 (2009).

[195] S. P. Das, Rev. Mod. Phys. **76**, 785 (2004).

[196] A. L. Thorneywork, S. K. Schnyder, D. G. A. L. Aarts, J. Horbach, R. Roth, and R. P. A. Dullens, Mol. Phys. **116**, 3245 (2018).

[197] R. Großmann, F. Peruani, and M. Bär, Eur. Phys. J. Spec. Top. **224**, 1377 (2015).

[198] R. Schilling and T. Scheidsteger, Phys. Rev. E **56**, 2932 (1997).

[199] T. E. Angelini, E. Hannezo, X. Trepat, J. J. Fredberg, and D. A. Weitz, Phys. Rev. Lett. **104**, 168104 (2010).

[200] L. Caprini, U. M. B. Marconi, C. Maggi, M. Paoluzzi, and A. Puglisi, Phys. Rev. Res. **2**, 023321 (2020).

[201] L. Caprini and U. Marini Bettolo Marconi, Soft Matter **17**, 4109 (2021).

[202] S. Henkes, K. Kostanjevec, J. M. Collinson, R. Sknepnek, and E. Bertin, Nat. Commun. **11**, 1405 (2020).

[203] S. Ramaswamy, Annu. Rev. Condens. Matter Phys. **1**, 323 (2010).

[204] A. Sharma and J. M. Brader, J. Chem. Phys. **145**, 161101 (2016).

[205] G. Szamel and H. Löwen, Phys. Rev. A **44**, 8215 (1991).

[206] J. Reichert, *Transport coefficients in dense active brownian particle systems*, Ph.D. thesis (2020).

[207] B. W. van de Waal, J. Non-Cryst. Solids **189**, 118 (1995).

[208] N. de Macedo Biniossek, H. Löwen, T. Voigtmann, and F. Smallenburg, J. Phys.: Condens. Matter **30**, 074001 (2018).

[209] M. Bayer, J. M. Brader, F. Ebert, M. Fuchs, E. Lange, G. Maret, R. Schilling, M. Sperl, and J. P. Wittmer, Phys. Rev. E **76**, 011508 (2007).

[210] C. Maggi, U. M. B. Marconi, N. Gnan, and R. Di Leonardo, Sci. Rep. **5**, 10742 (2015).

[211] F. Kümmel, B. ten Hagen, R. Wittkowski, I. Buttinoni, R. Eichhorn, G. Volpe, H. Löwen, and C. Bechinger, Phys. Rev. Lett. **110**, 198302 (2013).

[212] P. Patra, K. Beyer, A. Jaiswal, A. Battista, K. Rohr, F. Frischknecht, and U. S. Schwarz, Nat. Phys. **18**, 586 (2022).

[213] B. Zhang, A. Sokolov, and A. Snezhko, Nat. Commun. **11**, 4401 (2020).

[214] A. I. Campbell, R. Wittkowski, B. ten Hagen, H. Löwen, and S. J. Ebbens, J. Chem. Phys. **147**, 084905 (2017).

[215] R. J. Archer, A. I. Campbell, and S. J. Ebbens, Soft Matter **11**, 6872 (2015).

[216] E. Lauga, W. R. DiLuzio, G. M. Whitesides, and H. A. Stone, Biophys. J. **90**, 400 (2006).

[217] Z.-F. Huang, A. M. Menzel, and H. Löwen, Phys. Rev. Lett. **125**, 218002 (2020).

[218] Z. Ma and R. Ni, J. Chem. Phys. **156**, 021102 (2022).

[219] Q.-L. Lei, M. P. Ciamarra, and R. Ni, Sci. Adv. **5**, eaau7423 (2019).

[220] B. Liebchen and D. Levis, Phys. Rev. Lett. **119**, 058002 (2017).

[221] C. Chen, S. Liu, X.-q. Shi, H. Chaté, and Y. Wu, Nature **542**, 210 (2017).

[222] C. Scholz, A. Ldov, T. Pöschel, M. Engel, and H. Löwen, Sci. Adv. **7**, eabf8998 (2021).

[223] C. Reichhardt and C. J. O. Reichhardt, Phys. Rev. E **100**, 012604 (2019).

[224] G.-J. Liao and S. H. L. Klapp, Soft Matter **14**, 7873 (2018).

[225] G.-J. Liao and S. H. L. Klapp, Soft Matter **17**, 6833 (2021).

[226] M. J. Bowick, N. Fakhri, M. C. Marchetti, and S. Ramaswamy, Phys. Rev. X **12**, 010501 (2022).

[227] B. Liebchen and D. Levis, EPL **139**, 67001 (2022).

[228] T. Ohta and T. Ohkuma, Phys. Rev. Lett. **102**, 154101 (2009).

[229] R. Di Leonardo, D. Dell'Arciprete, L. Angelani, and V. Iebba, Phys. Rev. Lett. **106**, 038101 (2011).

[230] J. Yan, S. C. Bae, and S. Granick, Soft Matter **11**, 147 (2015).

[231] K. Drescher, K. C. Leptos, I. Tuval, T. Ishikawa, T. J. Pedley, and R. E. Goldstein, Phys. Rev. Lett. **102**, 168101 (2009).

[232] K. Drescher, R. E. Goldstein, N. Michel, M. Polin, and I. Tuval, Phys. Rev. Lett. **105**, 168101 (2010).

[233] T. Ishikawa, T. J. Pedley, K. Drescher, and R. E. Goldstein, J. Fluid Mech. **903**, A11 (2020).

[234] C. W. Gardiner, *Handbook of Stochastic Methods*, Vol. 3 (Springer, 1985).

[235] E. Woillez, Y. Kafri, and N. S. Gov, Phys. Rev. Lett. **124**, 118002 (2020).

[236] C. Abaurrea-Velasco, C. Lozano, C. Bechinger, and J. de Graaf, Phys. Rev. Lett. **125**, 258002 (2020).

[237] J. R. Gomez-Solano, A. Blokhuis, and C. Bechinger, Phys. Rev. Lett. **116**, 138301 (2016).

[238] C. Lozano, J. R. Gomez-Solano, and C. Bechinger, Nat. Mater. **18**, 1118 (2019).

[239] E. Irani, Z. Mokhtari, and A. Zippelius, Phys. Rev. Lett. **128**, 144501 (2022).

[240] D. Chaudhuri and A. Dhar, J. Stat. Mech. Theory Exp. **2021**, 013207 (2021).

[241] S. Jahanshahi, H. Löwen, and B. ten Hagen, Phys. Rev. E **95**, 022606 (2017).

[242] M. Merkel and M. L. Manning, New J. Phys. **20**, 022002 (2018).

[243] D. Bi, J. H. Lopez, J. M. Schwarz, and M. L. Manning, Nat. Phys. **11**, 1074 (2015).

[244] M. Chiang and D. Marenduzzo, EPL **116**, 28009 (2016)

Summary

Active glasses, i.e., dense disordered systems composed of self-propelling particles, have rapidly emerged as an important new materials class in nonequilibrium condensed matter science and biophysics. In a biological context, it is now becoming evident that active glassy behavior plays a vital role in the functionality of cells, crucially governing many biological processes such as embryonic development, cancer metastasis, and cytoplasmic transport. Furthermore, in soft matter, the recent advent of synthetic active glasses has opened an exciting new playground for colloidal science far away from equilibrium. In this thesis, we have theoretically and computationally investigated the impact of self-propelled or active motion on glassy dynamics. The overarching goal is to further aid the fundamental understanding of active glassy dynamics, especially in relation to its well-known passive counterpart. For this purpose, we have employed two archetypical active particle models, active Brownian particles (ABPs) and active Ornstein-Uhlenbeck particles (AOUPs), in combination with conventional glassy model systems and mode-coupling theories (MCTs).

We have first considered the previous lack of consensus on the question how activity affects glassy dynamics in these model systems. In recent studies different conflicting results have been reported – ranging from a monotonic speedup or slowdown of the dynamics to even nonmonotonic changes upon increased activity. Using numerical simulations of thermal and athermal active quasi-hard spheres, we show that their dynamics is nonmonotonic and most enhanced by activity when the intrinsic active length scale (e.g., the persistence length) is equal to the cage length, i.e., the length scale of local particle caging. This insight, which we attribute to the most efficient scanning of local particle cages, allows us to reconcile and explain the disparate results in these previous studies. Subsequently, we have demonstrated by means of extensive computer simulations that the argument sketched above remains fully intact for softer spheres with varying interaction ranges. We have also explored the relaxation dynamics upon approaching dynamical arrest and find that the cage length marks the threshold beyond which our active system starts behaving qualitatively distinct (manifested by changes in the fragility) from its passive Brownian counterpart. To complement our simulations, we

have developed a distinct active MCT for mixtures of athermal self-propelled particles (based on an analogy between our overdamped active system and an underdamped passive one), whose predictions are qualitatively fully consistent with our simulation results.

Next, we have sought to gain more insight into the role of the self-propulsion mechanism on the glassy dynamics. For passive glassy materials, it is well established that the details of the microscopic dynamics, e.g., Newtonian or Brownian, do not influence the long-time glassy behavior. To address whether this also holds in the active case, we have derived a mode-coupling theory (MCT) for thermal AOUPs which can be directly compared to a recently developed MCT for ABPs. Both theories are the first active MCTs that explicitly take into account the active degrees of freedom. We solve the AOUP- and ABP-MCT equations in two dimensions and demonstrate that both models give almost identical results for the intermediate scattering function over a large variety of control parameters (packing fractions, active speeds, and persistence times). We have also confirmed this theoretical equivalence between the different self-propulsion mechanisms via simulations, thereby establishing, that, at least for these model systems, the microscopic details of self-propulsion do not alter the active glassy behavior. Moreover, we have then used the active MCT results in conjunction with the integration-through-transients formalism to theoretically demonstrate, from first principles and using only a passive structure factor as input, the emergence of non-equilibrium spatial velocity correlations. These form one of the key hallmarks of dense active matter, as they are strictly absent in passive glassy matter.

We have finalized the thesis by exploring the effect of chirality, which can be attained by, e.g., asymmetries in shape or self-propulsion mechanism, on active glassy dynamics. Via simulations we have studied the glassy dynamics of interacting chiral active Brownian particles (cABPs) and demonstrate that when our chiral fluid is pushed to glassy conditions, it exhibits highly nontrivial dynamics (especially compared to common ABPs) with in some cases remarkably strong reentrant behavior. We have fully rationalized the observed dynamical regimes by invoking analytical results for a chiral ABP in a harmonic trap and spatial velocity correlation functions. To explain the significant reentrant behavior, a ‘hammering’ mechanism is introduced which is unique to rapidly spinning particles high-density conditions.

Samenvatting

Actieve glazen, i.e., dichte wanorderlijke systemen bestaande uit zelfvoortstuwende deeltjes, hebben zich in rap tempo gepresenteerd als een belangrijke klasse van nieuwe materialen in de wetenschap van de condenseerde materie buiten evenwicht en de biofysica. In een biologische context begint het namelijk duidelijk te worden dat actief glasachtig gedrag een zeer belangrijke rol speelt in de functionaliteit van cellen, in het bijzonder in biologische processen zoals embryonale ontwikkeling, kanker metastase en transport in het cytoplasma. In de zachte materie heeft de recente experimentele realisatie van synthetische actieve glazen bovendien de weg vrij gemaakt voor een nieuw en intrigerend subveld van de buiten-evenwicht colloïdale wetenschap. In deze thesis hebben wij theoretisch en computationeel de invloed van zelfvoorstuwende ofwel actieve beweging op glasachtige dynamica bestudeerd. Het overkoepelende doel is bij te dragen aan het fundamentele begrip van actieve glasachtige dynamica, vooral in relatie tot de beter bekende phenomenologie van zijn passieve tegenhanger. Derhalve gebruiken wij twee standaard actieve-deeltjes modellen, de actieve Brownse deeltjes (ABPs) en de actieve Ornstein-Uhlenbeck deeltjes (AOUPs), in combinatie met conventionele modellen voor glasachtige systemen en modekoppelingstheorieën (MCTs).

Ten eerste hebben we het vorige gebrek aan consensus ten aanzien van hoe in deze modellen activiteit glasachtige dynamica beinvloedt beschouwd. In recente studies zijn er namelijk verschillende conflicterende resultaten gevonden - van monotone versnelling of vertraging van de dynamica tot zelfs niet-monotone veranderingen wanneer men de activeit laat toenemen. Gebruikmakend van numerieke simulaties van thermische en niet-thermische actieve quasi-harde bollen, tonen we aan dat hun dynamica niet-monotoon is en het meest versneld is door activiteit wanneer de intrinsieke actieve lengteschaal (e.g., de persistentielengte) gelijk is aan de kooilengte, i.e., de lengteschaal gerelateerd aan de insluiting door omringende deeltjes. Dit inzicht, wat we toeschrijven aan het meest efficiënt scannen van lokale deeltjeskooien, staat ons toe de verschillende resultaten in vorige studies onder een noemer te brengen. Vervolgens hebben we via uitgebreide computersimulaties aangetoond dat het bovengenoemde argument volledig intact blijft voor zachtere deeltjes met variërende interactielengtes. We hebben ook steeds tragere relaxatiedynamica verder verkend en vinden dat de kooilengte de drempelwaarde vormt voorbij welke ons actief systeem qualitatief ander gedrag gaat vertonen (gemeten in termen van de fragiliteit) ten opzichte van een equivalent passief Browns systeem. Ter aanvulling van onze simulaties, hebben we een onderscheidende actieve MCT voor mengsels van niet-thermische zelfvoorstuwende deeltjes ontwikkeld. Deze is gebaseerd op een analogie tussen een overgedempt actief en een ongedempt passief systeem en zijn voorspellingen zijn qualitatief volledig consistent met onze simulatieresultaten.

Aansluitend hebben we getracht meer inzicht te verschaffen in de rol van het zelfstuwingsmechanisme ten aanzien van de glasachtige dynamica. Voor passieve materialen is het namelijk algemeen bekend dat de precieze microscopische dynamica, e.g., Newtoniaans of Browns, geen invloed hebben op de trage glasachtige dynamica. Om te testen of dit ook geldt in het actieve geval hebben wij een MCT afgeleid voor thermische AOUPs die direct vergeleken kan worden met een recent ontwikkelde MCT voor ABPs. Beide theorieën vormen de eerste actieve MCTs die expliciet de actieve vrijheidsgraden in acht nemen. We lossen de AOUP- en ABP-MCT vergelijkingen op in de twee-dimensionale ruimte en tonen aan dat beide modellen nagenoeg identieke resultaten geven voor een groot aantal waardes van de relevante controleparameters (pakkingsdichtheid, actieve snelheid en persistentietijd). We hebben deze theoretische equivalentie van de verschillende voortstuwingsmechanismen ook bevestigd via simulaties. Daarmee stellen we vast dat, tenminste voor de gebruikte modelsystemen, de microscopische details van het zelfstuwingsmechanisme het actieve glasachtig gedrag niet beinvloeden. We hebben vervolgens de actieve-MCT resultaten gebruikt in combinatie met het integratie-via-overgangen formalisme om theoretisch aan te tonen, vanuit eerste beginselen en gebruikmakend van alleen een passieve structuurfactor als input, dat ruimtelijke snelheidscorrelaties spontaan ontstaan in actieve systemen. Deze vormen een van de typische kenmerken van dichte actieve materie aangezien ze strict afwezig zijn in een passief glasachtig materiaal.

De thesis is afgesloten met een exploratie van het effect van chiraliteit op actieve glasachtige dynamica, wat kan ontstaan door bijvoorbeeld asymmetrieën in de vorm of het voorstuwingsmechanisme van deeltjes. Via simulaties hebben we de glasachtige dynamica van interacterende chirale actieve Brownse deeltjes (cABPs) bestudeerd en tonen aan dat wanneer onze chirale vloeistof glasachtige condities ondervindt het hoogst niet-triviale dynamica vertoont (vooral vergeleken met reguliere ABPs) met in sommige gevallen verrassend sterk herintredingsgedrag. De geobserveerde dynamische regimes zijn volledig gerationaliseerd met behulp van analytische resultaten voor een chiraal ABP in een harmonische potentiaal en ruimtelijke snelheidscorrelatiefuncties. Om het significante herintredingsgedrag te duiden hebben we een nieuw 'hamermechanisme' geïntroduceerd wat uniek is voor sneldraaiende deeltjes bij een hoge dichtheid.

Curriculum Vitae

8 maart 1994	Born in Roermond.
2006–2012	**Gymnasium** *Lyceum Schöndeln High School, Roermond* – Courses: Dutch, English, Greek, Geography, Maths, Physics, Chemistry, Biology
2012–2016	**Bachelor Applied Physics** *(cum laude)* *Eindhoven University of Technology* – Research internship at the Coherence and Quantum Technology (CQT) group: Efimov physics for deep square well potentials under the supervision of dr. ir. S.J.J.M.F. Kokkelmans
2016–2019	**Master Applied Physics** *(cum laude)* *Eindhoven University of Technology* – Specializations: Bio- and nanophysics & Plasma physics and radiation technology – Research internship at University College London (UCL): Diffusion of virus-like particles on the cell membrane under the supervision of dr. A. Šarić – Graduation project at the Theory of Polymers and Soft Matter (TPS) group: Collective cell dynamics in cancer metastasis under the supervision of dr. L.M.C. Janssen, prof. dr. C. Storm, and dr. A. Šarić (partly conducted at UCL)
2019–2023	**PhD in Physics** *Soft Matter and Biological Physics* *Eindhoven University of Technology*

List of publications

Published

1. *Characterising the diffusion of biological nanoparticles on fluid and cross-linked membranes.*
   V.E. Debets, L.M.C. Janssen, and A. Šarić.
   Soft Matter **16**, 10628 (2020).

2. *Enhanced persistence and collective migration in cooperatively aligning cell clusters.*
   V.E. Debets, L.M.C. Janssen, and C. Storm.
   Biophysical Journal **120**, 1483 (2021).

3. *Multi-component generalized mode-coupling theory: Predicting dynamics from structure in glassy mixtures.*
   S. Ciarella*, C. Luo*, V.E. Debets*, and L.M.C. Janssen.
   European Physical Journal E **44**, 91 (2021).

4. *Tagged-particle motion of Percus-Yevick hard spheres from first principles.*
   C. Luo, V.E. Debets, and L.M.C. Janssen.
   The Journal of Chemical Physics **155**, 034502 (2021).

5. *Durotaxis of passive nanoparticles on elastic membranes.*
   I. Palaia*, A. Paraschiv*, V.E. Debets, C. Storm, and A. Šarić.
   ACS Nano **15**, 15794 (2021).

6. *Generalized mode-coupling theory for mixtures of Brownian particles.*
   V.E. Debets, S. Ciarella, C. Luo, and L.M.C. Janssen.
   Physical Review E **104**, 065302 (2021).

7. *Cage length controls the nonmonotonic dynamics of active glassy matter.*
   V.E. Debets, X.M de Wit, and L.M.C. Janssen.
   Physical Review Letters **127**, 278002 (2021).

8. *Many-body correlations are non-negligible in both fragile and strong glassformers.*
   C. Luo, J.F. Robinson, I. Pihlajamaa, V.E. Debets, C.P. Royall, and L.M.C.

Janssen.
Physical Review Letters **129**, 145501 (2022).

9. *Influence of particle softness on active glassy dynamics.*
   V.E. Debets and L.M.C. Janssen.
   Physical Review Research **4**, L042033 (2022).
10. *Active glassy dynamics is unaffected by the microscopic details of self-propulsion.*
    V.E. Debets and L.M.C. Janssen.
    The Journal of Chemical Physics **157**, 224902 (2022).
11. *Glassy dynamics in chiral fluids.*
    V.E. Debets, H. Löwen, and L.M.C. Janssen.
    Physical Review Letters **130**, 058201 (2023).
12. *A deep learning approach to the measurement of long-lived memory kernels from generalised Langevin dynamics.*
    M.K. Winter, I. Pihlajamaa, V.E. Debets, and L.M.C. Janssen.
    The Journal of Chemical Physics (in press).

Submitted

13. *Dead or alive: Distinguishing active from passive particles using supervised learning.*
    G. Janzen[*], X.L.J.A. Smeets[*], V.E. Debets, C. Luo, C. Storm, L.M.C. Janssen, and S. Ciarella.
14. *Classifying the age of a glass based on structural properties: A machine learning approach.*
    G. Janzen, C. Smit[*], S. Visbeek[*], V.E. Debets, C. Luo, C. Storm, S. Ciarella, and L.M.C. Janssen.
15. *Mode-coupling theory for mixtures of athermal self-propelled particles.*
    V.E. Debets and L.M.C. Janssen.

In preparation

16. *Nonequilibrium correlation functions in thermal and athermal dense active fluids.*
    V.E. Debets[*], L. Sarfati[*], T. Voigtmann, and L.M.C. Janssen.
17. *Unveiling the anatomy of mode-coupling theory.*
    I. Pihlajamaa, V.E. Debets, C.C.L. Laudicina, and L.M.C. Janssen.

---

[*] These authors contributed equally.

Dankwoord

Het is gelukt, mijn thesis is voltooid en de PhD is hopelijk binnen! Tegelijkertijd betekent dit ook dat er een einde gaat komen aan vijf (inclusief afstuderen) super jaren in de SMB (en voorheen TPS) groep. Een tijd waar ik nu al met veel genoegen op terugkijk. Ik durf dan ook wel zo vrij te zijn om mijn promotietraject te bestempelen als bovengemiddeld comfortabel. Dit heb ik natuurlijk voor een groot deel te danken aan een aantal bijzondere mensen die ik bij deze graag zou willen bedanken.

Om te beginnen natuurlijk mijn eerste promotor, *Liesbeth Janssen*, en tweede promotor, *Kees Storm*. *Liesbeth*, je hebt me in grote mate wegwijs gemaakt in de academische wereld en geleerd dat wetenschap zoveel meer is dan alleen het doen van onderzoek. Ik heb ontzettend veel bewondering voor hoe je ogenschijnlijk makkelijk inhoudelijke scherpzinnigheid combineert met een uiterst menselijke benadering. De betrokkenheid die je, ondanks een steeds drukkere agenda, altijd naar mij (en al je studenten) hebt getoond, heb ik zeer gewaardeerd. Bedankt voor de geweldige begeleiding, al de fijne gesprekken, het vertrouwen, de kansen en de vrijheid die je mij hebt gegund tijdens mijn promotie. *Kees*, ook al was je minder direct betrokken bij mijn onderzoek, je vernieuwende manier van wetenschap bedrijven en leidinggeven aan SMB (en inmiddels de hele faculteit) zijn voor mij erg inspirerend. Dit heeft er zeker aan bijgedragen dat ik gelukkig nooit in “the valley of despair” ben terechtgekomen waarvoor veel dank.

Chengjie and *Simone*, my PhD predecessors, you have set an extremely high bar for all of Liesbeth’s students. Thank you for the valuable discussions and the great collaborations. *Corentin* and *Ilian*, though sometimes feeling a little bit like the third wheel, it has been an absolute joy to discuss science, abuse the whiteboard, and attend conferences with you. It goes without saying that the future of MCT is in great hands. I look forward to a review and/or perspective article. *Lila*, it has been great supervising you. Thank you for the nice collaboration that has resulted in one of the chapters in this thesis. I apologize for missing your infamous board game nights (that continue to this date), but you have been a fantastic addition to the group. *Xander*, ook al lag je affiniteit uiteindelijk meer bij de stromingsleer, bedankt voor de goede samenwerking. Je ABP-code heeft menig student in de groep waaronder mijzelf veel geholpen. *Wouter*, veel dank voor alle IT-gerelateerde zaken en, als vaste vertegenwoordiger van de PIs, natuurlijk ook voor de gezelligheid op de vele borrels. *Helmi*, bedankt voor alle hulp omtrent niet-wetenschappelijke zaken en de leuke gesprekken over allesbehalve fysica. Je enthousiasme en behulpzaamheid werken zeer aanstekelijk en dragen in grote mate bij aan de fijne werkomgeving. *Paul, Alexey, Janne-Mieke, Thijs, Chiara, Anwesha, Shari, Bart, René, Guido, Maarten, Giulia, Max, Nikos, Max, Quirine* and all other SMB/TPS-colleagues throughout the years, thank you all for creating such a wonderful atmosphere in our group. I look back with great pleasure on all the borrels, faculty parties, group outings, football tournaments, Christmas lunches, conferences, and of course the many coffee breaks.

I would also like to thank my committee members for taking the time to review my thesis and travel to Eindhoven to attend the defense in person. It is greatly appreciated. *Anđela Šarić*, *Hartmut Löwen*, and *Thomas Voigtmann*, thank you all for superb international collaborations during my PhD that have resulted in several publications.

Een goede werkomgeving is natuurlijk pas het halve werk en ik wil dit moment vooral ook aangrijpen om mijn vrienden te bedanken. Het is fijn om zoveel leuke mensen om me heen te hebben en het maakt dan ook niks uit dat mijn onderzoek de meeste van jullie vrij weinig zal interesseren. Dit geldt gelukkig niet voor mijn paranimfen *Sjoerd Loenen* en *Brian Schaap*, waar een goede vriendschap is samengegaan met een gedeelde voorliefde voor de natuurkunde. In het bijzonder wil ik *Brian*, wiens promotietraject aan de TU Eindhoven nagenoeg parallel liep met de mijne, bedanken. Enne *Brian*, bedankt voor alle squashwedstrijdjes, hardloopsessies, wandelingen, koffietjes, biertjes, dinertjes, en ga zo maar door, waarin meestal het hele spectrum van Limburgse onnozelheid tot aan theoretische fysica de revue passeerde. Wat een verrijking was je niet alleen voor mijn promotie maar ben je vooral ook voor mijn persoonlijke leven.

Behalve vrienden wil ik ook graag mijn familie bedanken. *Mam*, bedankt voor alle onvoorwaardelijke steun, alle keren dat je geprobeerd hebt om iets te begrijpen van mijn onderzoek (vaak tegen beter weten in) en je grenzeloze optimisme. Het blijft verdrietig dat pap dit niet heeft mogen meemaken, maar ik koester des te meer dat jij er wel bent. *Simone, Roald, Saskia* en *Luc*, ik voel me altijd gesteund door de Debets-clan en ben blij dat jullie er zijn. *Felix* bedankt voor je oprechte interesse in mijn artikelen. *Ans* en *Geert*, bedankt voor jullie betrokkenheid, warmte en steun.

Tot slot, lieve *Heleen*, bedankt voor je (absurde) humor waarmee je me altijd opvrolijkt, je steun, geduld, maar bovenal je liefde en compassie. Ik ben elke dag blij dat je er bent.